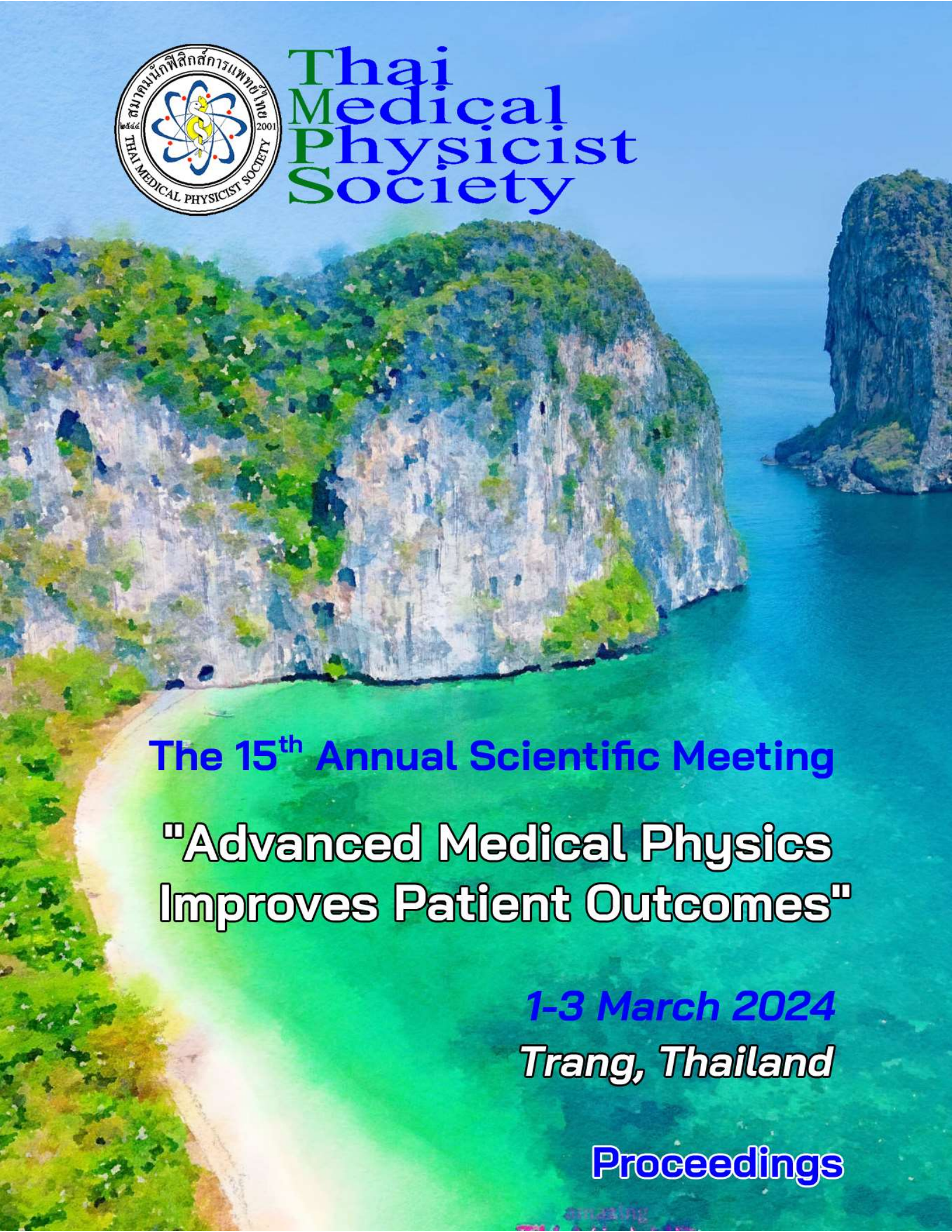
Thai Medical Physicist Society
The 15th Annual Scientific Meeting
"Advanced Medical Physics Improves Patient Outcomes"
1-3 March 2024
Trang, Thailand
Proceedings

The 15th Annual Scientific Meeting of Thai Medical Physicist Society

"Advanced Medical Physics Improves Patient Outcomes"

@ Rua Rasada Hotel

Trang, Thailand

1-3 March 2024

Organizing Committee

President	Anchali Krisanachinda
Vice President, Treasurer	Tanawat Sontrapornpol
Scientific	Puangpen Tangboonduangjit Chirapha Tannanonta Chumpot Kakanaporn Wannapha Nobnop Anirut Watcharawipha Nauljun Stansook Suphaluck Khajonkom Sirinya Ruangchan
Registration	Paranee Sahachjesdakul Lakkana Apipanyasopon
Commercial Exhibitor	Sivalee Suriyapee Panya Pasawang Tanawat Thawonwong Mintra Keawsamur
Social	Kitiwat Khamwan Thitithip Tippayamontri
Transportation	Amporn Funsian
Audiovisual	Pitchayut Nakkrasae
Webmaster	Tawatchai Chaiwatanarat
Secretary General	Taweap Sanghangthum

TMPS President Message

Ladies and gentlemen, esteemed colleagues,

I stand before you today with great pleasure and excitement as we gather for the 15th Annual Scientific Meeting, held from March 1st to March 3rd, 2024, at the Rua Rasada Hotel in the captivating province of Trang, Thailand. The theme of this year's conference is "Advanced Medical Physics improves Patient Outcomes," a subject that lies at the heart of our profession and touches the lives of countless individuals.

Trang province, located in the picturesque southern region of Thailand, is a place of unparalleled beauty. Its towering limestone karsts and pristine white sand beaches make it a truly stunning destination. In a nation that attracts tourists from all corners of the globe, Trang stands out as a hidden gem, offering a multitude of incredible attractions and activities without the crowds that often accompany more well-known destinations.

For those who venture through Trang City, a gateway to the nearby islands of Koh Muk, Koh Kradan, and Koh Ngai, there is a unique opportunity to experience an authentic Thai city that remains unspoiled by mass tourism. Trang is divided into two distinct sections, Trang City and Trang Old Town, where a rich and diverse culture thrives, harmoniously bringing together Buddhists, Catholics, and Muslims, all of whom take immense pride in their traditions, their culinary heritage, and their way of life. It is a truly remarkable place, and I encourage each of you to consider extending your stay to explore this captivating corner of Thailand.

The scientific program we have meticulously arranged for this event focuses on radiation oncology, diagnostic radiology, and nuclear medicine, with a special emphasis on medical imaging and medical physics. Over the course of two and a half days, our program will feature the prestigious Pradub Atthakorn Memorial Lecture, invited lectures, symposia, proffered papers, and a commercial exhibition, all designed to enrich our knowledge and spark fruitful discussions. I am delighted to inform you that TMPS members attending this meeting will be eligible to earn 12 credits, a valuable contribution towards the renewal of your Medical Physicist License.

Moreover, our Gala Dinner will be an occasion to celebrate the Certification of CQMP - ROMP, DRMP, and NMMP, recognizing the dedication and excellence of our colleagues.

I would like to take this moment to express our gratitude for your constant support and cooperation in making the Thai Medical Physicist Society what it is today. Your presence here underscores the strength and dedication of our community. We are all united by a common purpose: to advance the field of medical physics and ultimately improve patient outcomes. Let us continue to work together in pursuit of this noble goal.

With that, I wish you all an enriching and enjoyable experience at the 15th Annual Scientific Meeting, and I hope your time in Trang leaves you with lasting memories. Safe travels and thank you for your commitment to our profession.

Warm regards,

Anchali Krisanachinda, Ph.D., FIOMP, FIUPESM
President, TMPS
February 29, 2024

Opening Remark

Mr. Songklod Sawangwong
Governor of Trang

President, Thai Medical Physicist Society, Distinguished guests, and esteemed colleagues.

I am honored and thrilled to stand before you as we inaugurate the commencement of the 2024 Annual Scientific Meeting of the Thai Medical Physicist Society, focusing on the theme **"Advanced Medical Physics Improves Patient Outcomes."** My name is Mr. Songklod Sawangwong, and it is with great pleasure that I have been invited to preside over this momentous occasion.

The field of medical physics is one that merits admiration, encompassing a multidisciplinary profession crucial to the examination, diagnosis, and treatment of patients. Medical physicists play a pivotal role in utilizing the science of medical physics across diagnostic radiology, radiotherapy, and nuclear medicine. Their responsibilities extend to calculating and planning radiotherapy, ensuring the quality of radiological equipment, and ultimately delivering precise and effective patient treatments. Through their expertise, we witness advancements that elevate the quality and efficiency of patient healthcare.

The organization of this annual academic conference underscores our commitment to supporting and advancing the knowledge within the Thai Medical Physicist Society. Our goal is to harness modern technology, enabling us to enhance and evolve radiation treatment services for patients, placing us on par with international standards.

On behalf of the people of Trang Province, I extend heartfelt gratitude for choosing our province as the venue for this significant conference. Though Trang may be considered a secondary province, it boasts a rich history as a center for international trade and possesses a unique cultural heritage. Notably, it is home to Thailand's first rubber tree, introduced by Phya Rasadanupradit Mahison Phakdi brought from Malaysia. With ten districts and a population of approximately six hundred thousand, Trang is committed to maintaining a city with a high and sustainable quality of life.

Trang Province also possesses numerous tourist attractions, including Hat Chao Mai National Park, Kantang hot spring, Koh Mook, Emerald Cave, and more. I extend a warm invitation to all participants to explore and revel in the beauty of Trang Province at your leisure.

As we embark on the 2024 Annual Academic Conference, themed **"Advanced Medical Physics Improves Patient Outcomes"**, I sincerely hope that this gathering serves as a platform for the exchange of knowledge and experiences among Thai medical physicists nationwide. May this conference propel us toward further progress in the diagnosis and treatment of patients with radiation.

With great enthusiasm, I declare the 2024 Annual Scientific Meeting of the Thai Medical Physicist Society officially open. I extend my best wishes for the success of this meeting, with the hope that all objectives are met. Thank you

คำกล่าวพิธีเปิด

นายทรงกลด สว่างวงศ์
ผู้ว่าราชการจังหวัดตรัง

ท่าน นายกสมาคมนักฟิสิกส์การแพทย์ ท่านวิทยากร และผู้เข้าร่วมประชุมทุกท่าน

กระผมมีความยินดีและรู้สึกเป็นเกียรติอย่างยิ่ง ที่ได้รับเชิญเป็นประธานในพิธีเปิดการประชุมวิชาการประจำปี 2567 ของสมาคมนักฟิสิกส์การแพทย์ไทย ในหัวข้อ **"ความก้าวหน้าของฟิสิกส์การแพทย์เพิ่มประสิทธิผลของการรักษาผู้ป่วย"** ในครั้งนี้ เป็นที่น่าชื่นชมที่ทราบว่า วิชาชีพนักฟิสิกส์การแพทย์ เป็นสหสาขาวิชาชีพทางการแพทย์ที่มีบทบาทสำคัญในการตรวจ วินิจฉัยและรักษาผู้ป่วย โดยใช้ศาสตร์ทางฟิสิกส์การแพทย์ ด้านรังสีวินิจฉัย รังสีรักษาและเวชศาสตร์นิวเคลียร์ ทั้งการคำนวณวางแผนการรักษาด้วยรังสีและตรวจสอบคุณภาพของเครื่องมือทางรังสี ซึ่งส่งผลให้การรักษาผู้ป่วยมีความถูกต้องแม่นยำ ทำให้การตรวจวินิจฉัยและรักษาผู้ป่วยมีคุณภาพและประสิทธิภาพสูง การจัดให้มีการประชุมวิชาการประจำปี ถือเป็นกิจกรรมที่ช่วยสนับสนุนและพัฒนาองค์ความรู้ของวิชาชีพนักฟิสิกส์การแพทย์ไทย ให้สามารถนำเทคโนโลยีที่ทันสมัยมาปรับปรุงพัฒนาการบริการตรวจรักษาผู้ป่วยด้วยรังสีมีประสิทธิภาพสูงขึ้น เท่าเทียมกับนานาชาติ ต่อไป

กระผมในฐานะตัวแทนของชาวจังหวัดตรัง ขอขอบคุณที่เลือกจังหวัดตรังของเราเป็นสถานที่จัดประชุมวิชาการประจำปีในครั้งนี้ และยินดีต้อนรับผู้เข้าร่วมประชุมทุกๆท่าน จังหวัดตรังแม้จะเป็นจังหวัดรอง แต่ในอดีตเป็นศูนย์กลางการค้าขายกับต่างประเทศ มีวัฒนธรรมที่เก่าแก่ ที่สำคัญมีต้นยางพาราต้นแรกของประเทศไทยโดยท่านพระยารัษฎานุประดิษฐ์มหิศรภักดี ที่นำมาจากมาเลเซีย จังหวัดตรังของเรามี 10 อำเภอ ประชากรประมาณหกแสนคน โดยมุ่งเน้นให้เป็นเมืองแห่งคุณภาพชีวิตที่ดีและยั่งยืน จังหวัดตรังมีสถานที่ท่องเที่ยวสำคัญมากมาย เช่น อุทยานแห่งชาติหาดเจ้าไหม บ่อน้ำร้อนกันตัง เกาะมุกถ้ำมรกต เป็นต้น หากพอมีเวลา ขอเชิญทุกท่านเดินทางท่องเที่ยวเยี่ยมชมความสวยงามของจังหวัดตรังด้วยความยินดียิ่ง

สุดท้ายนี้ผมหวังเป็นอย่างยิ่งว่าการประชุมวิชาการประจำปี 2567 ของสมาคมนักฟิสิกส์การแพทย์ไทย ในหัวข้อ **"ความก้าวหน้าของฟิสิกส์การแพทย์เพิ่มประสิทธิผลของการรักษาผู้ป่วย"** ในครั้งนี้ จะเป็นเวที การแลกเปลี่ยนเรียนรู้ และประสบการณ์ของนักฟิสิกส์การแพทย์ไทยทั่วประเทศ เพื่อนำองค์ความรู้ไปพัฒนาการ ตรวจวินิจฉัยและรักษาผู้ป่วยด้วยรังสีให้มีความเจริญก้าวหน้า ยิ่งๆขึ้นไป

บัดนี้ ถึงเวลาอันสมควรแล้ว ผมขอเปิดการประชุมวิชาการประจำปี 2567 สมาคมนักฟิสิกส์การแพทย์ไทย ในหัวข้อ "ความก้าวหน้าของฟิสิกส์การแพทย์เพิ่มประสิทธิผลของการรักษาผู้ป่วย" และขอให้การประชุมวิชาการในครั้งนี้ประสบความสำเร็จ บรรลุตามวัตถุประสงค์ทุกประการ ขอบคุณครับ

Contents

Oral Presentation: Radiotherapy

Oral Presentation: Medical Imaging

Floor Plan

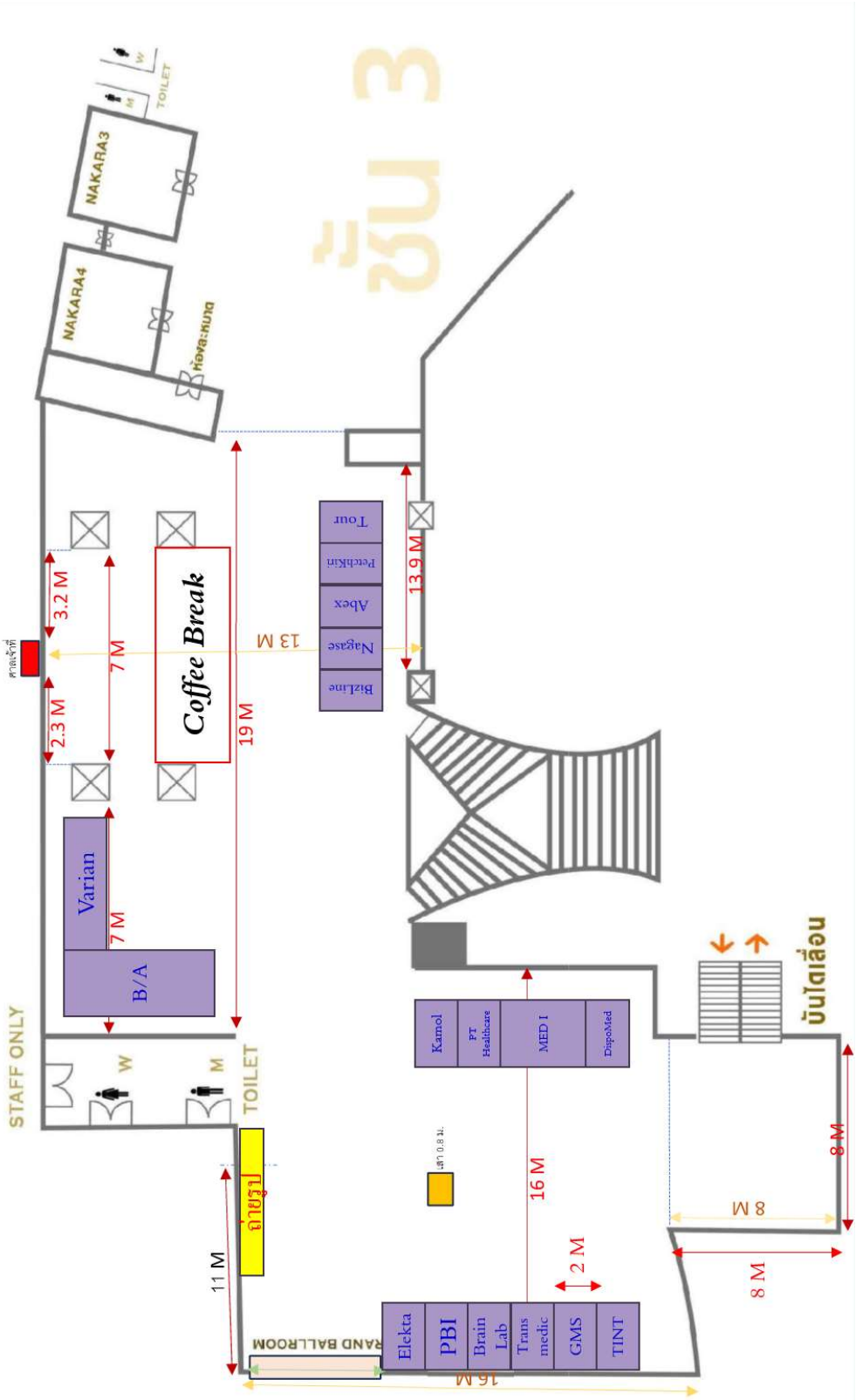
ชั้น 3
NAKARA3
NAKARA4
nova:หนาว
TOILET
Coffee Break
Tour
PetchKin
Abex
Nagase
BizLine
13.9 M
13 M
19 M
3.2 M
7 M
2.3 M
Varian
7 M
B/A
STAFF ONLY
W
M
TOILET
ฉายฐาน
11 M
Kamol
PT Healthcare
MED I
DispoMed
บันไดเลื่อน
16 M
8 M
8 M
8 M
2 M
Elekta
PBI
Brain Lab
Trans medic
GMS
TINT
16 M

Program at a Glance

Time	1 March 2024	
	Radiotherapy	Medical Imaging
08:00-08:10	Registration @ Nakara 4	
08:10-08:20		
08:20-08:30		
08:30-08:40		
08:40-08:50		
08:50-09:00		
09:00-09:10	Opening Ceremony	
09:10-09:20		
09:20-09:30	Pradub Atthakorn Memorial Lecture	
09:30-09:40	Monte Carlo Simulation in Medical Physics	
09:40-09:50	*Kosuke MATSUBARA*	
09:50-10:00		
10:00-10:10	Opening Commercial Exhibition & Coffee Break	
10:10-10:20		
10:20-10:30		
10:30-10:40	AI in Medical Imaging	
10:40-10:50	*Takayuki ISHIDA*	
10:50-11:00		
11:00-11:10	Proton Therapy: New Trend of Radiation Therapy Treatment	
11:10-11:20	*Chonlakiet Khorprasert, Kanjana Shotelersuk, Napapat Amornwichet*	
11:20-11:30		
11:30-11:40		
11:40-11:50		
11:50-12:00		
12:00-12:10	BA-Varian Lunch Symposium: HyperSight and Halcyon: Technical Breakthrough Empowering IGRT and Adaptation	
12:10-12:20	*Taoran Li*	
12:20-13:00		
13:00-13:10	What is AAPM Medical Physics 3.0?	
13:10-13:20	*Cheng B Saw*	
13:20-13:30		
13:30-13:40	Chulalongkorn Summer School in Advanced Medical Physics	
13:40-13:50	*Franco Milano*	
13:50-14:00		
14:00-14:10	Intraoperative Radiation Therapy for Early Stage Breast Cancer	
14:10-14:20	*Adhisabandh Chulakadabba, Tanawat Tawonwong*	
14:20-14:30		
14:30-14:40	Coffee Break	
14:40-14:50		
14:50-15:00		
15:00-15:10	Future Technology in Medical Physics	Academic Research on Liver MRI
15:10-15:20	*Taweap Sanghangthum*	*Yasuo TAKATSU*
15:20-15:30		
15:30-15:40	Treatment Planning Symposium	QA in Advanced Medical Imaging
15:40-15:50	*Komkrit Krongkietleart, Warinthorn*	Sawwanee Asavaphatiboon
15:50-16:00	*Rattanaareeyakorn, Naruepom Pischom*	
16:00-16:10		Radiomics: Current Status and Future Direction
16:10-16:20		Yothin Rakvongthai
16:20-16:30		
17:00	Heading to Hat Yao (หาดยาว)	
18:00-21:00	Gala Dinner @ Hat Yao	

Program at a Glance

Time	2 March 2024	
	Radiotherapy	Medical Imaging
08:00-08:10	3D Dosimetry System *Geoffrey Ibbott*	Let's understand the details of the MR signal *Noriyuki Tawara*
08:10-08:20		
08:20-08:30		
08:30-08:40	Moving to ART Strategies, Technological Consideration and Clinical Experience *Suphalak Khachonkham, Chirasak Khamfongkhruea, Wisawa Phongprapan*	Feasibility of single-time-point dosimetry for molecular radiotherapy *Kitiwat Khamwan*
08:40-08:50		
08:50-09:00		
09:00-09:10		225Ac-PSMA in Theranostic Prostate Cancer Therapy *Shuichi Shiratori*
09:10-09:20		
09:20-09:30		
09:30-09:40	Audit Dosimetry in Advanced Techniques RT *Supriyanto Pawiro*	IndoQCT: A software for comprehensive CT image quality assessment *Choirul Anam*
09:40-09:50		
09:50-10:00		
10:00-10:10	Coffee Break	
10:10-10:20		
10:20-10:30		
10:30-10:40	บทบาทนักฟิสิกส์การแพทย์ด้านรังสีรักษา: ความคาดหวัง(วิชาชีพและบริหาร) *Somsak Khuanchana*	Clinically Qualified Medical Physicists in Thailand *Anchali Krisanachinda, Puangpen Tangboonduangjit, Taweap Sanghangthum*
10:40-10:50		
10:50-11:00		
11:00-11:10	Challenges in Brachytherapy *Mintra Keawsamur*	DRLs: Clinical Indication *Anchali Krisanachinda*
11:10-11:20		
11:20-11:30		
11:30-11:40	Modified Electron Beam Calibration Procedures *Supriyanto Pawiro*	National DRLs for PCIs *Suphot Srimahachota*
11:40-11:50		
11:50-12:00		
12:00-12:10	Med-I Lunch Symposium: From the Production of Radioisotopes to the Precision Dispensing of Radiopharmaceutical Injections: the Complete Spectrum *Mario Malinconico*	
12:10-12:20		
12:20-13:00		
13:00-13:10	Proffered Papers in Radiotherapy	Proffered Papers in Medical Imaging
13:10-13:20		
13:20-13:30		
13:30-13:40		
13:40-13:50		
13:50-14:00		
14:00-14:10		
14:10-14:20		
14:20-14:30		
14:30-14:40	Coffee Break	
14:40-14:50		
14:50-15:00		
15:00-15:10	Proffered Papers in Radiotherapy	Proffered Papers in Medical Imaging
15:10-15:20		
15:20-15:30		
15:30-15:40		
15:40-15:50		
15:50-16:00		
16:00-16:10		
16:10-16:20		
16:20-16:30		
17:00	Business Meeting	

Program at a Glance

Time	3 March 2024	
	Radiotherapy	Medical Imaging
08:00-08:10		
08:10-08:20		
08:20-08:30		
08:30-08:40	Treatment Planning Systems for Small Field Dosimetry *Puangpen Tangboonduangjit*	CZT Digital Detectors: SPECT/CT *Panya Pasawang*
08:40-08:50		
08:50-09:00		
09:00-09:10	Stereotactic Radiosurgery in Tomotherapy *Anirut Watcharawipha*	Luminescence Dosimetry: Theory and Applications *Kosuke Matsubara*
09:10-09:20		
09:20-09:30		
09:30-09:40	Move Forward: More Effective and Efficient with Automatic QA in RT *Sawanee Suntiwong*	Photon Counting CT: Principles and Clinical Applications *Picha Shunhavanich*
09:40-09:50		
09:50-10:00		
10:00-10:10	Coffee Break	
10:10-10:20		
10:20-10:30		
10:30-10:40	Eclipse 18.0 A new era of efficiency and accuracy *Piyanan Liammookda (Varian, B/A)*	
10:40-10:50		
10:50-11:00	CT and MR Simulation : The Role of Imaging in Radiation Therapy *Patompong Polham (GE)*	
11:00-11:10		
11:10-11:20	Med-I & Tema Sinergie: Tema Sinergie: cutting-edge solutions for Nuclear Medicine, Radiopharmacy and beyond" *Alessandro Treré*	
11:20-11:30		
11:30-11:40	Med-I & Ammo imaging's solutions: GMP requirements in the production of rediophamaceuticals *Nicola Ceccamencini*	
11:40-11:50		
11:50-12:00	Medical Physics National License : Renewal Issues- การจัดเก็บคะแนนใบประกอบโรคศิลปะ ศาสตร์ฟิสิกส์การแพทย์ *Tanawat Sontrapornpol*	
12:00-12:10		
12:10-12:20	Closing Ceremony	
12:20-13:00	Lunch	

Grand Ballroom: All & Radiotherapy
Imaging: Nakara 3
Exhibition: In front of Grand Ballroom

Thai Medical Physicist Society
The Fifteenth Annual Scientific Meeting,
1-3 March 2024
Rua Rasada Hotel, Trang, Thailand
Theme: "Advanced Medical Physics Improves Patient Outcomes"

FRIDAY 1 MARCH 2024

MEETING ROOMS

Room	***Grand Ballroom (Opening & Radiotherapy & Business Meeting)***
	Nakara 3 (Medical Imaging, AI)
	Nakara 4 (Registration, Presentation Preparation)
	In front of Grand Ballroom (Commercial Exhibition & Coffee Break)

MEETING PROGRAM

08:00-09:00 REGISTRATION

09:00-09:20 OPENING CEREMONY

Room ***Grand Ballroom***
Chair: ***Anchali Krisanachinda***

09:20-10:00 **Pradub Atthakorn Memorial Lecture**
Monte Carlo Simulation in Medical Physics
Kosuke Matsubara

10:00-10:30 OPENING COMMERCIAL EXHIBITION & COFFEE BREAK

Room ***Grand Ballroom***
Chair: ***Taweap Sanghangthum***

10:30-11:00 **Current Status of the JSRT and AI Research in the Field of Medical Imaging**
Takayuki Ishida

11:00-12:00 **Proton Therapy: New Trend of Radiation Therapy Treatment**
Chonlakiet Khorprasert, Kanjana Shotelersuk, Napapat Amornwichet

12:00-13:00 **BA-VARIAN LUNCH SYMPOSIUM**
HyperSight and Halcyon: Technical Breakthrough Empowering IGRT and Adaptation
Taoran Li, PhD, Sr Medical & Clinical Science Liaison Manager, Varian Medical Affairs

Room ***Grand Ballroom***
Chair: ***Puangpen Tangboonduangjit***

13:00-13:30 **What is AAPM Medical Physics 3.0?**
Cheng B Saw

13:30-14:00 **Chula Summer School in Advanced Medical Physics**
Franco Milano

14:00-14:30 **Intraoperative Radiation Therapy for Early Stage Breast Cancer**
Adhisabandh Chulakadabba, Tanawat Tawonwong

14:30-15:00 COFFEE BREAK

Room ***Grand Ballroom***
Chair: ***Suphalak Khachonkham***

15:00-15:30 **Future Technology in Medical Physics**
Taweap Sanghangthum
15:30-16:30 **Treatment Planning Symposium**
Komkrit Krongkietleart, Warinthorn Rattanaareeyakorn, Narueporn Pischom

Room ***Nakara 3***
Chair: ***Kitiwat Khamwan***

15:00-15:30 **Academic Research on Liver MRI**
Yasuo TAKATSU
15:30-16:00 **QA in Advanced Medical Imaging**
Sawwanee Asavaphatiboon
16:00-16:30 **Radiomics: Current Status and Future Direction**
Yothin Rakvongthai

17:00 **HEADING to HAT YAO**
18:00-21:00 **GALA DINNER @ HAT YAO**

SATURDAY 2 MARCH 2024

Room ***Grand Ballroom***
Chair: ***Wannapa Nobnop***

08:00-08:30 **3D Dosimetry of Proton Beams and Influences on Response**
Geoffrey Ibbott
08:30-09:30 **Moving to ART Strategies, Technological Consideration and Clinical Experience**
Chirasak Khamfongkhruea, Wisawa Phongprapan, Suphalak Khachonkham
09:30-10:00 **Audit Dosimetry in Advanced Techniques RT**
Supriyanto Pawiro

10:00-10:30 COFFEE BREAK

Room ***Nakara 3***
Chair: ***Anchali Krisanachinda***

08:00-08:30 **Let's Understand the Details of the MR Signal**
Noriyuki Tawara
08:30-09:00 **Feasibility of Single-Time-Point Dosimetry for Molecular Radiotherapy**
Kitiwat Khamwan
09:00-09:30 **225Ac-PSMA in Theranostic Prostate Cancer Therapy**
Shuichi Shiratori
09:30-10:00 **IndoQCT: A Software for Comprehensive CT Image Quality Assessment**
Choirul Anam

Room ***Grand Ballroom***
Chair: ***Sivalee Suriyapee***

10:30-11:00 **The Role of Medical Physicist in Radiotherapy: Expectations of the Professional Boards.**
บทบาทนักฟิสิกส์การแพทย์ด้านรังสีรักษา: ความคาดหวัง (วิชาชีพและบอร์ดบริหาร)
Somsak Khuanchana

11:00-11:30 **Challenges in Brachytherapy**
Mintra Keawsamur

11:30-12:00 **Modified Electron Beam Calibration Procedures**
Supriyanto Pawiro

Room ***Nakara 3***
Chair: ***Anchali Krisanachinda***

10:30-11:00 **Clinically Qualified Medical Physicists in Thailand**
Anchali Krisanachinda, Puangpen Tangboonduangjit, Taweap Sanghangthum

11:00-11:30 **Anatomical-Based VS Clinical Indication Diagnostic Reference Levels (DRL)**
Anchali Krisanachinda

11:30-12:00 **Establishment of NDRLs for PCIs in Thailand**
Suphot Srimahachota

Room ***Grand Ballroom***

12:00-13:00 **MED-I LUNCH SYMPOSIUM**
From the Production of Radioisotopes to the Precision Dispensing of Radiopharmaceutical Injections: the Complete Spectrum
Mario Malinconico

Proffered Paper in Radiotherapy

Room ***Grand Ballroom***
Chair: ***Puangpen Tangboonduangjit***
Co-Chair: ***Lakkana Apipanyasopon***

13:00-13:10 **RT1_Treatment plans comparison between Halcyon and VersaHD for ultra-hypofractionated of high-risk prostate cancer using multicriteria optimization**
Kanyapat Prangnuan

13:10-13:20 **RT2_An evaluation of the impact of 4D-CBCT acquisition parameters on image quality and geometric accuracy in lung SBRT: a phantom study**
Sireetorn Choocherd

13:20-13:30 **RT3_Comparison of modified formalism output and TRS-398 absorbed dose to water in electron beams reference dosimetry in multiple radiotherapy centers**
Yasumon Thinka

13:30-13:40 **RT4_Dosimetric characterization of high-resolution diode array for patient-specific quality assurance of Stereotactic Radiotherapy**
Tongrak Yimpak

13:40-13:50 **RT5_Dose evaluation of a deep learning-based synthetic CT generation for head and neck cancer in photon and proton therapy**
Ailada Kuibumrung

13:50-14:00 **RT6_ Enhancing adaptive radiation therapy accuracy with Cyclegan-generated Synthetic CT from CBCT in pelvic region**
Paritt Wongtrakool

14:00-14:10 **RT7_Confidence limit of gamma passing rate for patient-specific quality assurance in pencil beam scanning proton therapy**
Nuttida Rawiwan

14:10-14:20 **RT8_Machine learning-based dose prediction in lung cancer radiation therapy for enhanced decision support systems**
Thitaporn Chaipanya

14:20-14:30 **RT9_A simple method of evaluation of real-time respiratory motion tracking accuracy utilizing the Exactrac Dynamic system**
Mongkol Kongsak

14:30-15:00 COFFEE BREAK

Room ***Grand Ballroom***
Chair: ***Chumpot Kakanaporn***
Co-Chair: ***Anirut Watcharawipha***

15:00-15:10 **RT10_Dosimetric comparison of IMRT, co-planar VMAT, non-coplanar VMAT and HyperArc for multiple brain metastases SRS**
Aksarapak Thawornnittayakul

15:10-15:20 **RT11_Machine learning-based patient selection for deep inspiration breath hold radiotherapy in left breast cancer**
Chanatinat Chotchuchuang

15:20-15:30 **RT12_A simple radiation-induced DNA damage model for proton therapy based on DBSCAN algorithm**
Sanhanat Chaibura

15:30-15:40 **RT13_Designing an in-house phantom daily QA for range verification for proton beam using GEANT4**
Paphatchaya Kheawyoi

15:40-15:50 **RT14_Monte Carlo model for out-of-field dosimetry during volumetric modulated arc therapy (VMAT)**
Daranporn Pongmettasanti

15:50-16:00 **RT15_A comparative analysis of geometric and dosimetric outcomes in atlas-based versus deep learning-based automated segmentation for head and neck radiation therapy**
Warisara Thanusilp

16:00-16:10 **RT16_Dose prediction in prostate cancer**
Pumipat Chaikamthorn

16.10-16.20 **RT17_ Determination of the surface dose correction factors for various detectors in spot scanning beam proton therapy**
Pakjira Saruang

Proffered Paper in Medical Imaging & AI

Room	***Nakara 3***
Chair:	***Yothin Rakvongthai***
Co-Chair:	***Picha Shunhavanich***
13:00-13:10	**IMAGE1_Absorbed dose calculation in thoracic CT using ICRP voxel phantoms and Monte Carlo simulation** *Shu Watanabe*
13:10-13:20	**IMAGE2_Assessment of patient radiation dose and image quality for trans-arterial chemoembolization from digital subtraction angiography combined with IVR-CT** *Sasi Boonsuan*
13:20-13:30	**IMAGE3_Optimal dual-time-point dynamic 68Ga-PSMA-11 PET/CT protocols for parametric imaging generation in prostate cancer patients** *Paphawarin Burasothikul*
13:30-13:40	**IMAGE4_Accuracy of 177Lu quantification for dosimetry calculation using 12-swiveling CZT detectors SPECT/CT camera** *Panattha Damthongsen*
13:40-13:50	**IMAGE5_Establishment of typical adult CT diagnostic reference levels (DRLs) in Ramathibodi hospital: a comparison of different dose collection methods** *Nichaphat Srisumetawupakit*
13:50-14:00	**IMAGE6_Kotaro Fukuoka_Effect of dosimeter location on the eye lens dose measurements for endoscopist** *Kotaro Fukushima*
14:00-14:10	**IMAGE7_Development of tungsten-doped borosilicate glass as a lead-free transparent radiation shield in nuclear medicine** *Satawatchara Suwanprateep*
14:10-14:20	**IMAGE8_Minimizing Slice-Overlap Artifacts in MRI Lumbar Spine: A Phantom Study** *Kannikar Kanyakam*
14:20-14:30	**IMAGE9_Impact of contrast agent administration on water equivalent diameter for size-specific dose estimate (SSDE) calculation in chest CT angiography** *Nuttanit Kaewsan*
14:30-15:00	COFFEE BREAK
Room	***Nakara 3***
Chair:	***Anchali Krisanachinda***
Co-Chair:	***Panya Pasawang***
15:00-15:10	**IMAGE10_Impact of Deep Learning-based Image Reconstruction on Arm-induced Artifacts in Abdominal CT** *Suppakit Wongvit-olarn*
15:10-15:20	**IMAGE11_Localization of Epileptogenic Zones Using Radiomic Analysis of Ictal and Interictal SPECT Data** *Jinjuthathip Thuwarojsakul*

15:20-15:30 **IMAGE12_Prediction of axillary lymph node metastasis in clinically node-negative breast cancer magnetic resonance imaging-based radiomics**
Wichasa Sukumwattana

15:30-15:40 **IMAGE13_Distant metastasis prediction after radiation treatment in patients with esophageal squamous cell carcinoma using CT-based radiomics**
Thanakrit Chanchayanon

15:40-15:50 **IMAGE14_Development of gold nanoparticle-incorporated gelatin-based hydrogel for radiation dosimetry**
Phavinee Choosin

15:50-16:00 **IMAGE15_Prediction of diabetic peripheral neuropathy in patient's limbs using inverse problem algorithm and Taiwan population-based clinical data**
Huang Shih-Hsun

16:00-16:10 **IMAGE16_Inverse problem algorithm application to analyze the peripheral visual field damage of glaucoma patients from clinical dataset: a Taiwan population-based survey**
Huang Shih-Hsun

Room ***Grand Ballroom***

16:20-16:50 BUSINESS MEETING
16:50-17:30 TMPS and JSRT Committee Meeting

SUNDAY 3 MARCH 2024

Room ***Grand Ballroom***
Chair: ***Chirapha Tannanonta***

08:30-09:00 **Treatment Planning Systems for Small Field Dosimetry**
Puangpen Tangboonduangjit

09:00-09:30 **Stereotactic Radiosurgery in Tomotherapy**
Anirut Watcharawipha

09:30-10:00 **Move Forward: More Effective and Efficient with Automatic QA in RT**
Sawanee Suntiwong

Room ***Nakara 3***
Chair: ***Anchali Krisanachinda***

08:30-09:00 **CZT Digital Detectors: SPECT/CT**
Panya Pasawang

09:00-09:30 **Luminescence Dosimetry: Theory and Applications**
Kosuke Matsubara

09:30-10:00 **Photon Counting CT: Principles and Clinical Applications**
Picha Shunhavanich

10:00-10:30 COFFEE BREAK

Room	***Grand Ballroom***
Chair:	***Taweap Sanghangthum***
10:30-10:50	**BA-Varian Presentation** **Eclipse 18.0 A new era of efficiency and accuracy** *Piyanan Liammookda*
10:50-11:10	**GE-Presentation** **CT and MR Simulation: The Role of Imaging in Radiation Therapy** *Patompong Polharn*
11:10-11.30	**Med-I & Tema Sinergie** **Tema Sinergie: Cutting-edge solutions for Nuclear Medicine, Radiopharmacy and beyond** *Alessandro Treré*
11:30-11:50	**Med-I & Ammo imaging's solutions-Presentation** **GMP requirements in the production of radiopharmaceuticals and beyond** *Icola Ceccomencini*
11:50-12:10	**Medical Physics National License: Renewal Issues -** **การจัดเก็บคะแนนใบประกอบโรคศิลปะ ศาสตร์ฟิสิกส์การแพทย์** *Tanawat Sontrapornpol*
12:10-12:30	**PRESENTATION AWARDS** **INVITATION TO 16th TMPS- 23th SEACOMP 2025** **CLOSING**
12:30-13:30	LUNCH SAFELY RETURN HOME

Abstracts: *Invited Lectures*

Monte Carlo Simulation in medical physics

Matsubara Kosuke

Department of Quantum Medical Technology, Faculty of Health Sciences, Institute of Medical, Pharmaceutical and Health Sciences, Kanazawa University, Kanazawa, Japan

matsuk@mhs.mp.kanazawa-u.ac.jp

The Monte Carlo (MC) simulation is a numerical experimental method that uses random numbers to reproduce events that include stochastic elements. Since all interactions between radiation and substances occur randomly according to a certain probability distribution, it makes sense to apply it to reproduce radiation interactions. The MC simulation plays an important role in the field of medical physics related to medical imaging, nuclear medicine, and radiotherapy, especially as a method for evaluating physical properties that are impossible or difficult to measure. Random number generators are required for the MC simulation to produce a large set of uncorrelated numbers. When a γ ray photon is incident on a substance, calculations are performed as follows: 1) random sampling of the free path length is performed to determine the interaction point, 2) the type of interaction is determined, 3) depending on the type of interaction, the presence or absence of characteristic X-ray and its angle, scattering angle and energy of scattered photon, *etc.*, are determined. For example, by placing a counter at the position where energy is deposited, the absorbed energy within the substance can be determined. The MC simulation has been used in various purposes, including designing new detectors, calculating absorbed doses, extracting physical properties, and reproducing interactions between radiation and deoxyribonucleic acids. Recently, a lot of effort has been made to improve and accelerate MC simulation with the help of machine learning including deep learning.

Keywords: Monte Carlo simulation, random number, radiation interaction, artificial intelligence

New trend of radiation therapy treatment

Khoprasert C, Shotelersuk K, Amornwichet N

Department of Radiology, Faculty of Medicine, Chulalongkorn University, Bangkok, Thailand

Radiation therapy has played a pivotal role in cancer treatment for many decades. In recent times, radiotherapy centers have increasingly adopted advanced technologies, such as 3-D conformal radiotherapy, intensity-modulated radiotherapy, and volumetric arc therapy. While these techniques enhance the precision of delivering radiation to the target, concerns persist about low-dose exposure to surrounding normal tissue. Particle beam therapy, with its unique Bragg peak physical property, presents an opportunity to further restrict radiation dosage to the target volume.

Notably, proton therapy, a form of particle beam therapy, has gained global traction in clinical practice. Data from the Particle Therapy Co-Operative Group (PTCOG) reveals a substantial rise in the number of proton therapy machines worldwide, from 19 units in 2000 to more than 250 units in 2023. The escalating use of proton therapy is reflected in the increasing number of treated patients and the expanding range of indications.

The proton Therapy machine has been operational at King Chulalongkorn Memorial Hospital (KCMH) since August 2021, marking a significant milestone as the first of its kind in Southeast Asia at that time. Table 1 displays the number of patients who have undergone proton therapy treatment from the year 2021 to 2023. Among the various types of cancer addressed by this cutting-edge technology, the most prevalent cases treated with the proton therapy machine include liver cancer (154 cases), brain and head and neck cancer (124 cases), breast cancer (93 cases) and pediatric craniospinal irradiation (15 cases).

Table 1 demonstrate number of patients treated with proton therapy at KCMH

Year	Number of patients (cases)
2021	61
2022	288
2023	342

Proton therapy has found a particularly accepted role in treating childhood cancers worldwide. With the improved outcomes and higher chances of long-term survival in pediatric cancer, the potential benefits of proton beam therapy in minimizing acute and late complications are compelling. Proton therapy's increasing application in pediatric brain tumors is evident in various studies. Retrospective analyses from Emory and Massachusetts General Hospital indicate comparable relapse-free survival and overall survival between proton and photon therapy in pediatric medulloblastoma. Notably, proton therapy exhibits fewer acute hematologic toxicities in craniospinal irradiation compared to photon therapy. Regarding late toxicities, studies suggest a significant reduction in hypothyroidism, sex hormone deficiency, and the need for endocrine replacement therapy in pediatric medulloblastoma patients undergoing proton therapy. Furthermore, superior intellectual function is observed in standard-risk medulloblastoma patients treated with proton therapy compared to photon therapy.

Proton therapy extends its application beyond pediatric CNS tumors to include non-CNS tumors like neuroblastoma, Hodgkin lymphoma, and rhabdomyosarcoma. Reports from MD Anderson Cancer Center demonstrate that proton therapy is well-tolerated and effective in pediatric neuroblastoma, offering high rates of local control with acceptable toxicities. Proton beam therapy

also presents a challenge in patients requiring re-irradiation, offering a means to limit unnecessary dose exposure to adjacent normal tissue.

However, despite its promising advantages, proton beam therapy faces limitations due to machine availability and high treatment costs. Therefore, cost-effectiveness studies across various diseases become crucial.

Current status of the JSRT and AI research in the field of medical imaging

Takayuki Ishida

Representative Director of the JSRT
Department of Medical Physics & Engineering, Graduate School of Medicine,
Osaka University

Congratulations on holding the 15th Annual Scientific Meeting of the Thai Medical Physicist Society (TMPS). The TMPS and the Japanese Society of Radiological Technology (JSRT) have an academic agreement and have been exchanging knowledge and technologies in the field of radiological technology at annual academic conferences. In the future, we could further deepen our exchanges and promote initiatives for academic development.

In this lecture, I will first introduce myself as the new representative director and discuss the current situation of JSRT. I would then talk about the latest artificial intelligence (AI) research in the medical imaging field.

The AI research topics in this talk are (1) development of artificial intelligence-based dual energy subtraction (AI–DES) technology for chest radiography, and (2) generation of synthesized-CC view mammogram from MLO view mammograms using the CR-GAN framework to synthesize novel-view images from MLO-view mammograms.

What is AAPM Medical Physics 3.0?

Cheng B Saw

Northeast Radiation Oncology Centers (NROC), Dunmore, PA 18512, USA

cbsaw2014@yahoo.com

The health care is undergoing a period of rapid transformation driven by economical, technological, and regulatory forces. MEDICAL PHYSICS 3.0 (MP3.0) is an initiative of the American Association of Physicists in Medicine (AAPM) charged with devising strategic guidance to ensure the sustainable and impactful contribution of medical physics to human health in this rapidly changing landscape.

What is Medical Physics 3.0? (https://www.aapm.org/education/VL/vl.asp?id=12385) MP 3.0 aims toward sustainable excellence by a stronger focus on the patient as opposed to the technology and by harnessing a scientific, service, and system-minded orientation to tailor medical interventions for greater precision and patient-specificity. MP 3.0 is aligned with a number of similar initiatives in other areas of health care, each of which has also recognized the importance of re-evaluation their traditional modes of practice to remain viable in this climate.

The broad MP 3.0 strategy entails three trajectories: (1) Expertize: encapsulating excellence in the knowledge and application of medical physics in both areas within the scope of practice (clinical, scientific, education, and leadership) and new areas where medical physicists can improve human health, (2) Sustainability: to enable and to ensure long term viability of the profession, (3) Visibility: the necessity that the critical role of medical physicists is recognized by clinical colleagues, administrators, and patients. MP 3.0 committee under the AAPM has created a web presence (https://mp30.aapm.org/) with content including good practices, areas of growth opportunities, inspiring stories, and video productions oriented toward prospective students, medical physicists, patients, and administrators.

Chula summer school in advanced medical physics

Milano F.

University of Florence, Italy

franco.milano.unifi@gmail.com

Introduction: Continuous and advanced training in the field of Medical Physics is essential. The field of Medical Physics is extremely dynamic, with advancements in applications of Data Science, technology, imaging modalities, treatment techniques, and research continually shaping the landscape. Continuous education and training are crucial for Medical Physicists to stay abreast of the latest developments, methodologies, and technologies.

Goal of a Summer School: The goals of a Summer School in Medical Physics can vary depending on the specific program and its intended audience. However, some common objectives include: Education and Training: Provide participants with a comprehensive understanding of the fundamental principles and advanced concepts in Medical Physics. This may include topics such as radiation physics, medical imaging, radiation therapy, and nuclear medicine. Skill Development: Enhance participants' practical skills related to Medical Physics techniques and technologies. This could involve hands-on training with equipment such as imaging devices or radiation therapy machines. Networking: Facilitate opportunities for participants to connect with professionals and experts in the field. Networking can be valuable for career development, mentorship, and collaboration on research or projects. Exposure to Emerging Technologies: Introduce participants to the latest advancements and innovations in Medical Physics. This may involve discussions, demonstrations, or even visits to relevant facilities to observe cutting-edge technologies in use. Research Opportunities: Provide a platform for participants to engage in research activities or projects under the guidance of experienced mentors. This can contribute to the advancement of Medical Physics knowledge and may lead to publications or presentations.

Chula Summer School: The teachers of Chulalongkorn University have been able not only to contribute to the birth and growth of the Thai Medical Physics Society but also to acquire international visibility and widespread credit so much so as to be a point of reference for the IAEA in South East Asia and other Countries. Their experience and the successes achieved will certainly allow the birth and growth of the Chula Summer School which will also bring enormous benefits to all of Thai Medical Physics in terms of training and international visibility.

Keywords: Long life training, Summer School, Education of Medical Physicists

Intraoperative radiation therapy for early-stage breast cancer

Chulakadabba A[1] and Tawonwong T[2]

1 Queen Sirikit Centre for Breast Cancer, Thai Red Cross Society, Bangkok, Thailand

2 Department of Radiology, Division of Radiation Oncology, King Chulalongkorn Memorial Hospital, Thai Red Cross Society, Bangkok, Thailand

Breast cancer has become the leading cancer for women. The risk of breast cancer increases with variety reasons, such as age, family history, and others. With the mammography and ultrasound examination, the breast cancer can be finding. Most of the early-stage breast cancer are treated with surgery, and often followed by external beam radiation therapy (EBRT) which take time about a month. The intraoperative radiation therapy (IORT) is a procedure where a single dose radiation delivered to the tumor bed during a lumpectomy. The IORT is chosen for elderly early-stage breast cancer to shorten the time for eliminates the microscopic cancer cell.

Breast Cancer has been operated, IORT, for 259 patients at Queen Sirikit Centre since 2010. The dedicated operating theatre with the radiation safety survey report was used. The lead shielding adding to the wall, ceiling, and floor is not needed for 50 kVp x-ray source. After the suitable applicator size was inserted in the operated cavity, the sterilized lead rubber sheet was used to cover the surgical breast for radiation safety purpose. The prescribed dose of 20 Gy at the applicator surface drops to 5 Gy at 1 centimeter in surround suspicious breast tissue. The irradiation time takes about 20 to 50 minutes for 20 Gy dose at the surface of applicator depends on the size of removal tumor. The satisfy outcome of IORT compared to EBRT considering the costs effectiveness was observed, especially elderly patients.

Future technology in medical physics

Sanghangthum T

Division of Radiation Oncology, Department of Radiology, Faculty of Medicine, Chulalongkorn University, Bangkok, Thailand.

mairt34@yahoo.com

ChatGPT (Chat Generative Pre-trained Transformer) is a chatbot developed by Open AI. Based on a large language model, it enables users to refine and steer a conversation towards a desired length, format, style, level of detail, and language. Successive prompts and replies, known as prompt engineering, are considered at each conversation stage as a context.

From ChatGPT3.5, the future of medical physics is likely to be shaped by several innovative technologies that will revolutionize patient care in radiation therapy and diagnostic imaging. These are some anticipated future technologies: next-generation imaging technology, AI-integrated treatment planning, real-time adaptive radiotherapy, quantitative imaging and radiomics, advanced particle therapy, nanotechnology applications, functional and molecular imaging integration, smart treatment delivery systems, enhanced safety measures and quality assurance. These anticipated technologies are poised to significantly improve treatment precision, efficacy, and patient outcomes, ushering in a new era of personalized and highly effective medical care in the field of medical physics.

Keywords: ChatGPT, Future Technology, Medical Physics

Treatment planning symposium

Krongkietleart K[1*], Rattanaareeyakorn W[2], Pischom N[3]

1 Division of Radiation Oncology, Lopburi Cancer Hospital, Lopburi, Bangkok, Thailand

2 Division of Radiation Oncology, Songkhlanagarind Hospital, Songkhla, Thailand

3 Division of Radiation Oncology, Surin Hospital, Surin, Thailand

**komrt39@hotmail.com*

Symposium on treatment planning in radiotherapy demonstrate a valuable opportunity for professionals in the field to share knowledge, discuss new technologies, and review best practices. Treatment planning is a critical component of radiotherapy, where clinicians use information from medical images and patient data to determine the optimal way to deliver radiation doses to target tumors while minimizing exposure to surrounding healthy tissues. Typically involves a series of presentations, workshops, and discussion panels covering various aspects of treatment planning. In this symposium, the speakers with experiences in different commercial treatment planning systems (Eclipse, Monaco, RayStation) will discuss the interesting cases of treatment planning among other speakers & audience and share their ideas including knowledge, tips & tricks to perform the high quality of treatment planning.

Keywords: Treatment planning system, Symposium, Eclipse, Monaco, RayStation

Academic research on liver MRI

Takatsu Yasuo

Molecular Imaging, School of Medical Sciences, Fujita Health University

yasuo.takatsu@fujita-hu.ac.jp

Currently, gadolinium-ethoxybenzyl-diethylenetriamine penta-acetic acid (Gd-EOB-DTPA; Primovist®; Bayer Schering Parma, Berlin, Germany) is a widely used contrast medium for tumor detection with magnetic resonance imaging (MRI).

Gd-EOB-DTPA act as a conventional nonspecific extracellular contrast medium in the early phase (i.e., in the vascular phases), thus allowing us to study the tissue vascularity. In the late phase, this contrast medium is distributed in hepatic cells over a set amount of time. Gd-EOB-DTPA is taken up by functional hepatocytes via organic anion transporters (OATPs), and excreted into the biliary canaliculi via multidrug resistance-associated proteins (MRPs). Thus, hepatocellular uptake and biliary excretion can be assessed.

Gd-EOB-DTPA is distributed in hepatic cells over time, improving tumor visibility by creating a contrast between the liver parenchyma and tumor in the hepatobiliary phase (HBP).

This presentation will show how to evaluate whether an appropriate HBP image or not.

When evaluating images of the HBP, liver function must be considered. This is because liver function can affect HBP images. Several studies determined that predictions of liver parenchymal enhancement depend on liver function according to the HBP of Gd-EOB-DTPA distribution. comprehensive liver function can be assessed by a blood test, but this cannot assess the function of liver segments or subsegments. The area of low distribution of Gd-EOB-DTPA (e.g., dysfunctional area) could be assessed visually or quantitatively from HBP images as the tool for diagnosis or treatment. Segmental liver information that assesses the dysfunctional area may also be helpful for studying liver transplantation in future studies.

On the other hands, it is necessary to predict an appropriate delay time to avoid long examination times for the diagnosis of patients, thereby facilitating the imaging examination in more patients in a short time and avoiding fatigue in patients. How to predict an appropriate delay time?

This presentation focuses on the studies that have been performed using Gd-EOB-DTPA and introduces the analysis method using images.

I hope that the above analysis information will be useful and contribute to clinical practice in liver MRI

QA in Advanced Medical imaging

Asavaphatiboon S

Diagnostic Radiology Division, Therapeutic and Diagnostic Radiology Department, Faculty of Medicine Ramathibodi Hospital, Mahidol University, Bangkok, Thailand.

Quality Assurance (QA) is a key to a continuous quality improvement program. The QA of advanced medical imaging in this session will mention the quality control (QC) or quality accreditation of computed tomography (CT) and magnetic resonance imaging (MRI) systems, which are the widely used imaging to diagnose or follow up the treatment. There are many recommendations and guidelines, e.g., the American Association of Physicists in Medicine (AAPM), American College of Radiology (ACR), International Atomic Energy Agency (IAEA), etc., to perform the QC of each imaging modality. The IAEA published the handbook of basic quality control tests for diagnostic radiology, IAEA human health series no. 47, in 2023.

New CT technology is rapidly developing and data is acquired using the helical mode with a wide radiation beam and multi-detector to get more coverage scan length per rotation time. It uses statistical and iterative reconstruction (IR) algorithms to decrease image noise to facilitate reduced radiation dose levels. The tube current modulation (TCM) techniques adjusts the tube current appropriate to patient body part. The AAPM published "Performance Evaluation of Computed Tomography Systems: The report of AAPM Task Group 233" in 2019 to introduce advanced performance assessment methods. This publication aims to supplement and complement existing and prior guidelines (AAPM no. 74, 2002). Dual-energy CT or multi-energy CT (DECT or MECT) is becoming increasingly common in clinical practice due to its advantages over conventional single-energy CT in better differentiation and classification of different types of tissues or material compositions. The DECT utilizes two different energy image data using dedicated hardware and post-processing analyses deployed to detect, visualize, and quantify the various elements, tissues and features. The current QC guidelines cannot be ideally evaluated or monitored; therefore, a routine dual-energy QC program is required to ensure the accuracy and reproducibility of DECT data and associated applications. For the CT dosimetry, the recommendations to measure or verify the dose metrics in CT do not include dosimetry in the dual-source and kV switching DECT systems.

MRI technology is developed regarding the magnetic field strength and the radiofrequency coil to get the high signal-to-noise ratio and high spatial resolution for the image quality improvement. ACR guidelines are generally used to monitor the performance of MRI system. In 2022, ACR published "Large and Medium Phantom Test Guidance for the ACR MRI Accreditation Program" and released the medium ACR MRI phantom for use in modern phased array head coils, which typically have smaller open volumes than quadrature head coils. In 2023, ACR also revised and updated the ACR manual for MR safety due to the higher magnetic field strength and more updated data.

In brief, QA is useful to monitor the equipment performance and optimize the image quality. Due to the rapidly development of the equipment performances, the medical physicists should follow and update the new recommendations or guidelines to accredit the equipment's performance.

Radiomics: Current status and future directions

Rakvongthai Y

Division of Nuclear Medicine, Department of Radiology, Faculty of Medicine, Chulalongkorn University, Bangkok, Thailand.

Chulalongkorn University Biomedical Imaging Group, Department of Radiology, Faculty of Medicine, Chulalongkorn University, Bangkok, Thailand.

yothin.r@chula.ac.th

Radiomics is a technique that quantifies both the morphological and intraregional attributes of a region of interest within a medical image. This process yields numerical features, which are subsequently used in predictive modeling for the diagnosis and prognosis of various diseases. Rapidly evolving, radiomics has demonstrated its potential of increased precision across several oncologic and non-oncologic applications. This session will delve into the current state of radiomics and its relationship with artificial intelligence (AI). The progress made and the evolving landscape of radiomics will be reviewed. Moreover, we will explore the challenges that need to be overcome for translation of radiomics into clinical practice, and the future directions of radiomics in the domain of medical imaging.

3D dosimetry of proton beams and influences on response

Ibbott, Geoffrey

Department of Radiation Physics, University of Texas MD Anderson Cancer Center, 1515 Holcombe Blvd., Houston, TX 77030 USA

ibbott@me.com

Proton beams offer the ability to conform dose distributions exquisitely to target volumes, allowing radiation oncologists to avoid exceeding tolerance doses to sensitive normal tissues. Several volumetric dosimeters have shown potential in conventional radiotherapy modalities, but suffer from dose under-responding, or signal quenching, in proton therapy. This reduced response has been seen with gels as well as with radiochromic plastics and may result from dependences on dose rate and linear energy transfer (LET). Investigations have shown that the under-response is affected by the chemical concentration of the active components of materials such as the PRESAGE® dosimeter, and changes to the composition have been shown to reduce quenching. It is not clear if similar changes can be made to gels. This report reviews studies into the impact of formulation changes on signal quenching, and the degree to which mathematical corrections might still be needed to achieve accurate dosimetry.

Keywords: 3D dosimetry, protons, quenching

Moving to ART strategies, technological considerations, and clinical experience

Khamfongkhruea C, Phongprapan W, Khachonkham S

Adaptive Radiation Therapy (ART) revolutionizes oncology with its dynamic and patient-focused approach. In contrast to traditional treatments, ART adapts to changes in tumor characteristics, ensuring optimal therapy throughout the treatment course. This innovative strategy utilizes advanced imaging, sophisticated planning systems, and dynamic delivery techniques for precise and personalized cancer care. This session is structured to cover three key dimensions – ART strategies, technological considerations, and clinical experiences:

In the first part, ART Strategies, participants will explore diverse implementation methods, comparing offline and online strategies. The session will further explore the distinctive roles of each professional in the ART process and investigate the cost-effectiveness of adopting ART universally, highlighting challenges and proposing solutions to achieve widespread integration.

Moving on to Technological Considerations, attendees will gain insights into the technological foundations of ART, providing an in-depth analysis of current offline and online technologies such as MR/Linac and Ethos. Attendees will gain insights into the machine requirements for effective ART, encompassing treatment machines and treatment planning systems. The session will also explore the future of ART technology.

Finally, the Clinical Experiences section will bridge the theoretical knowledge into practical focus by examining the clinical implementation of ART. Attendees will be guided through the offline and online ART workflow, covering critical components such as image registration, treatment planning, treatment delivery, and patient-specific QA. A dedicated Q&A session will allow participants to share challenges and experiences specific to their institutions, fostering a collaborative environment for addressing real-world issues in the realm of ART.

Audit dosimetry in advanced technique RT

Supriyanto Pawiro

University of Indonesia, Kampus Basru UI Depok, DEPOK, INDONESIA

Several IMRT verification projects have been carried out in hospitals in several countries. This audit procedure covers dosimetry ranging from point dose measurement, 2D dosimetry with film and/or dosimeter array, to 3D dosimetry. Although IMRT verification is often applied locally in hospitals, some studies show that local QA results do not always match the results of independent audits. A common approach to evaluating dose distribution is using gamma analysis, which in some cases has shown inconsistencies between results performed with local QA equipment and from independent audits, which usually result in lower pass rates. Inconsistencies between local and independent audit QA results support the need for independent dosimetry audits (in addition to relying solely on local QA measurements) for consistent, accurate, and safe radiation therapy treatments using complex modalities. The methods of audit dosimetry and result from several implementations will be presented.

The role of the medical physicist in radiotherapy: Expectations of the profession and hospital boards

Khuanchana S

Radiotherapy Department, National Cancer Institute, Bangkok, Thailand.

s098030971@yahoo.co.th

Introduction: At present, the Civil Service Office has determined medical physicist. It is a new professional field in Thailand. And setting standards for positions of medical physicists at the operating level to be highly qualified and announced in the Royal Gazette. Therefore, an understanding of the role and performance of the medical physicist's competency is very important to provide patient service with the highest quality and efficiency. There are also expectations from the professional team working with them including from the hospital's executive board team to be a member of the team in planning the development of the hospital's radiotherapy service system. As well as the efficiency of service billing Including analysing unit costs and break-even points. in providing new services

Results and Conclusion: Currently, there are 95 medical physicists working in the radiotherapy department. in hospitals under the Thai Ministry of Public Health, and 82.11 percent work in radiotherapy in 25 radiotherapy units. Of these, 82 medical physicists received professional licenses in medical physics. The reason is that the number of patients has increased greatly, resulting in the expansion of the number of new radiation machines and radiotherapy units. Therefore, it is necessary to increase the number of new medical physicist positions in the Ministry of Public Health. To be able to appoint medical physicists with backgrounds in both radiological technology and other fields. Reassigning medical radiologists who are already performing medical physicist duties to be appointed as medical physicists is not a solution to the medical physicist shortage problem and unable to increase service potential for the currently increasing number of patients. Shortage of physicists Affects the quality of treatment for cancer patients in radiotherapy. Especially the radiation technique is highly complex. In addition, this makes it impossible to help support other management systems that the hospital management team requests, including the Service System Quality Development Committee and Procurement Committee Including the unit cost system development committee, etc.

Keywords: Medical physicist, Shortage, Role and Management.

Challenges in brachytherapy

Keawsamur M

Division of Radiation Oncology, Department of Radiology, Faculty of Medicine, Chulalongkorn University, Bangkok 10330, Thailand

mintra.ke@chula.ac.th

Brachytherapy is a cancer treatment modality that involves the placement of radioactive sources directly into or next to the tumor. This technique allows for the delivery of high doses of radiation to the tumor while minimizing exposure to surrounding healthy tissues. However, there are several challenges associated with brachytherapy that need to be addressed.

One of the primary challenges in brachytherapy is the precise placement of the radioactive sources. Accurate positioning is crucial to ensure that the radiation effectively targets the tumor while minimizing damage to nearby healthy tissues. This requires advanced imaging techniques and specialized equipment to guide the placement of the radioactive sources.

Another challenge is ensuring optimal dose distribution within the tumor. Achieving uniform radiation dose throughout the tumor volume while sparing critical structures is essential for treatment success. Advanced treatment planning systems and imaging technologies are needed to accurately calculate and deliver the prescribed radiation dose.

Additionally, managing potential side effects for patients undergoing brachytherapy is a significant challenge. The proximity of radioactive sources to healthy tissues can lead to adverse effects such as inflammation, scarring, and damage to nearby organs. Therefore, strategies for mitigating these side effects and improving patient comfort during and after treatment are essential.

Addressing these challenges requires ongoing research and innovation in brachytherapy technology, treatment planning, and delivery techniques. Furthermore, education and training programs are essential for ensuring that healthcare professionals have the necessary expertise to perform brachytherapy procedures safely and effectively.

In conclusion, overcoming these challenges in brachytherapy is crucial for optimizing treatment efficacy and patient safety. Continued advancements in technology, treatment planning, and education are necessary to enhance the outcomes of brachytherapy as a cancer treatment modality.

Keywords: brachytherapy, localized delivery, optimizing treatment

Modified electron beam calibration procedure

Supriyanto Pawiro

University of Indonesia, Kampus Basru UI Depok, DEPOK, INDONESIA

Several international dosimetry protocols recommend using parallel-plate chambers for electron beam measurements, especially for low-energy electrons. Electron beam measurement using a parallel-plate chamber can effectively minimize fluence perturbation as the front windows of a parallel-plate chamber are thin and composed of materials with similar properties to water; therefore, the effect of the wall can be neglected. Some protocols do not recommend using a cylindrical chamber for electron beam dosimetry at low energies. This is because a cylindrical chamber can have a large fluence correction factor, which could be a source of high uncertainty. A more recent publication states that the variability in perturbation corrections for cylindrical chambers is 0.4%, and the results are not significantly different from those for parallel-plate chambers with the same specifications. They proposed a cylindrical chamber for reference dosimetry of all electron beams. Additionally, literature has shown superior long-term stability of a cylindrical chamber in an electron beam than parallel-plate chambers. The implementation of modified electron beam procedure which is tested in several institutions in both standard and high dose rate electron beams will be presented.

Anatomical-based VS clinical indication diagnostic reference levels (DRL)

Krisanachinda A[1*], Suksancharoen W[2], Jantawong H[3], Kanyakham K[4], Admontree S[5], Poosiri S[6]

1 Department of Radiology, Faculty of Medicine, Chulalongkorn University, Bangkok, Thailand.
2 Department of Radiology, King Chulalongkorn Memorial Hospital, Bangkok, Thailand.
3 Imaging Department, Bumrungrad International Hospital, Bangkok, Thailand
4 Imaging Center, Phyathai 2 Hospital, Phya Thai, Bangkok, Thailand
5 Advanced Diagnostic Imaging Center (AIMC), Faculty of Medicine, Ramathibodi Hospital, Mahidol University, Bangkok 10400, Thailand
6 Department of Radiology, Songklanagarind Hospital, Hat Yai District, Songkhla, Thailand

**anchali.kris@gmail.com*

Introduction: DRLs are defined for an anatomical location, with lacking information on the image quality for a specific clinical indication. The clinical indication strengthens the significance of DRLs, as they correspond to a better specified setting and would ultimately provide a stronger tool for optimization and comparisons between centers. Therefore, the definition of clinical indication-based, cDRLs, should be a combination of disease and symptoms, anatomical location and of the used technique required for different image quality levels. The concept had been introduced by IAEA for CT examinations in Thailand.

Methods: 11 clinical indications-based protocols are Head (Trauma, Stroke, Infarction), Head (Tumor, Infection, Metastasis), Sinus (Sinusitis), Cervical Spine (Trauma), Chest (Unclear chest symptoms, screening lung cancer), Chest (Follow up exam, Metastasis, Staging), Chest (Thrombus detection), Chest (Interstitial Lung disease, Bronchiectasis), Cardiac (Coronary Calcium score), Abdomen (Detection and Follow up of HCC) and Abdomen-pelvis (Detection of urinary track stones). Five centers with radiation dose monitoring software collected the data of $CTDI_{vol}$, DLP per phase, total DLP and the scan length in order to establish the local cDRLs. Patient size had been selected from BMI, 19-29 kg/m^2. Optimization had been performed after radiation dose reduction and image quality assessment. The second clinical DRLs is obtained and led to the establishment of NcDRLs, Thailand in 2023.

Results: The anatomical-based national DRLs on CT procedures consisted of CT brain, chest, whole abdomen with and without contrast media was announced in 2021. The dose metric for clinical DRLs were mostly lower than NDRLs. Both Head protocols showed approximately the same CTDIvol of 51 mGy, DLP of 1042 mGy.cm, and the scan length of 21 cm. Total DLP was double (2,103 mGy.cm) in Head (Tumor, Infection, Metastasis) because of 2 phases scan (without and with contrast) which all dose metrics were lower than the NDRLs. Chest examinations demonstrated the less variation of dose metrics among the different indications and the centres. Cardiac (Coronary Calcium score) examination showed the low dose of 7 mGy CTDIvol, 90 mGy.cm of DLP and total DLP and 16 cm scan length. Abdomen (Detection and Follow up of HCC) showed the highest total DLP due to 4 phases scans based on the clinical indications. The Abdomen-pelvis (Detection of urinary track stones) showed lower CTDIvol of 10 *V*S 11 mGy, and total DLP, 440 *VS* 1,423 mGy.cm, than abdomen protocol although anatomical coverage is larger. This due to the detection of stones requires lower image quality and number of phase than that the detection of HCC. When the NcDRLs Thailand was compared to the EUCLID data, our NcDRLs were higher than or similar to the EUCLID. There still be the areas of improvement or optimization

in Cardiac (Calcium score) and Sinus (Sinusitis) where the high intrinsic anatomical contrast is the anatomical of interest.

Conclusion: The establishment of NcDRLs is important especially for the examination with the anatomical of interest is high intrinsic contrast where the lower dose level with noise images is acceptable for image interpretation. This information suggests for further optimization of the CT dose and harmonize the clinical protocol among different centers.

Keywords: clinical indication DRLs, anatomical based DRLs, CTDIvol, DLP, EUCLID

Establishment of national diagnostic reference levels for percutaneous coronary interventions (PCIs) in Thailand

Srimahachota S

Department of Medicine, Faculty of Medicine, Chulalongkorn University, Bangkok, Thailand

Purpose: To establish national diagnostic reference levels (DRLs) for percutaneous coronary intervention (PCI) in Thailand for lesions of different complexity.

Methods: Radiation dose quantity, kerma-area-product (KAP) and cumulative air-kerma at reference point (CAK) from 76 catheterization labs in 38 hospitals in PCI registry of Thailand was transferred online to central data management unit. Sixteen - month data was analyzed. We also investigated role of different factors that influence radiation dose the most.

Results: Analysis of 22,737 PCIs resulted in national DRLs for PCI of 91.3 Gy.cm^2 (KAP) and 1360 mGy (CAK). The KAP values for type C, B2, B1 and A lesions were 106.8, 82.6, 67.9, and 45.3 Gy.cm^2 respectively and for CAK, 1705, 1247, 962, and 790 mGy respectively. Thus, as compared to lesion A, lesion C had more than double of the dose and B2 had nearly 1.6 times and B1 had 1.2 times. Our DRL values are lower than other Asian countries like Japan and Korea and are in the middle range of Western countries. University hospital had significantly higher dose than private or public hospital possibly because of higher load of complex procedures in University hospitals and trainees performing the procedures. Transradial approach showed lower doses than transfemoral approach.

Conclusions: This large multi-centric study established DRLs for PCIs which can act as reference for future studies. A hallmark of our study is establishment of reference levels for coronary lesions classified as per ACC/AHA and thus for different complexities.

Keywords: Diagnostic reference levels (DRL), radiation dose PCI, radiation dose CTO, Thailand DRLs for PCI, PCI complexity

IndoQCT: A software for comprehensive CT image quality assessment

Anam Choirul

Department of Physics, Faculty of Sciences and Mathematics, Diponegoro University, Jl. Prof. Soedarto SH, Tembalang, Semarang 50275, Central Java, Indonesia.

anam@fisika.fsm.undip.ac.id

Introduction: Assessment of computed tomography (CT) image quality is essential part in the regular quality control (QC) procedure. Manual assessment of CT image quality can be time-consuming and lead to a bias due to the subjectivity of examiners. IndoQCT is a software to automatically assess CT image quality. In this paper, the basic feature of IndoQCT to assess CT image quality on the American College of Radiology (ACR) phantom was examined.

Methods: As an initial study, the ACR phantom was scanned by GE Discovery LS. The scanning parameters were in axial mode, tube current of 250 mA, tube voltage of 120 kV, slice thickness of 5 mm, rotation time of 1 s, and field of view (FOV) of 240 mm. In this study, many parameters of CT image quality were automatically measured using IndoQCT. The parameters were (a) CT number accuracy, (b) CT number uniformity, (c) CT number linearity, (e) noise level, (f) noise uniformity, (g) peak frequency of the noise power spectrum (NPS), (h) average frequency of the NPS, (i) 10% modulation transfer function (MTF), minimum size of resolvable low-contrast, and (j) contrast-to-noise ratio of low-contrast object.

Results: It is found that the water CT number is -1.0 HU, CT number uniformity is 3.3 HU, CT number linearity has $R^2 = 0.9984$, image noise is 5.3 HU, noise uniformity is 1.0 HU, peak frequency of NPS is 0.29 mm^{-1}, average frequency of NPS is 0.33 mm^{-1}, 10% MTF is 0.68 mm^{-1}, the smallest size of resolvable low-contrast is 4 mm, and CNR is 1.3.

Conclusion: IndoQCT is able to automatically and accurately assess many image quality parameters on the ACR phantom. The results obtained from this study show that it is within the tolerance limits recommended by the ACR. IndoQCT has the potential to increase the efficiency of QC procedure.

Keywords: computed tomography, image quality, ACR CT phantom, IndoQCT

^{225}Ac-PSMA in theranostic prostate cancer therapy

Shiratori S

Department of Radiology, Faculty of Medicine Siriraj Hospital, Mahidol University, Bangkok, Thailand

shuichi.shi@mahidol.ac.th

Theranostic platform has been started in Thailand since 2018. Recently, theranostic centers provided routinely personalized medicine for neuroendocrine tumor and prostate cancer through targeted diagnosis and therapy are increasing. Most of the theranostic cases are metastatic castration-resistant prostate cancer (mCRPC). ^{68}Ga-PSMA-11, ^{68}Ga-PSMA-I&T, ^{18}F-PSMA-1007 are employed for diagnostic propose while ^{177}Lu-PSMA-617, ^{177}Lu-PSMA-I&T, ^{225}Ac-PSMA-617, ^{225}Ac-PSMA-I&T are effectively utilized for therapeutic purpose.

Although ^{177}Lu-PSMA has convinced the response of serum prostate-specific antigen level and radiologic findings with low relevant hematologic toxicity, ^{225}Ac-PSMA demonstrates better results especially radioresistance to Lu-177. The exploration of ^{225}Ac-PSMA marks a significant stride towards personalized and effective interventions for prostate cancer patients.

Therefore, ^{225}Ac-PSMA is concerned as the most promising paradigm in the realm of prostate cancer treatment in theranostic approach.

This presentation encompasses the synthesis, radiolabeling techniques, and quality control of ^{225}Ac-PSMA, emphasizing its specificity for prostate-specific membrane antigen (PSMA) and its potential as a theranostic agent. Through an analysis of current research findings, it also aims to elucidate the evolving landscape of ^{225}Ac-PSMA radiopharmaceuticals, providing valuable insights for researchers as well as clinicians invested in advancing prostate cancer diagnostics and treatment modalities.

Keywords: ^{225}Ac-PSMA, Theranostics, Prostate cancer therapy

Feasibility of single-time-point dosimetry for molecular radiotherapy

Khamwan K

Division of Nuclear Medicine, Department of Radiology, Faculty of Medicine, Chulalongkorn University, Bangkok 10330 Thailand

kitiwat.k@chula.ac.th

Radiopharmaceutical radiotherapy (RPT) has emerged as a promising and targeted approach for treating various cancers by delivering radiation directly to cancer cells. For example, RPTs with ^{177}Lu-prostate-specific membrane antigen (PSMA) ligands have demonstrated promising results for the treatment of metastatic castration-resistant prostate cancer. However, accurate dosimetry is critical and necessary in ensuring the efficacy and safety of using RPT. The traditional approach to calculating radiation dosimetry in targeted nuclear medicine therapies typically involves the acquisition of multiple imaging time points to determine the distribution of radiopharmaceuticals within the patient's body. While this method has been effective in providing comprehensive data for dosimetry calculation, it comes with inherent challenges, requiring considerable resources in terms of imaging equipment, personnel, and time, potentially leading discomfort and burdensome for the patients. Recognizing these challenges in clinical implementation, there is a growing interest in exploring alternative dosimetric approaches in performing routine personalized dosimetry in RPTs, such as single-time-point dosimetry (STP). This method aims to streamline the process by determining essential dosimetric data at a strategically chosen time point post-administration of the radiopharmaceutical, particularly using only a single SPECT scan. There are several previous studies indicate that STP dosimetry provides a reliable estimate of absorbed doses to target tissues, allowing for a more efficient and cost-effective dosimetric evaluation. However, simplified STP dosimetry methods may compromise the accuracy of dose estimates, with some exceptions, such as for ^{177}Lu-DOTATATE and for kidney dosimetry in different radiopharmaceuticals. This presentation delves into a cutting-edge investigation on the feasibility of adopting a single-time-point dosimetry paradigm for radiopharmaceutical radiotherapy, representing a novel and potentially transformative approach in the field of nuclear medicine.

Keywords: MIRD, radiopharmaceutical therapy, theranostics, STP dosimetry, lutetium-177.

Clinically qualified medical physicists in Thailand

Krisanachinda A[1*], Sanghangthum T[1], Tangboonduangjit P[2]

1 Department of Radiology, Faculty of Medicine, Chulalongkorn University, Bangkok, Thailand.

2 Department of Radiology, Faculty of Medicine, Ramathibodi Hospital, Mahidol University, Bangkok, Thailand.

**anchali.kris@gmail.com*

Introduction: Clinically qualified medical physicists are physicists working in healthcare who have received adequate academic postgraduate education in medical physics and relevant supervised clinical training. Clinically qualified medical physicists also work in other areas where ionizing or non-ionizing radiation or physics principles are used for diagnosis and treatment of patients. Imaging and therapeutic processes, procedures and interventions are dependent on the safe and effective use of information, science and technologies, and thus require qualified professionals to ensure optimal and appropriate patient care through quality assurance and optimization. The knowledge and competencies of medical physicists are acquired through academic education and clinical training programmes that fulfil internationally defined criteria. International Organizations for Medical Physics, IOMP, recognizes the need for continuing education and professional development and promote the certification of medical physicists to ensure a high standard of patient care.

Methods: In Thailand, six academic programs offer the medical physics education and five hospitals offer the structured clinical training in radiation oncology, ROMP, diagnostic radiology DRMP, and nuclear medicine NMMP under the cooperation of Thai Medical Physicist Society, TMPS. After completion of the clinical training, the final assessment consists of written, oral and practical examinations, were arranged. IAEA offers three external examiners for oral and practical assessments. Certifications are arranged at the annual meeting of TMPS.

Results: Currently, there are about 350 medical physicists in Thailand. Among these, there are about 100 CQMPs from 4 classes of clinical training in ROMP, DRMP and NMMP. Residents are Thai, Myanmar, Laos, Cambodian, Nepalese, and Vietnamese obtained clinical training in ROMP and NMMP. Medical Physics National License has been established in 2021 with the Continued Medical Physics Education (CMPE) program.

Conclusion: Thailand piloted the IAEA clinical training in 2007 and AMPLE in 2016. The successful of the CQMP are acknowledged to IAEA, TMPS, and the Royal Thai Government on their continuous support and strengthening the medical physics profession for the healthcare at high standard.

Keywords: medical physics education, clinical training, ROMP, DRMP, NMMP.

Let's understand the details of the MR signal!

Noriyuki Tawara

Department of Medical Radiological Technology*, *Faculty of Health Sciences and Graduate School of Health Sciences, Kyorin University, Mitaka-shi, Tokyo, Japan.

noriyuki-tawara@ks.kyorin-u.ac.jp

The origin of the MR signal is the electromotive force generated by Faraday's electromagnetic induction in the receiving RF coil, but little is known in the field of medical physics about how the MR spectrum is processed from the originating signal and how these parameters are derived. MRI system vendors also black box this part of the system, making it difficult for users such as medical physicists and radiologists to understand the principles related to MR signals because they cannot obtain and check actual data.

On the other hand, since MR signals are a phenomenon based on the Bloch equation, if the Bloch equation can be solved completely, MR signals can be obtained as data from simulation results without using actual equipment. In recent years, computer computing power has improved dramatically, and it is now possible to perform MRI simulations using the Bloch equation (Bloch simulation).

In this lecture, I will attempt to understand the MR signal generation process related to MR spectrum acquisition by using simulations of MR signal generation with Bloch simulation, which can also design pulse sequences.

(Supplement) If you are interested in attending this lecture, please review the following key words to facilitate your understanding.

Quadrature detection: Quadrature detection in one-dimensional NMR means that there are two detectors, which. are 90-degrees" out of phase, of the signal.

Phase difference sensitive detection: An application of heterodyne technology in which the target AC signal is converted to a DC signal by multiplication and extracted by a low-pass filter (LPF) that allows only low-frequency components to pass through.

Heterodyne: The generation of a new frequency by combining or multiplying two oscillating waveforms in radio or signal processing.

Frequency modulation (FM): The encoding of information in a carrier wave by varying the instantaneous frequency of the wave.

Carrier wave: A waveform (usually sinusoidal) that is modulated (modified) with an information-bearing signal (called the message signal or modulation signal) for the purpose of conveying information.

Treatment planning systems for small field dosimetry

Tangboonduangjit P[1], Suphaphong S[2], Rutchantuek S[2]

1 Master of Science Program in Medical physics, Faculty of Medicine Ramathibodi Hospital, Mahidol University, Bangkok, Thailand.

2 Radiation and Oncology Division, Therapeutic and Diagnostic Radiology Department, Faculty of Medicine Ramathibodi Hospital, Mahidol University, Bangkok, Thailand.

The treatment planning system employed for small field dosimetry serves the purpose of dose calculation. Various dose algorithms, namely correction-based, model-based, and principle-based algorithms, are utilized within the system. In the initial stages, prior to the development of CT images, correction-based algorithms are employed to calculate point doses in homogeneous medium. The determination of scattered doses involves the utilization of scattered correction factors measured in air and water to achieve collimator scattered factor (Sc) and phantom scattered factor (Sp), respectively. The attenuation by depth is addressed through metrics such as tissue-air ratio (TAR), tissue-maximum ratio (TMR), tissue-phantom ratio (TPR), and percentage depth dose (PDD), which also includes the consideration of wedge factors. Subsequent to the development of CT images, the model-based algorithm is implemented, featuring the convolution of primary and scattered radiation. Terms such as Total Energy Released per unit Mass (TERMA) represent primary radiation, while the Kernel represents scattered radiation. Varying vendors generate different types of kernels, such as point kernels and pencil beam kernels.

Calculating doses in heterogeneous medium involves determining the equivalent path length (EPL) for both correction- and model- based dose calculation. However, accuracy at the interface remains a challenge, prompting the development of Monte Carlo (MC) simulations. Despite being known for a few decades, recent technological advancements in computer speed have facilitated the contemporary use of MC simulations. This method involves simulating electron transport based on photon and electron interaction cross-sections, requiring a profound understanding of physics.

Accurate modeling in small field dosimetry using Monte Carlo simulations necessitates fine tuning the electron energy and focal spot size. To achieve this, parameters such as percentage depth dose (PDD) and beam profile serve as references for tuning the energy of electrons striking the target. Two methods currently employed for fine-tuning electron focal spot size. The first method includes referencing the output factor through the TRS483 protocol. The second one is using the dose divided by a full width at half maximum as a reference. The latter method involves scanning a beam across the detector as long as no source occlusion during measurement, making it independent of detector type and size.

In brief, the treatment planning system is a complex tool that requires comprehensive knowledge for input during beam configuration. Specifically, for small field conditions, precise adjustment of electron energy and focal spot size is imperative when treatment planning algorithms necessitate these parameters for beam modeling, particularly in the context of Monte Carlo simulations.

Stereotactic radiosurgery in Tomotherapy

Watcharawipha A

Division of Radiation Oncology, Department of Radiology, Faculty of Medicine, Chiang Mai University, Chiang Mai, Thailand.

Stereotactic Radiosurgery (SRS) is widely used in the neurosurgery when the case of the open surgery was limited. Many treatment modalities such as Gamma Knife, C-arm based linear accelerator (C-arm Linac), CyberKnife and so forth employed this technique. By various treatment machines, the American Association of Physicist in Medicine (AAPM) then published the guideline of this technique in the publication number 54 (AAPM NO.54). This guideline emphasized the processes that achieved the treatment goal by the non-restricted treatment modalities. The Tomotherapy (TT) then was one of the treatment machines that can be utilized on this treatment technique. Although the non-coplanar technique was the major technique in the SRS, AAPM NO.54 had not also restricted on the coplanar technique. Some publications thus provided the technique of treatment planning that can achieve the steep dose gradient in the coplanar treatment plans. Although the high dose gradient of the TT treatment planning cannot be compatible the non-coplanar technique of the C-arm Linac, the different distance of these is not further than 1-2 mm. However, the treatment time is one consideration that might be raised on the TT. The shorten treatment time can be attained by not only the large field width with dynamic jaws but also the high dose rate of this modality.

Move forward: More effective and efficient with automatic QA in RT

Suntiwong S

Radiation Oncology Department, Chulabhorn Hospital, Chulabhorn Royal Academy, Bangkok, Thailand

Quality Assurance (QA) in Radiation Therapy is essential for guaranteeing the accuracy of cancer treatment. It involves exact processes to verify equipment precision, dosimetric calculations, and overall treatment procedures. The ongoing evolution of QA methodologies ensures patient safety and drives technological advancements in radiation therapy. This session explores advancements in quality assurance (QA) methodologies, transitioning from manual approaches to semi-automatic and fully automatic systems. The first focus area investigates the realm of Automatic QA Machines, addressing the integration of mechanical, dosimetry, imaging, and safety aspects. The latest developments in automatic QA technologies will be discussed, exploring how these innovations streamline processes, reduce human error, save time, and enhance overall treatment quality. The second focal point revolves around Patient-Specific QA. The discussion will shift from traditional measurement-based QA to novel virtual and prediction-based QA approaches. Attendees will gain insights into cutting-edge techniques that leverage technology to tailor treatment plans to individual patient characteristics, ultimately optimizing therapeutic outcomes.

CZT digital detectors: SPECT/CT

Pasawang P

Division of Nuclear Medicine, Department of Radiology, King Chulalongkorn Memorial Hospital, Thai Red Cross Society, Bangkok, Thailand

Sodium iodide-thallium activated, NaI (Tl), has been used as the detector of scintillation camera until today. The scintillation camera was invented by Hal Oscar Anger and was called Anger Camera. NaI (Tl) detector offers extremely high light yield, high stopping power and good linearity of measurement. The principal characteristic of scintillators is that the absorbed photon energy is converted to visible light in proportion to the deposited energy. The light is detected by PMTs, converted to electrons at the cathode surface of the PMTs and attracted to a sequence of dynodes to create an avalanche of electrons that results in an electrical signal. Because of the many steps involved, the uncertainty in the measured energy signal is quite large percentage of energy resolution. Recently, SPECT systems based on cadmium zinc telluride (CZT) has been introduced. CZT is a solid-state detector that generates signals from the collection of induced charge created by the ionizations from photoelectric interactions or Compton scattering. The charges are collected by individual anodes, since a high voltage is applied between the cathode and the pixelated anodes. Each anode therefore acts as an individual detector. The benefits of CZT over NaI (Tl) detector in SPECT system are less scatter, better lesion contrast, improved energy resolution, shorter scan times and lower injected-activity. However, CZT SPECT detects photons in the energy range of 40–200 keV, which limits the use of certain isotopes.

Luminescence dosimetry: Theory and applications

Matsubara Kosuke

Department of Quantum Medical Technology, Faculty of Health Sciences, Institute of Medical, Pharmaceutical and Health Sciences, Kanazawa University, Kanazawa, Japan

matsuk@mhs.mp.kanazawa-u.ac.jp

Luminescence dosimetry is the process of quantifying the radiation dose using detectors that emit luminescence. Storage phosphors have been used for luminescent-type dosimeters including thermoluminescence (TL), optically stimulated luminescence (OSL), and radio-photoluminescence (RPL) dosimeters. When the energy of ionizing radiations is absorbed by the storage phosphor, carriers are generated, and the number of carriers is proportional to the absorbed radiation energy. These carriers are then captured and stably stored at trapping center. These trapped carriers are stimulated to release, recombine at the luminescence center, and emit light. Because the emission intensity of TL, OSL, and RPL is proportional to the incident radiation dose, it can be converted into absorbed dose, kerma, and personal dose equivalent by calibrating these dosimeters and applying appropriate correction factors. An advantage of luminescence dosimeters is that they can be reused after removing the original signal. For TL and RPL dosimeters, the signal can be erased by annealing the detectors. For OSL dosimeters, the signal can be erased by exposing the detectors to visible light, *i.e.*, bleaching them. The luminescence dosimetry is useful not only for radiotherapy field but also for medical imaging field. Examples of applications in the field of medical imaging include such as skin dose measurement, organ dose measurement using anthropomorphic phantoms, and occupational radiation dose monitoring. However, major challenges of the luminescence dosimetry for medical imaging field are the energy and angular dependence of the dosimeters. It is unlikely that they can be completely corrected, resulting in increased uncertainty in the final dose estimate.

Keywords: thermoluminescence, optically stimulated luminescence, radio-photoluminescence

Photon counting CT: Principles and clinical applications

Shunhavanich P

Department of Radiology, Faculty of Medicine, Chulalongkorn University, Bangkok, Thailand

picha.s@chula.ac.th

Abstract: Photon-counting-detector CT (PCD CT) with new detector technology has many advantages over conventional, energy-integrating-detector CT, including elimination of electronic noise, increased spatial resolution, improved contrast-to-noise ratio, and constant availability of spectral information. In this review, the principles and benefits of PCDs are described. We also discuss different clinical applications and possible nonidealities of the system and mention different implementations of PCD CT. This emerging technology has the potential to change future medical imaging in CT.

Keywords: Computed Tomography, Photon-counting detectors, Spectral CT

การจัดเก็บคะแนนหนังสือขออนุญาตให้ทำการประกอบโรคศิลปะโดยอาศัยศาสตร์ฟิสิกส์การแพทย์

ผศ.(พิเศษ) ธนวัฒน์ สนทราพรพล

สาขาเวชศาสตร์นิวเคลียร์ ฝ่ายรังสีวิทยา โรงพยาบาลจุฬาลงกรณ์ สภากาชาดไทย

ประกาศกระทรวงสาธารณสุข เรื่อง การอนุญาตให้บุคคลทำการประกอบโรคศิลปะโดยอาศัยศาสตร์ฟิสิกส์การแพทย์ ลงในราชกิจจานุเบกษา เมื่อวันที่ ๒ พฤศจิกายน ๒๕๖๓ ทำให้นักฟิสิกส์การแพทย์ไทยทำงานภายใต้เงื่อนไขหนังสือขออนุญาตให้ทำการประกอบโรคศิลปะโดยอาศัยศาสตร์ฟิสิกส์การแพทย์ ที่ดำเนินการด้วยอนุกรรมการพิจารณาการอนุญาติให้บุคลทำการประกอบโรคศิลปะโดยอาศัยศาสตร์ฟิสิกส์การแพทย์ ภายใต้การกำกับดูแลด้วยคณะกรรมการการประกอบโรคศิลปะ ปัจจุบันมีนักฟิสิกส์ที่มีหนังสืออนุญาตทั้งสิ้น ๓๑๙ ท่าน หนึ่งในเงื่อนไขหนังสืออนุญาตก็คือมีอายุสองปี ต้องทำการต่ออายุหนังสืออนุญาตด้วยการเก็บคะแนนให้ได้ ๑๒ หน่วยคะแนน และยื่นคำขอต่ออายุใบประกอบต่อผู้อำนวยการกองสถานพยาบาลและการประกอบโรคศิลปะ กรมสนับสนุนบริการสุขภาพ พร้อมด้วยเอกสารหรือหลักฐาน ก่อนวันที่หนังสืออนุญาตหมดอายุสามสิบวัน ซึ่งหน่วยคะแนนได้จากคณะทำงานพิจารณาหน่วยคะแนนการขอต่ออายุหนังสือขออนุญาต ที่พิจารณาจากการพัฒนาความรู้ความสามารถทางวิชาชีพอย่างต่อเนื่อง อย่างใดอย่างหนึ่ง ในเรื่อง เข้าร่วมประชุม อบรม สัมมนา เกี่ยวกับศาสตร์ฟิสิกส์การแพทย์ เขียนบทความทางวิชาการเกี่ยวกับศาสตร์ฟิสิกส์การแพทย์ลงในวารสารนิตยสาร เป็นวิทยากรให้ความรู้เกี่ยวกับศาสตร์ฟิสิกส์การแพทย์ กลั่นกรองบทความหรือโครงร่างงานวิจัย การอ่านผลงานเพื่อประเมินตำแหน่งทางวิชาการ หรือเป็นผู้ฝึกอบรมทางคลินิก ให้ความรู้แก่ผู้ศึกษาดูงาน เป็นกรรมการการควบคุมการวิจัยของนักศึกษาที่เกี่ยวกับศาสตร์ฟิสิกส์การแพทย์ หรือศาสตร์อื่นที่เกี่ยวข้อง

Abstracts: *Oral Presentation: Radiotherapy*

Treatment plans comparison between Halcyon and VersaHD for ultra-hypofractionated of high-risk prostate cancer using multi-criteria optimization

Prangnuan K[1*], Tangboonduangjit P[1], Khachonkham S[1], Thuratong S[2], Thiranuntakul N[2]

1 Master of Science Program in Medical Physics, Faculty of Medicine Ramathibodi Hospital, Mahidol University, Bangkok, Thailand.

2 Thammasat Radiation and Oncology Center, Thammasat university Hospital, Pathum Thani, Thailand.

**kanyapat.jzy@gmail.com*

Introduction: The innovative approach of multi-criteria optimization aids in the creation of treatment plans. This research compares the plan quality and deliverability of various linear accelerator architectures in a multi-vendor setting while utilizing the same treatment planning system with multicriteria optimization in ultra-hypofrationated high-risk prostate cancer.

Methods: Nine image sets of high-risk prostate cancer treated by Halcyon with a prescription dose of 40 Gy in 5 fractions were re-planned for the VersaHD traditional C-arm machine using 6 MV energy with flattening filter-free (FFF) and auto dosage rate mode. Anisotropic analytical algorithm (AAA) calculation with multicriteria optimization was used in Eclipse treatment planning system version 16.1 to generate the new plans. The entire plan underwent a dry run to correct the delivery data. All dose-volume histograms, conformity index, homogeneity index, and delivery parameters were assessed and compared using the student's pair t-test on the PASW statistic 18 application.

Results: The multi-criteria optimization technique offered equivalent coverage in PTV40 and PTV30 but exhibited the distinction of dose coverage in D98 and D95, with corresponding p-values of 0.044 and 0.037 in PTV25. The mean dose in surrounding organs was not differ appreciably in any PTV. The conformity index demonstrated a difference in PTV30 and PTV25 with p-values of 0.049 and 0.005, respectively. The homogeneity index showed a distinct difference only for PTV25, with a p-value of 0.014. The mean total monitor units for VersaHD and Halcyon were 3226.92 and 3581.06 MUs, respectively. The typical beam on time figured for Halcyon and VersaHD were 4.66 and 5.17 minutes, respectively. Overall, both devices showed the same capabilities in the delivery section.

Conclusion: The combination of the SBRT approach with simultaneous integrated boost (SIB) pelvic node irradiation in ultra-hypofractionated for high-risk prostate cancer patients on the Halcyon and VersaHD is comparable in terms of plan quality and deliverability.

Keywords: Halcyon, VersaHD, high-risk prostate cancer, multi-criteria optimization.

An evaluation of the impact of 4D-CBCT acquisition parameters on image quality and geometric accuracy in lung SBRT: A phantom study

Choocherd S[1*], Changkaew P[2], Khachonkham S[1,2], Stansook N[1,2]

1 Master of Science Program in Medical Physics, Department of Diagnostic and Therapeutic Radiology, Faculty of Medicine, Ramathibodi Hospital, Mahidol University, Bangkok, Thailand

2 Division of Radiotherapy and Oncology, Department of Diagnostic and Therapeutic Radiology, Faculty of Medicine, Ramathibodi Hospital, Mahidol University, Bangkok, Thailand

**Fonsireetorn@gmail.com*

Introduction: Stereotactic Body Radiation Therapy (SBRT) in the lung delivers precise, high-dose radiation to enhance local control and reduce toxicity. Four-dimensional cone-beam computed tomography (4D-CBCT) that can generate images related to the patient's breathing is required. However, the acquisition parameters and breathing patterns affect geometric accuracy and image quality. The objective of this study is to identify suitable 4D-CBCT parameters that yield high image quality and geometric accuracy in lung SBRT.

Methods: The moving phantom with a normal breathing pattern was performed in 4D-CBCT using various acquisition parameters as the modified protocols, including tube current, frame rate, and gantry speed. Percentage volume difference, signal-to-noise ratio (SNR), contrast-to-noise ratio (CNR), and edge response width (ERW) were used to evaluate the geometric accuracy and image quality of the 4D-CBCT. The protocol, which consistently provided superior outcomes compared to the default protocol, was employed throughout the trial to analyze different breathing patterns, including the retrospective breathing of SBRT patients. The results of the modified protocol were analyzed and compared to those of the default protocol using the same image quality metrics.

Results: The modified protocol significantly enhances geometric accuracy and image quality, increasing SNR and CNR by 25.21% and 10.26%, respectively, while decreasing ERW and the percentage difference in volume by 18.08% and 2.88%, respectively. Compared to the default protocol, there is no significant difference in quantitative results ($p > 0.05$) among abnormal breathing patterns and patient patterns. However, the modified protocol demonstrates a noticeable reduction in aliasing and streak artifacts in 4D-CBCT images.

Conclusion: The modified protocol indicates excellent performance in providing high-quality images, accurate geometry, and fewer streak artifacts in 4D-CBCT images. These advancements are adequate for SBRT imaging. However, the expense of additional time and imaging doses should be considered.

Keywords: Stereotactic Body Radiation Therapy, Four-Dimensional cone-beam computed tomography acquisition parameters, geometric accuracy, image quality

Comparison of modified formalism output and TRS-398 absorbed dose to water in electron beams reference dosimetry in multiple radiotherapy centers

Thinka Y[1], Tawonwong T[2], Supriyanto A. P[3], Tangboonduangjit P[4], Intanin P[5], Kittiva N[6], Maknitikul S[7], Dachaworakul K[8], Sanghangthum T[1*]

1 Medical Physics Program, Department of Radiology, Faculty of Medicine, Chulalongkorn University, Bangkok, Thailand
2 Division of Radiation Oncology, Department of Radiology, King Chulalongkorn Memorial Hospital, Bangkok, Thailand
3 Department of Physics, Faculty of Mathematics and Natural Sciences, Universitas Indonesia, Depok, Indonesia
4 Radiation Oncology Division, Department of Radiology Faculty of Medicine, Ramathibodi Hospital, Mahidol University, Bangkok, Thailand
5 Radiation Oncology Department, Chulabhorn Hospital, Chulabhorn Royal Academy, Bangkok, Thailand
6 Department of Radiology, Faculty of Medicine Vajira Hospital, Navamindradhiraj University, Bangkok, Thailand
7 Department of Radiation Oncology, Phramongkutklao Hospital, Bangkok, Thailand.
8 Cancer Center Thainakarin Hospital, Bangkok, Thailand

**fangyasumon@gmail.com*

Introduction: In electron beam therapy, the absorbed dose calibration relies on IAEA's TRS-398 and AAPM's TG-51 standards. For low-energy electron beams, plane-parallel chambers are recommended. This study aimed to compare absorbed dose to water using the modified formalism with cylindrical chambers against TRS-398 protocols in multiple centers.

Methods: Data collection involved six centers in Bangkok, where the absorbed dose to water was measured using Varian linear accelerators for all electron beam energies, specific to each institute's electron beam model. Modified calibration employed cylindrical chambers for all energy beams, while TRS-398 used them for high-energy and plane-parallel chambers for low-energy, requiring cross-calibration. Charge readings utilized IBA FC-65G, PTW30013, and PPC40 ionization chambers. The results expressed as absolute dose per monitor unit (cGy/MU), underwent a comparative analysis between the modified formalism and TRS-398, with mean differences assessed using Bland-Altman plots.

Results: In all six centers, the dose comparisons yielded acceptable results, all below ±2% difference, as set by TRS-398's tolerance limit. For low-energy electron beams, percent dose discrepancies ranged from -1.57% to 0.75%, and ranged from -0.37% to 1.02% for high-energy. The wider discrepancies range of low-energy may arise from chamber-to-chamber variations, setup errors, interpolating of $k_{Q,Qcross}$ values. The mean difference between the two protocols was only 0.0002%, indicating no significant bias on average. Results within the 95% confidence interval affirmed the methods' similarity, ensuring reliable measurements.

Conclusion: The modified calibration method and TRS-398 protocols prove compatible and suitable for electron beam calibration. Furthermore, the modified approach emerges as a potentially superior alternative, reducing uncertainty by eliminating the need for cross-calibration.

Keywords: IAEA TRS-398, AAPM TG-51, electron beam calibration, absorbed dose to water, modified calibration, cylindrical chamber

Dosimetric characterization of high-resolution diode array for patient-specific quality assurance of stereotactic radiotherapy

Yimpak T[1*], Tangboonduangjit P[1], Khachonkham S[1], Pimthong J[2], Watthanasarn T[2], Krongkietleart K[2]

1 Master of Science Program in Medical Physics, Department of Diagnostic and Therapeutic Radiology, Faculty of Medicine Ramathibodi Hospital, Mahidol University, Bangkok, Thailand.

2 Department of Radiotherapy, Lopburi Cancer Hospital, Lopburi, Thailand.

**t.yimpak@gmail.com*

Introduction: The accuracy of patient-specific quality assurance (PSQA) measurements in stereotactic radiotherapy is challenging due to the unique properties of small-field dosimetry. The high-resolution detector array is essential. The SRS MapCHECK (SMC), a two-dimensional high-resolution diode array with dedicated phantom StereoPHAN, was introduced as a stereotactic radiotherapy PSQA tool. The aim of this study was to investigate the dosimetric characteristics of SMC for stereotactic radiotherapy PSQA.

Methods: SMC was evaluated at 6 MV-FFF beams for dosimetric characteristics, including angular dependence, beam directivity, dose rate dependence, output factors (OPFs), dose linearity, and reproducibility. Angular and dose rate dependencies were assessed with and without correction, and results were compared to the 0.016 cc Pinpoint3D ionization chamber (IC). OPFs were measured and compared against the IC for field sizes down to 1×1 cm^2. SMC responses to anterior and posterior beam incidents were studied due to the unique alignment of diode detectors on the two-facing printed circuit boards. Reproducibility was assessed in short- and mid-term periods through every three-hour and weekly session.

Results: Angular dependence stayed within 2% of the IC when applying angular correction, except for beam directions nearly parallel to the detector plane. The maximum deviation was -8.97% at a 92° gantry angle. Beam directivity response on both sides of the array showed good agreement. There was no dose rate dependency from 400 to 1400 MU/min; variation was within 0.2% from the IC when the dose rate correction was applied. OPFs agreed within 1.5% of the IC for field size down to 2×2 cm^2. Dose linearity with MU showed sufficient performance with R^2 equal to 1. Short- and mid-term reproducibility was good at 0.3% and 0.4%, respectively.

Conclusion: Results indicate that SMC with StereoPHAN phantom has sufficient dosimetric characteristics to be useful for stereotactic radiotherapy PSQA.

Keywords: SRS MapCHECK, Diode array, Dosimetric characteristics, Stereotactic radiotherapy.

Dose evaluation of a deep learning-based synthetic CT generation for head and neck cancer in photon and proton therapy

Kuibrumrung A[1], Ruangchan S[2], Sanghangthum T[3*]

1 Master of Science in Medical Physics Program, Department of Radiology, Faculty of Medicine, Chulalongkorn University, Bangkok, 10300 Thailand

2 Division of Radiation Oncology, Department of Radiology, King Chulalongkorn Memorial Hospital, Thai Red Cross Society, Bangkok, 10300 Thailand

**mairt34@yahoo.com*

Introduction: MRI has been increasingly implemented for the treatment planning process and for MRI-only workflow in both photon and proton therapy. This study aims to investigate and explore the accuracy of dose calculations in head and neck region based on synthetic CT, using the commercial software methods for both volumetric modulated arc therapy (VMAT) and intensity modulated proton therapy (IMPT) plans.

Methods: The synthetic CT images were generated from MRI images for five head and neck cancer cases that underwented VMAT and IMPT by commercial software (MRI Planner™). The mean absolute error (MAE) and mean error (ME) within the body contour and dice scores in bone mask were used for evaluation. The treatment plans of VMAT (3 arcs) and IMPT (0, 40, 140, 200, and 300 beam angles) were generated and optimized in the Eclipse treatment planning system (Version 16.1). The treatment plans were originally optimized and calculated on planning CT images and subsequently recalculated on synthetic CT images. The dose distributions were evaluated at $D_{98\%}$, $D_{95\%}$ and $D_{50\%}$ of PTV/CTV, D_{mean} and D_{max} of organs at risk. Moreover, the dose comparisons between original CT and pseudo-CT were analyzed at 1%/1mm, 2%/2mm, 3%/2mm gamma criteria.

Results: The MAE over the patient population of the sCT within the intersection of body contours was 45 ± 45 Hounsfield Units (HU), and the ME was 5 ± 12 HU. Dice scores of the bone masks (CT vs sCT) were 0.9 ± 0.08. Dosimetric analysis showed no statistically significant dose differences between clinical CT and synthetic CT for both VMAT plan and IMPT plan. The average gamma passing rate at 1%/1mm, 2%/2mm, 3%/2mm were 87%, 94%, 97% for VMAT plan and 78%, 90%, 91% for IMPT plan, respectively.

Conclusion: The commercial software used for generating synthetic CTs (sCTs) has demonstrated significant dose differences for IMPT over VMAT plans for the head and neck region. The dose calculations based on these sCTs lead to more inaccurate dosimetric results; therefore it should be considered when dealing with proton treatment plans.

Keywords: deep learning, head and neck cancer, MR-guided therapy, MR-only radiotherapy, synthetic CT

Enhancing adaptive radiation therapy accuracy with CycleGAN-generated synthetic CT from CBCT in pelvic region

Wongtrakool P[1*], Puttanawarut C[2,3], Changkaew P[4], PiasanthiaS [4], Earwong P[1], Stansook N[1,4], Khachonkham S[1,4]

1 Master of Science Program in Medical Physics, Department of Diagnostic and Therapeutic Radiology, Faculty of Medicine, Ramathibodi Hospital, Mahidol University, Bangkok, Thailand.

2 Department of Clinical Epidemiology and Biostatistics, Faculty of Medicine, Ramathibodi Hospital, Mahidol University, Bangkok, Thailand

3 Chakri Naruebodindra Medical Institute, Faculty of Medicine, Ramathibodi Hospital, Mahidol University, Samut Prakan, Thailand

4 Division of Radiation and Oncology, Department of Diagnostic and Therapeutic Radiology, Faculty of Medicine, Ramathibodi Hospital, Mahidol University, Bangkok, Thailand.

**paritt.w@gmail.com*

Introduction: Adaptive Radiation Therapy (ART) using Cone-beam CT (CBCT) offers a way to enhance radiotherapy accuracy by adjusting radiation plans in response to daily anatomical changes during treatment. However, HU distortions in CBCT limit their dose calculation accuracy. Synthetic CT (sCT) generated from CBCT using deep learning-based approaches has emerged to address this problem. Objective of this study is to evaluate performance of "CycleGAN" in generating sCT from CBCT in pelvic region.

Methods: The study included 33 pairs of planning CT (pCT) and 1st fraction CBCT from pelvic region cancer cases treated with VMAT at Ramathibodi Hospital. Both images underwent registration and pre-processing, including removing non-anatomical regions, HU clipping to [-1000,1000], and HU rescaling to [-1,1]. CycleGAN model was trained on 23 cases, validated on 5, and tested on 5. The performance of sCT and CBCT was compared in terms of image similarity, geometric accuracy, and dosimetric accuracy using pCT as a reference.

Results: A comparative evaluation between sCT and CBCT revealed compelling findings. In terms of image similarity, sCT had shown lower mean absolute error (MAE) for body and soft tissue (47.05 vs. 65.67 HU for body, 40.55 vs. 61.26 HU for soft tissue) but a higher MAE for bone (153.90 vs.135.94 HU). For geometric accuracy, sCT and CBCT exhibited similar dice similarity coefficient (DSC) (0.97 vs. 0.96 for soft tissue, 0.79 vs 0.80 for bone, 0.98 vs. 0.97 for body). For dosimetric accuracy, sCT demonstrated lower percentage dose difference (-0.58% vs 1.15 for PTV $D_{95\%}$, -0.11% vs 1.19% for PTV $D_{2\%}$, -0.31% vs 1.12% for PTV D_{mean}). sCT also produced slightly higher gamma pass rate using 2% 2 mm criteria (99.88% vs 99.85%).

Conclusion: CycleGAN generated-sCT demonstrates promising results for improving image similarity, geometric accuracy, and dosimetric accuracy, potentially enhancing ART effectiveness.

Keywords: Adaptive radiation therapy, Synthetic CT, Deep learning

Confidence limit of gamma passing rate for patient-specific quality assurance in pencil beam scanning proton therapy

Rawiwan N[1*], Nichakan C[2], Vimolnoch M[2], Kingkaew S[2], Oonsiri P[2], Oonsiri S[2]

1 Medical Physics Program, Department of Radiology, Faculty of Medicine, Chulalongkorn University, Bangkok, Thailand, 10330

2 Division of Radiation Oncology, Department of Radiology, King Chulalongkorn Memorial Hospital, Bangkok, Thailand, 10330

**nuttida_ra@hotmail.com*

Introduction: Proton therapy is an advanced technique that can spare normal tissue and increase tumor control probability in external treatment. In radiotherapy, patient-specific quality assurance (PSQA) is essential to ensure the delivery dose and avoid errors that may occur with patients. Although there are end-to-end verification criteria in proton therapy, the criterion for PSQA is not defined. This research aims to determine the confidence limit of the gamma passing rate for PSQA in pencil beam scanning proton therapy.

Methods: The PSQA measurements were performed by the Varian ProBeam Compact spot scanning system and measured with PTW OCTAVIUS 1500XDR array in solid water phantom with perpendicular composited method. The dose distributions were compared between the measured dose and calculated dose by Eclipse treatment planning system using gamma index criteria of 3% dose-difference and 2 mm distance-to-agreement in five regions, including head and neck, chest, breast, abdomen, and pelvis with 173 plans. The confidence limit was calculated by mean and standard deviation of the gamma passing rate.

Results: The gamma passing rate was above 98% in every region, with the minimum and maximum values of 98.7% and 99.6%, respectively. It had no significant differences between treatment sites ($p=0.10$). The overall result of the gamma passing rate of PSQA was 99.1 ± 1.6%. The confidence limit, which was calculated from the overall gamma passing rate that excluded the lowercase from the first calculation was 97.4%.

Conclusion: The gamma passing rate of 3%/ 2 mm was a reasonable criterion for PSQA in pencil beam scanning proton therapy, and the confidence limit was 97.4%.

Keywords: Pencil beam scanning proton therapy, Patient-specific quality assurance, Confidence limit.

Machine learning-based dose prediction in lung cancer radiation therapy for enhanced decision support systems

Chaipanya T[1]*, Nimjaroen K[1,2], Chamchod S[1,2], Intanin P[1,2], Thongsawad S[1,2], Owasirikul D[3], Khamfongkhruea C[1,2]

1 Princess Srisavangavadhana College of Medicine, Chulabhorn Royal Academy, Bangkok, Thailand

2 Radiation Oncology Department, Chulabhorn Hospital, Chulabhorn Royal Academy, Bangkok, Thailand

3 Kanchanabhishek Institute of Medical and Public Health Technology, Nonthaburi, Thailand

*****Thitaporn.chi@edu.cra.ac.th*

Introduction: Lung cancer patients usually undergo concurrent chemoradiotherapy, but those with large tumor volumes might receive chemotherapy alone if normal tissues exceed tolerance doses. Gathering radiation dose information from the treatment plan is time-consuming and labor-intensive. Utilizing machine learning to predict doses can streamline this and assist in treatment decisions. Thus, this study focuses on developing a machine learning-based dose prediction model for lung cancer.

Methods: In this study, 59 plans utilizing volumetric modulated arc therapy for lung cancer were collected, with patients prescribed doses ranging from 50-66Gy. The data were divided into 80% for training and 20% for model testing. Anatomical information, medical records, treatment intent, and radiation transport were used to extract 1299 features. Ultimately, 81 features were selected for training. Ensemble and Gaussian Process Regression models were used to train the model. Mean Absolute Error (MAE) assessed the model's predictive accuracy for organ volumes receiving 5Gy (V5) and 20Gy (V20) in the right lung, left lung, and total lung against ground truth data. The study also explores the model's potential as an automated decision support system, considering accuracy, sensitivity, and specificity metrics.

Results: The anatomical feature is the primary determinant of the outcomes. The V5 of total lung showed a slight difference, registering a 9.11 MAE. In contrast, the V5 of left lung displayed the most significant difference, recording a 23.86 MAE. Notably, the model predicting the V20 of the left lung showcased superior performance in accuracy, sensitivity, and specificity, with values of 0.83, 1, and 1, respectively.

Conclusions: The proposed model holds promise for developing automated decision support systems, assisting clinicians in deciding between concurrent chemoradiotherapy and standalone chemotherapy, particularly for patients with large tumor volumes. This approach can result in more efficient planning, reduced workload, and improved treatment quality.

Keywords: Dose prediction, Machine learning, Radiation therapy, Lung cancer

A simple evaluation method of real-time respiratory motion tracking accuracy utilizing the ExacTrac Dynamic system

Kongsak M[1*], Suphaphong S[2], Khaothong P[2], Stansook N[1], Tangboonduangjit P[1]

1 Master of Science Program in Medical Physics, Department of Diagnostic and Therapeutic Radiology, Faculty of Medicine Ramathibodi Hospital, Mahidol University, Bangkok, Thailand.

2 Radiation and Oncology Division, Therapeutic and Diagnostic Radiology Department, Faculty of Medicine Ramathibodi Hospital, Mahidol University, Thailand

**chatmongkol0540@gmail.com*

Introduction: Real-time respiratory tracking accuracy is crucial in radiation treatment for lung and breast cancer patients due to respiratory motion-induced degradation of precision. The purpose of this study is to evaluate the real-time tracking system and the influence of the period and amplitude of the ExacTrac Dynamic (EXTD) system.

Methods: 9 sinusoidal breathing pattern curves were simulated by Quasar programmable respiratory motion phantom, each curve consisting of a pair of phases and amplitudes (15-, 20-, and 25-BPM, and 5-, 10-, and 15-mm peak to peak, respectively). The respiratory motion monitoring of the phantom was performed by the EXTD system with 4 conditions of thermal and surface shape on the phantom. The tracking accuracy was simply assessed by utilizing statistical analysis tools of Pearson's correlation coefficient (PCC) and root mean square error (RMSE) in a commercial Microsoft Excel program. In addition, all respiratory tracking curves were transformed to the frequency domain by Fourier transform before analysis.

Results: RMSE and PCC for the sine curves in the time and frequency domain showed excellent results of respiratory tracking accuracy with 0.1527- 1.8854 mm and 0.9181-0.9963 for the time domain and 0.0189-0.1870 mm and 0.9762-0.9983 for the frequency domain. More phase and amplitude could cause more error. However, the phase and amplitude variations had a negligible effect on the respiratory tracking of both systems, which can cause a huge error.

Conclusion: The EXTD system has a high accuracy for respiratory motion tracking. Furthermore, Applying the Fourier transform can eliminate the uncertainty of manual determination of the starting point in the time domain. The phase and amplitude slightly affect tracking accuracy. The 4D thermal surface can improve respiratory tracking accuracy on a phantom, which has a thermal surface.

Keywords: EXTD, RMSE, PCC, Fourier transform

Dosimetric comparison of IMRT, co-planar VMAT, non-coplanar VMAT and HyperArc for multiple brain metastases SRS

Thawornnittayakul A[1], Plangpleng N[2], Sanghangthum T[1]*

1 Master of Science in Medical Physics Program, Department of Radiology, Faculty of Medicine, Chulalongkorn University, Bangkok, 10330 Thailand

2 Division of Radiation Oncology, Department of Radiology, King Chulalongkorn Memorial Hospital, Thai Red Cross Society, Bangkok, 10330 Thailand

**mairt34@yahoo.com*

Introduction: A single isocentric VMAT technique called HyperArc is an automated setting for couch and collimator angles for non-coplanar. This study aimed to compare the dosimetric effect for single isocenter among Intensity Modulated Radiation Therapy (IMRT), Coplanar Volumetric Modulated Arc Therapy (co-VMAT), Non-coplanar VMAT (non-co VMAT), and HyperArc for multiple brain metastases stereotactic radiosurgery (SRS).

Methods: The 20 patients with multiple brain metastases (2-4 targets) were collected. The IMRT (9 fields), co-VMAT (2 full coplanar arcs), non-co VMAT, and HyperArc plans with a prescription dose of 18 Gy in single-fraction were generated with 6 MV flattening filter-free energy. For non-co VMAT and HyperArc plans, the 1 full coplanar arc and 3 half arcs with non-coplanar planes at 45, 90, and 135 couch angles were set. The organs at risk (OARs) dose constraints at D_{max} of the brainstem was 8 Gy, while D_{max} of the eye lens, optic nerve, and optic chiasm should be less than 5 Gy. Paddick gradient index (GI), Paddick conformity index (CI), homogeneity index (HI), total number of monitor units (MUs), delivery time and normal brain volume (V_2-V_{16}) were used to evaluate the plan quality.

Results: The OAR doses were lower than the dose limits for all plans. HyperArc presented the best results with the lowest GI (5.18 ± 1.15), and the highest CI (0.63 ± 0.14) values compared with other techniques. For HI all techniques were comparable. The moderate to low dose spreads of normal brain were also significantly reduced in HyperArc plan. Eventually, HyperArc plans led to a significant reduction in both MUs and delivery time.

Conclusion: HyperArc plans provided a significantly better in rapid dose falloff and dose conformity to the targets. This is consistent with the computed reduction in V_{12} to the normal brain. Ultimately, HyperArc treatments were accomplished within around 4 minutes, signifying a noteworthy reduction in time compared to the other plans.

Keywords: Brain metastases, SRS, IMRT, VMAT, HyperArc.

Machine learning-based patient selection for deep inspiration breath hold radiotherapy in left breast cancer

Chotchuchuang C[1*], Khamfongkhruea C[1,2], Chamchod S[1,2], Thongsawad S[1,2], Deeharing A[2]

1 Princess Srisavangavadhana College of Medicine, Chulabhorn Royal Academy, Bangkok, Thailand

2 Radiation Oncology Department, Chulabhorn Hospital, Chulabhorn Royal Academy, Bangkok, Thailand

**Chanatinat.cho@edu.cra.ac.th*

Introduction: Treating breast cancer on the left side is particularly challenging due to the proximity of the heart to the irradiation field. At present, the application of deep inspiration breath hold (DIBH) can address this challenge. However, it has drawbacks such as time consumption and heightened staff workload. Therefore, this study aims to employ machine learning to generate a predictive model for mean heart dose (MHD) by enabling the selection of an optimal management technique for each patient before the treatment planning process.

Methods: Eighty-six patients with left breast cancer undergoing the field-in-field technique were assigned to training (80%) and testing datasets (20%) for machine learning in MATLAB. One hundred seven features were extracted using CT images and structured contours. Ultimately, sixteen features were selected for training with the Gaussian process model. In the testing model, mean absolute error (MAE) was employed to measure the difference between the actual and predicted MHD. Furthermore, the model's performance was evaluated with binary classification, using an MHD threshold of 7 Gy, in terms of accuracy, sensitivity, and specificity.

Results: The predictive precision of MHD is characterized by an MAE of 1.73. In binary classification, the findings demonstrated favorable model accuracy and specificity at 0.65 and 1, respectively. However, there was notably low sensitivity at 0.14, possibly attributed to data imbalance, where positive cases were fewer than negative cases. Addressing this imbalance could enhance results in future studies.

Conclusion: This study contributes to optimizing radiation treatment planning for left breast cancer patients by developing a dose prediction model. The model serves as a decision support system for selecting individualized management techniques, thereby reducing both time and workload for staff in the planning process.

Keywords: Machine learning, Mean heart dose (MHD), Deep inspiration breath hold (DIBH), Breast cancer, Radiotherapy.

A simple radiation-induced DNA damage model for proton therapy based on DBSCAN algorithm

Chaibura S[1*], Autsavapromporn N[2], and Liamsuwan T[1]

1 Princess Srisavangavadhana College of Medicine, Chulabhorn Royal Academy, Bangkok 10210 Thailand

2 Department of Radiology, Faculty of Medicine, Chiang Mai University, Chiang Mai 50200, Thailand

**sanhanat.cha@edu.cra.ac.th*

Introduction: Proton beam therapy (PBT) optimizes cancer treatment by utilizing the Bragg peak for precise tumor targeting while minimizing damage to healthy tissues. However, the variation of the relative biological effectiveness (RBE) in proton therapy underscored the need for a deeper understanding of the mechanisms of proton-induced biological effects. In this study, we explored the application of the Density-Based Spatial Clustering of Applications with Noise (DBSCAN) approach as a simplified model for characterizing radiation-induced early DNA damage in the context of PBT.

Methods: The Geant4-DNA Monte Carlo track structure toolkit was used to simulate track structures of protons with energies ranging from 500 keV to 200 MeV or linear energy transfer (LET) ranging from 41–0.4 keV/μm in water in the physical stage. Early DNA damage yields, including single strand break (SSB) and double strand break (DSB) were calculated using a simple DNA damage model. This model integrated the DBSCAN cluster analysis algorithm to discern spatial patterns in the distribution of interaction points (ionization and excitation) within the proton track structures. The optimal DBSCAN parameters, including epsilon, minPts, and energy thresholds, were iteratively determined to yield DNA damage results consistent with experimental and other simulation data.

Results: The optimal DBSCAN parameters for calculating DNA damage yields were determined to be epsilon of 2.1 nm, minPts of 2, and energy thresholds of 17.5 eV. This approach used only one conversion factor to calculate DNA damage yield. The agreement with experimental DNA damage yields was within 10% for SSB and DSB, except for very low LET protons.

Conclusion: This simple approach reveals a linear correlation between the number of clusters and the DSB yield. Additionally, it provides a quality assessment for proton beams based on the occurrence of clusters per beam, measured per μm and per keV.

Keywords: DNA damage, Clustering, DBSCAN, Proton beams, Geant4-DNA.

Designing an in-house phantom daily QA for range verification for proton beam using GEANT4

Kheawyoi P[1*], Keawsamur M[1], Chaiwongkhot K[2] and Israngkul Na Ayuthaya I[3]

1 Medical Physics Program, Department of Radiology, Faculty of Medicine, Chulalongkorn University, Pathumwan, Bangkok 10330, Thailand

2 Department of Physics, Faculty of Science, Mahidol University, Bangkok, Thailand

3 Division of Radiation Oncology, Department of Radiology, King Chulalongkorn Memorial Hospital, Bangkok, Thailand

**6570050930@student.chula.ac.th*

Introduction: This study aims to develop an in-house phantom proton therapy for daily quality assurance based on TG-224 to ensure the safety and effectiveness of treatment machines. Thus, each identical facility's in-house proton therapy QA procedure is required. To develop an in-house phantom, the simulation algorithm for particle interactions in the substance using GEANT4 was prepared to evaluate the phantom response before the experiment.

Methods: In this work, the beamline and database setup in the simulation were verified to confirm consistent results with the experimental data. The ionization chamber array detector (PTW Octavius 1500 ^{XDR}) which is currently implemented in King Chulalongkorn Memorial Hospital, was used as a detector with proton beam energies to evaluate the relation between Bragg peak position and proton kinetic energy. The in-house phantom for daily QA is composed of 4x7x2 cm^3 with an acrylic module for accuracy range checks of proton energy (70 MeV, 100 MeV, 150 MeV, and 200 MeV). The spot sizes were evaluated.

Results: There are four verified proton beam energies: 70 MeV, 100 MeV, 150 MeV, and 200 MeV which correspond to our overall proton beam energy range. The spot sizes of 70 MeV, 100 MeV, 150 MeV, and 220 MeV are 14.04 mm, 9.59 mm, 7.52 mm. and 7.34 mm, respectively. The results indicate that the proton beams in the experiment are reasonably agreed in the simulation.

Conclusion: The results from the range verification show that all the beam energies agree well with the referenced data from the simulation. Additionally, the linear relationship between dose and proton energy and the variation in spot size and dose of each proton energy will also be presented.

Keywords: Proton therapy, GEANT4 simulation, Range verification, In-house phantom.

Monte Carlo model for out-of-field dosimetry during volumetric modulated arc therapy

Pongmettasanti D[1*], Thongsawad S[1,2], Suntiwong S[2], Liamsuwan T[1]

1 Princess Srisavangavadhana College of Medicine, Chulabhorn Royal Academy, Bangkok, Thailand

2 Radiation Oncology Department, Chulabhorn Hospital, Chulabhorn Royal Academy, Bangkok, Thailand

**daranporn.pon@edu.cra.ac.th*

Introduction: Volumetric modulated arc therapy (VMAT) provides precision with minimal collateral damage, however, challenges remain in mitigating out-of-field dose (OFD) to normal tissues. Determination of OFD lacks standardized methods and OFD is often underestimated by treatment planning systems (TPSs). Monte Carlo (MC) simulation offers a solution for OFD determination but requires validation against direct measurements. This study aimed to develop an accurate MC model for 6 MV VMAT with Varian TrueBeam linear accelerator for OFD evaluation. The presentation focuses on the validation of jaws and multileaf collimator (MLC) models.

Methods: The MC model was developed with the Particle and Heavy Ion Transport code System (PHITS). The simulation started with field-independent phase-space data above the jaws. The jaws and MLC were modeled from the vendor-provided blueprint. MLC leave positions were extracted from RT Plan. The MC model was validated against commissioning data for 10x10 cm^2 and 40x40 cm^2 fields, including percentage depth dose (PDD), lateral profiles, and diagonal profiles. For the MLC model, the simulated fluence maps at the aperture were compared with those reconstructed from RT Plan. All treatment plans were generated using Eclipse TPS with the AAA algorithm.

Results: For low dose gradient, the analysis revealed a maximum difference of 1% in the diagonal profiles at 5 cm depth. At high dose gradients, worst-case gamma passing rates (GPRs) were 70%, 80%, and 85% with 2%/2 mm for PDD before d_{max}, lateral, and diagonal profiles at the penumbra region of 40x40 cm^2. For the MLC model, GPRs for MC vs. RT Plan were 85%, 90%, and 97% at criteria 1%/1 mm, 2%/2 mm, and 3%/3 mm, respectively.

Conclusion: The MC model demonstrates good agreement with the commissioning data and reconstructed fluence maps. Future efforts will focus on model validation in phantoms.

Keywords: Volumetric modulated arc therapy (VMAT), Monte Carlo simulation, Out-of-field dose (OFD), fluence map

A comparative analysis of geometric and dosimetric outcomes in atlas-based versus deep learning-based automated segmentation for head and neck radiation therapy

Thanusilp W[1*], Fuangrod T[1], Chamchod S[1,2], Masa-Nga W[1,2], Kummanee P[1]

1 Princess Srisavangavadhana College of Medicine, Chulabhorn Royal Academy, Bangkok, Thailand

2 Radiation Oncology Department, Chulabhorn Hospital, Chulabhorn Royal Academy, Bangkok, Thailand

**Warisara.tha@edu.cra.ac.th*

Introduction: This study presents a comparative evaluation of the geometric and dosimetric results in head and neck (HN) radiation therapy, specifically focusing on the performance of Atlas-Based (AB) versus Deep Learning-Based (DLB) automated segmentation techniques. The objective is to evaluate the accuracy and clinical applicability of these methods in delineating eleven organs-at-risk (OAR), including the brainstem, eye left, eye right, larynx, len left, len right, optic nerve left, optic nerve right, parotid glands left, parotid gland right, and spinal cord.

Methods: A retrospective analysis of thirty patient image datasets underwent head and neck cancer undergoing the advanced technique, specifically Intensity-Modulated Radiation Therapy (IMRT) and Volumetric Modulated Arc Therapy (VMAT). These datasets were assigned to test by two commercial software tools, MIM version 7.1.3 (AB methods) and AccuCountour version 3.1 (DL methods). During the investigation, geometric evaluation focused on determining the accuracy of automated segmentation outputs. The evaluation is based on fundamental metrics of the Dice Similarity Coefficient (DSC). The dosimetric analysis aims to quantify segmentation discrepancies between AB and DLB techniques and their impact on dose distribution. Additionally, dosimetric metrics included the dose-volume histograms (DVH), D_{mean} and D_{max}.

Results: Results indicate that the deep-learning algorithm demonstrates higher accuracy compared to the atlas-based algorithm in auto-segmentation, particularly for smaller or low-contrast organs.

Conclusion: This study's auto-segmentation contributes to the precision of treatment planning for head and neck OAR. However, while DLB segmentation demonstrates promising advancements in accuracy and dosimetric consistency, integrating DLB segmentation into clinical practice requires further validation and standardization to ensure reliability and patient safety.

Keywords: Auto-Segmentation, Atlas-Based (AB), Deep Learning Based (DLB), Organ-At-Risk (OAR), Head and Neck (HN)

Dose prediction in prostate cancer

Chaikamthorn P[1], Na Ayuthaya I[2]

1 Medical Physics Program, Department of Radiology, Faculty of Medicine, Chulalongkorn University, Pathumwan, Bangkok 10330, Thailand

2 Division of Radiation Oncology, Department of Radiology, King Chulalongkorn Memorial Hospital, Bangkok 10330, Thailand

**6470051430@student.chula.ac.th*

Introduction: **T**his study aimed to to develop and evaluate the feasibility of machine learning-based dose prediction models.

Methods: The study followed a two-phase approach. The first phase involved data preprocessing, where 25 approved prostate cancer treatment plans that contain PTV and organ at risk (OARs), i.e., bladder, rectum, femoral heads, and penile bulb were selected. The second phase involved creating and evaluating a machine learning model using the data collected in the data preprocessing phase with Python 3. The model was trained with a 5-fold cross-validation method.

Results: The model was evaluated with the test set to see the absolute difference and root mean square error value. The results demonstrated a tendency for the model to overestimate the DVHs of every organ compared to the referenced treatment plan. The penile bulb prediction performed the worst of all predictions due to the high variation of the penile bulb's volume between each treatment plan, which depends on the individual's organ structure and each planner. Combining this with the low number of samples causes the machine learning model to overpredict compared to the treatment plan.

Conclusion: This discrepancy suggests that further refinement is necessary for the model to achieve optimal dosimetric accuracy and effectively generate clinically relevant DVHs for treatment planning. In conclusion, developing and evaluating the feasibility of machine learning-based dose prediction models can help reduce the time and effort required for radiation therapy planning and improve the accuracy and effectiveness of the treatment.

Keywords: Dose distribution, machine learning, prostate cancer.

Determination of the surface dose correction factors for various detectors in spot scanning beam proton therapy

Saruang P[1], Sanghangthum T[1], Yamram N[1], Keawsamur M[1*]

1 Medical Physics Program, Department of Radiology, Faculty of Medicine, Chulalongkorn University, Pathumwan, Bangkok, Thailand

**mintra.ke@chula.ac.th*

Introduction: Proton therapy effectively administers precise doses while minimizing harm to vital organs, yet concerns arise regarding skin toxicity caused by energy dispersion beyond the Bragg peak. This research aims to determine the surface dose correction factors (Scf) for various detectors in spot scanning beam proton therapy and study the effect of surface dose according to various clinical factors.

Methods: The advanced Markus chamber and FC65-G Farmer chamber were utilized to measure the skin dose in a water phantom. A reference point located 0.07 mm below the phantom's surface was defined to represent the skin position, and the doses were normalized to the doses at 3 cm depth. The obtained surface doses from the experiment were compared to the reference results obtained from FLUKA Monte Carlo simulations under the same conditions to determine the Scf of the detectors. Additionally, the study investigated the impact of various factors affecting surface dose, including variations in energy (100, 150, and 200 MeV), air gap distances (5, 15, and 42.1 cm), and range shifter (RS) thicknesses (2, 3, and 5 cm).

Results: The results indicated that the Scf from the Markus detector were 0.9938, 0.9922, and 0.9886 for 100, 150, and 200 MeV, respectively. Similarly, for the FC65-G, the factors were 0.9711, 0.9859, and 0.9764 for the same respective energy levels. As for the correlation with clinical variables, an increase in the air gap distance resulted in a decrease in surface dose. Introducing the range shifter (RS) amplified the surface dose compared to its absence, particularly evident with reduced air gap distances and increased RS thickness.

Conclusion: In this study, the surface dose correction factors demonstrated variability contingent upon the energies utilized. Furthermore, the introduction of a range shifter exhibited discernible alterations in surface dose, exhibiting variability contingent upon air gap distances.

Keywords: Surface dose, Correction factors, Proton therapy, Air gap, Range shifter.

Abstracts: *Oral Presentation: Medical Imaging*

Absorbed dose calculation in thoracic CT using ICRP voxel phantoms and Monte Carlo simulation

Watanabe S[1*], Matsubara K[2]

1 Department of Quantum Medical Technology, Division of Health Sciences, Graduate School of Medical Sciences, Kanazawa University, Kanazawa, Japan

2 Department of Quantum Medical Technology, Faculty of Health Sciences, Institute of Medical, Pharmaceutical and Health Sciences, Kanazawa University, Kanazawa, Japan

**h26s19@stu.kanazawa-u.ac.jp*

Introduction: Radiation dose from CT scans is relatively higher than those from other examinations. It is important to investigate the absorbed and effective doses, but they cannot be measured directly. This study aimed to calculate organ/tissue absorbed doses, equivalent doses and effective dose in thoracic CT using ICRP adult reference computational phantoms and Monte Carlo simulation code, and to compare the organ/tissue absorbed doses between male and female phantoms.

Methods: The Monte Carlo simulation code PHITS ver.3.28 was used in this study. To simulate thoracic CT, 120-kV X-ray photons were irradiated onto the ICRP voxel phantom placed on the CT scanner table by rotating the X-ray source, collimator, and bowtie filter every 9 degrees while simultaneously moving in the body axis direction. The tube current and X-ray tube rotation speed were adjusted by the normalization constant (totfact), to correspond to 100 mA and 1 s/rot, respectively. A total of 141 tally regions were set for organs/tissues, and the organ/tissue absorbed doses and effective dose were obtained by calculating the deposited energy due to radiation in each tally region.

Results: The absorbed doses in the lungs, breast, esophagus, heart, liver, and thyroid were higher than other organs/tissues. The absorbed doses in the lungs were 9.06 and 10.7 mGy for the male and female phantoms, respectively, and the effective dose as the sex-average value was 6.45 mSv. The absorbed doses for breast and liver in the female phantom were 2.08 and 1.26 times higher than those in the male phantom, respectively.

Conclusion: For thoracic CT, absorbed doses in the ICRP adult reference computational phantoms were higher in the lungs, breast, esophagus, heart, liver, and thyroid than in other organs/tissues. The absorbed doses were higher in the female phantom than in the male phantom, and there were large difference between the two, especially in the breast and liver.

Keywords: Monte Carlo simulation, computed tomography, voxel phantoms, organ dose, effective dose

Assessment of patient radiation dose and image quality for trans-arterial chemoembolization from digital subtraction angiography combined with IVR-CT

Boonsuan S[1*,2], Asavaphatiboon S[2], Tangboonduangjit P[2], Sodkokkruad P[2]

1 Master of Science Program in Medical physics, Department of Diagnostic and Therapeutic Radiology, Faculty of Medicine Ramathibodi Hospital, Mahidol University, Bangkok, Thailand.

2 Department of Diagnostic and Therapeutic Radiology, Faculty of Medicine, Ramathibodi Hospital, Mahidol University, Bangkok, Thailand

**sasisasibn19@gmail.com*

Introduction: Trans-arterial chemoembolization (TACE) combined with IVR-CT helps detect the arteries supplied to the liver tumor. However, using the combined modality, the patient can get more radiation dose. Finding the suitable protocol to decrease the radiation dose and improve image quality followed "ALARA". This research aimed to assess the patient radiation doses and image quality for TACE procedures from DSA combined with IVR-CT.

Methods: The radiation doses from sixty-six TACE with IVR-CT patients performed between January 2022 and December 2022 were collected. Evaluation of the Angio-CT's dose parameters regarding dose-area-product (DAP), fluoroscopy time, $CTDI_{vol}$, and dose-length-product (DLP) for IVR-CT can adjust the parameter in 3D SURE Exposure^{TM} automatic tube current control, and level of AIDR iterative reconstruction algorithm. Then, the optimal parameter related to radiation dose is used to reduce stochastic risk. This study evaluated the image quality in the CT model PBU-60 KYOTO KAGAKU anthropomorphic phantom of image noise, signal-to-noise ratio (SNR), and contrast-to-noise ratio (CNR).

Results: The average DAP and DLP from TACE's procedure combined with IVR-CT were about 413.94 ± 237.59 Gy.cm^2 (range: 84.42-1145.61 Gy.cm^2) and 665.65 ± 318.78 mGy.cm (range: 294.7—1730.8 mGy.cm), respectively. The low SURE Exposure^{TM} with strong AIDR iterative reconstruction algorithm can get a lower radiation dose than the routine protocol in 30.06% (p-value < 0.001) with a statistically significant difference. This new protocol can improve the image quality in less noise of –1.81% without difference statistically significant. SNR at the mean liver region was increased up 1.94% (p-value = 0.046) with a statistically significant difference. Other organs in the abdomen regions can improve the SNR and CNR of the routine protocol.

Conclusion: This study suggested that the low SURE Exposure^{TM} with a strong level of AIDR iterative reconstruction algorithm can improve image quality and decrease the radiation dose by 30.06% to reduce stochastic risk.

Keywords: Interventional Radiology, Trans-arterial Catheter Chemoembolization, Angiography-Computed Tomography, Radiation dose, Image quality.

Optimal dual-time-point dynamic ^{68}Ga-PSMA-11 PET/CT protocols for parametric imaging generation in prostate cancer patients

Burasothikul P[1,2,3*], Sukprakun C[4], Chantadisai M[4], Khamwan K[1,3]

1 Medical Physics Program, Department of Radiology, Faculty of Medicine, Chulalongkorn University, Pathumwan, Bangkok, Thailand.

2 School of Radiological Technology, Faculty of Health Science Technology, HRH Princess Chulabhorn College of Medical Science, Lak Si, Bangkok, Thailand.

3 Chulalongkorn University Biomedical Imaging Group, Department of Radiology, Faculty of Medicine, Chulalongkorn University, Pathumwan, Bangkok, Thailand.

4 Division of Nuclear Medicine, Department of Radiology, Faculty of Medicine, Chulalongkorn University, Pathumwan, Bangkok, Thailand.

**paphawarin.bur@gmail.com*

Introduction: Parametric imaging can enhance the accuracy of PET/CT quantification, but the prolonged acquisition time limits the effectiveness. This study aimed to investigate the optimal dual-time-point dynamic ^{68}Ga-PSMA-11 PET/CT protocols for generating parametric imaging for patients diagnosed with prostate cancer.

Methods: Fifteen prostate cancer patients were intravenously administered ^{68}Ga-PSMA-11 approximately 185 MBq, and a 60-minute dynamic PET/CT scan was acquired immediately after injection using Biograph Vision 600. The dynamic data were reconstructed into 25 time-frames, including intervals of 6 x 10 seconds, 8 x 30 seconds, and 11 x 300 seconds, and were corrected for motion and partial volume effects. Image-derived input functions were extracted from the right common iliac artery using a 3D region of interest in PMOD software. Dual-time-point protocols, involving 5-minute intervals and 10-minute intervals, with a time interval of at least 30 minutes, were employed to generate parametric images. Net influx rates (K_i) were derived by fitting a two-tissue compartmental model, and lesion-to-background ratios (LBRs) of K_i images and standardized uptake value (SUV) images were computed.

Results: The 5-10 minutes coupled with 40-45 minutes dual-time-point protocol indicated the highest intraclass correlation coefficient (ICC) of 0.988 compared to 60-minute K_i while the 0-5 minutes with 55-60 minutes and 0-10 minutes with 50-60 minutes showed the ICC values of 0.941. The LBRs of 60-minute K_i, 5-10 minutes with 40-45 minutes K_i, 0-5 minutes with 55-60 minutes K_i, 0-10 minutes with 50-60 minutes K_i, SUV_{mean}, and SUV_{max} were 19.14 (11.61-49.77), 6.64 (2.99-21.45), 20.66 (12.14-75.44), 26.48 (13.9-68.7), 10.65 (6.65-23.7), and 10.25 (7.03-29.96), respectively.

Conclusion: Parametric imaging generated from optimal dual-time-point protocols exhibits superior image quality and contrast compared to SUV imaging. The dual-time-point protocols at 0-5 minutes with 55-60 minutes and 0-10 minutes with 50-60 minutes, achieve a comparable image quality to standard 60-minute parametric imaging.

Keywords: Kinetic modeling, Compartmental model, Parametric imaging, Dynamic ^{68}Ga-PSMA-11 scan, Prostate cancer.

Accuracy of ^{177}Lu quantification for dosimetry calculation using 12-swiveling CZT detectors SPECT/CT camera

Damthongsen P[1,2*], Pasawang P[3], Sontaraponpol T[3], Phromphao B[3], Noipinit N[3], Sawatnatee T[3] and Khamwan K[2,4]

1 Medical Physics Program, Department of Radiology, Faculty of Medicine, Chulalongkorn University, Pathumwan, Bangkok 10330, Thailand

2 Chulalongkorn University, Biomedical Imaging Group, Department of Radiology, Faculty of Medicine, Chulalongkorn University, Pathumwan, Bangkok 10330, Thailand

3 Division of Nuclear Medicine, Department of Radiology, King Chulalongkorn Memorial Hospital, Pathumwan, Bangkok 10330, Thailand

4 Division of Nuclear Medicine, Department of Radiology, Faculty of Medicine, Chulalongkorn University, Pathumwan, Bangkok 10330, Thailand

**6570049330@student.chula.ac.th*

Introduction: This study aimed to determine the accuracy of ^{177}Lu quantification through a phantom study and to evaluate total-body dosimetry in patients undergoing ^{177}Lu therapy using 12-swiveling digital CZT detectors SPECT/CT camera.

Methods: The NEMA/IEC body phantom inserted with six fillable spheres (10-, 13-, 17-, 22-, 28-, and 37-mm inner diameter), filled with ^{177}Lu solution of 9.6:1 for target-to-background ratio (99.16 kBq/cc in background) was acquired by the Veriton-CT for 10 min at 0.5, 24, 144, and 168 hr post-injection, with a photopeak energy of 113 keV, and ±10% scatter window. The activity concentration was measured in each sphere and compared with the actual activity. The total-body SPECT/CT images were acquired at 2-4, 24, and 48 hr post-injection, with scan duration of 28 min in four patients who received either ^{177}Lu-DODATATE or ^{177}Lu-PSMA treatment. SPECT images were reconstructed using quantitative algorithm, and scatter correction was applied. The time-integrated activity (TIA) and absorbed dose in kidneys, liver, spleen, bone marrow, salivary glands, and tumors were calculated according to the Medical Internal Radiation Dose (MIRD) scheme using the voxel S-value convolution (VSV) method.

Results: The phantom study demonstrated good agreement between measured and calculated activity concentrations in the largest sphere with percentage differences between -8% to 6%, over 0.5 to 168 hr post-injection. For clinical study, the absorbed dose coefficients in the kidneys, liver, spleen, bone marrow, salivary glands, and tumors for ^{177}Lu-DOTATATE patients were 0.36, 1.00, 0.44, 0.02, 0.03, and 1.77 Gy/GBq, respectively and ^{177}Lu-PSMA patients were 0.71, 0.25, 0.13, 0.04, 0.45, and 0.42 Gy/GBq, respectively. These results were within the dose constraint recommended by the MIRD Pamphlet No.26 and comparable with conventional camera.

Conclusion: The 12-swiveling digital CZT detectors SPECT/CT can provide accurate ^{177}Lu SPECT/CT quantification and is reliable for determining the dosimetry in clinical study.

Keywords: 12-swiveling CZT detectors, Quantitative ^{177}Lu SPECT, Theranostics, MIRD, VSV-based dosimetry

Establishment of typical adult CT diagnostic reference levels (DRLs) in Ramathibodi hospital: A comparison of different dose collection methods

Srisumetawupakit N[1*], Asavaphatiboon S[1,2], Charoenphun P[1,3], Chuamsaamarkkee K[1,3]

1 Master of Science Program in Medical Physics, Department of Diagnostic and Therapeutic Radiology, Faculty of Medicine Ramathibodi Hospital, Mahidol University, Bangkok, Thailand

2 Division of Diagnostic, Department of Diagnostic and Therapeutic Radiology, Faculty of Medicine Ramathibodi Hospital, Mahidol University, Bangkok, Thailand

3 Division of Nuclear Medicine, Department of Diagnostic and Therapeutic Radiology, Faculty of Medicine Ramathibodi Hospital, Mahidol University, Bangkok, Thailand

**s.ynichaphat@gmail.com*

Introduction: Diagnostic Reference Levels (DRLs) is effective tools for optimization. Generally, typical DRLs can be established through various dose collection methods, however, the comparison of results is not yet reported and described. Therefore, this study aims to establish typical DRLs for adult CT procedures at Ramathibodi Hospital by comparing the different dose collection methods.

Methods: CT dose data (the computed tomography dose index volume ($CTDI_{vol}$) and dose length product (DLP)) were retrospective collected from June 2022 to June 2023 in two CT scanners from the ten most frequent CT examinations. Six dose collection methods have been used in this work: (a) all patient data , (b) weight-specific 45 to 75 kg. from all patient data, (c) a random selection of 30 patients, (d) a random selection of 30 patients with weight-specific, (e) one month with all patient data, and (f) a random selection of 30 patients in one month with weight-specific. Typical DRLs from different methods are established using the median of the dose distribution. The comparison of typical DRLs were performed using non-parametric (Mann-Whitney U test) to ascertain significant differences of typical DRLs from different dose collection methods.

Results: The DRLs from different dose collection methods including $CTDI_{vol}$ (median ± SD), DLP (median ± SD) and percentage difference (with all patient data) were reported. Most of the typical DRLs showed significant differences ($P < 0.05$) when compared to dose collection with all patient data.

Conclusion: Typical DRLs were established in two CT scanners for the ten most frequent at Ramathibodi Hospital. These values can improve dose optimization locally. Our finding reported the variation of typical DRLs results from different dose collection method. The limitations of each method were explained and discussed. This illustrated the importance of the dose collection method on the establishment of typical DRLs at a single hospital site.

Keywords: Diagnostic reference levels, DRLs, Typical DRLs, Dose collection, Optimization.

Effect of dosimeter location on the eye lens dose measurements for endoscopist

Fukushima K[1*], Matsubara K[2], Watanabe S[1]

1 Department of Quantum Medical Technology, Division of Health Sciences, Graduate School of Medical Sciences, Kanazawa University, Kanazawa, Japan

2 Department of Quantum Medical Technology, Faculty of Health Sciences, Institute of Medical, Pharmaceutical and Health Sciences, Kanazawa University, Kanazawa, Japan

**koutarou0802@stu.kanazawa-u.ac.jp*

Introduction: Even if an eye lens dosimeter is used, the accuracy of measured lens dose varies depending on the position of the dosimeter. This study aimed to verify the influence of dosimeter location on the measured values and to obtain the distribution of scattered X-rays around the head of an endoscopist.

Methods: The air kerma at the eye surface, the temple of the endoscopist phantom and the inside of the radioprotective glasses were obtained by attaching optically stimulated luminescence dosimeters at these positions and performing 10-min fluoroscopy with an X-ray fluoroscopy system assuming endoscopic retrograde cholangiopancreatography (ERCP) procedure. Two radioprotective glasses, PANORAMA SHIELD HF-480S (Toray Medical, referred to as Glasses 1) and HAGOROMO FG50-770 (Maeda, referred to as Glasses 2), were used to evaluate the effect of the shape and the size of the glasses on the measured air kerma. The distribution of scattered X-rays around the cylindrical phantom that simulated the head of an endoscopist was obtained using Monte Carlo simulation code PHITS ver. 3.31 by setting tallies at the same positions as the phantom study.

Results: The air kerma ratios of the inside of the glasses to the eye surface were 0.37–1.14 and 0.20–0.33 for Glasses 1 and 2, respectively. The air kerma ratios of the temple to the eye surface were 0.65–1.95 and 1.27–2.40 for Glasses 1 and 2, respectively. In the simulation, the amount of the scattered X-rays around the eye lens was higher than those elsewhere inside the glasses.

Conclusion: The air kerma at the inside of the glasses was smaller than that at the eye surface, and that at the temple was larger than that at the eye surface. Therefore, placing the dosimeter at the temple is a conservative method to assess the eye lens dose for endoscopists.

Keywords: eye lens, dosimeter, occupational exposure, Monte Carlo simulation, endoscopic retrograde cholangiopancreatography

Development of tungsten-doped borosilicate glass as a lead-free transparent radiation shield in nuclear medicine

Suwanprateep S[1*], Charoenphun P[1,2], Chuamsaamarkkee K[1,2], Meechoowas E[3], Sawangboon N[3] and Suriyoporn S[3]

1 Master of Science Program in Medical Physics, Department of Diagnostic and Therapeutic Radiology, Faculty of Medicine Ramathibodi Hospital, Mahidol University, Bangkok, Thailand

2 Division of Nuclear medicine, Department of Diagnostic and Therapeutic Radiology, Faculty of Medicine Ramathibodi Hospital, Mahidol University, Bangkok, Thailand

3 Division of Engineering Materials, Department of science service, Bangkok, 10400, Thailand

*****satawatchara.su27@gmail.com*

Introduction: Transparent radiation shield is significantly important for preparation of radiopharmaceuticals and administration to patients in nuclear medicine. Although lead glass is commonly used for radiation protection, lead is a highly toxic metal. The alternative lead-free materials with no toxicity should be beneficial. Therefore, this study aimed to develop a novel lead-free transparent material for using in nuclear medicine and to determine radiation shielding property.

Materials and methods: Borosilicate glasses doping with WO_3 filler were produced by melt-quenching technique based on the glass formulation of $25Na_2O$-$15B_2O_3$-(60-x)-SiO_2-(x) WO_3, where x = 0, 0.5, 1 and 1.5 % by weight. Density of the samples were determined. The radiation shielding properties were investigated using ^{137}Cs, ^{133}Ba and ^{57}Co sources to represent the common energies used in nuclear medicine. The linear attenuation coefficients of samples were estimated from measurement using NaI(Tl) scintillation detector coupled with multi-channel-analyzer (MCA) in a narrow beam geometry set up. Eventually, mass attenuation coefficients of the samples were calculated.

Results: Transparent glasses with various concentrations of WO_3, 0, 0.5, 1, 1.5 % were produced and their density were 2.54, 2.57, 2.60 and 2.62 g/cm^3, respectively. The linear attenuation coefficients of the produced samples with varying concentrations of WO_3 were 0.11, 0.22, 0.31 and 0.39 cm^{-1} for ^{137}Cs, 0.26, 0.38, 0.43 and 0.50 cm^{-1} for ^{133}Ba and 0.30, 0.42, 0.50 and 0.58 cm^{-1} for ^{57}Co. Then calculation of mass attenuation coefficients for ^{137}Cs, ^{133}Ba and ^{57}Co sources were 0.04, 0.09, 0.12, 0.15 cm^2/g, 0.10, 0.15, 0.16, 0.19 cm^2/g and 0.12, 0.16, 0.19, 0.22 cm^2/g, respectively, when the concentration of WO_3 varied from 0 to 1.5%.

Conclusion: Lead-free transparent material of borosilicate glass doping with WO_3 showed the promising results to attenuate the gamma radiations commonly used in nuclear medicine. Moreover, radiation shielding property was increased with the concentration of the WO_3 filler.

Keywords: Lead-free transparent shield, borosilicate glasses doping with WO_3

Minimizing slice-overlap artifacts in MRI lumbar spine: A phantom study

Kanyakham K[1], Loungwutiwong J[2], Krisanachinda A[3]

1 Imaging Center, Phyathai 2 Hospital, Phya Thai, Bangkok, Thailand

2 Imaging Center, Phyathai 2 Hospital, Phya Thai, Bangkok, Thailand

3 Department of Radiology, Faculty of Medicine, Chulalongkorn University, Bangkok, Thailand

**kanni.pp@gmail.com*

Introduction: Slice-overlap artifacts or crosstalk artifacts are dark signal lines that appear on MR images and are caused by overlapping of multiple slices during an MRI scan, which can occur due to imperfect multi-slice settings. These artifacts can degrade the image quality and make it difficult for radiologists to accurately diagnose patients. The objective of this study was to reduce the effects of slice-overlap artifact on T1W and T2W TSE sequences in MRI lumbosacral Spine imaging and improve the diagnostic value of the images by using an interleave method and optimizing the minimum number of packages based on the basic principles of MRI sequencing on the time concept.

Methods: The experiment was carried out by scanning a water phantom using a 3.0 T Philips MR System Achieva dStream. Different methods were used, including the slice scan order, interleave method with adjusted minimum number of packages, linear method (slice scan order: FH, HF, default, reverse central). In this study, the number of slice was 36 slices. The interleave method was set, and the minimum number of packages was estimated by the square root of the number of slices ($\sqrt{36} = 6$).

Results: The crosstalk artifact did not appear in the interleave method with the square root of the number of slices.

Conclusion: The interleave method and optimizing the minimum number of packages appropriately can effectively reduce the effects of overlapping artifacts in MRI imaging. The study found no evidence of overlapping artifacts when using Interleave method.

Keyword: interleave, minimum number of packages, slice-overlap artifact, MRI Lumbar spine

Impact of contrast agent administration on water equivalent diameter for size-specific dose estimate (SSDE) calculation in chest CT angiography

Kaewsan N[1,2*], Khamwan K[2,3]

1 Medical Physics Program, Department of Radiology, Faculty of Medicine, Chulalongkorn University 1873 Rama IV, Pathumwan, Bangkok, Thailand

2 Chulalongkorn University Biomedical Imaging Group, Department of Radiology, Faculty of Medicine, Chulalongkorn University 1873 Rama IV, Pathumwan, Bangkok, Thailand

3 Division of Nuclear Medicine, Department of Radiology, Faculty of Medicine, Chulalongkorn University, 1873 Rama IV, Pathumwan, Bangkok, Thailand

**6570028130@student.chula.ac.th*

Introduction: The study aimed to determine the impact of intravenous contrast enhancement on the calculation of water equivalent diameter (D_w) for size-specific dose estimate (SSDE) in chest CT angiography (CTA) using the different calculation methods in arterial phase images.

Methods: A cohort of 230 adult patients (145 males and 85 females) who underwent chest CT angiography at King Chulalongkorn Memorial Hospital between January 2018 and December 2023 was included. The 3D Slicer image computing software was used to automatically draw regions of interest in each axial CT image to measure area and mean CT number. The D_w values were calculated in both of non-contrast and arterial phase images following the AAPM report 220 utilizing three different methods: the D_w measured at mid-chest slice ($D_{w,\,mid}$); the average of 3-level slices at the 25th, 50th, and 75th percentiles of CT image series ($D_{w,\,3\text{-}levels}$); and the average of D_w values from the entire scan length ($D_{w,\,whole}$). A paired t-test was used to statistically analyze the differences in D_w values between non-contrast and arterial phase images.

Results: Statistically significant differences were observed between D_w values in non-contrast and arterial phases for all calculation methods ($p<0.001$) with the average percent difference of 4.24%, 2.67%, and 2.21% for $D_{w,\,mid}$, $D_{w,\,3\text{-}levels}$, and $D_{w,\,whole}$, respectively. Strong correlations were found between $D_{w,\,mid}$ and $D_{w,\,whole}$ as well as $D_{w,\,3\text{-}levels}$ and $D_{w,\,whole}$ with R^2 of 0.90 and 0.97, respectively. The $D_{w,\,3\text{-}levels}$ provided higher accuracy in estimating SSDE for chest CTA compared to $D_{w,\,mid}$, aligning with the values calculated from $D_{w,\,whole}$ approach.

Conclusion: This study demonstrated that the enhancement of contrast agent has a notable impact on D_w calculation in chest CTA, particularly concerning D_w calculated at the mid-chest level.

Keywords: Water equivalent diameter (D_w), Size-specific dose estimate (SSDE), Chest CT angiography

Impact of deep learning-based image reconstruction on arm-induced artifacts in abdominal CT

Wongvit-olarn S[1,2]*, Minchanat S[2], Bunnag N[2], Khamwan K[1,3], Shunhavanich P[1,3]

1 Medical Physics Program, Department of Radiology, Faculty of Medicine, Chulalongkorn University, Bangkok, Thailand

2 Department of Radiology, King Chulalongkorn Memorial Hospital, Thai Red Cross Society, Bangkok, Thailand

3 Department of Radiology, Faculty of Medicine, Chulalongkorn University, Bangkok, Thailand

**suppakit_beem@hotmail.com*

Introduction: Arm-induced streak artifacts are observed in abdominal CT images of patients who cannot elevate their arms during examination. This study aims to compare the arm-induced artifacts in abdominal CT with different arms-down positioning between deep learning-based image reconstruction (DLIR), adaptive statistical iterative reconstruction-Veo (ASIR-V), and filtered back projection (FBP).

Methods: A semi-anthropomorphic liver phantom was scanned with three different arm positions: (A) both arms down alongside the body, (B) both arms flexed and forearms on upper abdomen region, and (C) both arms crossed in front of the pelvic area. All scan data were acquired at the same CTDIvol and were reconstructed using DLIR (L-low, M-medium, and H-high), ASIR-V (50% and 100%), and FBP. 40 parallel line segments were placed perpendicular to streak artifacts in a liver parenchyma region and were used to calculate the location parameter of the Gumbel distribution, indicating the strength of the artifacts. Standard deviation in the same region was also examined. In addition, the abdominal contrast-enhanced CT images of 10 patients who underwent CT with arms down in position A were evaluated by two radiologists in terms of artifact reduction and overall image quality on a four-point scale.

Results: For all arm positions of the phantom study, DLIR-H achieved significantly lower image noise and location parameter than DLIR-M, DLIR-L, ASIR-V50%, and FBP ($p < 0.05$). Although DLIR-M and ASIR-V50% were not significantly different in phantom location parameter ($p = 0.0977$), DLIR-M showed better average qualitative scores than ASIR-V50% in patient data both in terms of artifact reduction and overall image quality. ASIR-V100% had lowest SD and location parameter, but worst overall image quality score. Among different arm positions, position C showed the least streaks followed by position B and A, respectively.

Conclusion: DLIR reduced arm-induced artifacts in abdominal CT with different arms-down positions more effectively than FBP and ASIR-V, and the image quality was improved with higher strength level of DLIR.

Keywords: Abdominal computed tomography, Deep learning-based image reconstruction, Arm-induced artifacts, Gumbel distribution.

Localization of epileptogenic zones using radiomic analysis of ictal and interictal SPECT data

Thuwarojsakul J[1,2*], Sukprakun C[3], Tepmongkol S[2,3], Sriswasdi S[4,5], Rakvongthai Y[2,3]

1 Medical Physics Program, Department of Radiology, Faculty of Medicine, Chulalongkorn University, Bangkok, Thailand.

2 Chulalongkorn University Biomedical Imaging Group, Department of Radiology, Faculty of Medicine, Chulalongkorn University, Bangkok, Thailand.

3 Division of Nuclear Medicine, Department of Radiology, Faculty of Medicine, Chulalongkorn University, Bangkok, Thailand.

4 Center of Excellence in Computational Molecular Biology, Chulalongkorn University, Bangkok, Thailand.

5 Center for Artificial Intelligence in Medicine, Research Affairs, Faculty of Medicine, Chulalongkorn University, Bangkok, Thailand.

**Jinjuthathip29@gmail.com*

Introduction: Epilepsy is one of the most common and burdensome neurological disorders. Achieving control over postoperative seizures largely depends on the precise identification of the epileptogenic zone (EZ). In this study, we constructed prediction models to identify the EZ location using radiomic features extracted from SPECT images.

Methods: Twenty ictal and interictal SPECT datasets were retrospectively collected. All images were preprocessed and registered to the statistical parametric mapping (SPM) SPECT brain template to calculate z-score images. Subsequently, the brain was segmented into 85 regions using the AAL2 atlas. For each region, radiomics features were extracted using Pyradiomics. Based on multivariate logistic regression and a five-fold cross-validation strategy, three models were constructed including the ictal model, the z-score model and the combined model whose radiomic features were from the ictal image, the z-score image, and their combination, respectively. Their performances were evaluated using the area under the receiver operating characteristic curve (AUC) and compared with readings from nuclear medicine physicians.

Results: The results in validation showed that, among the three models, the combined model had the highest AUC value (AUC = 0.918 ± 0.044) and sensitivity (0.954 ± 0.044), while the ictal model achieved the highest specificity (0.848 ± 0.052). In comparison, physician readings exhibited a sensitivity of 0.679 ± 0.277 and a specificity of 0.980 ± 0.007.

Conclusion: Radiomic analysis showed a promising potential in identifying the locations of the EZ from SPECT images in epilepsy patients These findings suggested that our radiomic models could serve as an initial screening tool for identifying potential EZ locations, thereby potentially aiding physicians in clinical decision-making.

Keywords: Epilepsy, SPECT imaging, Ictal-Interictal SPECT, Radiomics

Prediction of axillary lymph node metastasis in clinically node-negative breast cancer magnetic resonance imaging-based radiomics

Sukumwattana W[1,2*], Chirachamnienkal R[3], Sawaddeemongkhon V[3], Jirarayapong J[4], Khongwirotphan S[2,5], Sriswasdi S[6,7], Pipatpajong S[3,8], Rakvongthai Y[2,9]

1 Medical Physics Program, Department of Radiology, Faculty of Medicine, Chulalongkorn University, Bangkok, Thailand.
2 Chulalongkorn University Biomedical Imaging Group, Department of Radiology, Faculty of Medicine, Chulalongkorn University, Bangkok, Thailand.
3 Department of Radiology, King Chulalongkorn Memorial Hospital, Bangkok, Thailand.
4 Department of Radiology, King Chulalongkorn Memorial Hospital and The Thai Red Cross Society, Chulalongkorn University, Bangkok, Thailand.
5 Department of Radiological Technology and Medical Physics, Faculty of Allied Health Sciences, Chulalongkorn University, Bangkok, Thailand.
6 Center of Excellence in Computational Molecular Biology, Chulalongkorn University, Bangkok, Thailand.
7 Center for Artificial Intelligence in Medicine, Research Affairs, Faculty of Medicine, Chulalongkorn University, Bangkok, Thailand.
8 Department of Radiology, Faculty of Medicine, Chulalongkorn University, Bangkok, Thailand.
9 Division of Nuclear Medicine, Department of Radiology, Faculty of Medicine, Chulalongkorn University, Bangkok, Thailand.

**wichasa.suk@gmail.com*

Introduction: Axillary lymph node metastasis (ALNM) status is a crucial predictor of breast cancer. It is typically assessed invasively through axillary lymph node dissection (ALND) or sentinel lymph node biopsy (SLNB). The imaging examination is a non-invasive tool to evaluate ALNM, but it has a high false negative rate. In this study, we aimed to construct a magnetic resonance imaging (MRI)-based radiomic model as well as a combined model incorporating radiomic and clinical models to predict ALNM in breast cancer patients.

Methods: A cohort of 181 patients with clinically node-negative breast cancer was collected and split into 150 patients for training and validation, and 31 patients for testing. The model construction involved 4 steps. First, segmentation of the tumor was performed on MRI by 3 delineators. Second, radiomic features were computed via Pyradiomics. Third, features were selected through the intraclass correlation coefficient (ICC) and recursive feature elimination with cross-validation (RFECV). Finally, a multivariate logistic regression model was constructed. The model performance was assessed by the area under the receiver operating characteristic (ROC) curve (AUC) and was compared using the Benjamini–Hochberg procedure.

Results: Out of 3,577 radiomic features, 6 features were selected to build the MRI-based radiomic model. It achieved the AUCs of 0.805 ± 0.009 and 0.807 ± 0.043 in training and validation, and 0.800 in testing, outperforming the clinical model across all datasets ($p < 0.05$). The combined model yielded even better performance than the MRI-based radiomic model with an AUC of 0.836 ± 0.012 and 0.791 ± 0.050 in training and validation, and 0.845 in testing, but the difference was only significant at $p = 0.07$.

Conclusions: The MRI-based radiomic model outperformed the clinical model in predicting ALNM in clinically node-negative breast cancer patients, promising in guiding treatment decisions and reducing the risk of overtreatment.

Keywords: Clinically node-negative breast cancer, Axillary lymph node metastasis, Magnetic resonance imaging, Radiomics

Distant metastasis prediction after radiation treatment in patients with esophageal squamous cell carcinoma using CT-based radiomics

Chanchayanon T[1,2*], Kitpanit S[3], Kannarunimit D[4], Chakkabat C[4], Lertbutsayanukul C[4], Sriswasdi S[5,6], Khongwirotphan S[2,7], Prayongrat A[3], Rakvongthai Y[2,8]

1 Medical Physics Program, Department of Radiology, Faculty of Medicine, Chulalongkorn University, Bangkok, Thailand.
2 Chulalongkorn University Biomedical Imaging Group, Department of Radiology, Faculty of Medicine, Chulalongkorn University, Bangkok, Thailand.
3 Division of Radiation Oncology, Department of Radiology, King Chulalongkorn Memorial Hospital, Bangkok, Thailand.
4 Division of Radiation Oncology, Department of Radiology, Faculty of Medicine, Chulalongkorn University, Bangkok, Thailand.
5 Center for Artificial Intelligence in Medicine, Research Affairs, Faculty of Medicine, Chulalongkorn University, Bangkok, Thailand.
6 Center of Excellence in Computational Molecular Biology, Chulalongkorn University, Bangkok, Thailand.
7 Department of Radiological Technology and Medical Physics, Faculty of Allied Health Sciences, Chulalongkorn University, Bangkok, Thailand
8 Division of Nuclear Medicine, Department of Radiology, Faculty of Medicine, Chulalongkorn University, Bangkok, Thailand.

**6570036130@student.chula.ac.th*

Introduction: Esophageal cancer (EC) is the eighth most prevalent malignancy and sixth leading cause of mortality worldwide. This cancer poses a burden in Thailand due to its unfavorable prognosis and survival rates. In this study, our objective was to develop a radiomic-based model utilizing contrast-enhanced computed tomography (CECT) data, which aimed to predict distant metastasis following chemoradiotherapy in patients with esophageal cancer. If successful, this would assist healthcare professionals in treatment decision-making and patient management.

Methods: We retrospectively enrolled 143 patients from King Chulalongkorn Memorial Hospital, analyzing CECT images as part of a comprehensive cohort. Gross tumor volume (GTV) segmentation was performed by experienced radiation oncologists. PyRadiomics 3.0.1 was employed to extract radiomic features. Feature selection is using of intraclass correlation coefficient (ICC) and recursive feature elimination with cross-validation (RFECV). Multivariate logistic regression models were developed and tuned using a five-fold cross-validation scheme. Predictive performance of radiomic features was evaluated through the area under the receiver operating characteristic curve (AUROC), with statistical analysis using the sign test and Benjamini-Hochberg procedure.

Results: Of 1288 radiomic features extracted from CECT image, a set of 34 radiomic features were selected and incorporated with clinical and dosimetric variables to construct the optimal multivariate model. In validation, this combined radiomic-clinical-dosimetric model yielded an AUROC of 0.725±0.084, which was significantly higher than an AUROC of 0.613±0.048 from the combined clinical-dosimetric model ($p < 0.05$).

Conclusions: Our multivariate radiomic model holds potential as an effective tool for predicting distant metastasis in patients with esophageal cancer. This advancement may significantly improve treatment stratification in clinical settings.

Keywords: Esophageal cancer, chemoradiotherapy, Distant metastasis, Radiomic features, CECT imaging

Development of gold nanoparticle-incorporated gelatin-based hydrogel for radiation dosimetry

Choosin P[1,3*], Tippayamontri T[2], Thongnuek P[1], Pungkun V[3]

1 Department of Biomedical Engineering, Faculty of Engineering, Chulalongkorn University, Bangkok, Thailand.

2 Department of Radiological Technology and Medical Physics, Faculty of Allied Health Sciences, Chulalongkorn University, Bangkok, Thailand.

3 Nuclear and Radiation Metrology Section, Regulatory Technical Support Division, Office of Atoms for Peace, Bangkok, Thailand

**Phavinee.c@oap.go.th*

Introduction: Radiation dosimetry are required for the control of delivered dose and prediction of radiation effects which can be performed with a help of nano-sensors made of radiation sensitive materials - whose physical and/or chemical properties change due to exposure to radiation. Hydrogels, characterized by their hydrophilic-3D porous polymer networks, offer a versatile platform that can be tailored through the incorporation of noble metal nanoparticles. In this study, we present a novel approach involving the utilization of gold nanoparticles to engineer a colorimetric plasmonic gelatin-based hydrogel nanocomposite.

Methods: The investigation involved determining the optimal solution concentration of gelatin-based hydrogel gold nanosensors. Subsequently, the hydrogel was subjected to clinical radiation absorbed doses ranging from 1 to 5 Gy. To analyze the radiation-induced alterations in the hydrogels, a well-established UV-VIS spectrometry method was employed. Consequently, an assessment was conducted to evaluate the radiation response with respect to linearity, accuracy, reproducibility, and stability of the gelatin-based hydrogel gold nanosensors.

Results: In the development of this nanosensor, gold ions are confined within a gelatin hydrogel matrix. Upon exposure to radiation, a reduction process ensues, resulting in the formation of gold nanoparticles. This transformation leads to a swift and visually perceptible change in color, converting the initially colorless hydrogel into a distinctly colored state. The introduction of gold nanoparticles serves to augment the generation of hydroxyl radicals through the radiolysis of water, enabling effective clinical radiation-dose verification within the range of 0–5 Gy. This verification is supported by a high linear correlation coefficient, indicative of the nanosensor's strong sensitivity to radiation levels. Notably, the stability of the nanosensor was observed and maintained over a period of 72 hours, highlighting its robustness and reliability for extended use.

Conclusion: This innovative approach establishes a reliable and effective method for 3D dose verification, thereby ensuring the safety and efficiency of medical treatments. The outcomes of this study not only contribute to the advancement of 3D dose verification techniques but also serve as inspiration for the development of additional radio-nanosensing hydrogels. This collective progress holds promising implications for enhancing the accuracy and reliability of medical treatments in the field.

Keywords: Gold nanoparticle, Gelatin-based hydrogel, Nanosensor, Radiation dosimetry

Prediction of diabetic peripheral neuropathy in patient's limbs using inverse problem algorithm and Taiwan population-based clinical data

Huang Shih-Hsun[1], Pan Lung-Kwang[1], Pan Lung-Fa[1], Peng Bing-Ru[1*], Kittipayak S[2*]

1 Department of Medical Imaging and Radiological Science, Central Taiwan University of Science and Technology, Takun, Taichung 406, Taiwan, ROC.

2 School of Radiological Technology, Faculty of Health Science Technology, HRH Princess Chulabhorn college of Medical Science, Chulabhon Royal Academy, Bangkok, Thailand

**0953939793@gmail.com, Samrit.Kit@cra.ac.th*

Introduction: Diabetic peripheral neuropathy usually occurs in the early stages of the disease. It often results in physical discomfort, higher medical costs, and lower quality of life if it cannot detect and treat early. Yet, the sympathetic nerve skin response meter (SUDOSCAN2) is a rapid and reliable technique undertaken in most Taiwanese hospital to process the early diagnosis of diabetic peripheral neuropathy.

Methods: A retrospective approach with inverse problem algorithm integrated seven essential risk factors (BMI, mean arterial pressure, HbA1c, Creatinine, LDL-C, T. Cholesterol and GOT) of diabetic patients to predict the peripheral neuropathy in patient's limbs. The factors were collected and normalized to eliminate the dimension. This was essential to unify the contribution from every biological factor between [-1, +1]. Furthermore, a self-developed 29-term first order nonlinear semi-empirical formula according to the seven factors was proposed and run in STATISTICA 7.0 to predict the damage stage of various patients. Accordingly, a group of 755 patients with diabetic syndrome was analyzed and arranged into [755×29] dataset matrix then derived the expectation value of limb's damage stage. Another group of 186 patients with same syndrome was verified in the follow-up study to check the accuracy of this formula.

Results: The loss function, sample variance, and coefficient of correlation of the derived semi-empirical equation was 2.1267, 0.8845, and 0.9405, respectively in this survey indicating that there was no systematic or random error in the regression fit. The verified group also implied a high coefficient of correlation, 0.88772 indicating high coincidence in the numerical analysis.

Conclusion: The inverse problem algorithm well predicted the potential damage stage of limbs for diabetic patients.

Keywords: Inverse problem algorithm, diabetic, practical survey, semi-empirical formula.

Inverse problem algorithm application to analyze the peripheral visual field damage of glaucoma patients from clinical dataset: A Taiwan population-based survey

Ke Ching-Hsiu[1], Pan Lung-Kwang[1], Pan Lung-Fa[1], Peng Bing-Ru[1*], Kittipayak S[2*]

1 Department of Medical Imaging and Radiological Science, Central Taiwan University of Science and Technology, Takun, Taichung 406, Taiwan, ROC.

2 School of Radiological Technology, Faculty of Health Science Technology, HRH Princess Chulabhorn college of Medical Science, Chulabhon Royal Academy, Bangkok, Thailand

**0953939793@gmail.com, Samrit.Kit@cra.ac.th*

Introduction: Glaucoma is one of the major causes of blindness in the elderly population. It is hard to detect and treat early in the clinical field. However, without any regular examination, or active treatment after the diagnosis, blindness may still occur.

Methods: The inverse problem algorithm was adopted to quantify the damage, and all the clinical data was collected from Taiwanese patients with peripheral visual field damage (PVFD). In doing so, 398 patients with six risk factors assigned as age, blood sugar, mean arterial pressure (MAP), visual acuity, intraocular pressure, cup/disc ratio were collected and normalized to become a group of dimensionless values between [-1, +1]. This is an essential process to ensure the contribution of every risk factor having similar weighting. Thus, a data matrix of [398×22] was run by a self-developed program defined as first-order nonlinear semi-empirical formula with 22 terms of coefficients according to STATISTICA 7.0 default function. The derived numerical solution revealed the damage level of PVFD patients. Furthermore, another 66 patients were adopted as verified group to ensure the accuracy of program prediction in reality.

Results: The loss function, sample variance, and coefficient of correlation of the derived semi-empirical equation was 7.0390, 0.8810, and 0.9386, respectively in this survey indicating that there was no systematic or random error in the regression fit. The most dominant factors were cup/disc ratio. Therefore, the glaucoma could be effectively suppressed if having the early examination of cup/disc ratio for PVFD patients.

Conclusion: The inverse problem proves to be a powerful and effective technique in ophthalmologic survey.

Keywords: Inverse problem algorithm, glaucoma, practical survey, semi-empirical formula.

Full Papers: *Radiotherapy*

Treatment plans comparison between HALCYON and VERSAHD for ultra-hypofractionated of high-risk prostate cancer using multi-criteria optimization

Prangnuan K[1], Tangboonduangjit P[1], Khachonkham S[1], Thuratong S[2], Thiranuntakul N[2]

1 Master of Science Program in Medical physics, Faculty of Medicine Ramathibodi Hospital, Mahidol University, Bangkok, Thailand.

2 Thammasat Radiation and Oncology Center, Thammasat university Hospital, Pathum Thani, Thailand.

Corresponding author email: kanyapat.jzy@gmail.com

Abstract

Introduction**: The innovative approach of multi-criteria optimization aids in the creation of treatment plans. This research compares the plan quality and deliverability of various linear accelerator architectures in a multi-vendor setting while utilizing the same treatment planning system with multicriteria optimization in ultra-hypofractionated high-risk prostate cancer.**

Methods**: Nine image sets of high-risk prostate cancer that treated by Halcyon with a prescription dose of 40 Gy in 5 fractions were re-planned for the VersaHD traditional C-arm machine using 6 MV energy with flattening filter-free (FFF) and auto dosage rate mode. Anisotropic analytical algorithm (AAA) calculation with multicriteria optimization was used in Eclipse treatment planning system version 16.1 to generate the new plans. The entire plan underwent a dry run to correct the delivery data. All dose volume histograms, conformity index, homogeneity index, and delivery parameters were assessed and compared using the student's pair t-test on the PASW statistic 18 application.**

Results**: The multi-criteria optimization technique offered equivalent coverage in PTV40 and PTV30 but exhibited the distinction of dose coverage in D98 and D95, with corresponding p-values of 0.044 and 0.037 in PTV25. The mean dose in surrounding organs did not differ appreciably in any PTV. The conformity index demonstrated a difference in PTV30 and PTV25 with p-values of 0.049 and 0.005, respectively. The homogeneity index showed a distinct difference only for PTV25, with a p-value of 0.014. The mean total monitor units for VersaHD and Halcyon were 3226.92 and 3581.06 MUs, respectively. The typical beam on time figured for Halcyon and VersaHD were 4.66 and 5.17 minutes, respectively. Overall, both devices showed the same capabilities in the delivery section.**

Conclusion**: The combination of the SBRT approach with simultaneous integrated boost (SIB) pelvic node irradiation in ultra-hypofractionated for high-risk prostate cancer patients on the Halcyon and VersaHD is comparable in terms of plan quality and deliverability.**

Keywords**: Halcyon, VersaHD, high-risk prostate cancer, multi-criteria optimization.**

I. INTRODUCTION

For the treatment of cancer, there are various types of radiation machines. Every type has a unique design, particularly in the case of the multi-leaf collimator, which modifies the beam and influences the dose distribution in the plan [1]. In general, the machinery will receive the plans from a specific treatment planning system (TPS). In any case, modern technology may allow for the cross-use of TPS across many vendors [2]. The Eclipse treatment planning system has a multi-criteria optimization (MCO) feature. This study aims to compare the ultra-hypofractionated treatment plans for high-risk prostate cancer across Halcyon and VersaHD machines, which differ in terms of photon beam spectrum and MLC characteristic. This study also included a performance analysis of the multi-criteria optimization function in the Eclipse treatment planning system, utilizing a different vendor machine.

II. MATERIALS AND METHODS

A. Image set and dose prescription

Retrospective research was conducted using two sets of clinical images from nine patients who underwent CT and MRI scans after being immobilized in the head-first supine position with the arm raised using a pelvic mask (Klarity Medical Products, Guangzhou, China). A Siemens Healthcare Somatom Definition AS CT scanner possessing 64 slices, an 80 cm bore, and a level tabletop was utilized to acquire each CT image set. Coverage for the axial helical mode stretched from the L2 to the mid-femur when the full bladder and empty rectum protocols were followed. All MRI image sets were obtained using a 3 Tesla superconducting MRI scanner from Magnetom, Siemens Healthcare, which has a bore diameter of 60 cm, a length of 213 cm, a field of view (FOV) of 50×50×50 cm, and gradients of 80 mT/m at 200 m/s [49] for T2 weighted images and DWI sequences. Both 3D image sets were imported into Eclipse treatment planning system version 16.1 (Varian Medical Systems, Palo Alto, CA) and registered for structure contouring of both targets and organs at risk based on the ESTRO guidelines [3]. In high-risk prostate cancer, not only the tumor base at the prostate gland but also the lymph node, both elective and selective, was irradiated [4] with the simultaneous integrated boost (SIB) technique. The prescription for the prostate gland is 40 Gy, the positive node received 30 Gy, and the elective pelvic node is 25 Gy in 5 fractions.

B. Linear accelerators system

There are two systems of linear accelerators in this study. The first one is a ring-base Halcyon that is equipped with dual-layer MLCs. There is only one energy source (6 MV) without a flattening filter, a percentage dependent dose equal to 1.3 cm, and a dose rate of 800 monitor units (MU) per minute. The second one is a conventional C-arm base linac that is equipped with the single-layer Agility MLC. There are four energies (6MV, 6MV FFF, 10MV, and 10MV FFF). Otherwise, this study controls the energy using only 6 MV without a flattening filter with a percentage depth dose equal to 1.65 cm and an auto-dose rate that can raise up to 1400 MU/min.

C. Prostate ultra-hypofractionation treatment plans

The Eclipse treatment planning system version 16.1 (Varian Medical Systems, Palo Alto, CA) was used in this study using the multicriteria optimization (MCO) function with the anisotropic analytical algorithm (AAA) calculation algorithm. The plans were generated by the same planner for each patient. In the planning process, it was noted that the planner was not aware of any quantitative criterion for coverage, homogeneity, or conformity evaluation during the planning process to avoid bias and therefore to achieve the clinical routine goal. All that is fixed is the photon energy using 6 MV without a flattening filter. In accordance with the planner's concept, the remaining plan parameters are flexible and can be designed to fit the planner's vision. Both PTV coverage and dose to an organ at risk were captured in the dose volume histogram data. Furthermore, Paddick [5] and ICRU83 [6] equations were utilized to compute the conformity index and homogeneity index, respectively. All of the plans were dry-run to record the delivery parameter for both the total monitor unit and beam on time and then calculate the modulation factor (MF) using the total monitor unit divided by the prescription dose. Every piece of data was entered into Microsoft Excel and then analyzed with PAWS Statistic version 18. A p-value of less than 0.05 indicates a significant difference in the data.

III. RESULTS

The results are separated into two parts. Both plans consist of dose volume histogram analysis in terms of PTV coverage, hot dose area, dose conformity, homogeneity index, and dose to adjacent organs, and the delivery section in terms of the total monitor units (MU), modulation factor (MF), and beam on time (BOT).

A. Plan quality

The analysis of the dose volume histogram was conducted for both PTV coverage and dosage to adjacent organs. The results in Figure 1 show that only PTV25 has a different value. The maximum dosage data in PTV 25 exhibits a p-value of 0.046, whereas the coverage dose at 98 and 95 percent exhibits a

substantially different p-value of 0.044 and 0.037, respectively. Figure 2 shows that in both the Halcyon and VersaHD plans, the mean dosage to every surrounding organ had the same value. The considerably different PTV30 and PTV25 are shown by the conformance index in Figure 3A, with p values of 0.049 and 0.005, respectively. With a p-value of 0.014, Figure 3B illustrates the distinct homogenous dosage in just PTV25.

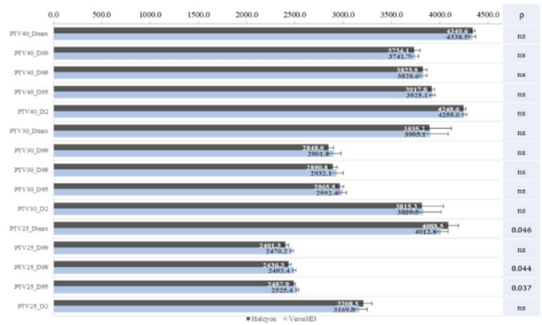

Figure 1. *The comparison of maximum dose and dose coverage in each PTV of plan (cGy) under multi-criteria optimization technique between Halcyon and VersaHD plans.*

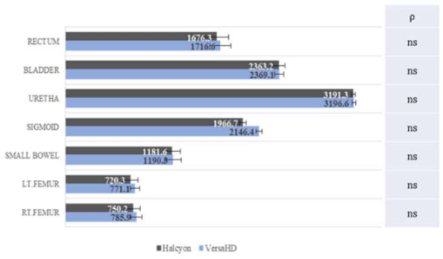

Figure 2. *The comparison of mean dose in surrounding organ (cGy) between Halcyon and VersaHD plans.*

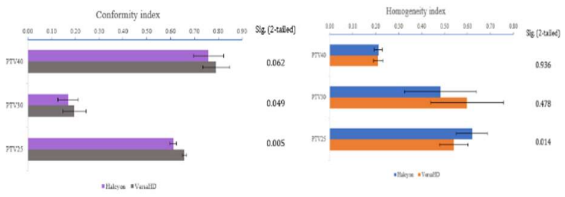

(A) (B)

Figure 3. *The conformity index (A) and the homogeneity index (B) in multi-criteria optimization process.*

B. delivery section

Both Halcyon and VersaHD plans provide the equivalent in total monitor unit, modulation factor, and beam on time, as indicated by the data in Table 1.

Table 1. *The result of delivery section; the average of total monitor unit, modulation factor, and beam on time (minute)*

Delivery parameters	MCO		
	Halcyon	VersaHD	p
Total monitor unit	3581.06	3226.92	ns
Modulation factor	0.9	0.81	ns
Beam on time (min)	4.66	5.17	ns

IV. DISCUSSION

In this study, the Halcyon was compared with the conventional C-arm base linac VersaHD using the same treatment planning system with the function of multi-criteria optimization.

A. Plan quality

In terms of PTV coverage, there is no difference in high-dose PTV that follows the trade-off technique in the multi-criteria optimization process. There are three steps to MCO optimization [7]. The first one was generated using the Pareto surface approximation algorithm. The second step was optimizing the dose volume histogram using the navigation algorithm. Finally, there was MLC segmentation to choose the best MLC style to deliver the beam. In the clinical trade-off process, pay close attention to the high dosage of PTV initially. This could explain why PTV40 does not differ in terms of conformance and homogeneity index in addition to dose coverage. In terms of mean dose to adjacent organ, there is no difference between both plans in all. The results are a bit different from the study by Tamihardja J. et al. [8] that compared the Halcyon and Elekta synergy platforms and showed a difference in the mean dose of both femoral heads. There can be effects from the MCO process mentioned in the previous reference above.

B. Delivery section

There is no significant difference in all parameters. Otherwise, when looking at the details, the results show the opposite results when compared with the Pokhrel D. et al. study

[9]. The VersaHD, which can raise the dose rate to 1400 MU/min, should provide a short beam on time, but the result shows a longer beam on time than the Halcyon plans. Such may have an impact on the algorithm in the multi-criteria optimization procedure that is based on the research conducted by Sebastiaan Breedveld and others [10]. They discuss the complexity of the MCO process's delivery technique. In order to maximize plan quality, dynamic MLC segmentation must balance multiple restrictions, including delivery feasibility, treatment duration, and plan quality.

V. CONCLUSION

The Halcyon machine can offer an equivalent clinical ultra-hypofractionation treatment plan for high-risk prostate cancer in both target coverage and surrounding organ sparing when using a multi-criteria optimization process.

ACKNOWLEDGEMENTS

The writers are grateful to their advisor, who provides me with the best support and is aware of every aspect of my condition. I would like to thank my co-workers for their help.

REFERENCES

[1] Flores-Martinez E, Kim GY, Yashar CM, Cerviño LI. Dosimetric study of the plan quality and dose to organs at risk on tangential breast treatments using the Halcyon linac. J Appl Clin Med Phys. 2019 Jul;20(7):58-67.

[2] Zhang Y, Le AH, Tian Z, Iqbal Z, Chiu T, Gu X, et al. Modeling Elekta VersaHD using the Varian Eclipse treatment planning system for photon beams: A singleinstitution experience. Journal of Applied Clinical Medical Physics. 2019;20(10):33-42.

[3] O Salembier C, Villeirs G, De Bari B, Hoskin P, Pieters BR, Van Vulpen M, et al. ESTRO ACROP consensus guideline on CT- and MRI-based target volume delineation for primary radiation therapy of localized prostate cancer. Radiotherapy and Oncology. 2018;127(1):49-61.

[4] Pinitpatcharalert A, Happersett L, Kollmeier M, McBride S, et al. Early Tolerance Outcomes of Stereotactic Hypofractionated Accelerated Radiation Therapy Concomitant with Pelvic Node Irradiation in High-risk Prostate Cancer. Adv Radiat Oncol. 2019;4(2):337-44.

[5] Paddick I. A simple scoring ratio to index the conformity of radiosurgical treatment plans. Technical note. J Neurosurg. 2000;93 Suppl 3:219-22.

[6] Grégoire V, Mackie TR. State of the art on dose prescription, reporting and recording in Intensity-Modulated Radiation Therapy (ICRU report No. 83). Cancer Radiother. 2011;15(6-7):555-9.

[7] Bokrantz R. Multicriteria optimization for volumetric-modulated arc therapy by decomposition into a fluence-based relaxation and a segment weight-based restriction. Med Phys. 2012;39(11):6712-25.

[8] Tamihardja J, Razinskas G, Exner F, Richter A, Kessler P, Weick S, et al. Comparison of treatment plans for hypofractionated high-dose prostate cancer radiotherapy using the Varian Halcyon and the Elekta Synergy platforms. J Appl Clin Med Phys. 2021;22(9):262-70.

[9] Pokhrel D, Tackett T, Stephen J, Visak J, Amin-Zimmerman F, McGregor A, et al. Prostate SBRT using O-Ring Halcyon Linac — Plan quality, delivery efficiency, and accuracy. Journal of Applied Clinical Medical Physics. 2021;22(1):68-75.

[10] Breedveld S, Craft D, van Haveren R, Heijmen B. Multi-criteria optimization and decision-making in radiotherapy. European Journal of Operational Research. 2019;277(1):1-19.

Contacts of the corresponding author:
kanyapat.jzy@gmail.com
Author: Kanyapat Prangnuan
Institute: Medical Physics program,
department of radiology,
Ramathibodi Hospital,
Mahidol University
Street: Rama VI Road
City: Bangkok
Country: Thailand
Email: kanyapat.jzy@gmail.com

An evaluation of the impact of 4D-CBCT acquisition parameters on image quality and geometric accuracy in lung SBRT: A phantom study

Choocherd Sireetorn[1], Changkaew Pimolpun[2], Khachonkham Suphalak[1,2], Stansook Nauljun[1,2*]

1 Master of Science Program in Medical Physics, Department of Diagnostic and Therapeutic Radiology, Faculty of Medicine, Ramathibodi Hospital, Mahidol University, Bangkok, Thailand

2 Division of Radiotherapy and Oncology, Department of Diagnostic and Therapeutic Radiology, Faculty of Medicine, Ramathibodi Hospital, Mahidol University, Bangkok, Thailand

**Corresponding author email: comet2522@gmail.com*

Abstract —**Four-dimensional cone-beam computed tomography (4D-CBCT) that can generate images of the patient's breathing is required for Stereotactic Body Radiation Therapy (SBRT) in the lung. However, the acquisition parameters and breathing patterns affect geometric accuracy and image quality. This study aims to identify suitable 4D-CBCT parameters that yield high image quality and geometric accuracy in lung SBRT. The moving phantom with a normal breathing pattern was performed in 4D-CBCT using various acquisition parameters, including tube current, frame rate, and gantry speed. Percentage volume difference, signal-to-noise ratio (SNR), contrast-to-noise ratio (CNR), and edge response width (ERW) were used to evaluate the geometric accuracy and image quality. The outperformed protocol was used throughout to analyze various breathing patterns, including the retrospective breathing of SBRT patients. The results of the modified protocol were analyzed and compared to the default protocol using the same image quality metrics. The modified protocol significantly enhances geometric accuracy and image quality, increasing SNR and CNR by 25.21% and 10.26%, respectively, while decreasing ERW and the percentage difference in volume by 18.08% and 2.88%, respectively. There is no significant difference in quantitative results ($p > 0.05$) among abnormal breathing patterns and patient patterns. However, the modified protocol provides images adequate for SBRT and fewer streak artifacts.**

Keywords — **Stereotactic Body Radiation Therapy, Four-Dimensional cone-beam computed tomography acquisition parameters, geometric accuracy, image quality**

I. INTRODUCTION

Stereotactic Body Radiation Therapy (SBRT) in the lung delivers precise, high-dose radiation [1]. Therefore, suitable Image-guided Radiation Therapy (IGRT) is critical for accurately detecting tumor location. An advanced 4D-CBCT image guide system has been developed to accurately account for internal organ movement during breathing, particularly in tumor regions significantly impacted by respiratory motion [2].

However, the 4D-CBCT acquisition parameters and the patient's breathing patterns can affect the image quality and geometric accuracy. Image quality and geometric accuracy improve as tube current and frame rate increase, in contrast to gantry speed [2-6]. These parameters can be adjusted by the user to obtain the best protocol for each institution under each vendor condition. An improper parameter adjustment can cause aliasing and streaking artifacts, resulting in poor image quality. However, there will be a trade-off between image quality, geometric accuracy, imaging dose, and acquisition time.

The purpose of this study is to identify suitable 4D-CBCT parameters that yield high image quality and geometric accuracy in the lung SBRT while maintaining a reasonable imaging dose and acquisition time.

II. MATERIALS AND METHODS

Prior to the experiment, the performance of the 4D-CBCT of Truebeam Varian was

verified following TG142 [7] and vendor specifications [8], as well as the Quasar™ phantom accuracy. To ensure that they were effective and could operate within the standard.

A. Optimize the parameters of 4D-CBCT

The normal breathing pattern [9], which contained a sinusoidal curve with a period of 4.5 seconds and an amplitude of 20 mm, was used to optimize the suitable acquisition parameters. The reference image was generated by performing a 4DCT of the Quasar™ phantom with a 3 cm target in the center while moving in a normal breathing pattern. In the treatment room, the moving phantom was set up as the same as the condition done in the CT simulation. Then the 4D-CBCT was performed by using default protocol parameters (125 kV, 0.8 mAs/projection, 7 fps, 3°/s) and adjusted parameters. The parameter adjustments were only performed in the direction that improved image quality, which was increased by the mAs/projection of 0.8, 1, and 1.2, a frame rate of 7, 11, and 15 fps, and decreased by the gantry speed of 2, 2.5, and 3°/s. The number of projections, scan time, and $CTDI_{vol}$ displayed in the CBCT mode editor were recorded. The 4D-CBCT images from various adjustment parameters were subsequently evaluated for image quality and geometric accuracy compared with the default protocol and found the outperformed parameter acquisition set.

B. Image Quality

Eclipse's measurement tool was used to create a 7x7 mm^2 ROI on both the target and the background to generate the histogram statistics. SNR and CNR were calculated using the mean and standard deviation of the HU as Equations (1) and (2), respectively. A higher SNR and CNR indicated better image quality.

$$\mathrm{SNR} = \frac{\bar{x}_{\mathrm{target}}}{S_{\mathrm{target}}} \quad (1)$$

$$\mathrm{CNR}_{\mathrm{target}} = \frac{\bar{x}_{target} - \bar{x}_{lung}}{\sqrt{S^2_{target} + S^2_{lung}}} \quad (2)$$

In addition, ERW was assessed to measure the sharpness of the image using the 25%-75% width of the linear intensity profile across the tumor and lung boundary in the coronal plane. Consequently, a larger ERW indicates a lower-shaped image. All image quality matric was also used in sections E and F.

C. Geometry accuracy

The auto-thresholding algorithm was used to contour the target volume on the MIP image. Determined by selecting a threshold range at random that yields a tumor volume comparable to the ground-truth volume. The percentage difference between the measured volume and the ground truth volume of the target in the phantom was calculated. This analysis was also used in sections E and F.

D. Find out the appropriate protocol

The parameter acquisition set that provided higher statistical quality metrics and differed significantly from the default protocol was chosen; this set was stated as a modified protocol. Furthermore, the imaging dose was chosen following TG 180 [10] recommendations, which is no more than 5% of the therapeutic dose, and the acquisition time was limited to 3 minutes, which is the expected amount of time the patient can remain still as much as possible. The modified protocol was used throughout to analyze various breathing patterns (E), including the retrospective breathing of SBRT patients (F).

E. The variable breathing patterns test

The various 12 breathing patterns (various in periods of 3, 4, 5, and 6 s and amplitudes of 10, 20, and 30 cm) were created on the Quasar™ phantom. The 4D-CBCT was then acquired for both the default protocol and the modified protocol.

F. The patient's breathing patterns test

11 retrospective breathing pattern data sets of lung cancer patients treated with SBRT in 2021–2023 at Ramathibodi Hospital were imported into the Quasar™ phantom. The 4D-CBCT was performed using both the default and modified protocols.

III. RESULTS

A. Optimize the parameters of 4D-CBCT

The imaging dose rose as the mAs/projection increased, while the projection count and scan time remained constant. The projection count and imaging dose increased parallel with the frame rate, while the scan time remained constant. On the other hand, the projection count, scan time, and imaging dose all increased when the gantry speed was slowed down. The parameter set of 125 kV, 0.8

mAs/projection, 15 fps, and 2°/s produced better image quality and geometric accuracy. There were significant differences with the default protocol ($p < 0.05$) which increased SNR and CNR by 25.21% and 10.26%, respectively, while decreasing ERW and the percentage difference in volume by 18.08% and 2.88%, respectively. In addition, the streak artifacts were less visible than the default protocol, as shown in Figure 1. Although the imaging dose and acquisition time were increased, the value was within a reasonable level of 5% of the therapeutic target dose and 3 minutes, respectively.

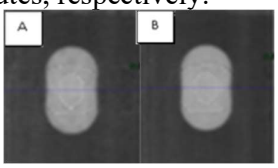

Figure 1. *The 4D-CBCT images in the coronal plane were obtained using A) the default protocol versus B) the modified protocol.*

B. The variable breathing patterns test

SNR and CNR decreased as the peak-to-peak amplitude increased, as shown in Figures 2A-2B. Both metrics were worse over a long period and had a high peak-to-peak amplitude. The largest ERW was observed in breathing patterns with the longest period (6 sec) and the highest peak-to-peak amplitude (30 cm), as shown in Figure 2C. ERW and the percentage difference in target volume for the modified protocol were generally better than the default protocol in almost all breathing patterns.

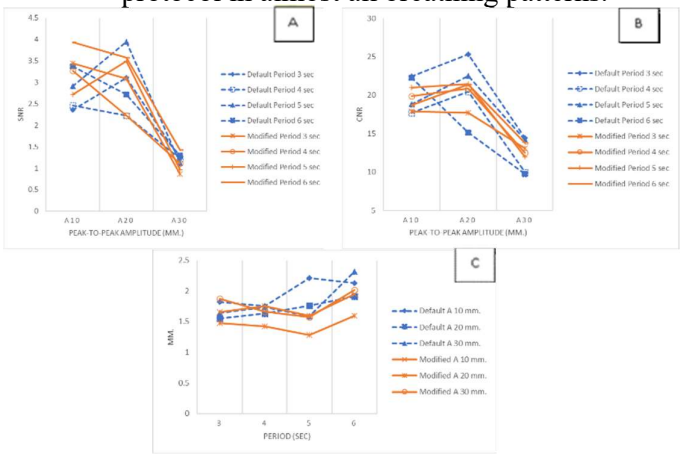

Figure 2*. The image quality metric analysis for various breathing patterns, which was acquired with default (blue color) and modified (orange color) protocol (A) SNR, (B) CNR, and (C) ERW.*

There was no significant difference between the two protocols in all quality and geometry metrics ($p > 0.05$). However, for the long period and higher amplitude breathing pattern, the modified protocol offers enhanced detailed and sharper images, including less visible streak artifacts than the default protocol, as shown in Figure 3.

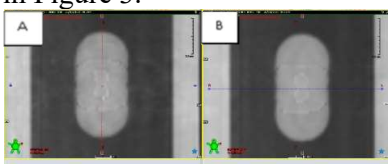

Figure 3. *A) The default protocol and B) the modified protocol were used to acquire 4D-CBCT images of a moving target with a period of 6 seconds and 30 cm amplitude.*

C. The patient's breathing patterns test

The results tended similar relationship between image quality and breathing parameters as the results in the previous section but with worse image quality. The non-periodic pattern of the patient's breathing results in an obvious degradation in image quality and geometric accuracy, as shown in Figure 4. There is also no significant difference between both protocols in all quality and geometry metrics ($p > 0.05$).

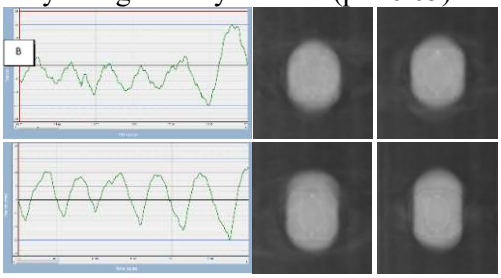

Figure 4. *The 4D-CBCT images depict patient patterns in rows A and B, with the default protocol in the middle and the modified protocol on the right.*

IV. DISCUSSION

A. Optimize the parameters of 4D-CBCT

The modified protocol differs significantly ($p < 0.05$) from the default protocol in all quality metrics because the number of projections increased by more than three times as the gantry speed decreased and the frame rate increased. The results are consistent with the Sonke J-J [3] study, which found that aliasing artifacts resulting from the limited number of projections acquired per breathing phase can be mitigated by decreasing the

gantry speed, and the Haga A [6] study found that increasing the gantry speed leads to a degradation in the image quality. The image acquisition time is extended by one minute, and the imaging dose in $CTDI_{vol}$ is roughly three times the default protocol. However, it is still within the TG180 recommendations when we compared the proportion of displayed doses ($CTDI_{vol}$) to Albarakati H's study [11], which used the Truebeam Varian machine to model Monte Carlo simulations to generate organ doses in lung cancer cases.

B. The variable breathing patterns test

SNR and CNR were worse over a long period and had a high peak-to-peak amplitude. This is due to fewer breathing cycles, resulting in a larger angular gap between projection groups in the same phase as well as an increase in the target's mobility [5, 9]. The largest ERW occurs at the longest duration and peak-to-peak amplitude of the breathing pattern, resulting in aliasing artifacts and edge blurring due to limited data. The modified protocol provided better image quality than the default protocol for long periods and a high-amplitude breathing pattern due to the slowing down of the gantry and increasing frame rate, which resulted in a larger number of projections.

C. The patient's breathing patterns test

Because the breathing patterns were quite consistent with the previous section's experiments, the relationship between image quality and breathing parameters was similar. The patient's breathing curves were irregular and non-periodic, resulting in poor image quality. The perturbation in cycle-to-cycle amplitude and period of pattern led to image blurring and artifacts [9]. The difference in image quality between the modified and default protocols is therefore less noticeable.

V. CONCLUSION

The modified protocol indicates excellent performance in providing high-quality images, accurate geometry, and fewer streak artifacts in 4D-CBCT images. These advancements are adequate for SBRT imaging. However, the expense of additional time and imaging doses should be considered.

ACKNOWLEDGEMENTS

The author would like to sincerely thank my advisor, co-advisor, and all staff from the Division of Radiation Oncology, Department of Diagnostic and Therapeutic Radiology, Faculty of Medicine, Ramathibodi Hospital, for their valuable assistance during my studies.

REFERENCES

[1] Kang KH, Okoye CC, Patel RB, Siva S, Biswas T, Ellis RJ, et al. Complications from Stereotactic Body Radiotherapy for Lung Cancer. Cancers. 2015;7(2):981-1004.

[2] Sweeney RA, Seubert B, Stark S, Homann V, Müller G, Flentje M, et al. Accuracy and inter-observer variability of 3D versus 4D cone-beam CT based image-guidance in SBRT for lung tumors. Radiat Oncol. 2012;7:81.

[3] Sonke J-J, Zijp L, Remeijer P, Herk M. Repiratory correlated cone beam CT. Medical physics. 2005;32:1176-86.

[4] Reynolds T, Lim P, Keall PJ, O'Brien R. Minimizing 4DCBCT imaging dose and scan time with Respiratory Motion Guided 4DCBCT: a pre-clinical investigation. Biomedical Physics & Engineering Express. 2021;7(2):025009.

[5] Li T, Xing L. Optimizing 4D cone-beam CT acquisition protocol for external beam radiotherapy. International Journal of Radiation Oncology, Biology, Physics. 2007;67(4):1211-9.

[6] Shibamoto Y, Miyakawa A, Iwata H, Otsuka S. Radiobiology of SBRT. 2015. p. 11-25.

[7] Klein EE, Hanley J, Bayouth J, Yin F-F, Simon W, Dresser S, et al. Task Group 142 report: Quality assurance of medical acceleratorsa). Medical Physics. 2009;36(9Part1):4197-212.

[8] Varian Medical Systems I. TrueBeam Technical Reference Guide—Volume 2: Imaging. 2018.

[9] Lee S, Yan G, Lu B, Kahler D, Li JG, Sanjiv SS. Impact of scanning parameters and breathing patterns on image quality and accuracy of tumor motion reconstruction in 4D CBCT: a phantom study. J Appl Clin Med Phys. 2015;16(6):195-212.

[10] Ding GX, Alaei P, Curran B, Flynn R, Gossman M, Mackie TR, et al. Image guidance doses delivered during radiotherapy: Quantification, management, and reduction: Report of the AAPM Therapy Physics Committee Task Group 180. Medical Physics. 2018;45(5):e84-e99.

[11] Albarakati H, Jackson P, Gulal O, Ramachandran P, Osbourne G, Liu M, et al. Dose assessment for daily cone-beam CT in lung radiotherapy patients and its combination with treatment planning. Phys Eng Sci Med. 2022;45(1):231-7.

Contacts of the corresponding author:
Author: Nauljun Stansook
Institute: Faculty of Medicine Ramathibodi Hospital, Mahidol University
Street: Rama-VI Rd
City: Bangkok
Country: Thailand
Email: comet2522@gmail.com

Comparison of modified formalism output and TRS-398 absorbed dose to water in electron beams reference dosimetry in multiple radiotherapy centers

Thinka Y[1], Tawonwong T[2], Supriyanto A. P[3], Tangboonduangjit P[4], Intanin P[5], Kittiva N[6], Maknitikul S[7], Dachaworakul K[8], Sanghangthum T[1*]

1 Medical Physics Program, Department of Radiology, Faculty of Medicine, Chulalongkorn University, Bangkok, Thailand
2 Division of Radiation Oncology, Department of Radiology, King Chulalongkorn Memorial Hospital, Bangkok, Thailand
3 Department of Physics, Faculty of Mathematics and Natural Sciences, Universitas Indonesia, Depok, Indonesia
4 Radiation Oncology Division, Department of Radiology Faculty of Medicine, Ramathibodi Hospital, Mahidol University, Bangkok, Thailand
5 Radiation Oncology Department, Chulabhorn Hospital, Chulabhorn Royal Academy, Bangkok, Thailand
6 Department of Radiology, Faculty of Medicine Vajira Hospital, Navamindradhiraj University, Bangkok, Thailand
7 Department of Radiation Oncology, Phramongkutklao Hospital, Bangkok, Thailand
8 Cancer center, Thainakarin Hospital, Bangkok, Thailand

**Corresponding author email: fangyasumon@gmail.com*

Abstract — **In electron beam therapy, the absorbed dose calibration relies on IAEA's TRS-398 and AAPM's TG-51 standards. For low-energy electron beams, plane-parallel chambers are recommended. This study aimed to compare absorbed dose to water using the modified formalism with cylindrical chambers against TRS-398 protocols in multiple centers. Data collection involved six centers in Bangkok, where the absorbed dose to water was measured using Varian linear accelerators for all electron beam energies, specific to each institute's electron beam model. Modified calibration employed cylindrical chambers for all energy beams, while TRS-398 used them for high-energy and plane-parallel chambers for low-energy, requiring cross-calibration. Charge readings utilized ionization chambers IBA FC-65G, PTW30013, and PPC40. Results, expressed as dose per monitor unit (cGy/MU), underwent a comparative analysis between the modified formalism and TRS-398, with mean differences assessed using Bland-Altman plot. In all six centers, the dose comparisons yielded acceptable results, all below ±2%, as set by TRS-398's tolerance limit. For low-energy electron beams, percent dose discrepancies ranged from -1.57% to 0.75%, and ranged from -0.37% to 0.91% for high-energy. The wider range in low-energy discrepancies may arise from chamber-to-chamber variations, setup errors, interpolating of $k_{Q,Q_{cross}}$ values. The mean difference of dose between the two protocols was 0.0002 cGy/MU, indicating no significant bias on average. Results within the 95% confidence interval affirmed the methods' similarity, ensuring reliable measurements. The modified calibration method and TRS-398 protocols prove compatible and suitable for electron beam calibration. Furthermore, the modified approach emerges as a potentially superior alternative, reducing uncertainty by eliminating the need for cross-calibration.**

Keywords — **IAEA TRS-398, AAPM TG-51, electron beam calibration, absorbed dose to water, modified calibration**

I. INTRODUCTION

Internationally recognized standards, such as IAEA's TRS-398 and AAPM's TG-51, play a crucial role in calibrating ionization chambers for measuring absorbed dose to water in electron beams. The cylindrical chambers are not recommended for low energy due to their large perturbation effects. Buckley et al. [1] used Monte Carlo simulations to determine correction factors, revealing up to 1.7% corrections needed for the NACP-02 plane-parallel chamber in low-energy electron beams. Muir[2] suggested a modified formalism based on AAPM TG-51 using cylindrical chambers, particularly effective for low-energy electrons. This study aimed to compare the absorbed dose to water between the

modified calibration and TRS-398 protocols in multiple centers.

II. MATERIALS AND METHODS

The study involved Varian linear accelerators from six radiotherapy centers in Bangkok. Absorbed dose to water measurements were carried out in all electron beam energies using two calibration methods: TRS- 398 protocol and the modified calibration. Ionization chambers, including both cylindrical and plane-parallel types, were utilized. Additionally, a 1D water phantom with a 10x10 cm² electron applicator provided a setup for the measurements in electron beams. Detailed information for each center is presented in Table 1.

Table 1. *The LINAC model and energies of the electron beam in this work.*

Center No.	LINAC model	Energy (MeV)
1	True beam	6, 9, 12, 15, 22
2	True beam	6, 9, 12, 16, 20
3	True beam	6, 9, 12, 15, 18
4	True beam	6, 9, 12, 15, 18, 22
5	Vital beam	6, 9, 12, 15, 20
6	Clinac 23Ex	4, 6, 9, 12, 16, 20

The FC65- G cylindrical chambers were used in centers 1 to 5 while center 6 used the PTW30013 chamber. PPC40 plane- parallel chambers were employed in all centers. Chambers were connected to the Dose1 electrometer in centers 1- 5 and the PTW Unidose electrometer in center 6. All chambers were irradiated to 100 MU with an operating voltage of ±300 V.

The reference depth, where chambers are positioned for dosimetry is given by $z_{ref} = 0.6R_{50} - 0.1\ cm$. Raw ionization chamber readings, M_{raw}, are corrected using:

$$M_Q = M_{raw} k_{TP} k_{pol} k_s k_{elec} \quad (1)$$

$$k_{TP} = \frac{(273.2+T)}{(273.2+T_0)} \frac{P_0}{P} \quad (2)$$

$$k_{pol} = \frac{|M_+(V)|+|M_-(V)|}{2M} \quad (3)$$

$$k_s = a_0 + a_1 \frac{M_1}{M_2} + a_2 \left(\frac{M_1}{M_2}\right)^2 \quad (4)$$

where: k_{TP} corrects for temperature and pressure, k_{pol} corrects for polarity effect, k_s corrects for recombination effect and k_{elec} is an electrometer calibration factor.

The output, absorbed dose to water, at maximum depth is presented in terms of dose per monitor unit (D/MU) in two ways:

1. IAEA TRS-398

The absorbed dose to water ($D_{w,Q}$) is calculated using the formula:

$$D_{w,Q} = M_Q N_{D,w,Q_0} k_{Q,Q_0} \quad (5)$$

where M_Q is the meter reading, N_{D,w,Q_0} is the calibration factor and k_{Q,Q_0} is the beam quality correction factor.

For beam qualities $R_{50} \geq 4$ g/cm² (E ≥ 10 MeV) , a cylindrical chamber is used and positioned at $0.5 r_{cyl}$ deeper than reference depth z_{ref}, where r_{cyl} is the radius of the air cavity. In contrast, a plane- parallel chamber must be used for beam qualities $R_{50} < 4$ g/cm² (E < 10 MeV) and positioned on the inner surface of the entrance window at z_{ref}.

In this research, cross- calibration is required, involving a plane- parallel chamber against a calibrated cylindrical chamber in high- energy electron beams of quality Q_{cross}. The calculated $N^{PP}_{D,w,Q_{cross}}$ (calibration factor) and $k_{Q,Q_{cross}}$ (beam quality correction factor) of a plane- parallel chamber are determined by the equation:

$$N^{PP}_{D,w,Q_{cross}} = \frac{M^{ref}_{Q_{cross}} \times N^{ref}_{D,w,Q_0} \times k^{ref}_{Q_{cross},Q_0}}{M^{PP}_{Q_{cross}}} \quad (6)$$

$$k_{Q,Q_{cross}} = \frac{k_{Q,Q_{int}}}{k_{Q_{cross},Q_{int}}} \quad (7)$$

where $k_{Q,Q_{int}}$ and $k_{Q_{cross},Q_{int}}$ are taken from Table 7.IV in TRS-398.

2. Modified calibration

The modified calibration method based on AAPM TG-51, eliminates the need to measure gradient effects P^Q_{gr} as this factor is incorporated into the beam quality conversion factors k'_Q through Monte Carlo simulation.[3] The absorbed dose to water ($D_{w,Q}$) is calculated using the following equation:

$$D_{w,Q} = M_Q k'_Q k_{Q,ecal} N_{D,w,Q_0} \quad (8)$$

where: $k_{Q,ecal}$ is the photon- electron conversion factor and k'_Q is the beam quality conversion factors can be expressed as follows:

$$k'_Q(cyl) = a + b \times R_{50}^{-C} \quad (9)$$

The coefficients a, b, c serve as fitting parameters for each cylindrical chamber type (FC65-G and PTW30013) based on Muir and Rogers.[3] For FC65-G: a = 0.971, b = 0.113, c = 0.680, and $k_{Q,ecal}$ = 0.904. For PTW30013: a = 0.978, b = 0.112, c = 0.816, and $k_{Q,ecal}$ = 0.901.

The cylindrical chamber was placed with its central electrode at z_{ref} used in all energies beam.

After obtaining the D_w at z_{ref}, the absorbed dose at the maximum depth $D_w(z_{max})$ was calculated as follows:

$$D_w(z_{max}) = \frac{D_{w,Q}(z_{ref})\times 100}{PDD_{(z_{ref})}} \qquad (10)$$

where $PDD_{(z_{ref})}$ is the percentage depth dose at reference depth obtained from the relative measurement of each institution.

The outputs from the modified calibration were compared with TRS- 398 protocol, analyzing data within the ± 2% dose tolerance limits established by TRS-398.[4]

III. RESULTS

The beam quality correction factor k_{Q,Q_0} for FC65-G and PTW30013 cylindrical chamber was only available for 12, 15, 16, 18, 20 and 22 MeV by interpolating data from Table7. III in TRS- 398.[4] This aligns with the recommendation that cylindrical chambers are suitable for energies ≥ 10 MeV. The k'_Q factors for modified calibration,[3] employing fitting parameters and using FC65-G and PTW30013 cylindrical chamber, can be calculated for all energies as presented in Table 2.

The absorbed dose to water results obtained using TRS-398 for 4, 6, and 9 MeV correspond to the plane- parallel chambers, while for energies ≥ 10 MeV, the results correspond to the cylindrical chambers.

The dose ratios between modified calibration to TRS-398 are shown in Figure 1.

Dose discrepancy from modified calibration and TRS- 398, calculated as $\frac{(\mathrm{D_w\ of\ modified\ calibtaion} - \mathrm{D_w\ of\ TRS{-}398})}{\mathrm{D_w\ of\ TRS{-}398}} \times 100$. Table 3 displays the dose discrepancies for low energy ranging from -1.57% to 0.75%, and for high energy, from -0.37% to 0.91%.

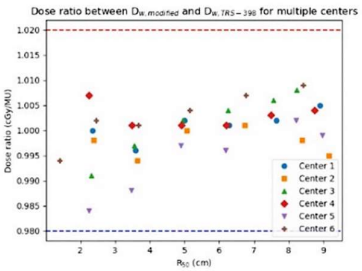

Figure 1. *The dose ratios between modified calibration to TRS-398 for each center*

Table 2. *The beam quality factors k_{Q,Q_0} and k'_Q used in this work.*

Center No.	Energy (MeV)	R_{50} (cm)	k_{Q,Q_0}	k'_Q
1	6	2.35	-	1.034
	9	3.59	-	1.018
	12	4.99	0.916	1.009
	15	6.29	0.912	1.003
	18	7.64	0.908	0.999
	22	8.90	0.905	0.997
2	6	2.39	-	1.034
	9	3.64	-	1.018
	12	5.07	0.916	1.009
	16	6.73	0.911	1.002
	20	8.38	0.906	0.998
3	6	2.31	-	1.035
	9	3.55	-	1.019
	12	4.95	0.916	1.009
	15	6.26	0.912	1.003
	18	7.55	0.908	1.000
4	6	2.25	-	1.036
	9	3.48	-	1.019
	12	4.91	0.916	1.009
	15	6.20	0.912	1.004
	18	7.49	0.909	1.000
	22	8.75	0.905	0.997
5	6	2.24	-	1.036
	9	3.46	-	1.020
	12	4.89	0.916	1.009
	15	6.18	0.912	1.004
	20	8.21	0.906	0.998
6	4	1.40	-	1.063
	6	2.45	-	1.032
	9	3.68	-	1.017
	12	5.16	0.907	1.007
	16	6.77	0.902	1.002
	20	8.42	0.897	0.998

Table 3. *Dose discrepancy comparison between modified calibration and TRS-398.*

Energy (MeV)	Dose discrepancy (%)					
	Center No.					
	1	2	3	4	5	6
4	N/A	N/A	N/A	N/A	N/A	-0.59
6	-0.03	-0.14	-0.91	0.75	-1.57	0.20
9	-0.42	-0.58	-0.35	0.13	-1.24	0.12
12	0.20	-0.04	0.22	0.05	-0.35	0.35
15	0.13	N/A	0.42	0.08	-0.37	N/A
16	N/A	0.09	N/A	N/A	N/A	0.65
18	0.19	N/A	0.65	0.30	N/A	N/A
20	N/A	-0.21	N/A	N/A	0.15	0.91
22	0.46	N/A	N/A	0.36	N/A	N/A

Figure 2 displays the Bland- Altman plot used for assessing the agreement between two methods. The mean dose difference is 0.0002 cGy/MU, with Limits of Agreement (LoA) at a 95% confidence interval: LoA Upper 0.0109 and LoA Lower -0.0105.

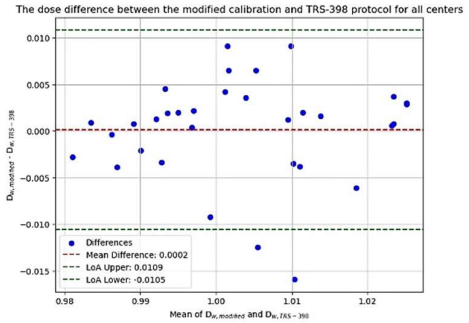

Figure 2. *The absorbed dose to water differences between the modified calibration and TRS-398 protocol for all centers*

IV. DISCUSSION

The $k_Q^{'}$ values determined through Monte Carlo simulation for the modified calibration were consistently greater than the k_{Q,Q_0} values in TRS-398 for all centers. This difference is attributed to the inclusion of gradient correction factors P_{gr}^{Q} which simplifies the setup for the modified calibration. Furthermore, the Monte Carlo simulation using the EGSnrc system provided accurate perturbation correction factors. P_{repl} corrects for changes in electron spectrum at the effective point of measurement, P_{cel} is a central electrode correction factor and P_{wall} corrects for the chamber's wall material. The relative statistical uncertainty in beam quality conversion factor $k_Q^{'}$ was less than 0.1%.[5]

Figure 1 shows higher variability in low-energy measurements (%CV=0.7%) compared to high-energy measurements (%CV=0.32%). This difference may arise from variations in dose comparison methodologies with different chamber types which use of a plane-parallel chamber for low- energy measurements introduces additional uncertainty through cross-calibration.

Table 3 demonstrates dose discrepancies consistently below ±1%, except at 6 and 9 MeV in center 5. This aligns with previous work,[6] which reported PTW 30013 dose discrepancies not exceeding 1%. The higher discrepancies at these energies are attributed to a broken holder for setting up a plane-parallel chamber. The setup error was the issue to make the error. Despite this, the mean difference of 0.0002 cGy/MU indicates strong agreement with no significant bias and demonstrates the reliability of the modified calibration. Only two points fall outside the Limits of Agreement (LoA), notably in center 5, as described previously.

V. CONCLUSION

The study concludes that dose discrepancies between the two methods, ranging from -1.57% to 0.75% for low energies and -0.37% to 0.91% for high energies, are within the ±2% tolerance limit specified by TRS- 398. The modified calibration method, utilizing cylindrical chambers, seems to demonstrate suitability across the energy range of 4- 22 MeV, potentially emphasizing its reliability. However, for a more comprehensive validation, future studies should explore different cylindrical chamber sizes.

REFERENCES

1. Buckley LA, Rogers DW. Wall correction factors, Pwall, for parallel-plate ionization chambers. Med Phys. 2006;33(6):1788-96.
2. Muir BR. A modified formalism for electron beam reference dosimetry to improve the accuracy of linac output calibration. Med Phys. 2020;47(5):2267-76.
3. Muir BR, Rogers DW. Monte Carlo calculations of electron beam quality conversion factors for several ion chamber types. Med Phys. 2014;41(11):111701.
4. IAEA-TRS-398. Absorbed dose determination in external beam radiotherapy: An International Code of Practice for Dosimetry based on standards of absorbed dose to water. Vienna International Atomic Energy Agency. 2000.
5. Muir BR, Rogers DW. Monte Carlo calculations of kQ, the beam quality conversion factor. Med Phys. 2010;37(11):5939-50.
6. Pawiro SA, Mahfirotin DA, Assegab MI, Wibowo WE. Modified electron beam output calibration based on IAEA Technical Report Series 398. J Appl Clin Med Phys. 2022;23(4):e13573.

Contacts of the corresponding author:
Author: Thinka Yasumon
Institute: Faculty of Medicine Chulalongkorn University
Street: Phayathai Road
City: Bangkok
Country: Thailand
Email: fangyasumon@gmail.com

Dosimetric characterization of high-resolution diode array for patient-specific quality assurance of stereotactic radiotherapy

Yimpak Tongrak[1,2*], Tangboonduangjit Puangpen [1], Khachonkham Suphalak [1], Pimthong Jeerawat[2], Watthanasarn Thepphithak[2], Krongkietleart Komkrit[2]

1 Master of Science Program in Medical Physics, Department of Diagnostic and Therapeutic Radiology, Faculty of Medicine Ramathibodi Hospital, Mahidol University, Bangkok, Thailand
2 Department of Radiotherapy, Lopburi Cancer Hospital, Lopburi, Thailand.

**Corresponding author: t.yimpak@gmail.com*

Abstract — **The accuracy of patient-specific quality assurance (PSQA) measurements in stereotactic radiotherapy is challenging due to the unique properties of small-field dosimetry. The high-resolution detector array is essential. SRS MapCHECK (SMC), a two-dimensional high-resolution diode array with StereoPHAN phantom, was introduced as a stereotactic radiotherapy PSQA tool. Therefore, this study aimed to investigate the dosimetric characteristics of SMC for stereotactic radiotherapy PSQA. SMC was evaluated at 6 FFF beam for dosimetric characteristics. Angular and dose rate dependencies were assessed with and without correction, and results were compared to the 0.016 cc Pinpoint3D ionization chamber (IC). Output factors (OPFs) were measured and compared against the IC for field sizes down to 1 × 1 cm^2. SMC responses to anterior and posterior beam incidents were studied due to the unique alignment of diode detectors on the two-facing printed circuit boards. Reproducibility was assessed in short- and mid-term periods through every three-hour and weekly session. Angular dependence stayed within 2% of the IC when applying angular correction, except for beam directions nearly parallel to the detector plane. The maximum deviation was -8.97%. Beam directivity response on both sides of the array showed good agreement. There was no dose rate dependency from 400 to 1400 MU/min; variation was within 0.2% from the IC when the dose rate correction was applied. OPFs agreed within 1.5% of the IC for field size down to 2 × 2 cm^2. Dose linearity with MU showed sufficient performance with R^2 equal to 1. Short- and mid-term reproducibility was good at 0.3% and 0.4%, respectively. In conclusion, the SMC with StereoPHAN phantom has sufficient dosimetric characteristic to be useful for stereotactic radiotherapy PSQA.**

Keywords — **SRS MapCHECK, Diode array, Dosimetric characteristics.**

I. INTRODUCTION

Stereotactic radiotherapy is commonly used for treating small tumors, involving a complex and high-precision procedure requiring submillimeter accuracy in dose placement. Those plans often utilize many small photon fields, high-resolution detectors are crucial for patient-specific quality assurance (PSQA). A single-detector with a sufficiently small active volume relative to the beam size is crucial to avoid volume averaging in high-dose gradient areas.

Radiochromic film is the gold standard for stereotactic plan verification due to its superior spatial resolution, but it is time-consuming and requires high user skills for accurate measurements [1]. Electronic detector arrays have become attractive due to real-time readout, ease of use, and setup. However, those did not have sufficient spatial resolution for stereotactic plan verification.

SRS MapCHECK with dedicated phantom StereoPHAN, a high-resolution diode array, was designed for stereotactic radiotherapy measurement. It consists of small diode detectors arranged with a 2.47 mm center-to-center. However, diode detector responses are influenced by various beam characteristics such as dose rate, mean energy photon, and incident beam direction [2]. Correction factors are necessary to improve measurement accuracy. SMC has a correction algorithm for those influencing factors. Thus, it is essential to understand its dosimetric characteristics before clinical dose verification. Although,

this device has been investigated, and the results were described by a few investigators [3, 4]. However, this device is not yet widely used. Therefore, this study aimed to evaluate the dosimetric characteristics of the SMC for a 6 FFF beam.

II. MATERIALS AND METHODS

The measurements were performed on Varian VitalBeam linear accelerator equipped with 120-leaf Millennium MLC with the leaves 5 mm width as projected to isocenter. The photon beam used was a 6 flattening filter free beam (6FFF).

A. Diode array and phantom

SRS MapCHECK (SMC) consists of 1013 n-type diode detectors (0.48 × 0.48 mm^2 cross-section, 0.007 mm^3 active volume) arranged on the two-facing 7.7 × 7.7 cm^2 printed circuit boards (PCBs)—detector spacing of 2.47 mm. The diode detectors are embedded in polymethyl methacrylate (PMMA) at a physical depth of 2.2 cm for an inherent buildup and backscatter.

StereoPHAN is a dedicated phantom built from PMMA with a hemisphere-shaped rounded superior end (Figure 1). Phantom has an inner cavity for SMC array and other plug-ins, such as an ion chamber and radiochromic film. The data acquisition system used the SNC Patient software version 8.1.

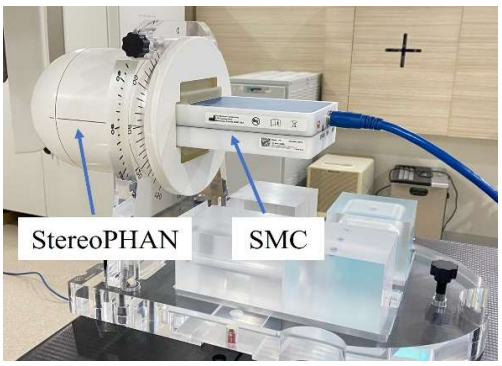

Figure 1. *SRS MapCHECK (SMC) in StereoPHAN phantom.*

B. Array and dose calibration

The array calibration accounts for the difference in diode sensitivity. It was performed at 10 × 10 cm^2 with sequential array shift and flip since the unique alignment of diode detectors on the two-facing PCBs (AP and PA calibrations) using 6 MV beam.

For absolute dose calibration, using the known calibration dose value from the treatment planning system (TPS) (Eclipse Ver.16.1), a dose distribution for an open field of 5 × 5 cm^2, 100 MU, and 6 FFF beam was calculated. The SMC installed in StereoPHAN was then irradiated with similar parameters as in the TPS, and the known dose was input into the SNC patient software.

C. Dosimetric characteristic test

All measurements were carried out using 6 FFF beam with a VitalBeam linear accelerator. The reference conditions for measurement were 5 × 5 cm^2, 0° gantry angle, dose rate 400 MU/min, delivered 100 MU, and repeated three times. Parameters varied depending on a given test.

C1. Angular dependence

This test was measured at every 10° gantry angle and decreased to 2° as the beam approached the detector plane, with and without angular correction.

C2. Dose rate dependence

This test was measured at 400, 600, 800, 1000, and 1400 MU/min with and without dose rate correction.

Central diode readings from the angular and dose rate dependence test were normalized to reference conditions and then compared to the 0.016 cc Pinpoint3D ion chamber (IC).

C3. Beam directivity dependence

Beam directivity dependence was tested by irradiating on both sides of the SMC array using 0° gantry angle with different array orientations—face-up and face-down.

C4. Output factors

Output factors (OPFs) was measured for square field ranging from 1 × 1 cm^2 to 7 × 7 cm^2 and compared against the Pinpoint3D IC. For small fields, detector specific field output correction factors from TRS483 protocol were applied for the Pinpoint3D IC.

C5. Dose linearity

The dose linearity test was performed by varying monitor units (MU), ranging from 2 to 2800 MU to cover the dose range used in clinical applications. The dose values were taken from the central diode.

C6. Reproducibility

This test was evaluated for short-term reproducibility with measurements every three hours over a 12-hour period, and for mid-term

reproducibility, weekly measurements were taken over four weeks. The output of the linear accelerator was checked before measurement. Average dose values were compared.

III. RESULTS

A. Dosimetric characteristics test

A.1 Angular dependence

SMC stayed within 2% of the IC when applying angular correction, except for beam directions nearly parallel to the detector plane, with a maximum deviation of -8.97% (Figure 2). The uncorrected response exhibited more significant deviations for a range of gantry angles, with a maximum deviation reaching -9.16%.

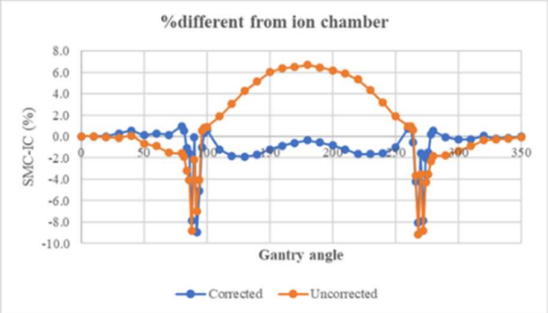

Figure 2. *Difference percentage between the SMC central diode and ion chamber (IC) for a range of gantry angles.*

A2. Dose rate dependence

With dose rate correction, SMC aligns with the ion chamber within 0.2% across the studied dose rates. Without correction, the percentage difference notably increases, with a maximum deviation of 1.37% at 1400 MU/min.

A3. Beam directivity dependence

Beam directivity response on both sides of the array showed a slight difference, with an average percent dose difference of -0.64% with the face-down orientation exhibiting a slightly lower response than the face-up orientation.

A4. Output factors

The measurement data were normalized to 4 × 4 cm^2 field size. The SMC OPFs agrees with the IC within ±1.5% across field sizes studied except the 1 × 1 cm^2 field, which shows the largest deviation of -4.72%. (Figure 3).

A5. Dose linearity

The central diode response showed linearity with monitor units ranging from 2 to 2800 MU with R^2 equal to 1 (Figure 4), which indicated that the diode readings were proportional to the actual dose.

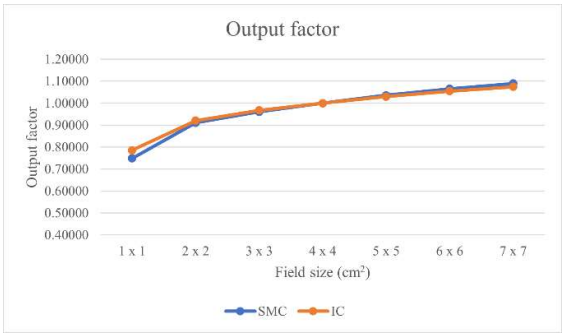

Figure 3. *Ratio of relative output factor, SMC vs Pinpoint3D ion chamber (IC).*

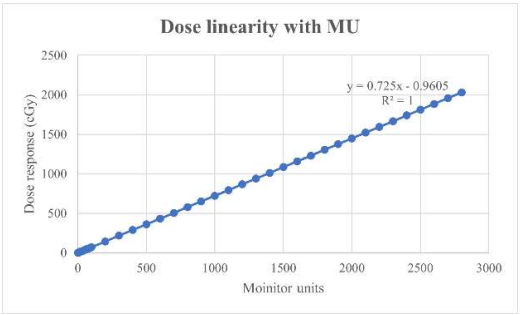

Figure 4. *Dose linearity from 2 to 2800 MU.*

A6. Reproducibility

The short- and mid-term reproducibility of SMC was good. The percentage difference between two consecutive sessions that taken from central diode were within 0.3%, and 0.4% for short- and mid-term reproducibility, respectively. The variation between measurements in the first week and those in the fourth week or monthly sessions was -0.14%.

IV. DISCUSSION

The various dosimetric characteristics for 6 FFF beam of SMC was evaluated and provided satisfactory results.

SMC's angular response, with correction, is closely aligned with IC across gantry angles, with only a 2% deviation. However, deviations become significant in narrow angles when the beam parallels the array plane, consistent with prior studies [3, 4]. This issue must be considered for IMRT verification. For VMAT, this issue is negligible since the dose contribution from this angle range is small compared to the total radiation during a full gantry rotation [5].

No dose rate dependency was observed between 400 and 1400 MU/min with applied dose rate correction. However, SMC exhibited an under-response at low dose rates (10 MU/min) [3]. In VMAT plans, the dose rate decreases during irradiation; it is important to understand the under-response due to the dose rate reduction.

The beam directivity responses on both sides of the array exhibited good agreement, which can be attributed to the angular and array corrections.

For OPFs, SMC agreed with the IC for field sizes down to 2 × 2 cm². However, the SMC exhibits an obvious under-response for field size 1 × 1 cm² compared to the Pinpoint3D IC (0.016 cc). This difference might be attributed to the IC being corrected for detector response according to the TRS483 protocol using 1 cm as the S_{clin}. In contrast, the SMC detector relies on manufacturer corrections, which users cannot access. Other studies also found that SMC exhibited an under-response by 7% relative to the microDiamond detector at 1 × 1 cm² field. This discrepancy could be attributed to the same reason mentioned above [5].

The SMC showed an excellent dose linearity. This is crucial for accurate measurements in stereotactic plans, which require high fractional doses and a large number of monitor units.

The short and mid-term reproducibility were less than 0.4%. The results can be considered stable over extended periods, including hours and weeks.

Although SMC has good dosimetric characteristics, it has limitations. Since a small active area of 7.7 × 7.7 cm^2 results in a large PTV size in SBRT plans that may not fit in the array active area.

V. CONCLUSION

The SRS MapCHECK diode array, incorporating a correction algorithm, has sufficient dosimetric characteristics to be a useful tool for stereotactic PSQA.

ACKNOWLEDGEMENTS

I extend my appreciation to my advisor and co-advisor for their valuable guidance. Gratitude to the medical physicist staff at Lopburi Cancer Hospital for their support in data collection. This thesis is partially supported by the Faculty of Graduate Studies, Mahidol University.

REFERENCES

[1.] Niroomand-Rad A, Chiu-Tsao S-T, Grams MP, Lewis DF, Soares CG, Van Battum LJ, et al. Report of AAPM Task Group 235 Radiochromic Film Dosimetry: An Update to TG-55. Medical Physics. 2020;47(12):5986-6025.

[2.] Rosenfeld AB, Biasi G, Petasecca M, Lerch MLF, Villani G, Feygelman V. Semiconductor dosimetry in modern external-beam radiation therapy. Phys Med Biol. 2020;65(16):16tr01.

[3.] Ahmed S, Zhang G, Moros EG, Feygelman V. Comprehensive evaluation of the high-resolution diode array for SRS dosimetry. J Appl Clin Med Phys. 2019;20(10):13-23.

[4.] Bai L, Xiao Q, Wang Q, Zhao J, Li G, Bai S. Dosimetric characteristics of a 2D silicon diode array for stereotactic radiotherapy end-to-end patient-specific QA. Radiation Physics and Chemistry. 2020;173:108885.

[5.] Sadowski BM, Fillmann M, Szałkowski D, Kukołowicz P. Evaluation of SRS MapCHECK with StereoPHAN phantom as a new pre-treatment system verification for SBRT plans. Polish Journal of Medical Physics and Engineering. 2022;28(2):84-9.

Contacts of the corresponding author:
Author: Ms.Tongrak Yimpak
Institute: Master of Science Program in Medical Physics, Department of Diagnostic and Therapeutic Radiology, Faculty of Medicine Ramathibodi Hospital, Mahidol University
Street: Rama VI Road
City: Bangkok
Country: Thailand
Email: t.yimpak@gmail.com

Dose evaluation of a deep learning-based synthetic CT generation for head and neck cancer in photon and proton therapy

Kuibrumrung A[1], Ruangchan S[2], Sanghangthum T[3*]

1 Master of Science in Medical Physics Program, Department of Radiology, Faculty of Medicine, Chulalongkorn University, Bangkok, 10300 Thailand

2 Division of Radiation Oncology, Department of Radiology, King Chulalongkorn Memorial Hospital, Thai Red Cross Society, Bangkok, 10300 Thailand

**Corresponding author: mairt34@yahoo.com*

Introduction**: MRI has been increasingly implemented for the treatment planning process and the MRI-only workflow in both photon and proton therapy. This study aims to investigate and explore the accuracy of dose calculations in head and neck region based on synthetic CT (sCT), using the commercial software methods for both volumetric modulated arc therapy (VMAT) and intensity modulated proton therapy (IMPT) plans.**

Methods**: The sCT images were generated from MRI images for five head and neck cancer cases that underwented VMAT and IMPT by MRI Planner™ commercial software. The mean absolute error (MAE) and mean error (ME) within the body contour and dice scores in bone mask were used for evaluation. The treatment plans of VMAT (3 arcs) and IMPT (0, 40, 140, 200, and 300 beam angles) were generated and optimized in the Eclipse treatment planning system (Version 16.1). The treatment plans were originally optimized and calculated on planning CT images and subsequently recalculated on synthetic CT images. The dose distributions were evaluated at $D_{98\%}$, $D_{95\%}$ and $D_{50\%}$ of PTV/CTV, D_{mean} and D_{max} of organs at risk. Moreover, the dose comparisons between original CT and pseudo-CT were analyzed at 1%/1mm, 2%/2mm, 3%/2mm gamma criteria.**

Results**: The MAE over the patient population of the sCT within the intersection of body contours was 45±45 Hounsfield Units (HU), and the ME was 5±12 HU. Dice scores of the bone masks (CT vs sCT) were 0.90±0.08. Dosimetric analysis showed no statistically significant dose differences between clinical CT and synthetic CT for both VMAT plan and IMPT plan. The average gamma passing rate at 1%/1mm, 2%/2mm, 3%/2mm were 87%, 94%, 97% for VMAT plan and 78%, 90%, 91% for IMPT plan, respectively.**

Conclusion**: The commercial software used for generating sCTs has demonstrated significant dose differences for IMPT over VMAT plans for the head and neck region. The dose calculations based on these sCTs lead to more inaccurate dosimetric results; therefore, it should be considered when dealing with proton treatment plans.**

Keywords — **deep learning, head and neck cancer, MR-guided therapy, MR-only radiotherapy, synthetic CT**

I. INTRODUCTION

Radiotherapy is recommended in more than two-thirds of cancer treatments. The photon-based radiotherapy, such as volumetric modulated arc therapy (VMAT) has been widely employed for head and neck cancers (HNC) treatments. Currently, the new era of radiotherapy using proton pencil beam scanning (PBS), and intensity-modulated proton therapy (IMPT) technique is promising in the treatment of HNC which could reduce the volume radiated dose of normal organs and the risk of radiation side effects (1).

In the radiotherapy process, a Computed Tomography (CT) scan is obtained CT data in terms of CT number (in Hounsfield unit, HU) that is directly proportional to the electron density and is used for dose calculation in the treatment planning system (TPS). Magnetic Resonance Images (MRI) offer superior tissue details compared to CT images, however, it's limited to providing the tissue electron density (2, 3). Besides this limitation, synthetic

Computed tomography (sCT) generation methods have been developed based on MRI data and have been implemented and tested in this study (4).

With the developments using machine learning techniques, sCT accuracy has continuously improved. Several studies have focused on the dose calculation for photon-based radiotherapy and demonstrated that sCT-based dose calculation has the potential to replace CT images. However, the geometric distortion and bone effects are still observed (2, 3) and could induce more range uncertainties and dosimetric errors, especially in HNC proton dose calculation which is surrounded by inhomogeneity tissues (bone, air, and soft tissue). Therefore, this study aims to assess the dose calculation accuracy using the sCT images generated by commercial sCT generation software in both photon and photon radiotherapy for HNC. The investigation of this work is a retrospective study and the differences in the dose calculation results between original CT and sCT are discussed.

II. MATERIALS AND METHODS

A. Data acquisition and sCT generation

The study was conducted retrospectively on patients who received treatment for HNC with photon and proton radiotherapy and was approved by the Institutional Review Board (IRB) of the Faculty of Medicine, Chulalongkorn University.

Five selected cases were undergone both CT and MRI scans in the head and neck region. The sCT images were generated using the MRI data through an automated process utilizing the transfer function estimation (TFE) algorithm. This algorithm is based on deep convolutional neural networks (CNNs) and operates on a single MRI sequence obtained from MRI Planner™ (v.2.3, Spectronic Medical AB, Helsingborg, Sweden).

B. Image registration and contour structure

The image parameters of sCT images such as slice thickness, image resolution, and matrix size were adjusted to be equal to reference CT (rCT) using the MICE software (ONPI Medical AB, Sweden). The new sCT data were imported to Mim software (MIM software, Ohaio) and registered with the rCT through the deformable registration process and later exported to the Eclipse TPS. The PTV, CTV, and normal organs were copied from the rCT to the sCT to assess the accuracy of using the sCT in the dose calculation.

C. Treatment planning

In total five HNC cases were investigated. The treatment plans were generated using Eclipse TPS (v.16.1, Varian Medical System, Palo Alto, CA), employing the rCT images. In photon therapy, the VMAT plans with 3 arcs were created and optimized for achieving a dose in the TPV, whereas the five beam arrangements (0, 40, 140, 200, and 300 beam angles), inserted with the 3 cm range shifter were generated and calculated based on CTV for IMPT proton therapy. Subsequently, to rCT-based calculation, plans were recalculated with the sCT images.

D. Data analysis

Geometric accuracy

The geometric accuracy of the sCT was evaluated by the Dice Similarity Coefficient (DSC) using equation (1).

$$DSC = \frac{2|rCT \cap sCT|}{|rCT| + |sCT|} \quad (1)$$

Hounsfield unit accuracy

The accuracy of HU on sCT was determined using the mean absolute error (MAE) of equation (2) and the mean error (ME) of equation (3) in the comparison of rCT-sCT, where N is the number of the total voxels in the structure.

$$MAE = \frac{\sum_{i=1}^{N} |rCT - sCT|}{N} \quad (2)$$

$$ME = \frac{\sum_{i=1}^{N} rCT - sCT}{N} \quad (3)$$

Dosimetric evaluation

The dosimetric evaluation was determined using a dose volume histogram (DVH) to determine the dose difference of PTV, CTV and organs at risk (OARs) by $D_{98\%}$, $D_{95\%}$, and $D_{50\%}$ for PTV/CTV and D_{mean} and D_{max} for OARs. The comparison of dose distribution between rCT and sCT was performed and analyzed by global gamma evaluation using the Verisoft software (PTW, Freiburg,

Germany) with criteria of 1%/ 1 mm, 2%/ 2 mm, and 3%/ 2 mm and 10% low dose cut-off.

III. RESULTS

A. Geometric accuracy

Table 1 illustrates the DSC, representing the structural similarity among images. Considering the segmented structures based on the 0.8 acceptance criterion, there was agreement observed in the mean DSCs for soft tissue and bone. The worst case occurred in the optic chiasm with a low mean DSC of 0.65 ± 0.11.

Table 1 *Dice similarity coefficient.*

Patient	Body	PTV	CTV	Brainstem	Optic chiasm	Rt.parotid	Lt.parotid	Spinal cord	Bone
P1	0.98	0.92	0.87	0.87	0.56	0.91	0.92	0.81	0.82
P2	0.98	0.98	0.97	0.90	0.51	0.96	0.95	0.94	0.95
P3	0.98	0.98	0.97	0.52	0.67	0.87	0.85	0.97	0.90
P4	0.93	0.98	0.97	0.96	0.79	0.96	0.96	0.95	0.96
P5	0.97	0.97	0.96	0.92	0.77	0.96	0.95	0.95	0.96
Mean	0.97	0.96	0.95	0.84	0.65	0.92	0.90	0.88	0.90
SD	0.02	0.02	0.04	0.16	0.11	0.05	0.07	0.13	0.08

Table 2 *Mean absolute error and mean error.*

Patient	MAE (HU)			ME (HU)		
	Body	Bone	Soft tissue	Body	Bone	Soft tissue
P1	123.90	555.70	16.30	-13.00	482.50	-3.49
P2	23.29	575.70	12.22	3.56	548.30	-5.07
P3	16.33	613.10	36.78	9.44	620.90	-7.55
P4	29.73	666.90	15.69	12.48	646.00	-12.04
P5	29.49	669.20	45.59	12.06	681.90	-12.77
Mean	44.55	616.12	25.32	4.96	595.92	-8.96
SD	44.81	51.70	13.43	12.46	80.09	4.66

B. Hounsfield unit accuracy

The MAE and ME for the five test patients are reported in Table 2. The MAE for all voxels (body) ranged from 16.33 HU to 123.90 HU with a mean of 44.55±44.81 HU. The mean MAE of bone and soft tissue were 616.12±51.70 HU and 25.32±13.43 HU, respectively.

The mean ME of all voxels (body), bone, and soft tissue were 4.96±12.46 HU, 595.92±80.09 HU, and -8.96 ± 4.66 HU, respectively. Both MAE and ME were notably high, particularly in the bone structures.

C. Dosimetric evaluation

The dose differences of PTV from VMAT plan between rCT and sCT were evaluated from DVH metrics. For all patients, the obtained p-values exceeded 0.05 for all parameters of $D_{98\%}$, $D_{95\%}$, and $D_{50\%}$, confirm no significant differences of PTV doses calculated on rCT and sCT.

The dose differences of CTV between rCT and sCT-based calculation, obtained from IMPT were found, however, no significant difference in the DVH values detected supported by p-values. The difference from IMPT was higher than VMAT plans.

For the gamma analysis, the treatment plans were compared between rCT and sCT-based dose calculation, shown in Figure 1. The mean percent gamma passed of 3%/2 mm, 2%/2mm, and 1%/1mm of the VMAT plans were 96.60±2.85%, 94.36±3.71%, and 87.08±4.62%, respectively. Besides the IMPT, the mean of percent gamma passed was lower than VMAT plans with the gamma passing rate of 91.04±13.45%, 89.64±14.93%, and 78.38±19.71% for 3%/2mm, 2%/2mm, and 1%/1mm, respectively.

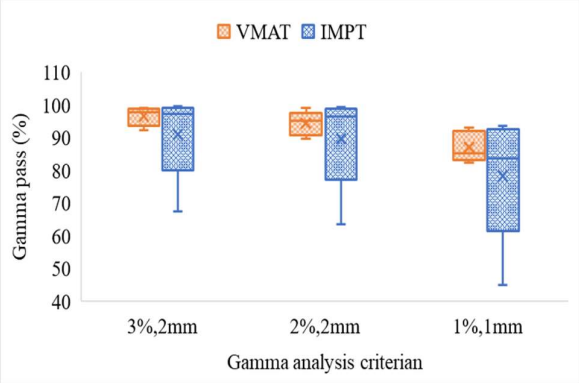

Figure 1 *Gamma analysis of VMAT and IMPT between rCT and sCT-based dose calculation.*

IV. DISCUSSION

The analysis of the sCT images generated by commercial software showed good agreement to rCT images, with a small difference in HU values across the body and soft tissue regions. However, notable discrepancies were observed in the bone region. This discrepancy may be attributed to the software's omission of certain HU values within the bone region during sCT image generation. The results are in line with Dinkla et al. (5), who reported high MAE in bone using deep learning methods. For geometric evaluation represented by the DSCs of the delineated and segmented structures. The commercial software's inability to accurately recognize the optic chiasm, as indicated by the lower DSCs obtained in this study compared to Puzniak et al.(6), reporting a DSC of 0.75± 0.03. This could potentially result in absorbed dose discrepancies. The results extracted from VMAT plans showed good agreement between rCT and sCT images for most DVH metrics, with a mean absolute difference below 0.5% (0.3 Gy) of the prescription dose for the PTV. The dose differences obtained from IMPT plans showed higher deviation from the rCT-based dose calculation compared to VMAT plans. Since the proton range uncertainties are sensitive to the tissue inhomogeneities and relate to this study, the target was surrounded by various tissues such as bone, air, and soft tissues. This could lead to dosimetric errors if the HU is wrongly predicted.

V. CONCLUSION

The commercial software used for generating sCT has demonstrated significant dose differences for IMPT over VMAT plans for the head and neck region. The dose calculations based on these sCTs lead to more inaccurate dosimetric results; therefore, it should be considered when dealing with proton treatment plans.

REFERENCES

[1] Moreno AC, Frank SJ, Garden AS, Rosenthal DI, Fuller CD, Gunn GB, et al. Intensity modulated proton therapy (IMPT) - The future of IMRT for head and neck cancer. Oral Oncol. 2019;88:66-74.

[2] Shafai-Erfani G, Wang T, Lei Y, Tian S, Patel P, Jani AB, et al. Dose evaluation of MRI-based synthetic CT generated using a machine learning method for prostate cancer radiotherapy. Med Dosim. 2019;44(4):e64-e70.

[3] Choi JH, Lee D, O'Connor L, Chalup S, Welsh JS, Dowling J, et al. Bulk Anatomical Density Based Dose Calculation for Patient-Specific Quality Assurance of MRI-Only Prostate Radiotherapy. Front Oncol. 2019;9:997.

[4] Persson E, Jamtheim Gustafsson C, Ambolt P, Engelholm S, Ceberg S, Bäck S, et al. MR-PROTECT: Clinical feasibility of a prostate MRI-only radiotherapy treatment workflow and investigation of acceptance criteria. Radiat Oncol. 2020;15(1):77.

[5] Dinkla AM, Florkow MC, Maspero M, Savenije MHF, Zijlstra F, Doornaert PAH, et al. Dosimetric evaluation of synthetic CT for head and neck radiotherapy generated by a patch-based three-dimensional convolutional neural network. Med Phys. 2019;46(9):4095-104.

[6] Puzniak RJ, Prabhakaran GT, Hoffmann MB. Deep Learning-Based Detection of Malformed Optic Chiasms From MRI Images. Front Neurosci. 2021;15:755785.

Contacts of the corresponding author:
Author: Asst. Prof. Taweap Sanghangthum
Institute: Division of Radiation Oncology, Department of Radiology, Faculty of Medicine, Chulalongkorn University.
City: Bangkok
Country: Thailand
Email: mairt34@yahoo.com

Enhancing adaptive radiation therapy accuracy with CycleGEN-generated synthetic CT from CBCT in pelvic region

Wongtrakool P[1*], Puttanawarut C[2,3], Changkaew P[4], Piasanthia S[4], Earwong P[1], Stansook N[1,4], Khachonkham S[1,4]

1 Master of Science Program in Medical Physics, Department of Diagnostic and Therapeutic Radiology, Faculty of Medicine, Ramathibodi Hospital, Mahidol University, Bangkok, Thailand.

2 Department of Clinical Epidemiology and Biostatistics, Faculty of Medicine, Ramathibodi Hospital, Mahidol University, Bangkok, Thailand

3 Chakri Naruebodindra Medical Institute, Faculty of Medicine, Ramathibodi Hospital, Mahidol University, Samut Prakan, Thailand

4 Division of Radiation and Oncology, Department of Diagnostic and Therapeutic Radiology, Faculty of Medicine, Ramathibodi Hospital, Mahidol University, Bangkok, Thailand.

**Corresponding author: paritt.w@gmail.com*

Abstract — **This study investigated the performance of CycleGAN, a deep learning model, to generate synthetic CT (sCT) from Cone-beam CT (CBCT) images in pelvic region. The aim was to overcome limitations caused by HU distortions in CBCT to enhance Adaptive Radiation Therapy (ART) accuracy. The study included 33 pairs of planning CT (pCT) and 1st fraction CBCT from pelvic region cancer cases that treated with VMAT at Ramathibodi Hospital. CycleGAN was trained on 23 cases, validated on 5, and tested on 5. The performance of sCT was compared with CBCT using pCT as a reference. The results show that sCT exhibits significant lower mean absolute error (MAE) for body and soft tissue, higher for bone but not significant. Geometric accuracy was comparable between sCT and CBCT. Dosimetric accuracy favored sCT with lower dose differences and higher percentage gamma pass rates (%GPR). Overall, CycleGAN-generated sCT demonstrated promising potential for enhance ART accuracy in pelvic region.**

Keywords — **Adaptive radiation therapy, Synthetic CT, Deep learning**

I. INTRODUCTION

The success of radiotherapy relies on precise radiation delivery to tumors while sparing healthy tissues. Adaptive Radiation Therapy (ART) addresses this challenge by adjusting plans based on daily imaging, avoiding inaccuracies from relying on a single anatomical snapshot during Computed Tomography (CT) simulation [1]. This approach helps enhance radiation delivery accuracy, increasing the chances of successful tumor control and lowering the risk of complications [2]. Despite its common use in ART imaging, Cone-beam CT (CBCT) accuracy for dose calculation is hindered by significant Hounsfield unit (HU) distortions [3]. To overcome this, " synthetic CT (sCT) generation using deep learning" have proven highly effective [4]. This study examines performance of CycleGAN [5], a well-known unpair training model [6–9] in generating sCT from pelvic CBCT at Ramathibodi Hospital, focusing on image similarity, geometric accuracy, and dosimetric accuracy, using planning CT (pCT) as a reference. The objective is to uncover CycleGAN strengths and limitations, contributing to overcome limitations caused by HU distortions in CBCT to enhance ART accuracy in pelvic region.

II. MATERIALS AND METHODS

The study comprised five phases: patient selection, data preprocessing, model training, model validation, and model testing.

A. Patient selection

A retrospective approach was utilized to identified 33 pairs of 512x512 pixels pelvic pCT and 1st fraction CBCT from cancer patients treated with VMAT at Ramathibodi Hospital and did not have major implantations. pCT was obtained from GE Optima 580W CT

simulation. CBCT was obtained from Varian TrueBeam®, iX® and Edge® Linac.

B. Preprocessing

Rigid registration aligned CBCT with pCT. Discarded non-shared slices. Dataset was split into train (23 cases), validation (5 cases), and test (5 cases) groups. Non-anatomical regions were removed and set to -1000 HU, then HU values of the image were clipped to a range of [-1000,1000] and rescaled to a range of [-1,1].

C. Model training

CycleGAN models were trained on training dataset using the Adam optimizer [10] with a learning rate of 0.0001 and learning rate decay was employed. Batch size was set to 4, and the training spanned 200 epochs.

D. Model validation

In each training epoch, the model generates sCT from the validation dataset, undergoes reverse preprocessing to HU, and compared to paired pCT. Using a threshold above -200 HU, body mean absolute error (MAE) was calculated to identify the optimal testing model.

E. Model testing

The selected model generated sCT from the test dataset. Region of interest (ROI) for body, soft tissue, and bone are segmented using a threshold method (soft tissue: -200 to 250 HU, bone: >250 HU, body: >-200 HU [11]). MAE was calculated for each ROI. Geometric accuracy was assessed by calculating dice similarity coefficient (DSC) for each ROI, then comparing it to criterion >0.8 from AAPM TG-132 [12]. For dosimetric accuracy, sCT was imported to Eclipse TPS, plan parameters were set to match their pair pCT, and recalculated. Dose different in ROIs are evaluated against <2% criterion [13]. Percentage gamma pass rates (%GPR) was calculated using a fast algorithm for gamma evaluation in 3D [14] with 2%/2mm criterion and low dose cutoff of 90% and compared to ≥90% criterion [15].

III. RESULTS

CycleGAN required 1.2 days to train 200 epochs, achieving lowest validation body MAE of 58.35 HU at epoch 111. This model was further used to test on test dataset. Visual examination of sCT derived from CBCT data in the test dataset (**Figure 1**) reveals effective reduction of streak artifacts from bone (**Figure 1A**), ring and cupping artifacts (**Figure 1B**), and star artifacts from air (**Figure 1C**) while maintaining anatomical accuracy except for air and bladder that are affected by star and cupping artifact respectively.

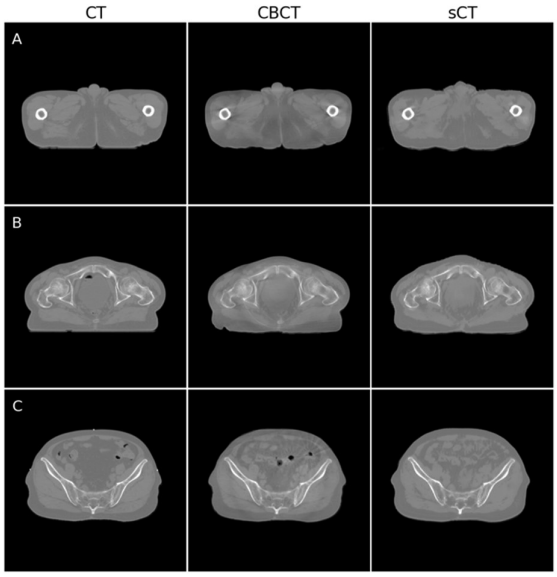

Figure 1. *Visual examination of sCT images derived from CBCT data in the test dataset. Demonstrates sCT ability to reduce (A) streak artifact, (B) ring artifact and (C) star artifact as well as its limitation in preserving air pockets.*

*A. I*mage similarity

To quantify image similarity, MAE was calculated for each ROI, as summarized in **Tables 1**. sCT exhibits significantly lower MAE for the body (p-value = 0.04) and soft tissue (p-value = 0.03) than CBCT. For bone, sCT have higher MAE than CBCT, though this difference is not significant (p-value = 0.09).

Table 1. *MAE (HU) of each ROI*

	CBCT	sCT
Body	65.67 ± 11.26	47.05 ± 4.97
Bone	135.94 ± 25.36	153.9 ± 18.07
Soft tissue	61.26 ± 11.2	40.55 ± 4.8

B. Geometric accuracy

Table 2 presents the DSC values of each ROIs. DSC of CBCT and sCT showed no significant difference (p-values = 0.14, 0.69, and 0.18 for body, bone, and soft tissue, respectively) and passed the criteria of 0.8. This finding suggests that CBCT and sCT were not anatomically different from pCT.

Table 2. *DSC of body, bone, and soft tissue ROIs.*

	CBCT	sCT	Criteria
Body	0.97 ± 0.02	0.98 ± 0.00	
Bone	0.8 ± 0.05	0.79 ± 0.05	>0.8
Soft tissue	0.96 ± 0.02	0.97 ± 0.01	

C. Dosimetric accuracy

In **Table 3** and **Figure 2**, sCT plans showed significantly lower dose different than CBCT (p-value = 0.06 for PTV $D_{95\%}$, <0.01 for PTV $D_{2\%}$, PTV D_{mean}, Body $D_{2\%}$, and Body D_{mean}, respectively), meeting the 2% criterion, whereas some CBCT plans exceeded this criterion. %GPR (**Table 4**) of CBCT and sCT plan was comparable (p = 0.4375) and surpassed the criteria of ≥90%.

Table 3. *Dose different of each ROIs in CBCT and sCT.*

	CBCT	sCT	Criteria
PTV $D_{95\%}$	1.15 ± 0.96%	-0.58 ± 0.63%	
PTV $D_{2\%}$	1.19 ± 0.91%	-0.11 ± 0.6%	
PTV D_{mean}	1.12 ± 0.93%	-0.31 ± 0.46%	<2%
Body $D_{2\%}$	1.28 ± 1.34%	-1.2 ± 1.21%	
Body D_{mean}	0.83 ± 1.15%	-1.21 ± 1.06%	

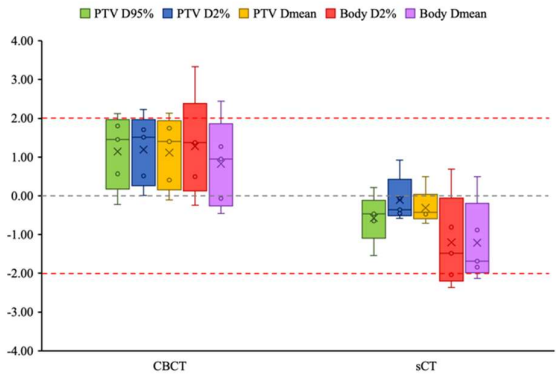

Figure 2. *Box plot of dose different of CBCT and sCT compared to pCT.*

Table 4. *%GPR using 2%/2mm criteria*

CBCT	sCT	Criteria
96.04 ± 7.1	99.92 ± 0.12	≥90%

IV. DISCUSSION

This study investigated the performance of CycleGAN for generating sCT images from CBCT data in the pelvic region.

Visually, sCT can reduced artifacts like streaks, rings, cupping, and star artifacts. However, sCT cannot preserve anatomical features like air pockets and the bladder, which were obscured by the artifacts. Quantitatively, sCT can significantly lower MAE for body and soft tissue regions, but not for bone regions. This MAE value was agreeing with the studies of Eckl et. al. [8], Rossi et.al. [6], and Zhao et al. [7]. DSC values for all tissues were above 0.8, indicating ability to preserve anatomy in CBCT and sCT. In terms of dose, sCT significantly reduced dose different making it pass the criteria of 2%. Both CBCT and sCT exceeded the 90% criteria for %GPR. The average %GPR of sCT exceeds CBCT, consistent with Eckl et. al. [8] study. These results showed that CycleGAN-generated sCT can effectively reduces CBCT image distortions and improving dose calculation accuracy. However, there are limitations like the loss of certain anatomical features in sCT images. Future research could explore methods such as increased training data or modify model architecture to improve CycleGAN performance.

V. CONCLUSION

In conclusion, this study investigated CycleGAN's effectiveness in generating sCT from pelvic CBCT for ART. Despite challenges in preserving certain anatomical features that effect by artifact, sCT showed promising results, with reduced MAE and improved dose calculations accuracy, reflected in lower dose different and higher %GPR. Suggestions for overcoming this limitation involve exploring increased training data or modifying model architecture. In summary, CycleGAN-generated sCT demonstrates promising potential to overcome limitations caused by HU distortions in CBCT to enhance ART accuracy in pelvic region.

ACKNOWLEDGEMENTS

The authors thank Ramathibodi Hospital, Mahidol University for support and acknowledge ChatGPT and Google Bard for revising and grammatical assistance.

REFERENCES

[1] Yan D, Vicini F, Wong J, Martinez A. Adaptive radiation therapy. Phys Med Biol 1997;42:123–32. https://doi.org/10.1088/0031-9155/42/1/008.

[2] Lim-Reinders S, Keller BM, Al-Ward S, Sahgal A, Kim A. Online Adaptive Radiation Therapy. Int J Radiat Oncol Biol Phys 2017;99:994–1003. https://doi.org/10.1016/j.ijrobp.2017.04.023.

[3] Gao L, Xie K, Wu X, Lu Z, Li C, Sun J, et al. Generating synthetic CT from low-dose cone-beam CT by using generative adversarial networks for adaptive radiotherapy. Radiation Oncology 2021;16:202. https://doi.org/10.1186/s13014-021-01928-w.
[4] O'Connor LM, Choi JH, Dowling JA, Warren-Forward H, Martin J, Greer PB. Comparison of Synthetic Computed Tomography Generation Methods, Incorporating Male and Female Anatomical Differences, for Magnetic Resonance Imaging-Only Definitive Pelvic Radiotherapy. Front Oncol 2022;12. https://doi.org/10.3389/fonc.2022.822687.
[5] Zhu J-Y, Park T, Isola P, Efros AA. Unpaired Image-to-Image Translation Using Cycle-Consistent Adversarial Networks. 2017 IEEE International Conference on Computer Vision (ICCV), IEEE; 2017, p. 2242–51. https://doi.org/10.1109/ICCV.2017.244.
[6] Rossi M, Cerveri P. Comparison of Supervised and Unsupervised Approaches for the Generation of Synthetic CT from Cone-Beam CT. Diagnostics 2021;11:1435. https://doi.org/10.3390/diagnostics11081435
[7] Zhao J, Chen Z, Wang J, Xia F, Peng J, Hu Y, et al. MV CBCT-Based Synthetic CT Generation Using a Deep Learning Method for Rectal Cancer Adaptive Radiotherapy. Front Oncol 2021;11. https://doi.org/10.3389/fonc.2021.655325.
[8] Eckl M, Hoppen L, Sarria GR, Boda-Heggemann J, Simeonova-Chergou A, Steil V, et al. Evaluation of a cycle-generative adversarial network-based cone-beam CT to synthetic CT conversion algorithm for adaptive radiation therapy. Physica Medica 2020;80:308–16. https://doi.org/10.1016/j.ejmp.2020.11.007.
[9] Kida S, Kaji S, Nawa K, Imae T, Nakamoto T, Ozaki S, et al. Visual enhancement of Cone-beam CT by use of CycleGAN. Med Phys 2020;47:998–1010. https://doi.org/10.1002/mp.13963.
[10] Kingma DP, Ba J. Adam: A Method for Stochastic Optimization 2014. https://doi.org/https://doi.org/10.48550/arXiv.1412.6980.
[11] Palmér E, Karlsson A, Nordström F, Petruson K, Siversson C, Ljungberg M, et al. Synthetic computed tomography data allows for accurate absorbed dose calculations in a magnetic resonance imaging only workflow for head and neck radiotherapy. Phys Imaging Radiat Oncol 2021;17:36–42. https://doi.org/10.1016/j.phro.2020.12.007.
[12] Brock KK, Mutic S, McNutt TR, Li H, Kessler ML. Use of image registration and fusion algorithms and techniques in radiotherapy: Report of the AAPM Radiation Therapy Committee Task Group No. 132. Med Phys 2017;44:e43–76. https://doi.org/10.1002/mp.12256.
[13] Edmund JM, Nyholm T. A review of substitute CT generation for MRI-only radiation therapy. Radiation Oncology 2017;12:28. https://doi.org/10.1186/s13014-016-0747-y.
[14] Wendling M, Zijp LJ, McDermott LN, Smit EJ, Sonke J, Mijnheer BJ, et al. A fast algorithm for gamma evaluation in 3D. Med Phys 2007;34:1647–54. https://doi.org/10.1118/1.2721657.
[15] Han T, Mikell JK, Salehpour M, Mourtada F. Dosimetric comparison of Acuros XB deterministic radiation transport method with Monte Carlo and model-based convolution methods in heterogeneous media. Med Phys 2011;38:2651–64. https://doi.org/10.1118/1.3582690.

Contacts of the corresponding author:
Author: Paritt Wongtrakool
Institute: Master of Science Program in Medical Physics, Department of Diagnostic and Therapeutic Radiology, Faculty of Medicine, Ramathibodi Hospital, Mahidol University
Street: 207 Rama VI Rd Phayathai Ratchathewi
City: Bangkok
Country: Thailand
Email: paritt.w@gmail.com

Machine learning-based dose prediction in lung cancer radiation therapy for enhanced decision support systems

Chaipanya Thitaporn[1]*, Nimjaroen Kampheang[1,2], Chamchod Sasikarn[1,2], Intanin Panatda[1,2], Thongsawad Sangutid[1,2], Owasirikul Dhammathat[3], Khamfongkhruea Chirasak[1,2]

1 Princess Srisavangavadhana College of Medicine, Chulabhorn Royal Academy, Bangkok, Thailand

2 Radiation Oncology Department, Chulabhorn Hospital, Chulabhorn Royal Academy, Bangkok, Thailand

3 Kanchanabhishek Institute of Medical and Public Health Technology, Nonthaburi, Thailand

**Corresponding author: chirasak.kha@cra.ac.th*

Abstract — Introduction**: Locally advanced lung cancer patients usually undergo concurrent chemoradiotherapy. However, individuals with substantial tumor volumes may opt for chemotherapy alone when normal tissues exceed tolerance doses. Gathering radiation dose information from the treatment plan is time-consuming and labor-intensive. Utilizing machine learning to predict doses can streamline this and assist in treatment decisions. Thus, this study focuses on developing a machine learning-based dose prediction model for lung cancer.**

Methods**: A study involving 96 lung cancer plans (50-66Gy doses) implemented an 80%-20% split for training and testing. It employed 1,299 features from anatomical data, medical records, treatment intent, and radiation transport, ultimately reducing to 81 for model training. The ensemble model evaluated predictive accuracy using Root Mean Square Error (RMSE) and Mean Absolute Error (MAE) for organ volumes (V5 and V20) in the right lung, left lung, and total lung against ground truth data. The research explores the model's potential as an automated decision support system, assessing accuracy, sensitivity, and specificity.**

Results**: The anatomical feature is the primary determinant of the outcomes. The total lung V20 showed the slightest difference, registering an 8.30 RMSE and 5.28 MAE. In contrast, the left lung V5 displayed the most significant difference, recording a 19.73 RMSE and 16.08 MAE. Notably, the model predicting the V20 of the left lung showcased superior performance in accuracy, sensitivity, and specificity, with values of 0.78, 1, and 1, respectively.**

Conclusions**: The proposed model holds promise for developing automated decision support systems, deciding between concurrent chemoradiotherapy and standalone chemotherapy, particularly for patients with large tumor volumes. This approach may support the physician's judgment and guide the physicist in planning a treatment that either conforms to or does not surpass the predicted dose.**

Keywords — **Dose prediction, Machine learning, Radiation therapy, Lung cancer**

I. INTRODUCTION

Cancer is a prominent cause of death in Thailand, especially lung cancer, with the highest incidence and mortality rate across age groups. Treatment depends on the disease stage, ranging from surgery in the early stages to a combination of chemotherapy and radiation. Advanced techniques like volumetric modulated arc therapy (VMAT) and intensity-modulated radiation therapy (IMRT) efficiently target tumors with high doses while preserving healthy tissue [1,2]. Managing large tumors near critical organs requires specialized expertise, leading to complex planning processes. If radiation doses surpass treatment protocol, the plan shifts to chemotherapy alone, requiring time-consuming strategy revisions. To overcome these challenges, dose prediction for treatment management is crucial.

Recently, artificial intelligence (AI) has gained prominence in the medical physics field, particularly in predicting treatment

doses. This AI-driven approach acts as a decision support system (DSS), especially knowledge-based planning (KBP), revolutionizing medical physics by predicting treatment doses. This study pioneers a machine learning (ML) model for lung cancer, surpassing KBP's limitations. [3-5]. Integrating additional features, the model automates decision support, optimizing the choice between concurrent chemoradiotherapy and standalone chemotherapy for patients with significant tumor volumes. Thus, this study focuses on developing a machine-learning-based dose prediction model for lung cancer.

II. MATERIALS AND METHODS

A. Patient selection

A total of 96 retrospective case studies were conducted on individuals diagnosed with lung cancer at the Radiation Oncology Department within Chulabhorn Hospital between 2015 and 2023. The research utilized IMRT and VMAT techniques, incorporating patient CT images, medical records, treatment intent, radiation transport, and dose volume histograms (DVH). The CT images were acquired using the Siemens Somatom Go OpenPro system (Siemens Healthineers AG, Erlangen, Germany). During the simulation process, these images were scanned with a reconstructed slice thickness of 3 mm. Patients were classified into five groups receiving prescription doses of 50 Gy, 54 Gy, 56 Gy, 60 Gy, and 66 Gy, respectively, over varying fractions. Each group received a conventional fraction of 1.8–2 Gy per fraction.

B. Model generation

Following NCCN guidelines in Table 1 [6], an ML model was used to predict lung dose volumes (5 Gy, 20 Gy) in lung cancer cases. Implemented in MATLAB 2023 with an ensemble method, the model utilized 1,299 features from anatomical info, medical records, treatment intent, and radiation transport. Radiomics integrated with CT images provided anatomical data; medical records included age; treatment intent represented fraction and total dose; and radiation transport involved energy. Afterward, the model used 81 features selected through Maximum Relevance — Minimum Redundancy (MRMR) in MATLAB. Training on 80% (77 cases) and testing on 20% (19 cases) of the dataset underwent ten grid searches and ten-fold cross-validation to prevent overfitting.

Table 1. *Lung dosage in the context of concurrent chemoradiotherapy according to NCCN guidelines [6]*

Target/OAR		Criteria
Lung (Right lung, Left lung, and total lung)	V5	≤ 65%
	V20	≤ 35%

C. Model evaluation

Model validation was performed to ensure the model's ability to predict the dose accurately. This validation process involved comparing model predictions to the ground truth using metrics such as the MAE and RMSE in Equations 1-2.

$$\mathrm{MAE} = \frac{1}{N}\sum|\mathrm{D_{Ground}} - \mathrm{D_{Pred}}| \quad (1)$$

$$\mathrm{RMSE} = \sqrt{\frac{1}{N}\sum|(\mathrm{D_{Ground}} - \mathrm{D_{Pred}})^2} \quad (2)$$

Where MAE = Mean absolute error
RMSE = Root mean square error
$\mathrm{D_{Ground}}$ = the ground truth value
$\mathrm{D_{Pred}}$ = the predicted value
N = the total number of data

To integrate the model into clinical trials, assessing CCRT or chemotherapy suitability, the prediction model's DVH is compared to clinical guidelines. Specifically, lung volume receiving 5 Gy (<65%) and 20 Gy (<35%) is examined. Exceeding cutoffs yields a true positive; falling below is a true negative. Ground truth below cutoff but prediction exceeding is a false positive, and a false-negative occurs when the predicted value is negative while the ground truth is positive. Evaluation utilizes binary classification metrics, including accuracy, sensitivity, and specificity, detailed in Equations 3–5.

$$\mathrm{Accuracy} = \frac{(\mathrm{TP} + \mathrm{TN})}{(\mathrm{TP} + \mathrm{TN} + \mathrm{FP} + \mathrm{FN})} \quad (3)$$

$$\mathrm{Sensitivity} = \frac{\mathrm{TP}}{(\mathrm{TN} + \mathrm{FN})} \quad (4)$$

$$\mathrm{Specificity} = \frac{\mathrm{TN}}{(\mathrm{TN} + \mathrm{FP})} \quad (5)$$

Where TP is correctly predicted positive instances.
TN is correctly predicted negative instances.
FP is incorrectly predicted positive instances.
FN is incorrectly predicted negative instances.

III. RESULTS

Comparisons of the DVH dose metrics between the predicted and ground truth scenarios are shown in Table 2. It presents the mean and standard deviation of lung dose volume (5 Gy and 20 Gy) for the right, left, and total lung. Additionally, it includes the percentage difference for each DVH. The percentage disparity varies between 3% and 36%, with the most negligible difference observed in the right lung V5. The most significant error occurs in the right lung V20.

Table 2. *Comparative analysis of predicted and ground truth results in mean, standard deviation, and percent difference.*

Parameter	Ground truth	Prediction	%Diff
RV_5 (Gy) [a]	59.35±14.50	61.22±80.56	3.15
RV_{20} (Gy) [b]	31.43±15.46	42.95±64.15	36.67
LV_5 (Gy) [c]	49.85±24.94	44.72±44.90	10.30
LV_{20} (Gy) [d]	22.10±20.60	28.43±29.80	28.66
TTV_5 (Gy) [e]	54.36±15.43	50.23±31.14	7.60
TTV_{20} (Gy) [f]	27.72±11.92	34.73±26.09	25.29

[a] Relative volume of the right lung receiving 5 Gy.
[b] Relative volume of the right lung receiving 20 Gy.
[c] Relative volume of the left lung receiving 5 Gy.
[d] Relative volume of the left lung receiving 20 Gy.
[e] Relative volume of the total lung receiving 5 Gy.
[f] Relative volume of the total lung receiving 20 Gy.

Evaluation of the prediction model's accuracy in terms of individual OAR doses using both RMSE and MAE, as shown in Figure 1. The most minor error among RMSE and MAE values occurs in TTV20, with values of 8.30 and 5.28, respectively.

Figure 2 displays the box plot representing the prediction model error. RV5 and RV20 exhibits numerous outliers, and TTV20 is a minor outlier. However, concerning the mean value, RV5 is closer between the ground truth and predicted value. RV20 shows a significant difference in mean value.

Table 3 assesses the classification algorithm performance, emphasizing accuracy, precision, and specificity. TTV5 stands out with the highest values: 0.842 for accuracy, 1.0 for sensitivity, and 1.1 for specificity.

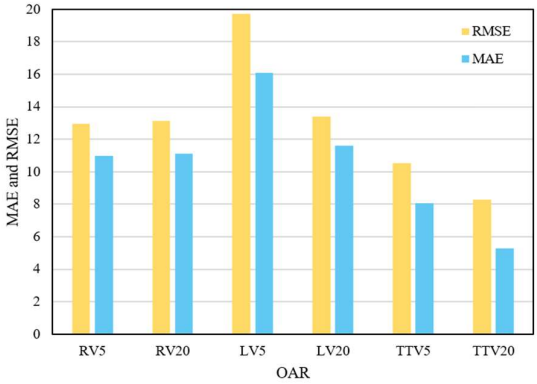

Figure 1. *The root mean square error (RMSE) and mean absolute error (MAE) of the prediction model in terms of each OAR dose.*

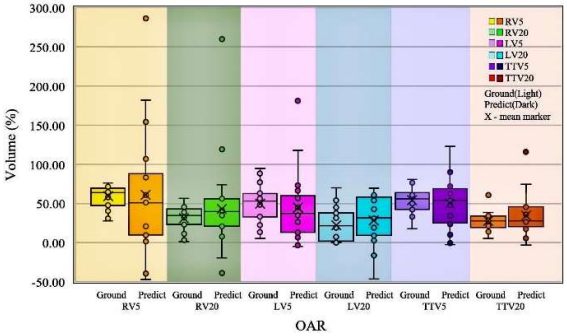

Figure 2. *The boxplot shows the distribution of ground truth and prediction dose metrics for each OAR and statistical measures of a dataset.*

Table 3. *Assessment of the classification algorithm performance for each OAR categorized according to the NCCN guideline, as delineated in Table 1.*

Parameter	*Accuracy*	*Sensitivity*	*Specificity*
RV_5 (Gy) [a]	*0.632*	*0.500*	*0.667*
RV_{20} (Gy) [b]	*0.632*	*0.667*	*0.667*
LV_5 (Gy) [c]	*0.789*	*0.500*	*0.867*
LV_{20} (Gy) [d]	*0.789*	*1.000*	*1.000*
TTV_5 (Gy) [e]	*0.842*	*1.000*	*1.000*
TTV_{20} (Gy) [f]	*0.632*	*0.667*	*0.909*

IV. DISCUSSION

ML efficacy in predicting lung IMRT and VMAT doses was assessed in a study with 19 patients across four prescription dose groups. Results showed a close match between the mean predicted DVH dose and ground truth

mean, but percentage differences in certain OARs were observed. These differences may stem from features integrated across models, particularly affecting specific OARs like RV20, LV20, and TTV20. The presence of RMSE and MAE is likely due to a common underlying issue. Future recommendations include focusing on one or two patient groups to reduce RMSE to a range of 3 to 5, following the approach of Brodin N. P. et al. [1].

The boxplot identifies outliers in predicted and actual values across models, potentially related to unique patient traits. Sole reliance on anatomical features for prediction models may yield suboptimal results. Additionally, many patients exhibit large right tumors, challenging the accurate prediction of right-side doses with the 81 employed features. Despite this, the mean closely aligns with the ground truth, though RV5 displays outliers. Employing a formula, RV5 showcases negative values in specific cases, leading to the mean converging to a balance between negativity and positivity. In TTV20's test data, only one case among 19 stands out as an outlier, impacting predictions due to aggregation and minor outliers. Enhancing model performance is recommended by integrating dosimetric features, as proposed by Ma M et al. [2].

Model adaptation for DSS shows good performance in predicting chemotherapy recommendations for lung cancer. Notably, issues with RV5 and RV20 arise from test case imbalances. Furthermore, a significant number of patients exhibit tumors on the right side, and the tumor volume displays variability. The absence of emphasis on the tumor side as a feature impacts error outcomes, specifically on the right side.

Limitations of this study are the necessity for large training sets to avoid problems with overfitting. The anatomy feature alone is insufficient to predict DVH dose accurately. Therefore, widespread clinical implementation would demand extensive datasets. This might involve creating new treatment plans based on the data from previous patients and adjusting prescription doses.

The further study involves incorporating new features with strong correlations for each model. Additionally, the focus shifts from traditional machine learning to deep learning methods to enhance accuracy.

V. CONCLUSION

This study uses machine learning to develop a lung cancer prediction model. The proposed model demonstrates elevated levels of accuracy, sensitivity, and specificity. These systems could be aided in choosing between CCRT and standalone chemotherapy, supporting physician judgment and guiding treatment planning.

REFERENCES

[1] Brodin N. P., Schulte L., Velten C., Martin W., Shen S., et al. Organ-at-risk dose prediction using a machine learning algorithm: Clinical validation and treatment planning benefit for lung SBRT. 2022; 23(6).

[2] Ma M., Kovalchuk N., Buyyounouski M. K., Xin L., Yang Y. Dosimetric features-driven machine learning model for DVH prediction in VMAT treatment planning. Medical physics. 2019;46(2):857-867.

[3] Jiao S. X., Chen L. X., Zhu J. H., Wang M. L., Liu X. W. Prediction of dose-volume histograms in nasopharyngeal cancer IMRT using geometric and dosimetric information. Physics in Medicine & Biology. 2019;64(23).

[4] Valdes G., Simone II C. B., Chen J., Lin A., Yom S. S., et al. Clinical decision support of radiotherapy treatment planning: A data-driven machine learning strategy for patient-specific dosimetric decision making. Radiotherapy and Oncology. 2017; 125(3):392-397.

[5] Jiao S. X., Wang M. L., Chen L. X., Liu X. W. Evaluation of dose-volume histogram prediction for organ-at risk and planning target volume based on machine learning. Scientific reports. 2021; 11(1).

[6] Gregory KN, Hughes M, Aisner D, et al. NCCN Guidelines Version 2.2023 Non-Small Cell Lung Cancer. Continue NCCN Guidelines Panel Disclosures. [Internet]. 2022 Feb 17;230520. Available from: [NCCN](https://www.nccn.org/guidelines/recently-published-guidelines)

Contacts of the corresponding author:
Author: Chirasak Khamfongkhruea
Institute: Princess Srisavangavadhana College of Medicine, Chulabhorn Royal Academy
Street: Kamphaeng Phet 6
City: Bangkok
Country: Thailand
Email: chirasak.kha@cra.ac.th

A simple evaluation method of real-time respiratory motion tracking accuracy utilizing the ExacTrac Dynamic system

Kongsak Mongkol[1*], Suphaphong S[2], Khaothong P[2], Stansook N[1], Tangboonduangjit P[1]

1 Master of Science Program in Medical Physics, Therapeutic and Diagnostic Radiology Department, Faculty of Medicine Ramathibodi Hospital, Mahidol University, Bangkok, Thailand.

2 Radiation and Oncology Division, Therapeutic and Diagnostic Radiology Department, Faculty of Medicine Ramathibodi Hospital, Mahidol University, Thailand

**Corresponding author: chatmongkol0540@gmail.com*

Abstract

Introduction**: Real-time respiratory tracking accuracy is crucial in radiation treatment for lung and breast cancer patients due to respiratory motion-induced degradation of precision. The purpose of this study is to evaluate the real-time tracking system and the influence of the frequency and amplitude of the ExacTrac Dynamic (EXTD) system.**

Methods**: 9 sinusoidal breathing pattern curves were simulated by Quasar programmable respiratory motion phantom, each curve consisting of a pair of frequencies and amplitudes 15-, 20-, and 25-BPM, and 5-, 10-, and 15-mm peak to peak, respectively. The respiratory motion monitoring of the phantom was performed by the EXTD system with four conditions of thermal and surface shape on the phantom. The tracking accuracy was simply assessed by utilizing statistical analysis tools of Pearson's correlation coefficient (PCC) and root mean square error (RMSE) in a commercial Microsoft Excel program. In addition, all respiratory tracking curves were transformed to the frequency domain by Fourier transform before analysis.**

Results**: RMSE and PCC for the sine curves in the time and frequency domain showed excellent results of respiratory tracking accuracy with 0.1527- 1.8854 mm and 0.9181-0.9963 for the time domain and 0.0189-0.1870 mm and 0.9762-0.9983 for the frequency domain. More frequency and amplitude could cause more errors. However, the frequency and amplitude variations had a negligible effect on the respiratory tracking of EXTD systems, which can cause a huge error.**

Conclusion**: The EXTD system has a high accuracy for respiratory motion tracking. Furthermore, Applying the Fourier transform can eliminate the uncertainty of manual determination of the starting point in the time domain. The frequency and amplitude slightly affect tracking accuracy. The 4D thermal surface can improve respiratory tracking accuracy on a phantom, which has a thermal surface.**

Keywords**: Motion tracking, EXTD, RMSE, PCC, Fourier transform**

I. INTRODUCTION

External radiotherapy aims to deliver a high dose to the tumor and can also spare surrounding normal tissues. Even though current treatment techniques can achieve that goal(1, 2), the respiratory-induced target motion presented during treatment is one of the most impacted factors, which can cause target localization inaccuracy from intra-fractional uncertainty. Respiratory motion management plays an important role in radiation treatment for lung and breast cancer patients in providing better treatment efficiency such as respiratory gating, and breath-hold techniques(3). However, these techniques require respiratory motion tracking systems to obtain accuracy and reproducibility of respiratory position.

ExacTrac Dynamic is a new peripheral device in the optical system from Brainlab AG company. It combines three imaging systems: optical surface, thermal, and kV to obtain high tracking accuracy. The 4D thermal surface is a new remarkable technology for surface-guided radiation therapy (SGRT) that could improve flat surface monitoring and increase patient monitoring accuracy. Nevertheless, it is imperative to note that the surface-guided

system in question was developed several years ago, and its adoption remains limited, with relatively few individuals having explored its capabilities thus far(4, 5).

The purpose of this study is to evaluate the real-time tracking system and the influence of the frequency and amplitude of the ExacTrac Dynamic (EXTD) system. In addition, the thermal and shape of surfaces are observed in this study.

II. MATERIALS AND METHODS

A. ExacTrac Dynamic and Quasar respiratory motion phantom

The ExacTrac Dynamic system (EXTD), as shown in Fig. 1a, is a tracking system with a combination of three imaging systems together: optical surface imaging, thermal imaging, and kV imaging. The system uses the structure light scanning (SLS) technique to acquire 3D surface data visualized and integrated thermal cameras detecting the patient's heat skin for creating the 2D thermal matrix. The 4D optical/thermal surface is calculated by matching these two matrices.

The Quasar respiratory motion phantom was applied for commissioning and quality assurance (QA) regarding real-time respiratory tracking on regularly scheduled testing. The phantom was implemented to simulate the respiratory motion surrogated as the patient's respiration. The phantom was modified to provide a detection plate for placing a shaped surface with a breast shape (Fig. 1b) and a chest shape representing a mastectomy patient (Fig. 1c). The detection plate was attached to a translation stage to move vertically along the anterior-posterior direction for simulating an amplitude that is closest to the patient's breathing.

B. Respiratory motion tracking accuracy

9 sinusoidal breathing pattern curves with amplitude and frequency variations were generated by Quasar programmable respiratory motion software for surrogating as the patient's respiration in this experiment. The impact of frequency and amplitude variations on the tracking accuracy, frequencies, and amplitudes of 15-, 20-, and 25-BPM, and 5-, 10-, and 15-mm peak-to-peak, respectively, was traced by the EXTD system. The tracking curves were compared with reference curves (the simulated curves from the Quasar software) by utilizing statistical analysis tools of Pearson's correlation coefficient (PCC) and root mean square error (RMSE) in a commercial Microsoft Excel program. These statistical analysis tools were applied to evaluate the respiratory motion tracking accuracy. PCC measured the similarity of the two data sets. RMSE measured the error between predicted and observed values in a linear regression analysis.

All respiratory tracking curves were transformed to the frequency domain by Fourier transform before analysis to eliminate the influence of starting point determination. Furthermore, the thermal and shape of the surface were measured by using two different topographic surfaces, shaped with breast and chest, and a heating pad to generate thermal on the shape surfaces surrogated as thermal skin of a patient.

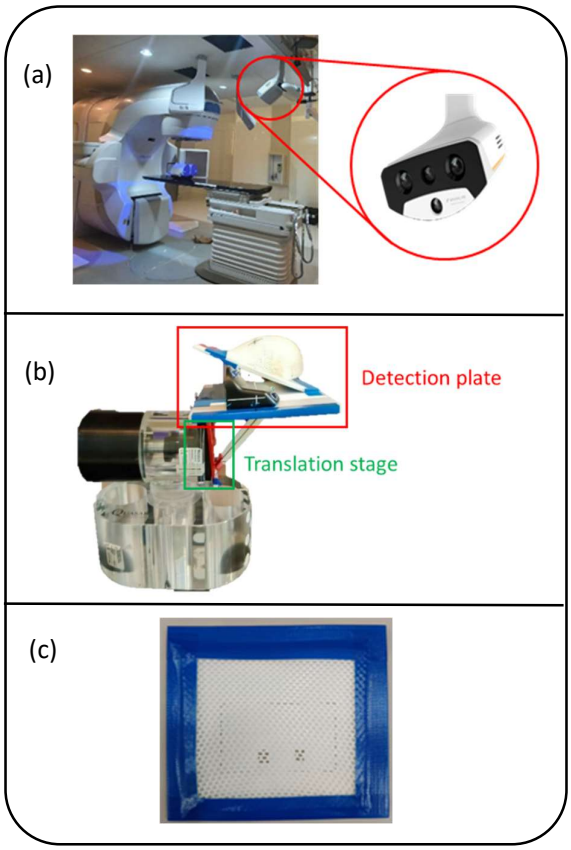

Figure 1.a *The ExacTrac Dynamic system.* ***b*** *the modified Quasar respiratory motion phantom, which the surface phantom placed on the detection plate.* ***c*** *a chest phantom which has a flat shape representing a mastectomy patient.*

III. RESULTS

The real-time respiratory tracking of the EXTD system showed excellent outcomes in both visual analysis (Fig. 2) and quantitative analysis (Table 1). RMSE and PCC values for the sine curves in the time domain were 0.1527- 1.8854 mm and 0.9181-0.9963, respectively. For the frequency domain, RMSE, and PCC values were 0.0189-0.1870 mm and 0.9762-0.9983, respectively. These values indicated that the EXTD system is negligibly affected by frequency and amplitude variations and remains high in real-time respiratory tracking accuracy. The RMSE increased with amplitude and frequency increase. The surface condition with a temperature and high topography established better tracking accuracy compared to other conditions.

Table 1. *The RMSE and PCC values of the sine wave with 10 mm peak-to-peak and 20 BPM. (t and f stand for time domain and frequency domain, respectively)*

Condition	RMSE		PCC	
	t	f	t	f
Breast	0.648	0.061	0.982	0.995
Thermal breast	0.453	0.064	0.991	0.994
Chest	0.663	0.071	0.981	0.993
Thermal chest	0.598	0.071	0.984	0.992

IV. DISCUSSION

The real-time respiratory motion tracking accuracy of the ExacTrac Dynamic system is evaluated by utilizing the RMSE and PCC analysis. This study demonstrated that the EXTD system provides high real-time respiratory tracking accuracy with RMSE of less than 1.885 mm and PCC greater than 0.918 in time domain analysis. Fourier transform was applied to respiratory curves to eliminate spatial position error from manual starting point determination and amplitude variation in signals(6). The RMSE and PCC from the frequency domain had better outcomes than the time domain and agreed with other institutions that have similar tracking systems(6, 7). However, the real-time respiratory tracking accuracy of the EXTD system is lower than those reported by other institutes because the EXTD system has a low data collection rate of every 0.1 seconds. It might have a trivial effect to cause a small error and an unsmooth respiratory tracking curve. The ITV margin in the institute should take the RMSE into account to prevent possible underdose from mis-exposure to PTV.

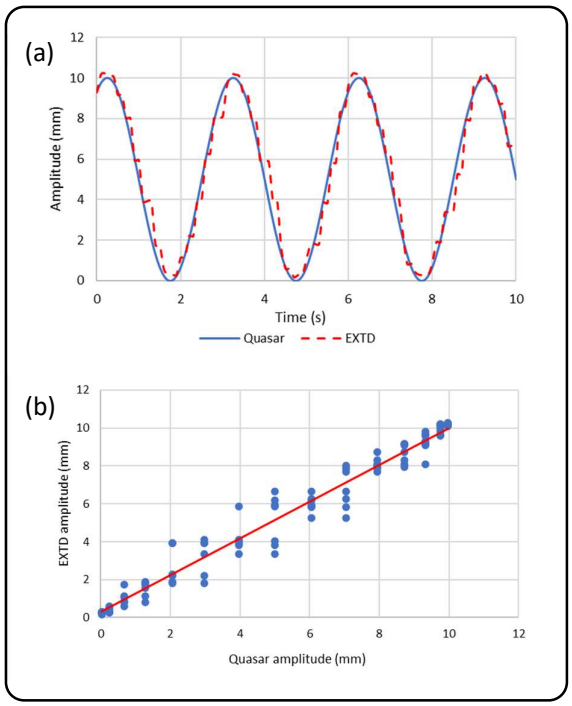

Figure 2. a *The measured curve (EXTD) and reference curve (Quasar) overlay in time-space.* ***b*** *linear regression between the measured curve and reference curve.*

The frequency and amplitude variations have a negligible effect on the system (Fig3). The RMSE increased with amplitude and frequency increase agreed with those reported by Chen et al.(7). This means that the system should be careful to trace the respiratory motion with a large amplitude such as the DIBH technique and breathing training is required before using the gate radiotherapy technique for controlling the patient's breathing rate during treatment. Moreover, figure 3 shows that thermal on the surface can help the system detect a surface better than non-thermal and might improve the frequency and amplitude variations. This new feature of the EXTD system is quite useful for surfaces with low topography such as mastectomy patients.

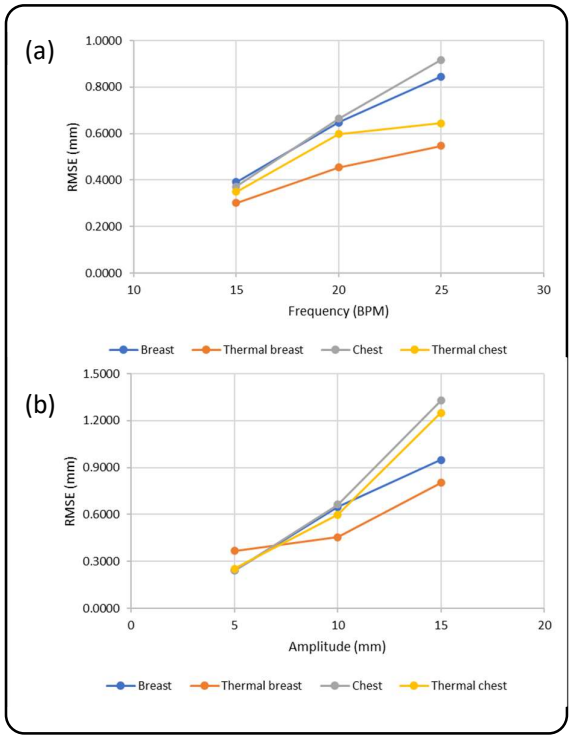

Figure 3. a *The* RMSE in time domain with amplitude 10 mm and frequency variations. ***b*** *the* RMSE in time domain with frequency 20 BPM and amplitude variations.

V. CONCLUSION

The ExacTrac Dynamic system has a high accuracy for real-time respiratory motion tracking. Applying the Fourier transform can eliminate the uncertainty of manual determination of the starting point in the time domain. The frequency and amplitude slightly affect the system but do not cause a huge error. The 4D thermal surface can improve respiratory tracking accuracy on a phantom, which has a thermal surface. In addition, a simple evaluation method using a commercial Microsoft Excel program is easy to use and remains highly accurate.

ACKNOWLEDGEMENTS

I extend my appreciation to my advisor and co-advisor for their valuable guidance. Gratitude to the medical physicist and radiologic technologist staff at Ramathibodi Hospital for their support in data collection, Mr.Paradorn Luangsa-ard for their help in breast phantom creation, and Mr. Kanit Tanthanawigrai for their consultation about product operation. This thesis is partially supported by the Faculty of Graduate Students, Mahidol University.

REFERENCES

[1.] Marta GN, Hanna SA, Gadia R. Treatment with intensity-modulated radiation therapy (IMRT) for breast cancer. Rev Assoc Med Bras (1992). 2014;60(6):508-11.

[2.] Merrow CE, Wang IZ, Podgorsak MB. A dosimetric evaluation of VMAT for the treatment of non-small cell lung cancer. J Appl Clin Med Phys. 2012;14(1):4110.

[3.] Keall PJ, Mageras GS, Balter JM, Emery RS, Forster KM, Jiang SB, et al. The management of respiratory motion in radiation oncology report of AAPM Task Group 76. Med Phys. 2006;33(10):3874-900.

[4.] Da Silva Mendes V, Reiner M, Huang L, Reitz D, Straub K, Corradini S, et al. ExacTrac Dynamic workflow evaluation: Combined surface optical/thermal imaging and X-ray positioning. J Appl Clin Med Phys. 2022:e13754.

[5.] Chow VUY, Cheung MLM, Kan MWK, Chan ATC. Shift detection discrepancy between ExacTrac Dynamic system and cone-beam computed tomography. J Appl Clin Med Phys. 2022;23(5):e13567.

[6.] Kauweloa KI, Ruan D, Park JC, Sandhu A, Kim GY, Pawlicki T, et al. GateCT™ surface tracking system for respiratory signal reconstruction in 4DCT imaging. Med Phys. 2012;39(1):492-502.

[7.] Chen L, Bai S, Li G, Li Z, Xiao Q, Bai L, et al. Accuracy of real-time respiratory motion tracking and time delay of gating radiotherapy based on optical surface imaging technique. Radiat Oncol. 2020;15(1):170.

Contacts of the corresponding author:
Author: Mr. Mongkol Kongsak
Institute: Master of Science Program in Medical Physics, Department of Diagnostic and Therapeutic Radiology, Faculty of Medicine Ramathibodi Hospital, Mahidol University
Street: Rama VI Road
City: Bangkok
Country: Thailand
Email: chatmongkol0540@gmail.com

Dosimetric comparison of IMRT, co-planar VMAT, non-coplanar VMAT and HA for multiple brain metastases SRS

Thawornnittayakul A[1], Plangpleng N[2], Sanghangthum T[1,*]

1 Master of Science in Medical Physics Program, Department of Radiology, Faculty of Medicine, Chulalongkorn University, Bangkok, 10330 Thailand

2 Division of Radiation Oncology, Department of Radiology, King Chulalongkorn Memorial Hospital, Thai Red Cross Society, Bangkok, 10330 Thailand

**Corresponding author: mairt34@yahoo.com*

Abstract — Introduction**: A single isocentric Volumetric Modulated Arc Therapy (VMAT) technique called HyperArc (HA) is an automated setting for couch and collimator angles for non-coplanar. This study aimed to compare the dosimetric effect for a single isocenter among Intensity Modulated Radiation Therapy (IMRT), Coplanar VMAT (Co-VMAT), Non-coplanar VMAT (NC-VMAT), and HA for multiple brain metastases stereotactic radiosurgery (SRS).**

Methods**: The 20 patients with multiple brain metastases (2-4 targets) were collected. The IMRT (9-field), Co-VMAT (2-full coplanar arcs), NC- VMAT, and HA plans with a prescription dose of 18 Gy in single-fraction were generated with 6 MV flattening filter-free energy. For NC- VMAT and HA plans, the 1 full coplanar arc and 3 half arcs with non-coplanar planes at 45, 90, and 135 couch angles were set. The organs at risk (OARs) dose constraints at D_{max} of the brainstem was 8 Gy, while D_{max} of the eye lens, optic nerve, and optic chiasm should be less than 5 Gy. Paddick gradient index (GI), Paddick conformity index (CI), homogeneity index (HI), total number of monitor units (MUs), delivery time, and normal brain volume (V_2-V_{16}) were used to evaluate.**

Results**: The OAR doses were lower than the dose limits for all plans. HA presented the best results with the lowest GI (5.99$\pm$1.34), and the highest CI (0.59$\pm$0.13) values compared with other techniques. For HI, all techniques were comparable. The moderate to low dose spreads of the normal brain were also significantly reduced in the HA plan. Eventually, HA plans led to a significant reduction in both MUs and delivery time.**

Conclusion**: HA plans provided a significantly better rapid dose falloff and dose conformity to the targets. This is consistent with the computed reduction in V_{12} to the normal brain. Ultimately, HA treatments were accomplished within around 4 minutes, signifying a noteworthy reduction in time compared to the other techniques.**

Keywords**: Brain metastases, SRS, IMRT, VMAT, HA.**

I. INTRODUCTION

The incident report of brain metastases found that more than 40-50% of patients with Lung cancer have a chance of developing brain metastases, followed by breast cancer at 15-20% [1]. Multiple brain metastases patients are typically treated by stereotactic radiosurgery (SRS) or whole brain radiation therapy (WBRT)[2]. Volumetric Modulated Arc Therapy (VMAT) has two techniques, the coplanar VMAT technique, and the non-coplanar VMAT technique that physicists had to determine the angle of rotation of the gantry itself. In the case of non-coplanar, there also be a rotation of the couch. Thus, radiological technologists must enter and rotate the treatment couch according to the pre-set angle which may make it inconvenient to use. Zhong-Hua N, et al.[3] compared the dosimetry difference and overall treatment time between noncoplanar VMAT (NC-VMAT) and coplanar VMAT (Co-VMAT). They found that the overall treatment time of the non-coplanar decreased significantly when compared to coplanar technique.

Recently, a new isocentric VMAT technique called HyperArc (HA) was developed for non-coplanar, it is an automated setting for couch angle and collimator angle.[4] HA has been applied to treat in head and neck cancers.[5] Further, Woods K.[6] showed that the HA treatment planning technique achieved conformal dose distributions with substantial dose escalation compared to the VMAT plans and with comparable OAR doses. Several investigations have reported that HA plans provided a higher conformity dose for the target and a lower radiation dose for the surrounding tissues compared to VMAT plans for patients with brain metastases. In Thailand, the use of this technique in the treatment of patients has not been studied. We use the technique of 3D-CRT, IMRT, or VMAT to treat brain metastases. This study aimed to compare the dosimetric differences for single isocenter among IMRT, VMAT, and HA for multiple brain metastases SRS.

II. MATERIALS AND METHODS

A. Patients and simulations

Twenty-five patients with multiple brain metastases with SRS treatment were retrospectively selected. The patients were performed both CT and MR simulations with an Encompass mask (Q-fixed Medical, Avondale, PA). The patient's position is supine and hand by side. All images were exported to the treatment planning system through ARIA. The MR images were used for target and organs at risk (OARs) contouring for brainstem, lens, optic chiasm, and optic nerves, while CT images were used for dose calculation.

B. Treatment Planning

Eclipse treatment planning software (Varian Medical System, Palo Alto, CA) version 16.1 was used for dose optimization and calculating IMRT, VMAT, and HA techniques on TrueBeam linear accelerator (Varian Medical System, Palo Alto, CA). IMRT and VMAT plans are an add-on of the Eclipse TPS. For IMRT plan, the coplanar 9 fields of 220°, 260°, 300°, 340°, 20°, 60°, 100°, 140°, and 180° were used.

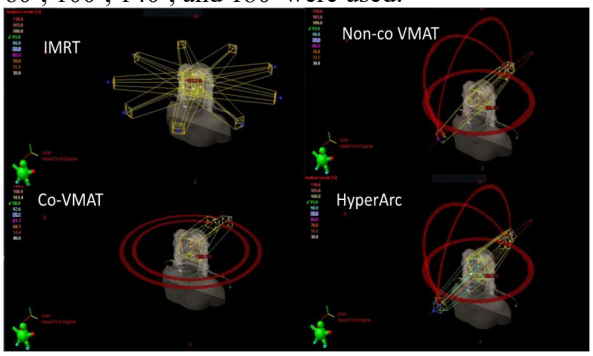

Figure 1. *Beam arrangement for IMRT, Co-VMAT, NC-VMAT, and HA plans.*

The VMAT consists of Co-VMAT and NC-VMAT. For Co-VMAT, 2 full coplanar arcs of 185° CW 175° coll 10° and 175° CCW 185° coll 350° were arranged. For NC-VMAT, 1 full arc and 3 half arcs of (1)179.9° CCW to 0° gantry, 357° coll, 45° couch, (2) 0° CCW to 180° gantry, 3° coll, 315° couch, and (3) 180.1° CW to 0° gantry, 357° coll, and 270° couch as shown in Figure 1. The HA plans automatically selected collimator angles with normal tissue objective (NTO). A single isocenter technique was chosen for all techniques. The prescription dose was 18 Gy in a single fraction. The dose limitations were set according to AAPM High Dose per Fraction, Hypofractionated Treatment Effects in the Clinic (HyTEC2106)[10] ใส่ ref with the maximum dose (D_{max}) of the brainstem lower than 8 Gy, while lens, optic chiasm, and optic nerves should be lower than 5 Gy.

C. Data analysis

IMRT, VMAT, and HA plans were evaluated by the comparison of dosimetric parameters in terms of the dose-volume metrics; homogeneity index (HI), Paddick conformity index (CI), and Paddick gradient index (GI).

HI[7] is defined as: $HI = (D_{2\%} - D_{98\%})/D_{50\%}$ where $D_{2\%}$, $D_{98\%}$, and $D_{50\%}$ denote the dose received by 2%, 98%, and 50%, respectively.

Paddick CI[8] represents the objective measure of how well the distribution of radiation follows the shape of the target: $CI = (PTV_{dp}/PTV)*(PTV_{dp}/V_{dp})$ where PTV_{dp} is the fraction of PTV covered by the prescription isodose, and V_{dp} is the prescription isodose volume.

Paddick GI[8], which is an evaluation of dose fall-off, is calculated as: $GI = V_{50\%dp}/V_{dp}$ where $V_{50\%dp}$ is the ratio of the volumes delimited by the 50%dp and the 100%dp isodoses, and V_{dP} is the prescription isodose volume (cm^3).

The total number of monitor units (MU) and beam on time (min) were also considered indicators of efficiency in irradiation and beam on time, respectively.

III. RESULTS

Table 1 shows the dosimetric parameter for the PTV. The doses were normalized at $D_{95\%}$ of 18 Gy, therefore all techniques showed the similar dose at 18 Gy.

Figure 2 shows the values of the plan dose volume quality for all techniques, The HA plans generated a significant rapid dose fall-off in GI (5.99±1.34, p<0.05) than other techniques. When comparing the CI values, the HA and NC-VMAT were not significantly different (0.59±0.14 and 0.59±0.13, respectively, p<0.05). However, when comparing HA with IMRT and Co-VMAT, the CI values were quite significantly different. (0.57±0.13 and 0.55±0.14, respectively, $p < 0.05$). For HI, all techniques are hardly different at 0.2 (p<0.05).

Table 2 shows the dosimetric parameter for OARs. The D_{max} of the brainstem was significantly lower (p<0.05) in the HA plans (402.1±308.0 cGy) compared to that in IMRT (438.5±411.9 cGy), Co-VMAT (475.8±325.1 cGy), and NC-VMAT plan (490.3±325.1 cGy). For lens and optic nerves, the D_{max} of HA plans (68.7±45.7, 151.4±130.9 cGy) significantly reduced the dose (p<0.05) than those of the IMRT (84.5±95.4, 152.8±200.0 cGy), Co-VMAT (73.9±63.7 cGy) and NC-VMAT plans (70.8±74.7 cGy). In contrast, the D_{max} for optic chiasm in the Co-VMAT was significantly lower (p<0.05) than other techniques (157.9±171.1 cGy). For the

volume receiving 16 to 2 Gy in a normal brain, the HA plan provided a significantly lower dose spread to the normal brain at all evaluated dose levels (p<0.05) than all techniques. Comparison of the beam-on-time (min) and the total number of MU, HA plans showed better than other plans in terms of both beam-on-time treatments being completed in 3.7 minutes and the total number of monitor units (5226.5±650.9 MU).

IV. DISCUSSION

This study compared the dosimetric parameters of the IMRT, Co-VMAT, Non-co VMAT, and HA plans for patients with brain metastases. Found that the results of HA plans can rapidly dose fall-off than other techniques, this result shows the same trend as the previous study of Ruggero Ruggieri et al.[9] their study also showed that HA had better rapid dose fall-off and better conformity than Co-VMAT plans.

Table 1: *Dosimetric results of the target.*

Structure	Dosimetric Parameter (Gy)	Technique			
		IMRT	Co-VMAT	Non-co VMAT	HA
PTV	$D_{2\%}$	2140.0 ± 38.5	2157.4 ± 44.9	2154.2 ± 53.1	2153.2 ± 53.1
	$D_{50\%}$	1961.0 ± 33.6	1980.8 ± 41.1	1991.5 ± 41.7	1988.9 ± 41.7
	$D_{95\%}$	1802.0 ± 1.3	1801.9 ± 2.3	1802.5 ± 1.4	1801.7 ± 1.4
	$D_{98\%}$	1768.5 ± 16.2	1768.2 ± 14.9	1771.6 ± 26.0	1764 ± 26.0

Table 2: *Dosimetric results of organs at risk (OARs).*

Structure	Dosimetric Parameter (cGy)	Technique			
		IMRT	Co-VMAT	Non-co VMAT	HA
Brainstem	D_{max}	438.5 ± 411.9	475.8 ± 325.1	490.3 ± 325.1	402.1 ± 308.0
Lens	D_{max}	84.5 ± 95.4	73.9 ± 63.7	70.8 ± 74.7	68.7 ± 45.7
Optic chiasm	D_{max}	181.4 ± 181.9	157.9 ± 171.1	293.4 ± 139.8	224.6 ± 111.7
Optic nerve	D_{max}	152.8 ± 200.0	156.0 ± 155.7	154.5 ± 150.8	151.4 ± 130.9

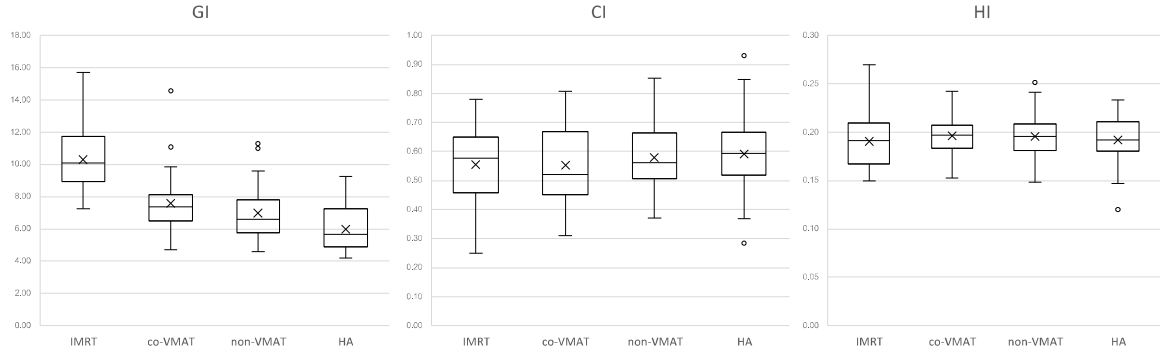

Figure 2. *Boxplots of dosimetric parameters of Paddick GI, Paddick CI, and HI of IMRT, coplanar VMAT, non-coplanar VMAT, and HA plans.*

The Paddick CI assesses the degree of conformity and overlaps between the prescribed isodose and the PTV, indicating how well the treatment adheres to the target dose coverage. Consequently, the CI value serves as an indicator of the likelihood of achieving local control and the capacity to protect neighboring critical serial OARs. In contrast, the Paddick GI characterizes the size of the 50% prescription isodose relative to the prescribed isodose, providing insight into the extent of the medium-to-high-dose region surrounding the PTV[9]. For the target, we normalize $D_{95\%}$ at the prescribed dose (18 Gy), so every technique received 18 Gy. For OARs, the HA technique showed a lower dose than other techniques because the optimization rotation collimator to automatically open the collimator was selected. However, the IMRT, Co-VMAT, and Non-co VMAT get a dose not exceeding the dose constraints. According to dose sparing of normal brain tissue, the mean value obtained to V_{12Gy} by the HA technique was the lowest value when compared to other techniques, although this is still a slight increase to the generally recommended threshold of 10 cm^3 for SRS[10]. Similarly to Clark et al.[11], an average V_{12Gy} was equal to 11.3±3.5 cm^3

for HA. Therefore, HA demonstrates effective performance in reducing the volume of medium-to-high dose regions surrounding the targets. Significantly enhanced irradiation efficiency was noted, with the average total number of monitor units for HA plans reduced when compared to the other techniques. According to Shingo O. et al.[12], the HA technique used higher MU than Co-VMAT due to the MU value depending on the modulation complexity score for VMAT (MCSV). The more complex the leaf is the larger the MU value will be, this study found the HA technique is the lowest than other techniques this may be caused by the unequal number of arcs in each technique. The HA technique is a significant reduction beam on time when compared with other techniques.

V. CONCLUSION

Our results demonstrated that HA plans provided a significantly better rapid dose falloff and dose conformity to the targets. This is consistent with the computed reduction in V_{12Gy} to the normal brain. Ultimately, HA treatments were accomplished within around 4 minutes, signifying a noteworthy reduction in time compared to the other techniques.

REFERENCES

[1] Khan M, Arooj S, Li R, Tian Y, Zhang J, Lin J, et al. Tumor primary site and histology subtypes role in radiotherapeutic management of brain metastases. Front Oncol. 2020;10:781.

[2] Radiological Society of North America (RSNA), American College of Radiology (ACR). Stereotactic radiosurgery (SRS) and stereotactic body radiotherapy (SBRT). Radiologyinfo.org. [cited 2023 Apr 20]. Available from: https://www.radiologyinfo.org/en/info/stereotactic

[3] Zhong- HN, Jing TJ, Xiao DL, Jin M M, Jun C M, Jian XJ, et al. Coplanar VMAT vs. noncoplanar VMAT in the treatment of sinonasal cancer. Strahlenther Onkol. 2015;191(1):34–42.

[4] Hawley ST, Jagsi R. Shared decision making in cancer care: Does one size fit all?: Does one size fit all? JAMA Oncol. 2015;1(1):58–9.

[5] Pokhrel D, Bernard ME, Johnson J, Fabian D, Kudrimoti M. HA VMAT stereotactic radiotherapy for locally recurrent previously-irradiated head and neck cancers: Plan quality, treatment delivery accuracy, and efficiency. J Appl Clin Med Phys. 2022;23(5):e13561.

[6] Woods K, Chin RK, Cook KA, Sheng K, Kishan AU, Hegde JV, et al. Automated non-coplanar VMAT for dose escalation in recurrent head and neck cancer patients. Cancers (Basel). 2021;13(8):1910.

[7] ICRU. Report 83: Prescribing, Recording, and Reporting Photon-Beam Intensity-Modulated Radiation Therapy (IMRT). J ICRU. 2010;10(1).

[8] Paddick I, Lippitz B. A simple dose gradient measurement tool to complement the conformity index. J Neurosurg. 2006;105(Suppl):194-201.

[9] Ruggieri R, Naccarato S, Mazzola R, Ricchetti F, Corradini S, Fiorentino A, et al. Linac-based VMAT radiosurgery for multiple brain lesions: comparison between a conventional multi-isocenter approach and a new dedicated mono-isocenter technique. Radiat Oncol. 2018;13(1).

[10] Michael T. Milano, MD, PhD, Jimm Grimm, PhD, Andrzej Niemierko, PhD, et al. HyTEC 2106 Single- and Multifraction Stereotactic Radiosurgery Dose/Volume Tolerances of the Brain. 2020;08:267.

[11] Clark GM, Popple RA, Young PE, Fiveash JB. Feasibility of single-isocentervolumetric modulated arc radiosurgery for treatment of multiple brain metastases. Int J Radiat Oncol Biol Phys. 2010;76(1):296–302.

[12] Ohira S, Inui S, Kanayama N, Ueda Y, Miyazaki M, Koizumi M, et al. Automated non-coplanar volumetric modulated arc therapy planning for maxillary sinus carcinoma. In Vivo. 2023;37(1):417–23.

Contacts of the corresponding author:
Author: Asst.Prof. Taweap Sanghangthum
Institute: Chulalongkorn University
Street: Rama IV Rd.
City: Prathumwan, Bangkok
Country: Thailand
Email: mairt34@yahoo.com

Machine learning-based patient selection for deep inspiration breath hold radiotherapy in left breast cancer

Chotchuchuang Chanatinat[1], Khamfongkhruea Chirasak[1,2,*], Chamchod Sasikarn[1,2], Thongsawad Sangutid[1,2], Deeharing Aphisara[2]

1 Princess Srisavangavadhana College of Medicine, Chulabhorn Royal Academy, Bangkok, Thailand

2 Radiation Oncology Department, Chulabhorn Hospital, Chulabhorn Royal Academy, Bangkok, Thailand

**Corresponding author: chirasak.kha@cra.ac.th*

Abstract — Introduction**: Treating breast cancer on the left side is particularly challenging due to the proximity of the heart to the irradiation field. At present, the application of deep inspiration breath hold (DIBH) can address this challenge. However, it has drawbacks such as time consumption and heightened staff workload. Therefore, this study aims to employ machine learning to generate a predictive model for mean heart dose (MHD) by enabling the selection of an optimal management technique for each patient before the treatment planning process.** Methods**: Eighty-six patients with left breast cancer undergoing the field-in-field technique were assigned to training (80%) and testing datasets (20%). Four hundred twenty-eight features were extracted. Ultimately, sixteen features were selected for training the model with a support vector machine (SVM) algorithm. In the testing model, root mean squared error (RMSE), mean squared error (MSE), and mean absolute error (MAE) were employed to measure the difference between the actual and predicted MHD. Furthermore, the model's performance was evaluated with binary classification, using an MHD threshold of 700 cGy, in terms of accuracy, sensitivity, and specificity.** Results**: The predictive precision of MHD is characterized by an RMSE of 186.2, an MSE of 34654.8, and a MAE of 157.8. According to binary classification, the results indicated an accuracy of 0.65, a sensitivity of 0.57, and a specificity of 0.7. However, this may be attributed to a data imbalance, where positive cases were fewer than negative cases.** Conclusion**: This study is promising towards optimizing radiotherapy planning for left breast cancer patients by developing a dose prediction model. The model serves as a decision support system for selecting individualized management techniques, thereby reducing both time and workload for staff in the planning process.**

Keywords **— Machine learning, Mean heart dose (MHD), Deep inspiration breath hold (DIBH), Breast cancer, Radiotherapy.**

I. INTRODUCTION

Breast cancer currently stands as the most prevalent cancer among women. Among the various treatments for breast cancer, radiotherapy plays a crucial role in administering high doses of radiation to destroy cancer cells. Despite its efficacy in reducing recurrence rates and improving overall survival, radiotherapy has potential patient complications [1]. Left-sided breast cancer radiotherapy explicitly targets the chest region, encompassing vital organs such as the heart and lungs, designated as organs at risk (OAR). Unintentional exposure of these organs to radiation poses risks of complications. Generally, two standard treatment techniques are employed for left-side breast cancer: the free breath (FB) and the deep inspiration breath-hold (DIBH) techniques. The FB technique involves breathing in and out normally. This may bring the heart into the radiation field and potentially expose the heart to radiation complications. On the other hand, DIBH requires patients to take and hold deep breaths, causing the heart to shift away from the radiation field. While DIBH effectively minimizes cardiac exposure, it introduces challenges, including increased

workload for physicists, prolonged treatment times, and potential discomfort for patients [1]. Hence, while the DIBH technique proves beneficial, it may not be necessary for all patients.

In radiotherapy, computed tomography (CT) imaging is a pivotal step, incorporating both FB and DIBH scans. Treatment planning predominantly relies on FB-CT images, with the FB plan selected unless the OAR dose tolerance is surpassed. However, challenges arise when DIBH-CT needs to be planned, leading to an augmented workload for physicists during the planning process. To address this challenge, the current research proposes developing a machine learning-based dose prediction model specifically tailored for left breast cancer patients undergoing the field-in-field (FIF) technique. The primary objective of this model is to predict OAR doses before the planning process, serving as a decision support system for clinicians.

II. MATERIALS AND METHODS

A. Data selection and collection

Eighty-six cases of female patients with left-sided breast cancer who underwent adjuvant radiotherapy at Chulabhorn Hospital (2018–2022) with post breast-conserving surgery or mastectomy. Employing the field-in-field (FIF) technique, the whole breast or chest wall received 50 Gy in 25 fractions (2 Gy per fraction). Patients with irradiated supraclavicular lymph nodes (SPC) are included, excluding those treated with different techniques or internal mammary node chain (IMC) irradiation. DICOM files were sourced from treatment plans employing the FB management technique, which includes irradiation using both FB and DIBH techniques. The dataset comprises CT images, structure contours, and doses, partitioned into an 80% training and validation set and a 20% test set.

B. Feature extraction and model generation

In the initial step of model construction to predict mean heart dose (MHD) in left-sided breast cancer patients, feature extraction was conducted from CT images and structured contours. These data were achieved through radiomics using the AccuContour 3.1 software, deriving 428 features. Subsequently, the MATLAB 2023 (R2023a) program was employed for feature selection. The Minimum Redundancy Maximum Relevance (MRMR) method was utilized, identifying 16 features deemed most pertinent for training the model with the support vector machine (SVM) algorithm. The constructed model underwent a training process and was subjected to 5-fold cross-validation to mitigate overfitting and enhance model accuracy.

C. Model evaluation

The effectiveness of the model will be evaluated by comparing the actual MHD with the predicted MHD through the calculation of root mean squared error (RMSE), mean squared error (MSE), and mean absolute error (MAE), as per Equations 1, 2, and 3, respectively.

$$RMSE = \sqrt{\frac{1}{n}\sum_{i=1}^{n}\left(Y_P^i - Y_c^i\right)^2} \quad (1)$$

$$MSE = \frac{1}{n}\sum_{i=1}^{n}\left(Y_P^i - Y_c^i\right)^2 \quad (2)$$

$$MAE = \frac{1}{n}\sum_{i=1}^{n}\left|Y_P^i - Y_c^i\right| \quad (3)$$

where n is the total number of pixels, Y_P^i is the i^{th} pixel value of the predicted dose, and Y_c^i is the i^{th} pixel value of clinical dose.

Additionally, as outlined in Equations 4, 5, and 6, an evaluation of accuracy, sensitivity, and specificity was conducted to ensure confidence in the model's ability to predict doses for selecting an appropriate management technique for individual patients in clinical settings. The predicted MHD was compared against the National Comprehensive Cancer Network (NCCN) guidelines, which recommend that MHD should not exceed 700 cGy.

$$Accuracy = \frac{TP+TN}{TP+TN+FP+FN} \quad (4)$$

$$Sensitivity = \frac{TP}{TP+FN} \quad (5)$$

$$Specificity = \frac{TN}{TN+FP} \quad (6)$$

where TP is True Positive, FN is False Negative, FP is False Positive, and TN is True Negative

III. RESULTS

The dose prediction model from machine learning demonstrates its predictive capability, as illustrated in Figure 1. This figure compares the actual and predicted MHD for 17 tested patients, represented in a bar chart. Upon calculating the percent difference from the

mean values of actual and predicted MHD, as shown in Table 1, the result is 1.81.

The accuracy of the dose prediction model was assessed through RMSE, MSE, and MAE on the test dataset, as indicated in Table 2. The corresponding values are 186.2, 34654.8, and 157.8, respectively.

Table 1. *Comparative mean MHD ± SD and percent difference between actual and predicted MHD in tested patients.*

Actual MHD	Prediction MHD	%Diff
672.37 ± 189.50	660.19 ± 84.78	1.81

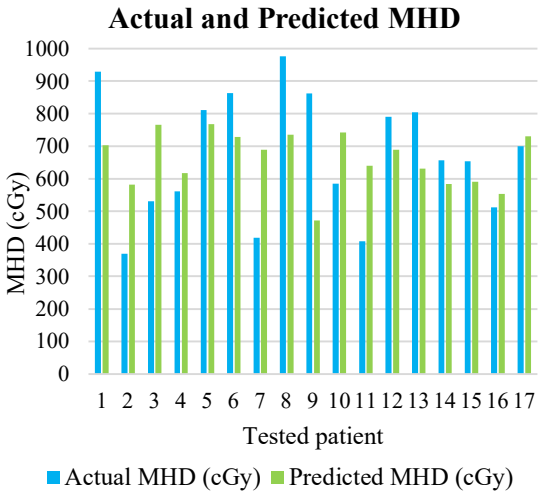

Figure 1. *The bar chart contrasts the actual and predicted MHD across 17 tested patients.*

Table 2. *RMSE, MSE, MAE values of dose prediction model.*

RMSE	MSE	MAE
186.2	34654.8	157.8

Table 3. *Confusion matrix of dose prediction model.*

	Predicted Positive	Predicted Negative
Actual Positive	TP = 7	FN =3
Actual Negative	FP = 3	TN = 4

Table 3 presents the confusion matrix, encompassing TP of 7, FN of 3, FP of 3, and TN of 4. This matrix is employed to evaluate the performance of predicting MHD with a threshold set at 700 cGy. In this context, values less than or equal to 700 cGy are considered negative, while values greater than 700 cGy are regarded as positive. Subsequently, these values are utilized to calculate accuracy, sensitivity, and specificity, yielding respective values of 0.65, 0.57, and 0.70, providing a comprehensive overview of the model's effectiveness, as outlined in Table 4.

Table 4. *Binary classification regarding the dose prediction model's accuracy, sensitivity, and specificity.*

Accuracy	Sensitivity	Specificity
0.65	0.57	0.70

IV. DISCUSSION

This study employed machine learning to develop a predictive model for MHD using the SVM algorithm. The focus was on left-sided breast cancer cases treated with the FIF technique, aiding in the selection of management techniques for individual patients.

In the process of selecting input data for model training, this research opted for a specific approach by exclusively utilizing anatomical information, namely CT images and structure contours. This study differs from the approach by Kamizaki et al. [2], who incorporated additional patient-related data such as chest wall thickness, body mass index, separation, age, height, and weight. The evaluation results show that Kamizaki et al.'s study outperforms the current research, demonstrating lower errors with an RMSE of 69.5, MSE of 4834, and MAE of 49.9. Furthermore, their accuracy, sensitivity, and specificity evaluation metrics were closer to 1, specifically 0.88, 0.89, and 0.87, respectively. A notable distinction lies in the definition of the tolerance dose, with Kamizaki et al. setting it at 300 cGy. Additionally, the dataset collected by Kamizaki et al. comprised 562 cases, presenting a more prominent and potentially more diverse set of patient data. Moreover, Kamizaki et al. employed a deep neural network (DNN).

In comparison to the study conducted by Ahn et al. [3], which utilized RapidPlan as a knowledge-based planning (KBP) tool to predict doses in left breast cancer cases. Their research computes the dose difference between

the actual and predicted doses for the heart, revealing a disparity of 0.88. This dose difference is notably less than that reported in our study, which stands at 1.81. The dissimilarity in the model creation process contributes to these variations. Ahn et al. specifically selected cases involving breast-conservative surgery without radiation exposure to the node region, totaling 55 cases. Additionally, they set the threshold for MHD at 400 cGy. These distinct choices in case selection and threshold determination may influence the efficacy of the model in predicting doses. The limited case selection in Ahn et al.'s study, focusing on a specific subset of breast-conservative surgery cases without nodal radiation, introduces a potential source of bias. In contrast, our study encompasses a more diverse set of cases involving both breast-conserving surgery and mastectomy, considering patients who underwent adjuvant radiotherapy with varying characteristics.

The research has certain limitations. Firstly, the input data for training the model comprises only anatomical information, including CT images and structure contours, excluding dosimetric information or other patient-related data. Secondly, the selection of patient cases is constrained by small data sizes, and data imbalance exists. Furthermore, the study focuses solely on a single treatment technique, the FIF technique.

For future studies, overcoming these limitations could involve creating models that utilize additional data beyond anatomical information. Increasing the dataset size and achieving data balance would enhance the robustness of the model. The model's predictive performance in dose prediction could be enhanced by investigating various treatment techniques, choosing cases from diverse sites, exploring alternative machine learning algorithms, or transitioning to deep learning approaches.

V. CONCLUSION

This study indicated the promising use of the prediction model as a decision support system, given its commendable performance. However, it is recommended that further improvements be made, including refining the model before clinical implementation. Once enhanced, the model has the potential to aid in the selection of optimal management techniques between FB and DIBH, thereby easing the planning workload for medical physicists.

ACKNOWLEDGEMENTS

The author extends gratitude to all advisors, colleagues, and friends who provided invaluable guidance and assistance throughout the completion of this study. Your insights, advice, and support have been instrumental in the successful execution of this research.

REFERENCES

[1] Chang CS, Chen CH, Liu KC, Ho CS, Chen MF. Selection of patients with left breast cancer for IMRT with deep inspiration breath- hold technique. J Radiat Res [Internet]. 2020 Apr 8 [cited 2023 Jun 8];61(3):431–9. Available from: https://pubmed.ncbi.nlm.nih.gov/32123912/

[2] Kamizaki R, Kuroda M, Al-Hammad W, Tekiki N, Ishizaka H, Kuroda K, et al. Evaluation of the accuracy of heart dose prediction by machine learning for selecting patients not requiring deep inspiration breath-hold radiotherapy after breast cancer surgery. Exp Ther Med [Internet]. 2023 Oct 2 [cited 2023 Dec 11];26(5). Available from: https://pubmed.ncbi.nlm.nih.gov/37869640/

[3] Ahn SH, Kim ES, Kim C, Cheon W, Kim M, Lee SB, et al. Deep learning method for prediction of patient-specific dose distribution in breast cancer. Radiation Oncology. 2021 Dec 1;16(1).

Contacts of the corresponding author:
Author: Chirasak Khamfongkhruea
Institute: Princess Srisavangavadhana College of Medicine, Chulabhorn Royal Academy
Street: Kamphaeng Phet 6
City: Bangkok
Country: Thailand
Email: chirasak.kha@cra.ac.th

A simple radiation-induced DNA damage model for proton therapy based on DBSCAN algorithm

Chaibura Sanhanat[1,*], Autsavapromporn Narongchai[2], Liamsuwan Thiansin[1]

1 Princess Srisavangavadhana College of Medicine, Chulabhorn Royal Academy, Bangkok 10210, Thailand

2 Department of Radiology, Faculty of Medicine, Chiang Mai University, Chiang Mai 50200, Thailand

**Corresponding author: sanhanat.cha@edu.cra.ac.th*

Abstract — **In this study, we explored the application of the density-based spatial clustering of applications with noise (DBSCAN) approach as a simplified model for characterizing radiation-induced early DNA damage in the context of proton beam therapy (PBT). Proton track structures were simulated using Geant4-DNA Monte Carlo track structure toolkit. DBSCAN was used to discern spatial patterns in the distribution of physical interaction points within the proton track structures. The number of clusters and noise points were converted to the yields of single strand break (SSB) and double strand break (DSB), respectively. We found a linear correlation between the number of clusters formed at the DNA diameter level and the DSB yield, making it possible to use a single conversion factor for calculating DSB and SSB yields for all proton energies. Additionally, DBSCAN provided a quality assessment for proton beams in term of the number of clusters per beam per µm.**

Keywords — **DNA damage, clustering, DBSCAN, proton beams, Geant4-DNA**

I. INTRODUCTION

Proton beam therapy (PBT) optimizes cancer treatment by utilizing the Bragg peak for precise tumor targeting while minimizing damage to healthy tissues. However, the variability in the relative biological effectiveness (RBE) in proton therapy [1] highlights the necessity for a deeper understanding of proton-induced biological effects.

To delve into the intricacies of ionizing radiation's biological effects, mechanistic models covering DNA damage induction and subsequent biological processes are essential. Various approaches exist for simulating or modeling DNA damage induced by ionizing radiation. Given that approximately 80% of human cells consist of water, simulating radiation interactions in water serves as a representative environment for cells. Detailed simulations aim to mimic water radiolysis, considering physical, physicochemical, and chemical stages, as well as the geometry and compositions of DNA strands susceptible to damage [2-3]. However, the computational resources required for such detailed simulations are substantial, leading to the proposal of simplified DNA damage simulations, including cluster analysis [4-5] and jump-the-detail [6] simulations.

Clustering is a fundamental unsupervised learning method that divides data points into specific batches or groups based on inherent patterns. Traditional algorithms like k-means or hierarchical clustering are well suited for datasets that exhibit a clustered or compact nature, characterized by clear distinctions between clusters. Traditional clustering algorithms may struggle with real-life datasets exhibiting diverse patterns and irregularities, such as those involving arbitrary shapes or noises. In contrast, the density-based spatial clustering of applications with noise (DBSCAN) excels in clustering spatial patterns [7], making it an effective tool for grouping proton beam interaction points to relate with early DNA damage.

In this study, we explored the application of the DBSCAN algorithm as a simplified model for characterizing radiation-induced early DNA damage and utilized a single conversion factor to calculate DNA damage yields from the number of clusters formed for each proton energy.

II. MATERIALS AND METHODS

The workflow diagram for this study is illustrated in Figure 1.

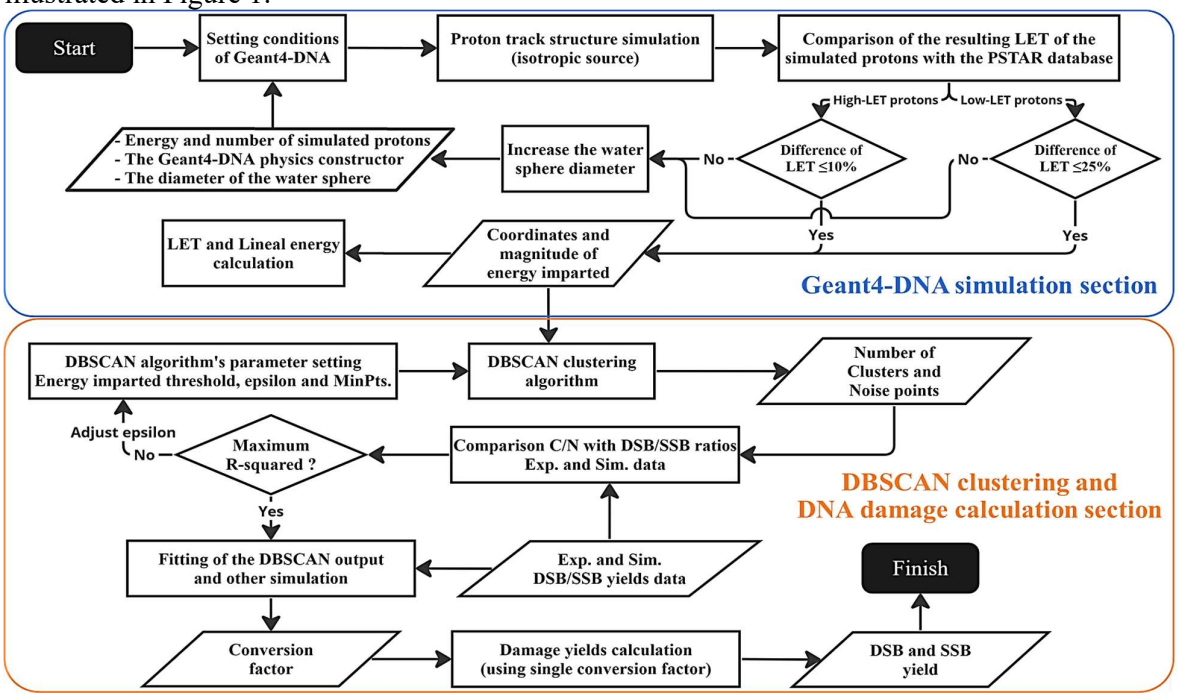

Figure 1. *The comprehensive workflow diagram of this work.*

A. Geant4-DNA simulation

Monoenergetic proton track structures were simulated in liquid water using the Geant4-DNA Monte Carlo track structure toolkit within Geant4 version 11.1 [8], following the procedure illustrated in Figure 1. The simulations encompassed a range of proton kinetic energies from 0.5-200 MeV, or linear energy transfer (LET) from 41-0.4 keV/µm. The proton particle motion direction was randomized, with the starting point set at the center of a working sphere, mimicking the arrangement of an isotropic proton source. The diameter of the water sphere varied from 0.5-5.0 µm, increasing with the energy of the protons, and ensuring that the energy loss of each proton in the water sphere remained below 2% of the incident proton energy. The Geant4-DNA physics constructor, specifically G4EmDNAPhysics_option4, was selected for simulating particle interactions in water. The number of simulated particles ranged from tens of thousands to hundreds of thousands, increased with the decreasing LET of the protons.

The simulations recorded the energy imparted and the coordinates of interactions, which were subsequently utilized for the analysis of DNA damage yields. To validate the track structure simulation, LET and microdosimetric quantities [9], such as, frequency-mean lineal energy ($\bar{y}_F$) and dose-mean lineal energy ($\bar{y}_D$), were calculated from the simulation outputs and compared with published data.

B. DBSCAN algorithm and DNA damage calculation

In this process, the first step involved setting the parameters of the DBSCAN algorithm, including E_{thres}, *MinPts* and ε. The energy imparted threshold, E_{thres}, was set at 17.5 eV, a value known to cause DNA damage in the form of SSB, based on the best agreement between empirical fitting of experimental data and various simulations conducted by Nikjoo et al. [10]. *MinPts* was set to 2 to define cluster formation as a DSB. ε represents the distance for cluster formation. DBSCAN outputted the number of clusters and noise points, enabling the calculation of the cluster/noise ratio (C/N), quality of beam (QoB) measured as the average number of clusters per beam per µm, and normalized QoB

expressed as the average number of clusters per keV imparted in the working sphere. In this study, C/N was assumed to represent the ratio of DSB to SSB yields. Thus, in the modeling, we varied ε to reproduce the ratios of DSB to SSB yields obtained by other simulations and experimental data. All stages of the DBSCAN algorithm were implemented using the scikit-learn machine learning library [11] in Python version 3.10. To calculate DNA damage yields, we related the normalized QoB to the DSB yield obtained by a detailed DNA damage simulation of Kundrat et al. [3].

III. RESULTS

A. Validation of simulated proton track structures

Figure 2 compares LET and microdosimetric quantities, such as, frequency-mean lineal energy ($\bar{y}_F$) and dose-mean lineal energy ($\bar{y}_D$), with those obtained from PSTAR [12] and the simulation of Liamsuwan et al. [13]. Both the LET and the values of $\bar{y}_F$ and $\bar{y}_D$ agreed well with the published data. A maximum discrepancy of 23% for the LET was observed for low LET protons.

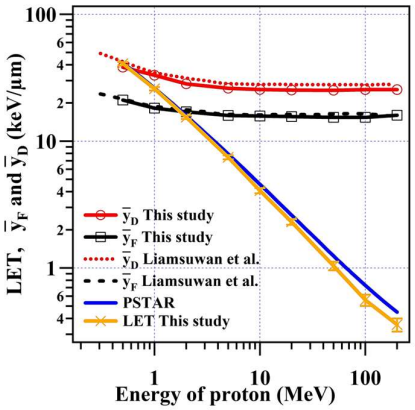

Figure 2. *LET and Lineal energy.*

B. DNA damage yields

The optimal value of ε in the DBSCAN, algorithm was determined to be 2.1 nm, similar to the DNA diameter. Table 1 shows the outputs of DBSCAN, including the number of clusters and noise points, the cluster/noise ratio (C/N), the quality of beam (QoB), and the normalized QoB.

Figure 3 shows the relationship between the normalized QoB and the simulated DSB yields of Kundrat et al. [3]. The slope of the linear fitting, or conversion factor, was 1.1498×10^{-10} keV Gy^{-1} Da^{-1} (R^2 = 0.997). Thus, the DSB yield was calculated by multiplying the normalized QoB with the conversion factor, while the SSB yield corresponded to the DSB yield divided by the C/N ratio. Figure 4 compares our results of SSB and DSB yields with other simulations and experimental data.

Table 1. *Outputs of DBSCAN.*

Proton energy (MeV)	C/N	QoB* ($beam^{-1}\cdot\mu m^{-1}$)	Normalized QoB* (keV^{-1})
0.5	0.1240	7.351	0.1806
1	0.0962	4.183	0.1609
2	0.0708	1.993	0.1284
5	0.0577	0.836	0.1117
10	0.0494	0.400	0.0980
20	0.0461	0.216	0.0933
50	0.0425	0.091	0.0874
100	0.0400	0.046	0.0831
200	0.0276	0.034	0.0956

* QoB = Quality of Beam.

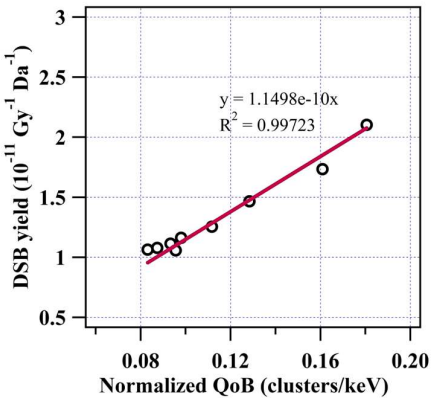

Figure 3. *Conversion factor fitting.*

IV. DISCUSSION

As shown in Table 1, the quality of beam (QoB) was influenced by the LET, reflecting the possibility to use QoB as a quality assessment of proton beams. Moreover, the normalized QoB had a linear correlation with the DSB yield (Figure 3). This correlation enabled the calculation of the absolute SSB and DSB yields from the simple DBSCAN algorithm and a single conversion factor.

Our results of DSB and SSB yields were consistent with Kundrat et al.'s simulation [3], except for 200 MeV protons, where a rise of the SSB yield was similar to the exprimental data of Leloup et al. [14]. The overall trend of the DNA damage yields in this study aligned qualitatively well with results from other

simulation studies. Additionally, the obtained DSB yields were slightly lower than those observed in the experiments with plasmid DNAs and marginally higher than those in cell line experiments. This discrepancy could be addressed by fine-tuning the conversion factor, either slightly higher or lower than the current setting, respectively.

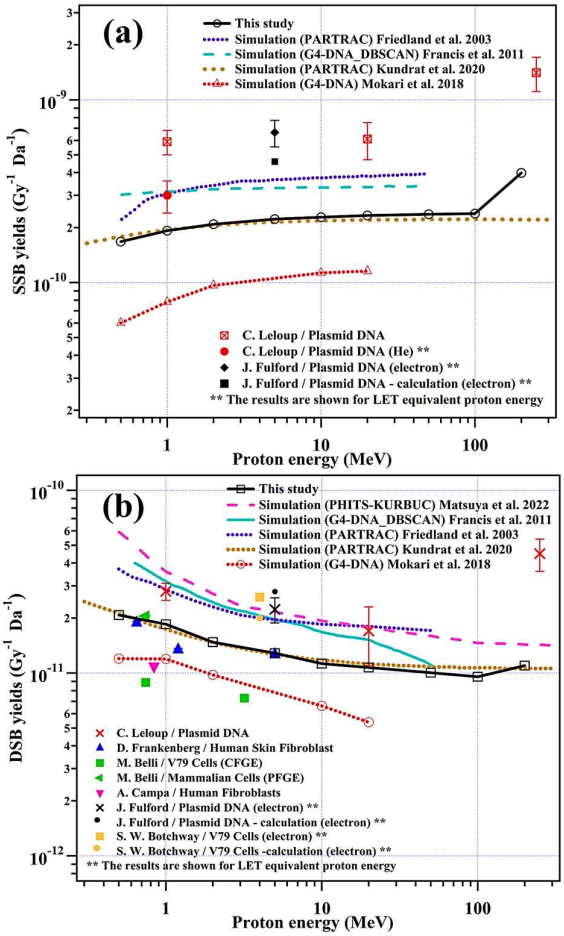

Figure 4. *(a) Single strand break (SSB) and (b) double strand break (DSB) yields.*

V. CONCLUSION

The proposed simple model for characterizing radiation-induced early DNA damage based on the DBSCAN algorithm revealed a linear correlation between the number of clusters formed at the DNA diameter level and the DSB yield. Additionally, DBSCAN provided a quality assessment for proton beams in term of the number of clusters per beam per µm.

ACKNOWLEDGEMENTS

S.C. acknowledges the scholarship of the Development and Promotion of Science and Technology Talent Project (DPST). This work was supported by the Thematic Funding of Princess Srisavangavadhana College of Medicine, Chulabhorn Royal Academy of the Fiscal Year 2022.

REFERENCES

[1] Paganetti H. Relative biological effectiveness (RBE) values for proton beam therapy: Variations as a function of biological endpoint, dose, and linear energy transfer. *Phys Med Biol*. 2014 Nov 21;59(22):R419–R472.

[2] Nikjoo H, Emfietzoglou D, Liamsuwan T, et al. Radiation track, DNA damage and response - A review. *Rep Prog Phys*. 2016 Sep 21;79(11):116601.

[3] Kundrát P, Friedland W, Becker J, et al. Analytical formulas representing track-structure simulations on DNA damage induced by protons and light ions at radiotherapy-relevant energies. *Sci Rep*. 2020 Sep 25;10(1):15775.

[4] Francis Z, Villagrasa C, Clairand I. Simulation of DNA damage clustering after proton irradiation using an adapted DBSCAN algorithm. *Comput Methods Programs Biomed*. 2011 Mar;101(3):265–270.

[5] Yoshii Y, Sasaki K, Matsuya Y, Date H. Cluster analysis for the probability of DSB site induced by electron tracks. *Nucl Instrum Methods Phys Res B*. 2015 May;350:55–59.

[6] Nikitaki Z, Nikolov V, Mavragani IV, et al. Measurement of complex DNA damage induction and repair in human cellular systems after exposure to ionizing radiations of varying linear energy transfer (LET). *Free Radic Res*. 2016 Nov;50(sup1):S64–S78.

[7] Ester M, Kriegel HP, Sander J, Xu X. A density-based algorithm for discovering clusters in large spatial databases with noise. [Internet]. 1996 Dec [cited 2024 Jan 22]. Available from: https://aaai.org/papers/kdd96-037-a-density-based-algorithm-for-discovering-clusters-in-large-spatial-databases-with-noise/.

[8] Incerti S, Kyriakou I, Bernal MA, Bordage MC, Francis Z, et al. Geant4-DNA example applications for track structure simulations in liquid water: a report from the Geant4-DNA Project. *Med Phys*. 2018 June 14;45:e722-e739.

[9] ICRU. ICRU Report 36. International Commission on Radiation Units and Measurements, Bethesda, MD, USA. 1983.
[10] Nikjoo H, O'Neill P, Terrissol M, Goodhead DT. Quantitative modelling of DNA damage using Monte Carlo track structure method. *Radiat Environ Biophys*. 1999 May;38(1):31-38.
[11] Pedregosa F, Varoquaux G, Gramfort A, et al. Scikit-learn: Machine learning in Python. *J Mach Learn Res*. 2011;12:2825−2830.
[12] Berger MJ, Coursey JS, Zucker MA, Chang J. ESTAR, PSTAR, and ASTAR: Computer Programs for Calculating Stopping-Power and Range Tables for Electrons, Protons, and Helium Ions (version 1.2.3) [Internet]. [cited 2024 Jan 22]. Available from: http://physics.nist.gov/Star
[13] Liamsuwan T, Uehara S, Emfietzoglou D, Nikjoo H. Physical and biophysical properties of proton tracks of energies 1 keV to 300 MeV in water. *Int J Radiat Biol*. 2011 Feb;87(2):141–160.
[14] Leloup C, Garty G, Assaf G, et al. Evaluation of lesion clustering in irradiated plasmid DNA. *Int J Radiat Biol*. 2005 Jan 3;81(1):41–54.

Contacts of the corresponding author:
Author: Sanhanat Chaibura
Institute: Princess Srisavangavadhana College of Medicine, Chulabhorn Royal Academy
Street: 906 Kampangpetch 6 Rd., Talat Bang Khen, Lak si
City: Bangkok 10210
Country: Thailand
Email: sanhanat.cha@edu.cra.ac.th

Designing an in-house phantom daily QA for range verification for proton beam using GEANT4

Kheawyoi Paphatchaya[1,*], Keawsamur Mintra[1], Chaiwongkhot Kullapha[2], and Israngkul Na Ayuthaya Isara[3]

1 Medical Physics Program, Department of Radiology, Faculty of Medicine, Chulalongkorn University, Pathumwan, Bangkok 10330, Thailand

2 Department of Physics, Faculty of Science, Mahidol University, Bangkok, 10400, Thailand

3 Division of Radiation Oncology, Department of Radiology, King Chulalongkorn Memorial Hospital, Bangkok, 10330, Thailand

**Corresponding author: 6570050930@student.chula.ac.th*

Abstract — **This study aims to develop an in-house phantom proton therapy for daily quality assurance based on TG-224 to ensure the safety and effectiveness of treatment machines. Thus, each identical facility's in-house proton therapy QA procedure is required. To develop an in-house phantom, the simulation algorithm for particle interactions in the substance using GEANT4 was prepared to evaluate the phantom response before the experiment. In this work, the beamline and database setup in the simulation were verified to confirm consistent results with the experimental data. The ionization chamber array detector (PTW Octavius 1500 XDR) which is currently implemented in King Chulalongkorn Memorial Hospital, was used as a detector with proton beam energies to evaluate the relation between Bragg peak position and proton kinetic energy. The in-house phantom for daily QA is composed of 400x700x200 mm^3 with an acrylic module for accuracy range checks of proton energy (70 MeV, 100 MeV, 150 MeV, and 200 MeV). The spot sizes were evaluated. There are four verified proton beam energies: 70 MeV, 100 MeV, 150 MeV, and 200 MeV which correspond to our overall proton beam energy range. The spot sizes of 70 MeV, 100 MeV, 150 MeV, and 220 MeV are 14.04 mm, 9.59 mm, 7.52 mm. and 7.34 mm, respectively. The results indicate that the proton beams in the experiment are reasonably agreed in the simulation. The results from the range verification show that all the beam energies agree well with the referenced data from the simulation. Additionally, the linear relationship between dose and proton energy and the variation in spot size and dose of each proton energy will also be presented.**

Keywords — **Proton Therapy, GEANT4 simulation, Range verification, In-house phantom.**

I. INTRODUCTION

Proton beam therapy is a rapidly growing technique in cancer treatment due to its Bragg peak and low exit dose. A quite common proton delivery system is pencil beam scanning (PBS), which is a highly precise radiation delivery technique. In a PBS system, the protons beamlets are delivered spot by spot within one energy layer and energy layer by energy layer in depth [1]. In radiation therapy, it is necessary to perform daily quality assurance (QA) before starting the first patient treatment to ensure the treatment delivery system is functioning correctly so, that patients are received safe and effective treatment. Task group (TG) 224 was established to determine quality assurance guidelines and methodologies for proton therapy. Daily QA report suggested range, measurement of Spread-out Bragg-peak (SOBP) width, spot constancy, and x-ray/proton beam isocenter tests, etc., Additionally, the technology in proton therapy is rapidly improving. Therefore, it may take manufacturers and proton therapy facilities sometime to incorporate the new technology into their products. Consequently, there are proton facilities must create their in-house solutions for proton therapy QA. Geant4 is one of Monte

Carlo simulations for the simulation interaction of particles passing through matter. Hence it can design and execute the simulation daily QA procedure before developing an in-house phantom for daily QA. [2]

The purpose of this work was to develop an in-house phantom proton therapy for range verification for daily QA.

II. MATERIALS AND METHODS

The set-up in this research consisted of an Octavius 1500XDR array detector (PTW Freiburg, Germany), which is available at our proton facility, for accuracy range checks and dosimetry measurement (AAPM TG 224) of proton energy. This detector is specified for use in particle therapy [3]. The OCTAVIUS 1500XDR is comprised of a two-dimensional detector array with ion chambers uniformly arranged as a matrix and a separate detector interface for data acquisition. [4]. The set-up is irradiated with various energy a homogenous proton beam from Varian ProBeam Compact Spot-Scanning System (Varian Medical System, Palo Alto, California) using the PBS technique.

The methods are divided into two parts, simulation setup and experimental setup.

A. Simulation setup

The whole simulation was divided in two segments. The first segment simulated an in-house daily QA phantom for range verification using GEANT4 code then obtained doses from depth dose curve and spot sizes, by determining the simulation parameters.The standard model, QGSP_BERT_EMV in GEANT4 (Version 11.0.0) was recommended to model all interactions. which QGSP stands for Quark Gluon string with Precompound model, BERT stands for Bertini intranuclear cascade model and EMV suffix is an option which was used for Bragg curve physics . The second segment was dedicated dose estimation and spot size in a phantom of h 70 MeV, 100 MeV, 150 MeV, and 200 MeV for proton energy.

B. Experimental setup

The experimental setup, a phantom was developed based on the simulation setup.

A homogenous proton beam directly incident on the surface, on the central phantom axis with 70 MeV, 100 MeV, 150 MeV, and 200 MeV. The doses and spot sizes were acquired. Then, the comparisons of the results were performed between the experimental setup and the Monte Carlo simulation.

It is necessary to provide a measurement position to control the accuracy of results.

III. RESULTS

A. Simulation setup

A 400 x 700 x 200 mm^3 with an acrylic module homogenous phantom was modeled as a water phantom which used water equivalent thickness (WET), that is directly correlated to the total stopping power ratio (SPR) for accuracy range checks. The whole geometry is placed within a 100 cm length of air. The dose detector tallies included 27 arranged in planes that are aligned along the central axis of a homogeneous phantom. The tally thickness was thin enough (1 mm) to obtain accurate data.

B. Experimental setup

An in-house phantom, which has 1.094 g/cm^3 mass density and 1.099 relative proton stopping power, was developed by using a simulated phantom as a reference., is shown in Fig.1

Proton range is the distance that particle penetrates an in-house phantom before losing all its energy and stopping completely. We remarked two-point doses, 8.5 mm. and 27.5 mm., on Bragg curve in phantom that passed and compared the dose ratio of two positions between simulation and experiment. is shown in Fig.2, and dose ratio was defined as

$$dose\ ratio = \frac{dose\ at\ position\ ②\ (Gy)}{dose\ at\ position\ ①\ (Gy)} \quad (1)$$

Simulated and experimental doses are shown in Table 1

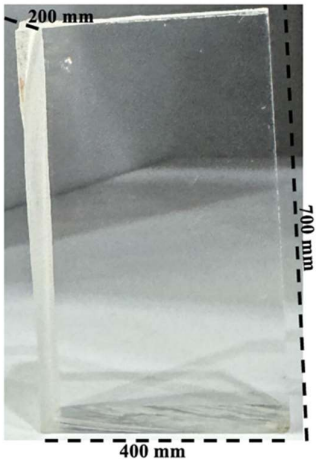

***Fig.** 1 An acrylic module for accuracy range checks of proton energy.*

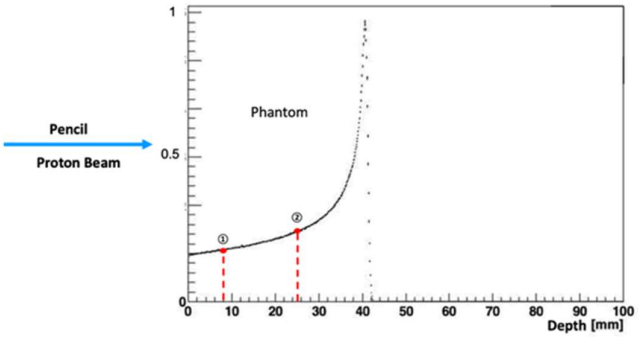

***Fig. 2** Simulated depth dose curve including the Bragg peak in a phantom, for an incident 70 MeV monoenergetic proton beam*

***Table 1** Percent dose ratio difference between the simulation and experiment*

Energy (MeV)	Dose (Gy)	Position ①	Position ②	dose ratio	percent differences (%)
70	Simulation	7.981	13.252	1.660	1.613
	Experiment	8.555	13.976	1.634	
100	Simulation	9.024	10.945	1.213	4.247
	Experiment	9.593	11.141	1.161	
150	Simulation	10.135	10.674	1.053	0.409
	Experiment	10.194	10.780	1.057	
200	Simulation	9.631	9.981	1.036	0.657
	Experiment	10.125	10.424	1.030	

For spot size comparison was made at 27.5 mm. depth on Bragg curve in phantom that proton passed. The relation between spot size and proton pencil beam both the x-axis and y-axis.

The spot size results from an experiment on x-axis are 13.933, 9.451, 7.545, and 7.279 mm. for 70 MeV, 100 MeV, 150 MeV, and 200 MeV proton energy, respectively. Then compared spot size results from a simulation are 14.210, 10.390, 7.672, and 7.236 mm. for 70 MeV, 100 MeV, 150 MeV, and 200 MeV proton energy, respectively.

As well as, the spot size results from an experiment on y-axis are 14.157 mm, 9.721 mm, 7.498 mm, and 7.404 mm. for 70 MeV, 100 MeV, 150 MeV, and 200 MeV proton energy, respectively. Then compared spot size results from a simulation are 14.312 mm, 10.570 mm, 7.591 mm, and 7.524 mm. for 70 MeV, 100 MeV, 150 MeV, and 200 MeV proton energy, respectively.

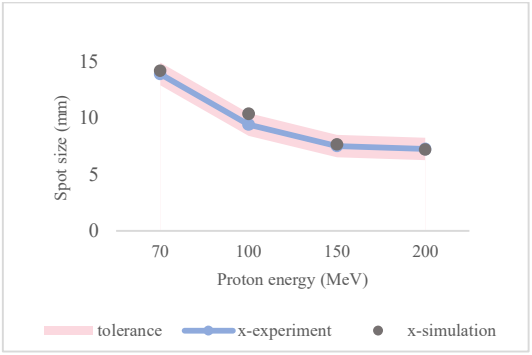

***Fig. 3** Comparison of spot size (mm) versus monoenergetic proton energies between simulation and experiment in a homogenous phantom on x-axis.*

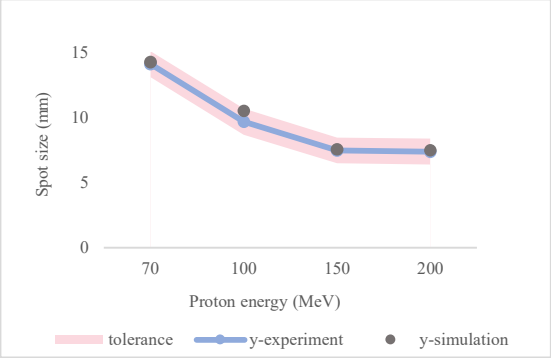

Fig. 4 *Comparison of spot size (mm) versus monoenergetic proton energies between simulation and experiment in a homogenous phantom on y-axis.*

IV. DISCUSSION

An in-house phantom was developed and employed the Octavius 1500XDR array detector. The dose ratio and spot size from the experiment are comparable to the simulation.

A. Dose ratio comparison

In dose ratio comparison, found all percentages difference of proton beam for all energies are within 5 % acceptable limit. [5] The percentage dose difference from the experiment corresponds to the simulation.

B. Spot size comparison

The relation between spot size and proton pencil beam both the x-axis and y-axis were similar trend between the simulation and the experiment, are shown in Figure 3,4. Overall, both the experimental and simulation results passed the 1 mm. range of tolerance based on TG-224. From spot size comparison can be indicated that the phantom is reasonably to represent the range verification for daily QA.

V. CONCLUSION

An in-house phantom for range verification for proton pencil beam was developed. The results from an in-house phantom could be represented as the range verification for further experiments, i.e., building an in-house phantom for daily QA.

ACKNOWLEDGEMENTS

The authors acknowledge the support from the team at the Division of Radiation Oncology, Department of Radiology, King Chulalongkorn Memorial Hospital. The authors also express sincere gratitude to Her Royal Highness Princess Maha Chakri Sirindhorn Proton Center for facilitating the experiment of this study.

REFERENCES

[1] Ding X, Younkin JE, Shen J, Bues M, Liu W. A critical review of the practices of proton daily quality assurance programs. Ther Radiol Oncol [Internet]. 2021;5:22–22. Available from: http://dx.doi.org/10.21037/tro-21-11.

[2] Allison J. Facilities and methods: Geant4 – A simulation toolkit. Nucl Phys News [Internet]. 2007;17(2):20–4. Available from:http://dx.doi.org/10.1080/10506890701404297

[3] Schuy C, Simeonov Y, Durante M, Zink K, Weber U. Technical note: vendor-agnostic water phantom for 3D dosimetry of complex fields in particle therapy. J Appl Clin Med Phys. 2020;21:227–32.

[4] OCTAVIUS Detector 1500XDR. PTW The Dosimetry Company. Accessed November 5, 2023. Available from: https://www.ptwdosimetry.com/en/products/octavius-detector-1500xdr/

[5] Ivanchenko VN. Geant4 toolkit for simulation of HEP experiments. Nucl Instrum Methods Phys Res A [Internet]. 2003;502(2–3):666–8. Available from: https://www.sciencedirect.com/science/article/pii/S0168900203005382

Contacts of the corresponding author:
Author: Paphatchaya Kheawyoi
Institute: Department of Radiology, Faculty of Medicine, Chulalongkorn University
Street: Rama IV Road
City: Bangkok
Country: Thailand
Email: *6570050930@student.chula.ac.th*

Monte Carlo model for out-of-field dosimetry during volumetric modulated arc therapy (VMAT)

Pongmettasanti D[1*], Thongsawad S[1,2], Suwanbat P[2], Liamsuwan T[1]

1 Princess Srisavangavadhana College of Medicine, Chulabhorn Royal Academy, Bangkok, Thailand

2 Radiation Oncology Department, Chulabhorn Hospital, Chulabhorn Royal Academy, Bangkok, Thailand

**Corresponding author: daranporn.pon@edu.cra.ac.th*

Abstract — **This study aimed to develop an accurate Monte Carlo (MC) model for 6 MV volumetric modulated arc therapy (VMAT) with Varian TrueBeam linear accelerator with Millenium 120 multileaf collimator (MLC) for out-of-field dose (OFD) evaluation. The study focussed on validation of the open-field configuration and model. The MC model was developed with the Particle and Heavy Ion Transport code System (PHITS). The simulation started with field-independent phase-space data above the jaws. The jaws, baseplate and MLC were modeled from vendor-provided blueprints. The MC model for the open field configuration was validated against with the commissioning data, including percentage depth dose (PDD), lateral profiles, and diagonal profiles for 10x10 and 40x40 cm^2 field sizes. The MLC model was validated using the commissioning data for MLC transmission and dose leaf gap (DLG). The average discrepancy for the PDDs behind dmax was 1.46%, and those for the central regions of the lateral profiles and diagonal profile were 3.74% and 5.58%, respectively. As expected, larger discrepancies were observed in the regions with high dose gradients. The simulated MLC transmission and DLG agreed within 18.18% and 15.86% with the commissioning data, respectively. Overall, the simulation agreed reasonably well to the measurements. Future work will focus on a more comprehensive validation of the MC model for VMAT, including the tongue-and-groove effect and the dynamic movement of the MLC in a form of the fluence map at each control point and dose in a phantom against measurements and/or treatment plans**

Keywords — **Volumetric modulated arc therapy (VMAT), Monte Carlo simulation, Out-of-field dose (OFD)**

I. INTRODUCTION

Cancer treatment through radiation therapy is effective but raises concerns about inducing secondary malignancies. Modern radiation therapy linear accelerators use multileaf collimators (MLCs) to concentrate high doses in tumors while sparing surrounding normal tissues. The quality of the achieved dose distribution relies heavily on MLC specifications, including leaf width, speed, maximum field size, and leakage. Despite the advantage in term of minimizing collateral damage, there is a growing concern regarding out-of-field dose (OFD) arising from the MLC application. In particular, for the advanced technique like volumetric modulated arc therapy (VMAT), high monitor units, collimator scatter and head leakage give rise to OFD [1]. As the advanced technology tends to increase the life expectancy of patients, OFD poses a concern about the risk for developing secondary cancer in patients [1]. Therefore, accurate determination of OFD is important.

To date, there is no standardized method for OFD quantification. Monte Carlo (MC) simulation and direct measurement were typically used for OFD determination [1]. MC modeling for VMAT requires careful validation due to the complex geometry and dynamic movement of the treatment head components. This study focused on MC modeling for VMAT with the Varian TrueBeam linear accelerator, with the aim to develop a computational tool for OFD evaluation.

II. MATERIALS AND METHODS

The MC model of the TrueBeam with Millenium 120 MLC was developed with the Particle and Heavy Ion Transport code System (PHITS) [2]. Vendor-provided phase space files for 6 MV photons were utilized as the radiation source, positioned above the jaws at 73.3 cm from the isocenter [3]. The MC model was validated by comparing with measurements, in this case, the commissioning data, following the AAPM TG 158 recommendations [1] as described in the following.

A. Validation of the MC model for open field configuration

The jaws model was modified from that of Suwanbut et al. [4]. In this work, the model of the baseplate was added. The model for the open field configuration was validated against the measured PDD curves and lateral profiles (10x10 cm^2 and 40x40 cm^2) at 5 and 10 cm depths, as well as diagonal profiles (40x40 cm^2) at the same depths. Specific indicators, such as, PDDs before dmax as well as penumbra and umbra regions of lateral and diagonal profiles, were utilized for out-of-field dose validation. For this validation, the number of simulated particles were ~$1.2x10^8$ at the phase space surface. The statistical uncertainties for PDDs behind dmax were within 5%.

B. Validation of the MLC model

The MLC transmission was used to validate the density and leaf thickness, while the dose leaf gap (DLG) was used to validate the rounded leaf end transmission. Both quantities were determined following Eclipse 10 Inverse Planning Administration and Physics Rev. 6.1.1 Protocol [5] at a depth of 5 cm in a water phantom (SAD 100 cm).

The MLC transmission was determined by averaging the closed MLC dose to the open field dose with a 10x10 cm^2 field size, as follows:

$$R_T = \left(\frac{R_{T,A}+R_{T,B}}{2}\right) \quad (1)$$

where R_T represents the average transmission and $R_{T,A}$ and $R_{T,B}$ are MLC transmissions for MLC Banks A and B, respectively. For the MC simulation, the relative dose was utilized instead of the reading values used in the commissioning data following Lin et al. [6].

The DLG was evaluated by measuring the integral ionizations for nominal gap widths of 2, 4, 6, 10, 14, 16, and 20 mm. The sweeping gap moved from -60 mm to 60 mm at a constant speed, with a dose rate of 400 MU/min for 6 MV. The average MLC transmission R_{gT} to the gap width g was calculated from [5]:

$$R_{gT} = R_T \times \left(1 - \frac{g[\mathrm{mm}]}{120[\mathrm{mm}]}\right) \quad (2)$$

The corrected gap reading (R'_g) without MLC transmission was calculated from:

$$R'_g = R_g - R_{gT} \quad (3)$$

To simplify the MC simulation, the simulated DLG was determined solely from the central gap. Also, the relative dose related to the readings of the ionization chamber (IC) was utilized in the MC simulation instead of the absolute readings. Then, a linear function was fitted to the relationship between the gap sizes (x-axis) and the corrected gap readings (y-axis). The DLG corresponded to the y-intercept of the line.

For the MLC model validation, the number of simulated particles were also ~$1.2x10^8$ at the phase space surface. The statistical uncertainty associated with the simulated MLC transmission was 30% and that for the simulated DLG was 5%.

III. RESULTS

A. Validation of the MC model for open field configuration

The results for PDDs, lateral profiles, and diagonal profiles are presented in Figures 1-3, respectively. The simulation and the commissioning data agreed reasonably well. In the regions with low dose gradient, i.e., PDDs after dmax and the central regions of the lateral and diagonal profiles, the average discrepancies for all investigated field sizes were 1.46%, 3.74% and 5.58%, respectively.

In the regions with high dose gradient, i.e., PDDs before dmax, and the penumbra regions of the lateral and diagonal profiles, the gamma passing rates (GPRs) with 3%/3 mm criterion for all investigated field sizes were within 81.25%, 66.67%, and 55.56%, respectively. In the umbra regions, the corresponding GPRs were within 90.16% and 78.87%, respectively.

B. Validation of the MLC model

The MLC model reproduced the commissioning data for MLC transmission and DLG reasonably well. In particular, the average transmission from the commissioning data was 1.43%, whereas the MC calculation yielded an average of 1.69%. For DLG, the values were 0.145 cm for the commissioning data and 0.122 cm for the MC calculation, across the gap sizes of 2, 4, 6, 10, 14, 16, and 20 mm, as shown in Figure 4.

IV. DISCUSSION

The MC simulation of the open field configuration showed reasonable agreement to the commissioning data in the regions with low dose gradient (PDDs after dmax and central regions of lateral and diagonal profiles). As expected, larger discrepancies were observed in the regions with high dose gradient (penumbra regions of lateral and diagonal profiles), where the agreement was sensitive to positioning and accuracy of both dose measurements and calculations. Nevertheless, we found that in the umbra regions out of the radiation field, the agreement between the MC simulation and measurements became reasonably good.

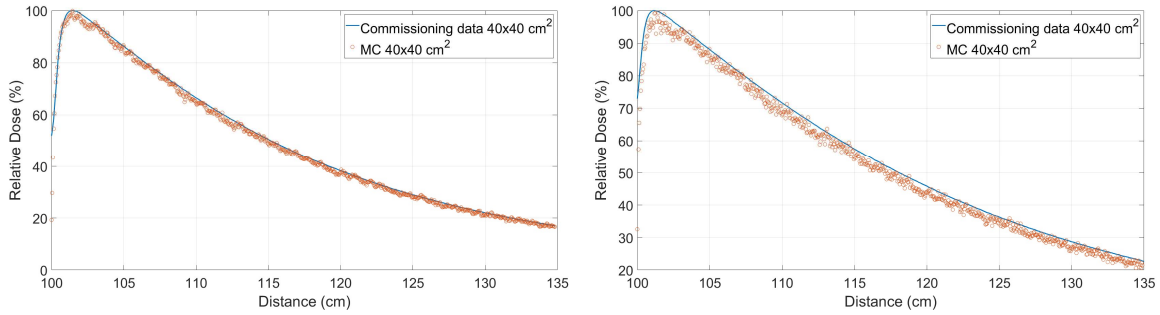

(a) (b)

Figure 1. *PDDs for 10x10 cm^2 (a) and 40x40 cm^2 (b) field sizes. Symbols are MC simulated results and lines are commissioning data.*

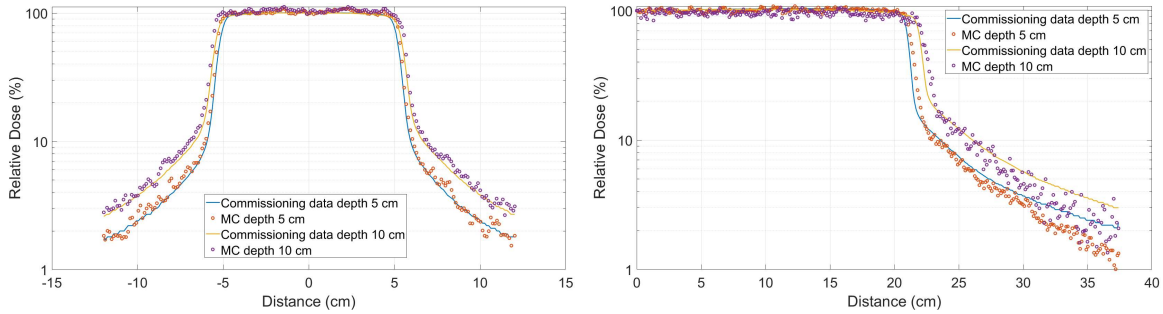

(a) (b)

Figure 2. *Lateral profiles for 10x10 cm^2 (a) and 40x40 cm^2 (b) field sizes at 5 and 10 cm depths. Symbols are MC simulated results and lines are commissioning data.*

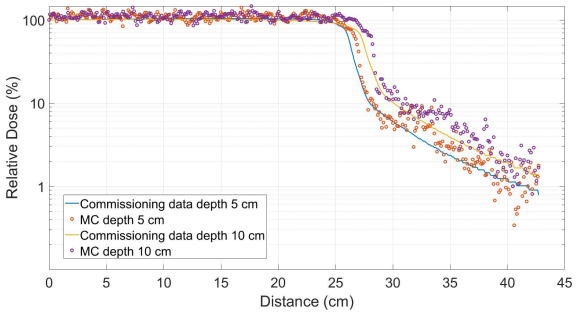

Figure 3. *Diagonal profile for 40x40 cm^2 field size at 5 and 10 cm depths. Symbols are MC simulated results and lines are commissioning data.*

For MLC transmission, although our MC calculation deviated ~18.18% from the commissioning data, our calculation demonstrated reasonable agreement with the range of values surveyed by Isono et al. [7] (median = 1.65%, 95% CI [1.38, 1.92]). The deviation between the simulated and measured DLG was ~15.86%, and our result was slightly

lower than those reported by Isono et al. [7] (median = 0.178 cm, 95% CI [0.149, 0.206]), which could be due to the simplified static evaluation of the DLG in the MC simulation.

One of the limitations of this work was that only 3 phase space files, equivalent to ~$1.2x10^8$ particles at the phase space surface, could be simulated due to computational constraints. To address this issue, we plan to increase the number of simulated particles to achieve more reliable simulation results.

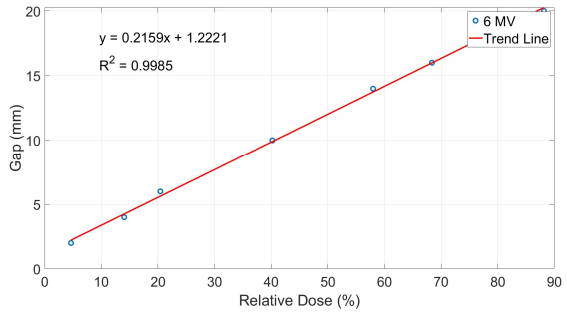

Figure 4. *A linear regression of relative dose and gap width.*

V. CONCLUSION

In this study, a Monte Carlo (MC) model for out-of-field dose (OFD) calculation for 6 MV VMAT with TrueBeam linear accelerator and Millennium 120 MLC was developed using PHITS Monte Carlo code. The validation process followed the AAPM TG 158 recommendations, including the validation of the open field configuration and the MLC model. The MC simulated results were compared with the commissioning data for PDDs, lateral profiles, diagonal profiles, MLC transmission and DLG. The agreement was reasonably good considering the limited number of particles simulated. Future work will focus on increasing the number of simulated particles to ensure reliable results. In addition, a more comprehensive validation of the MLC model, including the tongue-and-groove effect and the dynamic movement of the MLC in a form of the fluence map at each control point and dose in a phantom will be performed against measurements and/or treatment plans

ACKNOWLEDGEMENTS

D. P. acknowledges the Scholarship for Commemoration of the 60th Birthday of Her Royal Highness Princess Chulabhorn Krom Phra Srisavangavadhana for Development of Medical Physicists, Chulabhorn Royal Academy, Thailand.

REFERENCES

[1] Kry SF, Bednarz B, Howell RM, Dauer L, Followill D, Klein E, Paganetti H, Wang B, Wuu CS, George Xu X. AAPM TG 158: measurement and calculation of doses outside the treated volume from external-beam radiation therapy. Medical physics. 2017 Oct;44(10):e391-429.

[2] Sato T, Iwamoto Y, Hashimoto S, Ogawa T, Furuta T, Abe S-i, et al. Features of particle and heavy ion transport code system (PHITS) version 3.02. J Nucl Sci Technol. 2018; 55(6): 684-90.

[3] Varian Medical System. TrueBeam Monte Carlo Data Package version 1.1. California: Varian Medical system; 2014.

[4] Suwanbut P, Liamsuwan T, Nantajit D, Masa-Nga W, Tannanonta C. Assessment of fetal dose and health effect to the fetus from breast cancer radiotherapy during pregnancy. Life. 2022 Jan 7;12(1):84.

[5] Varian medical system. Eclipse 10 inverse planning administration and physics rev. 6.1.1.2011.

[6] Lin, CY., Shiau, AC., Ji, JH. et al. A simple method for determining dosimetric leaf gap with cross-field dose width for rounded leaf-end multileaf collimator systems. Radiat Oncol 13, 222 (2018).

[7] Isono M, Akino Y, Mizuno H, Tanaka Y, Masai N, Yamamoto T. Inter-unit variability of multi-leaf collimator parameters for IMRT and VMAT treatment planning: a multi-institutional survey. Journal of radiation research. 2020 Mar;61(2):307-13.

Contacts of the corresponding author:
Author: Pongmettasanti Daranporn
Institute: Princess Srisavangavadhana College of Medicine, Chulabhorn Royal Academy
Street: Kampangpetch 6
City: Bangkok
Country: Thailand
Email: daranporn.pon@edu.cra.ac.th

A comparative analysis of geometric and dosimetric outcomes in Atlas-Based versus Deep Learning-Based automated segmentation for head and neck radiation therapy

Thanusilp Warisara[1,*], Kummanee Patiparn[1], Masa-Nga Wilai[1,2], Chamchod Sasikarn[1,2], Fuangrod Todsaporn[1]

1 Princess Srisavangavadhana College of Medicine, Chulabhorn Royal Academy, Bangkok, Thailand
2 Radiation Oncology Department, Chulabhorn Hospital, Chulabhorn Royal Academy, Bangkok, Thailand

**Corresponding author:* warisara.tha@edu.cra.ac.th

Abstract —**This study evaluates the effectiveness of automated segmentation methods in head and neck IMRT and VMAT techniques. Two commercial software programs were used: MIM, which employs Atlas-based methods, and AccuContour, which utilizes a Deep Learning method, to compare the accuracy in segmenting 11 OARs (Organs at Risk) from 30 head and neck patients. The analysis metrics include dice similarity coefficient (DSC) for geometric accuracy. Maximum (D_{max}) and mean dose (D_{mean}) difference percentages from dose constructed using manual contour was used for dosimetric accuracy. Results indicate that the deep-learning algorithm demonstrates higher accuracy compared to the atlas-based algorithm in auto-segmentation, particularly for smaller or low-contrast organs. The study highlights the potential of implementing deep-learning-based auto-segmentation to accelerate the treatment planning process and to reduce variability between observers in head and neck cancer radiation therapy.**

Keywords —**Auto-Segmentation, Atlas-Based (AB), Deep Learning Based (DLB), Organ-At-Risk (OAR), Head and Neck (HN)**

I. INTRODUCTION

Advancements in radiotherapy techniques, such as Intensity-Modulated Radiotherapy (IMRT) and Volumetric Modulated Arc Therapy (VMAT), have led to more precise dose conformity to radiation targets, thereby reducing the radiation exposure to nearby at-risk organs (OARs). However, the challenge with manual OAR segmentation is that it is time-consuming and subject to significant interobserver variability. This issue is particularly pronounced in patients with head-and-neck (HN) cancer, whose anatomies are highly complex and feature numerous OARs. Variations in contouring can lead to significant dosimetric differences.

Automatic segmentation (AS) methods have become popular because they improve the accuracy of contouring, accelerate delineation, and reduce both intra- and inter-observer variation in treatment plans [1]. Deep learning-based (DLB) techniques offer a faster and more accurate alternative to atlas-based (AB) methods, although they require significant GPU computing power and extensive data collection. However, AS methods in DLB models face challenges in segmenting smaller volumes or organs with low image contrast. Additionally, comparing different models is difficult due to variations in datasets. While DLB methods surpass AB methods in performance, there is still room for improvement in the automated segmentation (AS) of computed tomography (CT) images, especially for small organs or those with limited image contrast.

This study aimed to assess the effectiveness of two commercial auto-segmentation software programs in treating HN cancers. The outputs of auto-segmentation for 11 OARs were evaluated to quantify both geometric and dosimetric accuracies.

II. MATERIALS AND METHODS

Fig. 1 presents the workflow of this study aimed to evaluate and compare clinical auto-segmentation software options. Radiation oncologists manually segmented and created treatment plans using Eclipse treatment planning system version.16.01.10 (Varian). This process involved using an anonymized patient code, registrations, internal structure sets, and treatment plans.

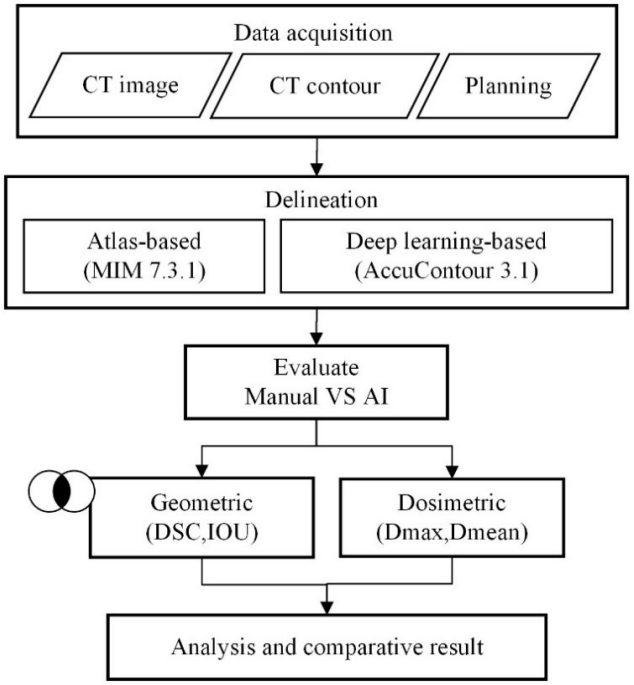

Figure 1. *The workflow diagram for this study.*

A. Data acquisition and auto-segmentation

A random selection of 30 HN IMRT / VMAT patient datasets, who received treatment at Chulabhorn Hospital, Thailand between 2012 to 2023 was acquired for this study. The data collection included patient plan CT images, structure set (RS-file) from manual contours crated by single radiologist at the department to minimize personal bias, treatment plan (RP-file), and dose calculation (RD-file). Eleven OARs (brainstem, left and right eyes, larynx, left and right lens, left and right optic nerves, left and right parotid glands, and spinal cord) were delineated using two commercial auto-segmentation software programs; 1) MIM version 7.1.3 (AB methods) and 2) AccuCountour version 3.1 (DLB methods). Examples of comparison between two auto-segmentation method and manual contour by radiologist is shown in Fig. 2.

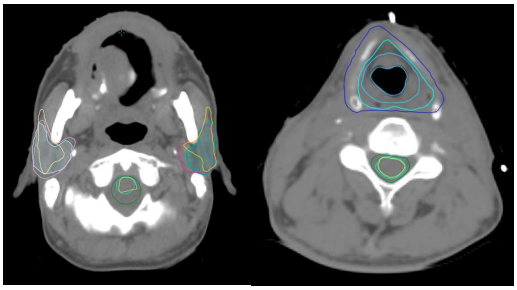

Figure 2. *Example of auto-segmentation uncertainties of two software compared with manual reference delineations in 11OARs HN, projected on an axial CT slice.*

B. Evaluation of geometric accuracy

Dice similarity coefficient (DSC) was used to access the geometric accuracy shown in equation 1.

$$DSC = \frac{2|A \cap B|}{|A| + |B|} \qquad (1)$$

Where |A∩B| represents the volumetric intersection between the ground truth contour (A) and the predicted segmentation (B). The value ranges from 0 to 1, which 0 indicating no overlap and 1 indicating perfect overlap. Higher values indicating closer agreement.

C. Evaluation of dosimetric impact of variation in contouring

For all patients, treatment plan was regenerated using new structures results from AB and DLB auto-segmentation, and manual delineation. The differences in dose distributions between these plans were evaluated for specific OAR using the maximum dose (D_{max}) and mean dose (D_{mean}) percentage difference. Clinically relevant dosimetric endpoints for OAR were considered based on the clinical protocol at the department that following the recommendations of the Radiation Therapy Oncology Group (RTOG) guideline. Fig. 3, shows dose variations at OAR boundaries (parotid left and right). The manual delineated showed a section with more radiation than DL and AB.

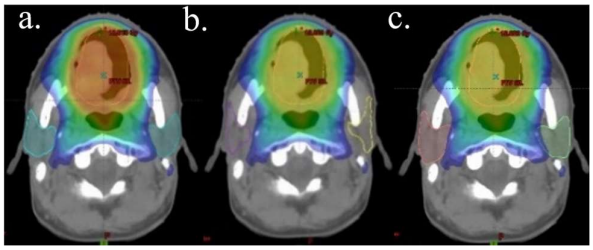

Figure 3. *The dose distribution (axial) for patient A in three contouring scenarios: a) Manual, b) AB, and c) DLB.*

III. RESULTS

The average computational time per patient was 7.5±0.6 min for AB method and less than 1 min for DLB method. For the geometric accuracy, the DICE results indicated that DLB algorithms were more accurate than AB algorithms for the auto-segmentation of HN OARs. DL outperformed AB in nine out of the 11 OARs, as demonstrated by the overlap values.

Table 1 shows the DSC averages ranged from 0.07±0.11 to 0.82±0.04 for AB and 0.41±0.09 to 0.93±0.03 for DLB.

In Fig. 4, DLB exhibited lower DSC values compared to AB, especially for certain organs like the larynx and spinal cord. DLB faced challenges when contouring these elongated organs. On the other hand, when AB was used, difficulties often arose in delineating boundaries for smaller organs such as the lens and optic nerve, and in some cases, the boundaries could not be defined at all.

Table 1 presents the results of geometric and dosimetric assessments between AB and DLB auto-segmentations. The highest percentage difference in D_{max} for AB is found in the right eye, with a value of 26.86%. In DLB, the Right Optic Nerve exhibits the highest percentage difference at 29.33%. Regarding D_{mean}, the maximum percentage difference for AB is observed in the left Parotid, with 32.98%, while for DLB, the highest percentage difference is seen in Larlynx, at 39.37%

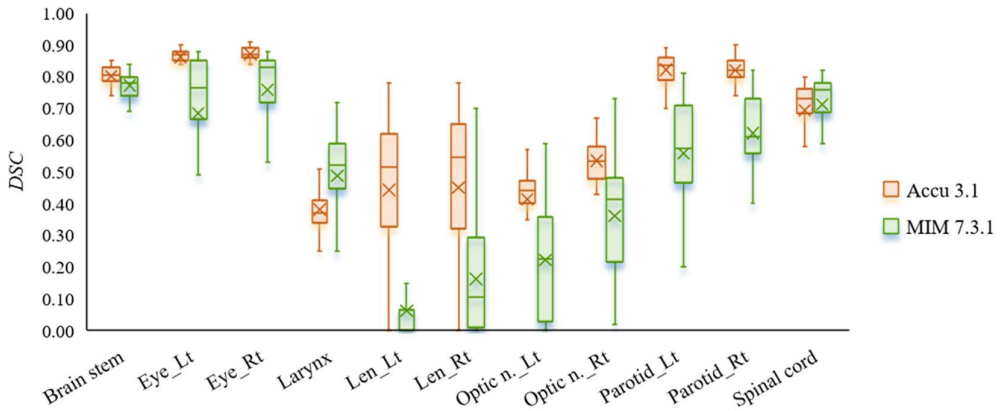

Figure 4. *Results of the DSC comparison OARs between software tools AB (MIM ver.7.3.1) and DLB(Accu ver.3.1) for the head to the original plan.*

Table 1. The results of HN OARs of DSC, $\%\Delta D_{max}$, and $\%\Delta D_{mean}$.

Structure	Manual [Gy]		Atlas-based			Deep learning		
	D_{max}	D_{mean}	DSC	$\%\Delta D_{max}$	$\%\Delta D_{mean}$	DSC	$\%\Delta D_{max}$	$\%\Delta D_{mean}$
Brain stem	36.55	12.38	0.82±0.04	16.24	13.47	0.86±0.04	4.49	9.22
Eye_Lt	4.51	2.01	0.73±0.24	26.24	1.82	0.92±0.04	7.02	2.46
Eye_Rt	4.53	2.10	0.81±0.16	26.86	1.93	0.93±0.03	5.18	0.64
Larynx	50.40	32.03	0.52±0.16	19.24	25.75	**0.41±0.09**	19.62	39.37
Len_Lt	2.33	1.95	**0.07±0.11**	18.37	1.62	0.47±0.24	9.79	2.68
Len_Rt	2.38	2.03	0.17±0.18	10.89	1.73	0.48±0.26	5.63	0.95
Optic n._Lt	4.03	2.80	0.24±0.17	15.95	2.58	0.44±0.16	6.77	3.41
Optic n._Rt	4.09	2.93	0.39±0.19	12.17	2.82	0.57±0.11	29.33	7.99
Parotid_Lt	58.05	33.68	0.60±0.19	1.85	32.98	0.88±0.05	1.19	2.53
Parotid_Rt	38.10	18.90	0.66±0.13	20.08	24.45	0.87±0.04	8.71	10.84
Spinal cord	25.60	15.52	0.76±0.14	10.30	15.25	0.74±0.13	5.04	2.91

IV. DISCUSSION

The primary objective of this study was to evaluate the performance of two commercially available auto-segmentation software programs, MIM (AB method) and AccuContour (DLB method), in the context of head-and-neck (HN) IMRT and VMAT treatments. Our investigation focused on assessing both the geometric and dosimetric accuracies and precision of these tools, providing valuable insights for their clinical adoption and implementation.

One of the key findings of our study was the significant efficiency in workload reduction afforded by the DLB method (less than 1 min/patient), which required fewer manual corrections compared to the AB method. This aspect is particularly significant in a clinical setting where time efficiency and accuracy are vital. Furthermore, when evaluating the dosimetric outcomes, our results revealed only minor variations in dose distributions compared to manual segmentation. This finding shows the potential of automated tools in maintaining treatment efficacy while streamlining the planning process.

However, our study presents some divergence from previous research, the study by Costea et al. [2], which reported slightly higher accuracy for the AB method compared to the DLB method. Such discrepancies could be attributed to differences in patient demographics, segmentation challenges, or software versions used. It is important to acknowledge that our study involved a relatively small patient sample and a single observer for manual segmentation, which could influence the results. Incorporating a larger patient cohort and multiple observers in future studies could enhance the statistical robustness and provide a more comprehensive comparison of these auto-segmentation methods.

The difference in inter-observer segmentation may be attributed to variations in patient counts. Therefore, including more patients or observers in future tests may increase statistical accuracy and improve comparison results.

V. CONCLUSION

In conclusion, the study provides values insights into the comparative efficiency of two auto-segmentation software tools, MIM (AB method) and AccuContour (DLB method) for HN IMRT/VMAT. Our finding showed DLB method had higher geometric accuracy and lower dose difference compared to the dose from manual segmentation treatment plan. DLB auto-segmentation shows promise for reducing manual workload and achieving closer alignment with manual segmentation and dose distribution.

REFERENCES

[1] Thor M, Apte A, Haq R, Iyer A, LoCastro E, Deasy JO. Using Auto-Segmentation to Reduce Contouring and Dose Inconsistency in Clinical Trials: The Simulated Impact on RTOG 0617. Int J Radiat Oncol Biol Phys 2021;109:1619–26.

[2] Costea, M., Zlate, A., Durand, M., Baudier, T., Grégoire, V., Sarrut, D., & Biston, M. C. (2022). Comparison of atlas-based and deep learning methods for organs at risk delineation on head-and-neck CT images using an automated treatment planning system. Radiotherapy and oncology: journal of the European Society for Therapeutic Radiology and Oncology, 177, 61–70.

Contacts of the corresponding author:
Author: Warisara Thanusilp
Institute: Princess Srisavangavadhana College of Medicine, Chulabhorn Royal Academy
Street: Kampangpetch 6 Rd., Lak si
City: Bangkok
Country: Thailand
Email: warisara.tha@edu.cra.ac.th

Dose prediction in prostate cancer

Chaikamthorn P.[1], Na Ayuthaya I.[2]

1 Medical Physics Program, Department of Radiology, Faculty of Medicine, Chulalongkorn University, Pathumwan, Bangkok 10330,
2 Division of Radiation Oncology, Department of Radiology, King Chulalongkorn Memorial Hospital, Bangkok 10330, Thailand

Abstract — **This study aimed to develop and evaluate a machine learning model for predicting dose-volume histograms (DVHs) for prostate cancer treatment plans. The study followed a two-phase approach, where the first phase involved data preprocessing, and the second phase involved dose prediction. The data preprocessing phase involved selecting 25 approved prostate cancer treatment plans that contain PTV and organ at risk (OARs), i.e., bladder, rectum, femoral heads, and penile bulb. The second phase involved creating and evaluating a machine learning model using the data collected in the data preprocessing phase with Python 3. The model was trained with a 5-fold cross-validation method and evaluated with the test set to see the absolute difference and root mean square error value. The results demonstrated a tendency for the model to overestimate the DVHs of every organ compared to the referenced treatment plan. The penile bulb prediction performed the worst of all predictions due to the high variation of the penile bulb's volume between each treatment plan, which depends on the individual's organ structure and each planner. Combining this with the low number of samples causes the machine learning model to overpredict compared to the treatment plan. This discrepancy suggests that further refinement is necessary for the model to achieve optimal dosimetric accuracy and effectively generate clinically relevant DVHs for treatment planning. In conclusion, developing and evaluating the feasibility of machine learning-based dose prediction models can help reduce the time and effort required for radiation therapy planning and improve the accuracy and effectiveness of the treatment.**

Keywords — **Dose prediction, machine learning, prostate cancer.**

I. INTRODUCTION

Prostate cancer is one of the most common cancers among men worldwide. Radiation therapy is a widely used treatment option that aims to deliver a high dose of radiation to the tumor while sparing the surrounding healthy tissues to prevent side effects and complications. Therefore, it is crucial to optimize the radiation dose distribution to achieve a balance between tumor control and normal tissue preservation. One of the challenges in radiation therapy planning is the variability of the patient's anatomy and the tumor shape and location. This requires a customized and individualized dose prescription for each patient, which can be time-consuming and labor-intensive. Moreover, the dose optimization and calculation process involve complex physical models and numerical algorithms that can introduce variations in dose dependent on planners. Therefore, there is a need for fast and accurate methods to predict the dose distribution for a given patient based on their anatomical features and clinical objectives. This is why we aim to develop and evaluate the feasibility of machine learning-based dose prediction models.

II. MATERIALS AND METHODS

In this study, we followed a two-phase approach to create and evaluate a machine learning model for prostate cancer treatment plans.

Phase I: Data preprocessing

Since treatment plans usually contain various contours, we had to select the plans that contain PTV and organ at risk (OARs), i.e., bladder, rectum, femoral heads, and penile bulb. We collected 25 approved prostate cancer treatment plans and extracted the following parameters from these plans: PTV

volume, OARs volume, the dose-volume metrics (DVH) of the organs, The OARs-PTV overlapping volume[1] (OPOV) at different distances from the PTV. This parameter can indicate the distance between the OARs and the PTV which is the key to optimizing the dose.

Phase II: Dose Prediction

We created and evaluated a machine learning model using the data collected in the Data preprocessing phase with Python 3. We separated the data into training and test sets with a ratio of 90:10, respectively. We train the machine learning model with the training set using a 5-fold cross-validation method. Then, we selected the best-performing model to evaluate with the test set to see the absolute difference and root mean square error value.

III. RESULTS

The model predictions of D_{mean} and D_{max} for OARs, and D_{95} and D_{max} for PTV were overpredicted compared to the clinical treatment plan, but the predictions were within the standard deviation, as illustrated in Figures 1-3. The prediction of PTV's D_{95} showed the best result, with an absolute dose difference of 0.6±0.24 Gy and a root mean square error of 1.85. The best D_{max} predictions were from the rectum, with an absolute dose difference of 0.86±0.82 Gy and a root mean square error of 1.09. The worst predictions were for the penile bulb, for both D_{mean} and D_{max}, with an absolute dose difference of 6.79±1.99 Gy and 29.90±24.16 Gy, respectively. The root mean square errors were 9.69 and 12.96, respectively, as shown in Tables 1-2.

Table 1. *Mean absolute dose difference between each organ.*

Organs	*Absolute Dose difference (Gy)*	
	D_{mean} (D_{95} for PTV)	D_{max}
PTV	*0.60±0.24*	*1.73±0.94*
Bladder	*5.94±3.08*	*1.69±1.32*
Rectum	*6.21±2.95*	*0.86±0.82*
Femoral heads	*3.16±4.55*	*4.81±4.86*
Penile bulb	*6.79±1.99*	*29.90±24.16*

Table 2. *Root mean square error between each organ.*

Organs	*Root mean square error (RMSE)*	
	D_{mean}	D_{max}
PTV	1.85	1.9
Bladder	5.48	2
Rectum	7.45	1.09
Femoral heads	2.57	7.99
Penile bulb	9.69	12.96

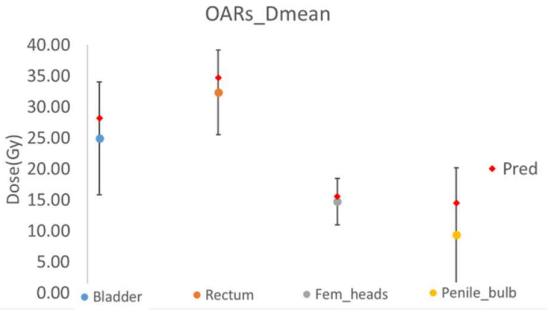

Figure 1. *The plot from one of the treatment plans shows that the D_{mean} prediction is a red diamond, which is overestimated but still within the standard deviation.*

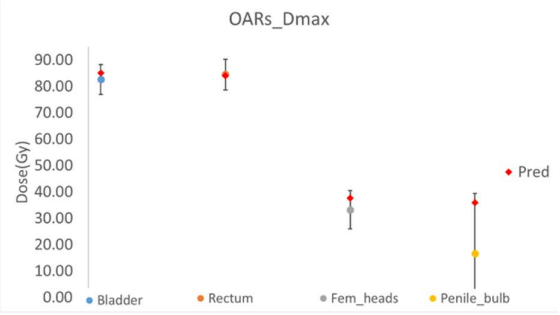

Figure 2. *The plot from one of the treatment plans shows that the D_{max} prediction is a red diamond.*

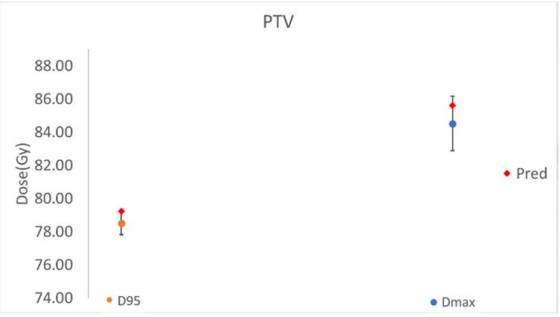

Figure 3. *The plot from one of the treatment plans shows that the prediction of D_{95} and D_{max} PTV is a red diamond, which D95 prediction is slightly overestimate outside the standard deviation.*

IV. DISCUSSION

Although most of the predictions are within the standard deviation, the root mean square error is high compared to the study by Jiao, Wang, and Chen LX, et al[1]. The penile bulb prediction performs the worst of all predictions because of the high variation of the penile bulb's volume between each treatment plan, which depends on the individual's organ structure and each patient. Combining this with the low number of samples causes the machine learning model to overpredict compared to the treatment plan. As a result, the machine learning model is not accurate enough to predict the optimized DVH for the actual treatment plan.

V. CONCLUSION

The study assessed the performance of a machine learning model in predicting dose-volume histograms (DVHs) for prostate cancer treatment plans based on the volume overlap between the planning target volume (PTV) and organs at risk (OARs). The results demonstrated a tendency for the model to overestimate the DVHs of every organ compared to the clinical treatment plan. This discrepancy suggests that further refinement is necessary for the model to achieve optimal dosimetric accuracy and effectively generate clinically relevant DVHs for treatment planning.

ACKNOWLEDGEMENTS

I would like to express my sincere gratitude to everyone who has supported me throughout this research project. First and foremost, I would like to thank my supervisor, Na Ayuthaya I., for their invaluable guidance, encouragement, and feedback. Their expertise and dedication have been instrumental in shaping this study. I am grateful to the Development and the Promotion of Science and Technology Talents Project for providing financial support that made this research possible. Their generosity and trust have enabled me to pursue my academic goals and contribute to the field of radiotherapy at Chulalongkorn University. I would like to acknowledge the contributions of all the participants who generously shared their time and experiences for this research. Their cooperation and enthusiasm have been essential to the success of this study. Finally, I would like to thank my family, friends, and colleagues for their unwavering support, encouragement, and understanding. Their love and care have sustained me throughout this journey.

REFERENCES

[1] Jiao SX, Wang ML, Chen LX, et al. Evaluation of dose–volume histogram prediction for organ-at risk and planning target volume based on machine learning. Sci Rep.2021; 11(1):3117.

[2] Wu B, Ricchetti F, Sanguineti G, et al. Patient geometry-driven information retrieval for IMRT treatment plan quality control. Med Phys. 2009;36(12):5497-5505.

[3] Polizzi M, Watkins RW, Watkins WT. Data-Driven Dose-Volume Histogram Prediction. Adv Radiat Oncol. 2022; 7:100841.

[4] Nguyen D, Long T, Jia X, et al. A feasibility study for predicting optimal radiation therapy dose distribution of prostate cancer patients from patient anatomy using deep learning. Sci Rep. 2017; 7:100841.

[5] Cao W, Gronberg M, Olanrewaju A, et al. Knowledge-based planning for the radiation therapy treatment plan quality assurance for patients with head and neck cancer. Radiat Oncol Phys. 2022.

[6] Nguyen D, Jia X, Sher D, et al. 3D radiotherapy dose prediction on head and neck cancer patients with a hierarchically densely connected U-net deep learning architecture. Med Phys. 2019; 36(12):5497-5505.

[7] Barragán-Montero AM, Nguyen D, Lu W, et al. Three-dimensional dose prediction for lung IMRT patients with deep neural networks: robust learning from heterogeneous beam configurations. Med Phys. 2019.

[8] Kandalan RN, Nguyen D, Rezaeian NH, et al. Dose prediction with deep learning for prostate cancer radiation therapy: Model adaptation to different treatment planning practices. Med Phys. 2020.

Contacts of the corresponding author:
Author: Chaikamthorn P., Na Ayuthaya I.
Institute: Chulalongkorn University.
King Chulalongkorn Memorial Hospital.
Street: Pathumwan
City: Bangkok
Country: Thailand
Email: 6470051430@student.chula.ac.th

Determination of the surface dose correction factors for various detectors in spot scanning beam proton therapy

Saruang P[1], Sanghangthum T[1], Yamram N[1], Keawsamur M[1*]

1 Medical Physics Program, Department of Radiology, Faculty of Medicine, Chulalongkorn University, Pathumwan, Bangkok, Thailand

**Corresponding author: mintra.ke@chula.ac.th*

Abstract — **Proton therapy effectively administers precise doses while minimizing harm to vital organs, yet concerns arise regarding skin toxicity caused by energy dispersion beyond the Bragg peak. This research aims to determine the surface dose correction factors (Scf) for various detectors in spot scanning beam proton therapy and study the effect of surface dose according to various clinical factors. The advanced Markus chamber and FC65-G Farmer chamber were utilized to measure the skin dose in a water phantom. A reference point located 0.07 mm below the phantom's surface was defined to represent the skin position, and the doses were normalized to the doses at 3 cm depth. The obtained surface doses from the experiment were compared to the reference results obtained from FLUKA Monte Carlo simulations under the same conditions to determine the Scf of the detectors. Additionally, the study investigated the impact of various factors affecting surface dose, including variations in energy (100, 150, and 200 MeV), air gap distances (5, 15, and 42.1 cm), and range shifter (RS) thicknesses (2, 3, and 5 cm).The results indicated that the Scf from the Markus detector were 0.9938, 0.9922, and 0.9886 for 100, 150, and 200 MeV, respectively. Similarly, for the FC65-G, the factors were 0.9711, 0.9859, and 0.9764 for the same respective energy levels. As for the correlation with clinical variables, an increase in the air gap distance resulted in a decrease in surface dose. Introducing the range shifter (RS) amplified the surface dose compared to its absence, particularly evident with reduced air gap distances and increased RS thickness. In this study, the surface dose correction factors demonstrated variability contingent upon the energies utilized. Furthermore, the introduction of a range shifter exhibited discernible alterations in surface dose, exhibiting variability contingent upon air gap distances.**

Keywords — **Surface dose, Correction factors, Proton therapy, Air gap, Range shifter**

I. INTRODUCTION

Proton therapy is esteemed for its precision in cancer treatment, harnessing proton particles to minimize collateral tissue damage. Nevertheless, observations in certain studies indicate instances of skin toxicity in patients undergoing proton therapy, attributed to the dispersion of proton beams beyond the tumor's targeted area[1,2]. This phenomenon necessitates a meticulous examination of the surface dose, which denotes the radiation dosage affecting the skin. This necessitates meticulous evaluation of the surface dose affecting the skin, a complex parameter influenced by factors like range shifters and air gaps. Secondary particle generation and altered electron fluence significantly impact this dose, affecting treatment outcomes[3].

This research aims to determine correction coefficients for various detectors in spot scanning beam proton therapy, which is crucial for accurately quantifying patient radiation doses. This pursuit acknowledges the inherent challenges in measuring this pivotal metric, emphasizing its clinical significance in treatment planning.

II. MATERIALS AND METHODS

A. Determination of the measured and surface dose correction factors

The measurement was performed using the proton pencil scanning beam delivery system, The ProBeam Compact (Varian Medical System, Palo, Alto, CA). Surface dose correction factors were obtained by measuring

the surface dose with two detectors: Advanced Markus plane parallel ion chamber (PTW, Freiburg, Germany) and FC65-G ionization chamber (IBA, Schwarzenbruck, Germany). The detectors were placed on the solid-water phantom surface, and a reference point located 0.07 mm below the phantom's surface was defined to represent the surface position [4]. The detector responses were then normalized at a depth of 3 cm. For measuring surface dose with the FC65-G, the setup was done using a water tank, with the detector placed at the water surface to prevent additional thickness caused by the chamber insertion slot in the slab water phantom. The test conditions for the measurement are shown in Table 1. All surface doses were recorded three times to obtain an average value. Subsequently, the average measured dose was calculated along with the dose obtained from FLUKA Monte Carlo simulation (version 2021.2.6) using Equation (1) to determine the surface dose correction factors (Scf) for each detector.

Table 1. *Conditions for measurement tests.*

Energy layering	Single quasi-monoenergetic layer
Proton energy [MeV]	100, 150, 200
Scanning field [cm^2]	10 x 10
Snout position [cm]	42.1
Gantry angle [degree]	0

$$\boldsymbol{Scf} = 1 - \left(\frac{(D_{M1st} - D_{0.07,FLUKA})}{D_{0.07,FLUKA}}\right) \qquad (1)$$

where D_{M1st} is the first depth measurement of the detectors and $D_{0.07,FLUKA}$ is the surface dose in 70 μm thickness determined with the FLUKA.

B. Clinical parameter alterations influence the variables impacting surface dose

The detectors were then used to determine the correlation between surface dose and changes in clinical parameters, including air gaps distances, the insertion and modification of the thickness of the range shifter (RS), using the correction factors obtained in the previous experiment. The experiment setups are presented in Table 1. In this experiment, detectors were used to measure the dose of the various air gaps which were 5, 10, 15, 20, and 42.1 cm under two conditions: with and without the RS. In the case of inserting RS, a study was conducted by varying air gaps at distances of 5, 15, and 42.1 cm to investigate the combined effects of both factors. Moreover, repeat the same experiment for each of the three thicknesses of the RS (PMMA, physical thickness = 2, 3, 5 cm), and then measure the surface dose three times to obtain the average value.

III. RESULTS

A. Surface dose correction factors in each detector

The outcomes derived from the actual surface dose measurements and simulated values, when subjected to calculation through Equation 1, yield correction factors as shown in Table 2. The correction factor for the advanced Markus detector was 0.992, which was the average of 0.994, 0.992, and 0.989 for 100, 150, and 200 MeV, respectively. Similarly, for the FC65-G, the factor was 0.978, which was the average of 0.971, 0.986, and 0.976 for the same respective energy levels. The difference among the three energies did not exceed 1%, with a margin of 0.3% for the Advanced Markus and 0.8% for the FC65-G, thus allowing the use of the average value for all three energies.

Table 2. *Surface dose correction factor (Scf) for all three energies: the Advanced Markus, FC65-G chamber.*

Detector	Surface dose correction factor (Scf)
Advanced Markus	0.992
FC65-G	0.978

B. Influence of Air Gap Distances

An increase in the air gap distance resulted in a decrease in surface dose as shown in Figure 1. This experiment led to the preference for the Advance Markus detector due to limitations in setting up the experimental configuration for dose measurements with the FC65G. From the results, it was evident that the surface dose increases with the rising proton energy. Additionally, when reducing the air gap distance from 20 cm downwards, the maximum increase was observed at an air gap distance of 5 cm for 100MeV, with a rise of 2.3%.

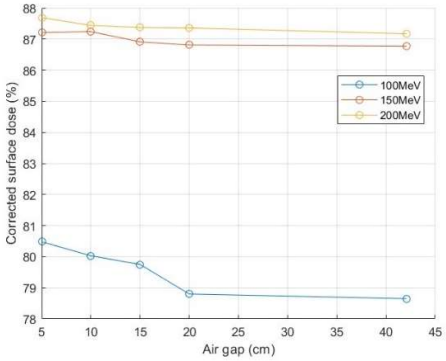

Figure 1. *The percentage of surface dose measured by the corrected advanced Markus detector, normalized to the dose at 3 cm [(D0.007/D3 cm)*100%], the values obtained at all air gap distances (5, 10, 15, and 42.1 cm) for all three proton energies.*

C. Role of Range Shifter and Air Gap Variation.

Figure 2, which illustrated the results of measuring surface dose using the Advance Markus detector, showed the insertion of the Range Shifter (RS) led to a proportional increase in surface dose corresponding to the increased thickness of the RS. This was observed notably at an air gap distance of 15 cm, with the maximum increases being 2%, 5%, and 7% for RS thicknesses of 2, 3, and 5 cm, respectively, at an air gap distance of 5 cm.

While at the initial air gap distance (42.1 cm), the insertion of RS results in minimal or almost negligible changes in surface dose. Compared to not using RS, the average percentage change was approximately 0.05%, showing a slight decrease, consistent with the thickness of the RS, as depicted in Figure 3. These observations were made in the context of experimental dose measurements using both the Advance Markus and FC65G detectors at an air gap distance of 42.1 cm.

However, it was noteworthy to observe that there were variations in surface dose when using the FC65G detector at 100 MeV proton energy. Specifically, there was a substantial change, namely a reduction of 10% and 22% when employing RS2 and RS3, respectively.

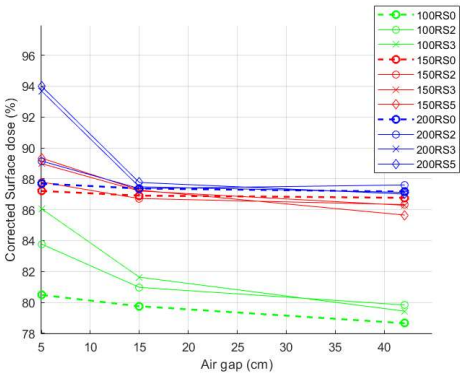

Figure 2. *Percentage of surface dose when considering the insertion of RS with thicknesses of 2, 3, and 5 cm, and varying air gap distances at 5, 15, and 42.1 cm for all three proton energies using the corrected Advance Markus detector. The graphs illustrate two scenarios: one without using RS (dashed line) and the other with RS (solid line).*

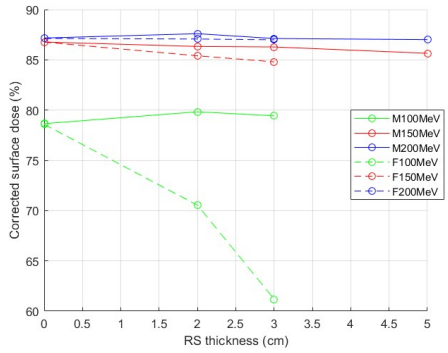

Figure 3. *The percentage of surface dose, which measured with calibrated detectors, presented for the case of inserting Range Shifter (RS) with thicknesses of 2, 3 and 5 cm in the Advanced Markus detector (solid lines), and 2 and 3 cm in the FC65G detector (dashed lines). The measurements were taken at an air gap distance of 42.1 cm for all three proton energies.*

IV. DISCUSSION

A. Determination of surface dose for proton pencil beam therapy

From this research, it was found that surface dose correction factors among the three energy levels did not surpass 1%. Consequently, these negligible variations allow for the adoption of the average correction factor across all three energy levels. This finding underscores the reliability and consistency of the correction factors derived, which could significantly contribute to

enhanced accuracy in subsequent measurements.

In the Advanced Markus chamber, the correction values are consistently close to 1 with the recommended value being 0.992. When comparing the actual surface dose values with FLUKA Monte Carlo simulations, considered the gold standard, it is deemed suitable for clinical surface dose measurements. Additionally, supporting research advocates for the use of plane parallel ion chambers in surface dose measurements due to their minimal uncertainty compared to other types of detectors, including radiochromic film, extrapolation chambers, and TLD[5]. Conversely, the recommended correction factor in the FC65-G chamber was 0.978. It exhibits a wider range of correction values, encompassing both higher and lower values than the Advanced Markus IC across all energy levels. This discrepancy arises from the thin shape and characteristics of the detectors, with thinner detectors proving more suitable for measuring dose near the surface due to less interference from their smaller size.

B. The correlation of the surface dose with the various clinical parameters

The insertion of the RS and the adjustment of the air gap distance significantly impact changes in surface dose. Specifically, reducing the air gap distance to less than 20 cm results in a statistically significant increase in surface dose. Furthermore, the introduction of an RS to shift the dose for treating lesions on the skin leads to alterations in surface dose, particularly when reducing the air gap distance to less than 15 cm. This is attributed to the increased electron fluence and the presence of secondary particles, including secondary protons, electrons, neutrons, and photons, emanating from the material of the RS, in agreement with Kern et al. [6] and Wang et al. [3].

V. CONCLUSION

Ensuring the more accurate determination of surface dose is a crucial process for enhancing treatment efficacy and safety. The use of corrective factors to adjust surface dose values obtained from detectors to suit the conditions of Proton Pencil Beam Therapy can help improve result accuracy. A comprehensive analysis of correction factors, air gap variations, and the influence of Range Shifter thickness provides valuable insights into optimizing surface dose measurements for proton therapy. The nuanced responses observed in different scenarios emphasize the importance of selecting appropriate detectors and configurations based on specific experimental conditions and proton energy levels.

REFERENCES

[1] DeCesaris CM, Rice SR, Bentzen SM, Jatczak J, Mishra MV, Nichols EM. Quantification of Acute Skin Toxicities in Patients With Breast Cancer Undergoing Adjuvant Proton versus Photon Radiation Therapy: A Single Institutional Experience. International Journal of Radiation Oncology*Biology*Physics. 2019 Aug;104(5):1084–90.

[2] Faithfull S, Hilton M, Booth DK. Survey of information leaflets on advice for acute radiation skin reactions in UK radiotherapy centres: a rationale for a systematic review of the literature. European Journal of Oncology Nursing. 2002 Sep;6(3):176–8.

[3] Wang M, Zhang L, Zheng J, Li G, Dai W, Dong L. Investigating the effects of a range shifter on skin dose in proton therapy. Nuclear Engineering and Technology. 2023 Jan 1;55(1):215–21.

[4] Measurements IC. Report 39: determination of dose equivalents resulting from external radiation sources, part 1. J Int Comm Radiat Units Meas. 1985.

[5] Kern A, Bäumer C, Kröninger K, Mertens L, Timmermann B, Jörg Walbersloh, et al. Determination of surface dose in pencil beam scanning proton therapy. Medical Physics. 2020 May 1;47(5):2277–88.

[6] Kern A, Bäumer C, Kröninger K, Wulff J, Timmermann B. Impact of air gap, range shifter, and delivery technique on skin dose in proton therapy. Medical Physics. 2021 Feb 1;48(2):831–40.

Contacts of the corresponding author:
Author: Mintra Keawsamur, Ph.D.
Institute: Faculty of Medicine,
Chulalongkorn University
Street: Rama IV Rd.
City: Bangkok
Country: Thailand
Email: mintra.ke@chula.ac.th

Full Papers: *Medical Imaging*

Assessment of patient radiation dose and image quality for trans-arterial chemoembolization from digital subtraction angiography combined with IVR-CT

Boonsuan S[1,2], Asavaphatiboon S[2*], Tangboonduangjit P[2], Sodkokkruad P[2], Chaknam K[2]

1 Master of Science Program in Medical physics, Department of Diagnostic and Therapeutic Radiology, Faculty of Medicine Ramathibodi Hospital, Mahidol University, Bangkok, Thailand.
2 Department of Diagnostic and Therapeutic Radiology, Faculty of Medicine, Ramathibodi Hospital, Mahidol University, Bangkok, Thailand

**Corresponding author: sawwanee.medphy@gmail.com*

Abstract — **This research aimed to assess the patient radiation doses and image quality for TACE procedures from digital subtraction angiography (DSA) combined with Interventional radiology-CT (IVR-CT). The patient's radiation dose was collected between January 2022 and December 2022. To evaluate the Angio-CT's dose parameters regarding dose-area-product (DAP), fluoroscopy time, and dose-length-product (DLP). IVR-CT can adjust the parameters in 3D SURE Exposure^{TM} and the level of AIDR iterative reconstruction algorithm. Then, the optimal parameter related to radiation dose is used to reduce stochastic risk. This study evaluated the image quality in the CT model PBU-60 KYOTO KAGAKU phantom according to image noise, signal-to-noise ratio (SNR), and contrast to noise ratio (CNR). The results shown in the patient radiation dose in the average dose area product (DAP) and dose length product (DLP) from TACE's procedure combined with IVR-CT were about 413.94 ± 237.59 Gy.cm^2 (range: 84.42-1145.61 Gy.cm^2) and 665.65 ± 318.78 mGy.cm (range: 294.70- 1730.80 mGy.cm), respectively. The result showed that the low SURE Exposure^{TM} with strong AIDR reconstruction algorithm demonstrated a lower radiation dose than the routine protocol in 30.06% (p-value <0.001) with a statistically significant difference. At the same time, this protocol showed the image quality regarding the insignificant difference in image noise (p-value>0.05). Still there was a significant change in the SNR of liver area (p-value =0.046). In conclusion, the variation of SURE Exposure^{TM} affects the radiation dose in contrast to AIDR iterative reconstruction, which improves the SNR and CNR when using the strong level. This study suggested that the low SURE Exposure^{TM} with a strong level of AIDR iterative reconstruction can maintain the image quality and decrease the radiation dose by 30.06% with reduced stochastic risk.**

Keywords — **Interventional Radiology, Trans-arterial Catheter Chemoembolization, Angiography- Computed Tomography, Radiation dose, Image quality.**

I. INTRODUCTION

Trans-arterial chemoembolization (TACE) combined with IVR-CT helps detect the supplied arteries in the liver tumor. However, the combined modality can get more radiation doses. The optimal protocol can decrease the radiation dose and improve image quality following "ALARA". The parameters can adjust of the hybrid angiography with Canon© medical systems (Toshiba©) model Infinix-i^{4D}CT with Aquilion LB in 3D SURE Exposure^{TM} and the AIDR iterative reconstruction level. This study investigated those parameters to evaluate the radiation dose and image quality in image noise, SNR and CNR (1) at the Vascular and Interventional Radiology Unit of King Chulalongkorn Memorial Hospital.

II. MATERIALS AND METHODS

A total of sixty-six examinations of the retrospectively TACE's patient data were collected from the PACS Synapse® for IVR-CT data from January 2022 to December 2022. The inclusion criteria were the patient's age ≥ 30 and

patient weight with a standard size of 60±15 kg. The type of tumor was HCC, which used lipiodol drug vector for liver tumor embolization. The patient dose received by IVR-CT all range of abdominal scans for HCC arterials diagnostic in the phase of portal-arterial phase, hepatic arterial phase, and scanned for post embolization at the end of procedures was from Radimetrics™ dose management software. The radiation dose of the TACE procedure in terms of Air-KERMA at the interventional reference point, Ka,r (Gy), and dose-area product, DAP (Gy.cm^2) were also gathered. The routine IVR-CT protocol is shown in Table 1.

Table 1. *The routine protocol in TACE procedure for IVR-CT*

Parameter	Routine Protocol
kVp	120
mA range	TCM* (200-250)
Rotation time (s)	0.5
Pitch factor	0.938
Collimation (mm)	0.5 x 16
Image thickness (mm)	2
SURE Exposure™	Standard dose
Reconstruction algorithm	FC19
Iterative Reconstruction	AIDR 3D Strong
Display FOV (mm)	400
Wedge filter type	Large (L)

* TCM = tube current modulation; maximum and minimum values

The 3D SURE Exposure™ automatic tube current control (off, low, standard, quality, and high) and level of AIDR iterative reconstruction algorithm (mild, standard, and strong level) were varied and acquired three times using the Whole-Body Phantom model PBU-60 KYOTO KAGAKU phantom. Then, the data of each variable protocol was compared to the routine protocol regarding the radiation dose and image quality in with image noise, SNR and CNR using a pair t-test with a p-value ≤0.05, which was considered statistically significant.

III. RESULTS

A. Retrospective TACE's patient radiation dose

A retrospective patient dose, including fluoroscopic series and time of TACE procedure, is demonstrated in Table 2. The dose area product (DAP) and dose length product (DLP) ranges were 84.42-1145.61 Gy.cm^2 and 294.7-1730.8 mGy.cm, respectively.

Table 2. *The retrospective TACE's patient radiation dose*

Dose Metrics	
total DAP for fluoroscopy (Gy.cm^2)	413.94 ± 237.59
total DLP (mGy.cm)	665.65 ± 318.78
total AIR KERMA for fluoroscopy (Gy)	3.06 ± 2.15
no.of DSA series	24
fluoroscopy time (min)	57.18

B. Radiation dose analysis of variable protocols in phantom

The main parameter that affected the radiation dose of IVR-CT was SURE Exposure™ automatic tube current control (ATCM). The results showed that the ATCM with low compared to the routine protocol with standard had the lowest average DLP (about -30%), as shown in Figure 1.

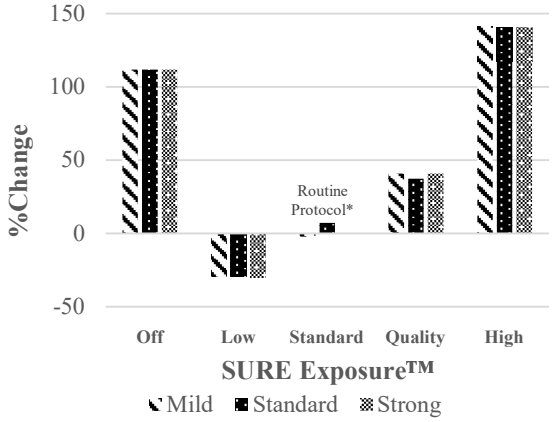

Figure 1. *The percentage change of each variable ATCM in IVR-CT compared to the routine protocol.*

C. Quantitative image assessment of variable protocols in phantom

Quantitative image assessment of liver area in terms of noise, SNR, and CNR was evaluated using PACS Synapse®, as shown in Table 3. The result showed that the AIDR iterative reconstruction algorithm with strong level had the lowest image noise and the highest SNR and CNR in all SURE Exposure™ techniques.

The image noise results showed a significant difference from the routine protocols found in low and standard ATCM using mild AIDR level and high ATCM using strong AIDR level with P-values 0.011, 0.049, and 0.047, respectively. In contrast to the SNR, there was a significant change in only low ATCM with mild ADIR level (p-value = 0.046) and no significant difference in CNR of all variable protocols. These results showed that the high ATCM technique with strong AIDR level had the lowest noise.

Table 3. *The mean ± SD of the quantitative image in terms of image noise, SNR, and CNR in each variable protocol with the percentage change and P-value.*

SURE Exposure	AIDR	Noise	% Change	P-value	SNR	% Change	P-value	CNR	% Change	P-value
Off	Mild	11.12 ± 2.78	5.28	0.776	6.99 ± 2.37	- 0.38	0.987	3.34 ± 0.67	1.39	0.949
	Standard	9.47 ± 1.94	-10.40	0.455	8.11 ± 1.95	15.49	0.434	3.70 ± 0.43	12.40	0.406
	Strong	8.95 ± 2.65	-15.31	0.437	8.83 ± 3.55	25.72	0.475	4.09 ± 1.00	24.31	0.420
Low	Mild	15.88 ± 0.69	50.32	0.011	4.69 ± 0.09	- 33.16	0.031	2.10 ± 0.23	-36.16	0.062
	Standard	13.63 ± 1.23	28.95	0.105	5.42 ± 0.35	- 22.81	0.130	2.33 ± 0.31	-29.09	0.140
	Strong	10.38 ± 0.37	-1.81	0.628	7.16 ± 0.42	1.94	0.046	3.37 ± 0.34	2.30	0.839
Standard	Mild	14.64 ± 0.85	38.57	0.049	5.21 ± 0.24	- 25.73	0.076	2.80 ± 0.39	-14.92	0.097
	Standard	12.33 ± 0.45	16.69	0.249	5.99 ± 0.26	- 14.68	0.223	2.38 ± 0.18	-27.46	0.345
	Strong*	**10.57 ± 0.84**	**-**	**-**	**7.02 ± 0.80**	**-**	**-**	**3.29 ± 0.71**	**-**	**-**
Quality	Mild	12.01 ± 0.65	13.70	0.166	6.27 ± 0.52	- 10.75	0.329	3.80 ± 1.53	15.50	0.712
	Standard	11.38 ± 0.85	7.69	0.392	6.58 ± 0.60	- 6.23	0.053	3.30 ± 0.38	0.22	0.966
	Strong	9.50 ± 1.21	-10.09	0.459	7.91 ± 1.17	12.64	0.514	3.95 ± 0.67	19.94	0.459
High	Mild	10.38 ± 0.40	-1.74	0.779	7.18 ± 0.48	2.31	0.818	3.43 ± 0.11	4.13	0.727
	Standard	8.94 ± 1.37	-15.36	0.286	8.42 ± 1.52	19.98	0.337	4.28 ± 0.38	30.09	0.257
	Strong	7.66 ± 0.37	-27.52	0.047	9.64 ± 0.41	37.25	0.064	4.68 ± 0.76	42.35	0.162

* The routine protocol was using the standard SURE Exposure™ with strong level of AIDR reconstruction algorithm.

IV. DISCUSSION

The TACE combined IVR-CT procedure had more radiation doses when using two modalities. So, it needs to be concerned and observe skin reactions or erythema. From Table 2, the radiation dose results demonstrated a high standard deviation, meaning there were more procedure variations (range of DAP and DLP: 84.42-1145.61 Gy.cm^2 and 294.70-1730.80 mGy.cm, respectively) due to the complicated case or more feeding arteries.

The phantom study the radiation dose of IVR-CT when using low SURE Exposure™ ATCM can reduce radiation dose by about 29-30% (p-value < 0.001), with a difference significant statistically from the routine protocol (standard). Similar to the studies of Sulieman et al. (2) with fixed tube potential (120 kVp) and using low SURE Exposure™ found that Sure Exposure™ with low-dose techniques provided without compromising image quality, with a mean dose reduction of up to 48% achievable using this protocol.

The results showed that the AIDR iterative reconstruction algorithm with a strong level reduced image noise and increased the

SNR and CNR compared to the other algorithms in all SURE Exposure™ techniques. These findings were the same as the studies of Milim Kim et al. (3); their results showed that the strong AIDR reconstruction technique improved CNR in all size phantoms in a range of 45-114% ($p < 0.05$). Like Kristin Jensen et al.'s study (4), the iterative reconstruction algorithms enhanced CNR in AIDR 3D providers by 0.8 to 5.2 and reduced noise by 29-67% when used with stronger techniques.

This study also demonstrated that the low SURE Exposure™ with a strong AIDR level algorithm could reduce the radiation dose by 30% and maintain the image noise, SNR, and CNR near the routine protocol. Therefore, it should be the optimal protocol for decreasing the patient radiation dose in TACE procedure using digital subtraction angiography (DSA) combined with Interventional Radiology-CT (IVR-CT).

V. CONCLUSION

It concludes that the variation of SURE Exposure™ affects the radiation dose in contrast to AIDR iterative reconstruction, which improves the SNR and CNR when using the strong level. The suggested protocol to compromise the radiation dose and image quality is the low SURE Exposure™ with a strong AIDR level algorithm. However, this study was based on the phantom; this optimal protocol should be conducted with the patient to evaluate the image quality.

ACKNOWLEDGEMENTS

The authors would like to thank the interventional radiological technologists and the medical physicist team at the unit of vascular and interventional radiology, King Chulalongkorn Memorial Hospital for the support on this research.

REFERENCES

[1] Månsson L. Methods for the Evaluation of Image Quality: A Review. Radiation Protection Dosimetry. 2000;90.

[2] Sulieman A, Adam H, Elnour A, Tamam N, Alhaili A, Alkhorayef M, et al. Patient radiation dose reduction using a commercial iterative reconstruction technique package. Radiation Physics and Chemistry. 2021;178:108996.

[3] Kim M, Lee JM, Yoon JH, Son H, Choi JW, Han JK, et al. Adaptive iterative dose reduction algorithm in CT: effect on image quality compared with filtered back projection in body phantoms of different sizes. Korean J Radiol. 2014;15(2):195-204.

[4] Jensen K, Martinsen A, Tingberg A, Aaløkken M, Fosse E. Comparing five different iterative reconstruction algorithms for computed tomography in an ROC study. European radiology. 2014;24.

Contacts of the corresponding author:
Author: Dr. Sawwanee Asavaphatiboon
Institute: Mahidol University
Street: Rama VI Road
City: Bangkok
Country: Thailand
Email: sawwanee.medphy@gmail.com

Optimal dual-time-point dynamic ^{68}Ga-PSMA-11 PET/CT protocols for parametric imaging generation in prostate cancer patients

Burasothikul Paphawarin[1,2,3,*], Navikhacheevin Chatchai[4], Pasawang Panya[4], Sontrapornpol Tanawat[4], Sukprakun Chanan[5], Khamwan Kitiwat[1,3,5]

1 Medical Physics Program, Department of Radiology, Faculty of Medicine, Chulalongkorn University, Bangkok, Thailand
2 School of Radiological Technology, Faculty of Health Science Technology, HRH Princess Chulabhorn College of Medical Science, Bangkok, Thailand
3 Chulalongkorn University Biomedical Imaging Group, Department of Radiology, Faculty of Medicine, Chulalongkorn University, Bangkok, Thailand
4 Division of Nuclear Medicine, King Chulalongkorn Memorial Hospital, Bangkok, Thailand
5 Division of Nuclear Medicine, Department of Radiology, Faculty of Medicine, Chulalongkorn University, Bangkok, Thailand

**Corresponding author: paphawarin.bur@gmail.com*

Abstract — **This study aimed to investigate the optimal dual-time-point dynamic ^{68}Ga-PSMA-11 PET/CT protocols for generating parametric imaging for patients diagnosed with prostate cancer. Fifteen prostate cancer patients were intravenously administered ^{68}Ga-PSMA-11 of 181.9 ± 47.2 MBq, and a 60-min dynamic PET/CT scan was acquired immediately after injection using Biograph Vision 600 PET/CT system. List-mode data were reconstructed into 25 time-frames, including intervals of 6 × 10 s, 8 × 30 s, and 11 × 300 s, and were corrected for motion and partial volume effect. Dual-time-point protocols, involving 5-min intervals and 10-min intervals, with a time interval of at least 30 min, were employed to generate parametric images. Net influx rates (K_i) were derived by fitting a two-tissue compartmental model, and lesion-to-background ratios (LBRs) of K_i images and standardized uptake value (SUV) images were computed. The 5-10 min coupled with 40-45 min dual-time-point protocol indicated the highest intraclass correlation coefficient (ICC) of 0.988 compared to 60-min K_i while the 0-5 min with 55-60 min and 0-10 min with 50-60 min showed the ICC values of 0.941. The LBRs of 60-min K_i, 5-10 min with 40-45 min K_i, 0-5 min with 55-60 min K_i, 0-10 min with 50-60 min K_i, SUV_{mean}, and SUV_{max} were 29.53 ± 27.33, 13.05 ± 15.28, 45.15 ± 53.11, 45.52 ± 70.31, 19.77 ± 23.43, and 25.06 ± 30.07, respectively. The optimal dual-time-point parametric imaging exhibits superior image contrast compared to SUV imaging. The dual-time-point protocols at 0-5 min with 55-60 min and 0-10 min with 50-60 min achieve image quality comparable to standard 60-min parametric imaging.**

Keywords — **kinetic modeling, 2-tissue compartmental model, parametric imaging, dynamic ^{68}Ga-PSMA-11 scan, prostate cancer, dual-time-point protocol**

I. INTRODUCTION

An analysis utilizing voxel-wise kinetic modeling with dynamic PET data can generate a parametric image containing diverse physiological factors, including blood perfusion, receptor binding potential, and metabolic activity. This enhances detection efficiency, provides accurate quantitative measurements, and enables earlier treatment response assessment [1]. However, the lengthy dynamic imaging protocol limits the clinical application of parametric imaging. Dual-time-point (DTP) parametric imaging with a population-based input function (PBIF) in ^{18}F-FDG provides a higher correlation with a 60-min net influx rate (K_i) compared to relative standardized uptake value (SUV) change [2]. This study aimed to investigate the optimal dual-time-point dynamic ^{68}Ga-PSMA-11 PET/CT protocols for parametric imaging in patients diagnosed with prostate cancer and to investigate the usefulness of the parametric K_i image through lesion-to-background ratio (LBR) evaluation in comparison to the SUV image.

II. MATERIALS AND METHODS

Fifteen prostate cancer patients, averaging 71.6 ± 10.3 years in age and 68.2 ± 12.3 kg in weight, participated in a cross-sectional paired study. The mean prostate-specific antigen (PSA) was 23.82 ± 30.42 ng/mL. Exclusions applied to those unable to undergo a 60-min dynamic PET/CT scan or currently on anticoagulant therapy. This study was approved by the Institutional Review Board of the Faculty of Medicine, Chulalongkorn University.

A. PET/CT scanning protocol

The patients received an intravenous administration of 181.9 ± 47.2 MBq of ^{68}Ga-PSMA-11 and underwent immediate 60-min dynamic PET/CT imaging over the pelvis using a Biograph Vision 600 PET/CT scanner. The list-mode data were reconstructed and binned into 25 time-frames (6 × 10 s, 8 × 30 s, and 11 × 300 s) using the ordered subset expectation maximization (OSEM) algorithm (4 iterations and 5 subsets) with point spread function (PSF) correction and time-of-flight (TOF). A routine static PET/CT scan at 60-min post-injection was acquired with continuous-bed-motion acquisition. Low-dose CT was applied for image acquisition, and the reconstruction protocol matched the dynamic data used to generate an SUV image, with corrections for decay, attenuation, and scatter.

B. Image-derived input functions

The correction for patient motion was applied to the dynamic data, and 10-mm diameter sphere regions of interest (ROIs) were drawn at the right common iliac artery to extract the time-activity curve (TAC) used as an image-derived input function (IDIF). Since a small vessel region was used, the IDIF was further corrected for partial volume effect (PVE) using a volume of interest (VOI)-based method in PMOD software version 4.101 as shown in Figure 1.

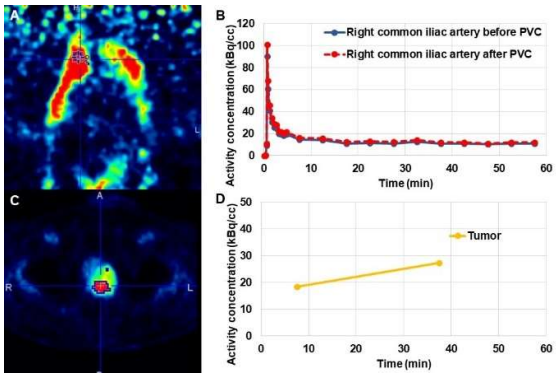

Figure 1. *3D ROI delineation of the right common iliac artery (A), image-derived input function (IDIF) without partial volume effect (PVE) correction (B, blue solid line), IDIF with PVE correction (B, red dashed line), 3D ROI delineation of the tumor (C), and the time-activity curve of dual-time-point tumor (D).*

C. Parametric imaging generation

DTP parametric images were generated using different 27 protocols involving 5-min intervals (0-25 min and 30-55 min) [2] and 10-min intervals (0-20 min and 30-50 min), with a time interval of at least 30 min. 3D iso-contouring ROIs were delineated over the tumor, setting a threshold at 40% of the maximum intensity to acquire the TAC of the tumor (Figure 1).

The irreversible two-tissue (2T) compartmental model (Figure 2) with the basic function method (BFM) [3] was utilized to generate the DTP K_i image. The model can be described as below [4]:

$$\frac{dC_1(t)}{dt} = K_1 C_P(t) - (k_2 + k_3) C_1(t) \quad (1)$$

$$\frac{dC_2(t)}{dt} = k_3 C_1(t) \quad (2)$$

where C_p is tracer concentration in whole blood, C_1 is the non-specifically bound tissue compartment, C_2 is the PSMA-specifically bound tissue compartment, K_1 is the tracer transport rate from blood to tissue, k_2 is the transport rate from tissue to blood, and k_3 is the transport rate between tissues.

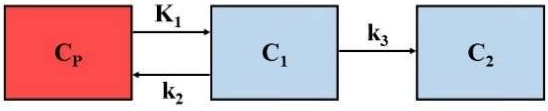

Figure 2. *The irreversible two-tissue (2T) compartmental model for model fitting.*

The minimum chi-square discrepancy of the voxel-wise model fitting resulted in kinetic rate constants in terms of K_1, k_2, and k_3 for each voxel, which is used for K_i calculation as follows [5]:

$$K_i = \frac{K_1 k_3}{k_2 + k_3} \quad (3)$$

where K_i is the net influx rate, K_1 is the tracer transport rate from whole blood to tissue, k_2 is the transport rate from tissue to whole blood, and k_3 is the transport rate between tissues.

To verify DTP K_i accuracy, the parametric K_i images using 60-min dynamic data were generated to obtain the 60-min K_i. The 3D ROI contouring and the model-fitted approach were identical to the DTP parametric imaging.

The 3D ROIs were drawn over the muscle to measure the K_i of the identical background area for both the SUV and parametric images [6], enabling the calculation of the LBRs for K_i, mean SUV (SUV_{mean}), and maximum SUV (SUV_{max}) as follows:

$$LBR_{parameter} = \frac{Mean\ pixel\ value_{lesion}}{Mean\ pixel\ value_{bg}} \quad (4)$$

where $LBR_{parameter}$ is the lesion-to-background ratio of the K_i or SUV, $mean\ pixel\ value_{lesion}$ is the measured mean pixel value over the lesion area, and $mean\ pixel\ value_{bg}$ is the measured mean pixel value over the muscle area.

D. Statistical analysis

The reliability between DTP K_i and 60-min K_i was assessed using the intraclass correlation coefficient (ICC). The optimal DTP protocols were determined based on the ICC and LBR.

III. RESULTS

The 5-10 min coupled with 40-45 min achieved the highest ICC of 0.988 for the 5-min DTP, while the 10-20 min interval with 40-50 min exhibited the highest ICC of 0.959 for the 10-min DTP parametric imaging protocol. In contrast, the lowest ICC value of 0.685 was found in the 0-5 min with 30-35 min DTP protocol as shown in Figure 3.

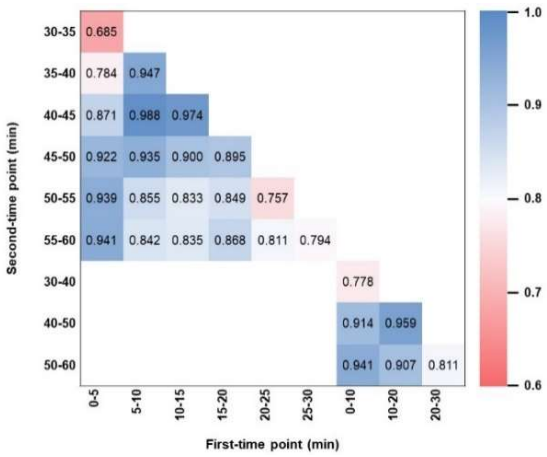

Figure 3. *Correlation heatmap of intraclass correlation coefficients between net influx rates (K_i) obtained from the dual-time-point (DTP) and 60-min parametric images.*

The LBR of 60-min K_i image was 29.53 ± 27.33 which is superior to SUV_{mean} and SUV_{max} of 19.77 ± 23.43 and 25.06 ± 30.07, respectively (Figure 4). The DTP protocols that ranked within the 3rd quartile of ICC also shown in the figure, including the 0-5 min with 55-60 min, 5-10 min with 35-40 min, 5-10 min with 40-45 min, 10-15 min with 40-45 min, 0-10 min with 50-60 min, and 10-20 min with 40-50 min DTP protocols.

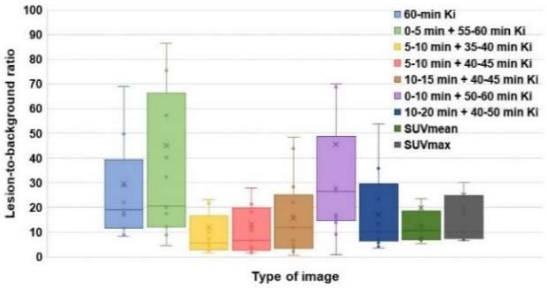

Figure 4. *Box plot of lesion-to-background ratios (LBRs) of the 60-min parametric K_i images, various 5-min and 10-min dual-time-point (DTP) parametric K_i images, mean SUV images, and maximum SUV images.*

To enhance the protocol for clinical use, The DTP protocols with high ICC and optimal LBR were selected. Thus, the DTP protocols of 0-5 min with 55-60 min, and 0-10 min with 50-60 min were identified as the recommended 5-min and 10-min optimal DTP parametric imaging in this study as shown in Figure 5.

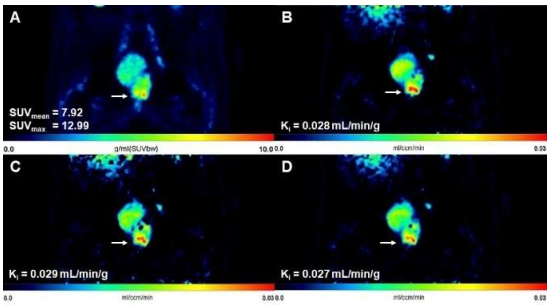

Figure 5. *Coronal images of a prostate cancer patient. The SUV image (A), 60-min parametric K_i image (B), 5-min DTP parametric K_i image (C), and 10-min DTP parametric K_i images (D).*

IV. DISCUSSION

This study investigated optimal DTP parametric imaging for prostate cancer patients using dynamic ^{68}Ga-PSMA-11 PET/CT. The protocols of 0-5 min with 55-60 min and 0-10 min with 50-60 min showed superior K_i accuracy and LBR.

The ICCs between DTP K_i and 60-min K_i showed excellent reliability, exceeding or equal to 0.9 in 12 of 27 protocols. The reliability improves as the extended time interval between DTP increases, aligning with the finding of Wu et al. [2]. The parametric K_i images demonstrated a 1.49 times enhancement in LBR compared to SUV images, consistent with a previous study [6]. Using the 10-min DTP approach reduced image noise, likely due to the extended dynamic time-frames and the lower muscle K_i compared to the 5-min DTP protocol. The late first-time points exhibited higher LBRs, consistent with the reported optimal uptake time of 60 min post-injection. Additionally, plasma-to-blood ratio correction is recommended. Further studies are suggested to investigate the reliability of the DTP protocols integrating the plasma-to-blood ratio. To apply DTP parametric imaging clinically, accurate kinetic parameters require image registration, motion correction between the two scans, as well as a PBIF due to the absence of entire 60-min dynamic data.

V. CONCLUSION

The optimal DTP parametric imaging accurately estimates K_i, comparable to 60-min parametric imaging, and offers superior image quality compared to routine SUV images. This improves prostate cancer detection efficiency, overcoming challenges of lengthy acquisition protocols while maintaining image quality.

ACKNOWLEDGEMENTS

The authors acknowledge the support from the team at the Division of Nuclear Medicine, Department of Radiology, King Chulalongkorn Memorial Hospital. The authors also express sincere gratitude to Prof. Dr. Guobao Wang from UC Davis for valuable suggestions in this study.

REFERENCES

[1] Wang G, Rahmim A, Gunn RN. PET parametric imaging: past, present, and future. IEEE Trans Radiat Plasma Med Sci. 2020;4(6):663-75.

[2] Wu J, Liu H, Ye Q, Gallezot JD, Naganawa M, Miao T, et al. Generation of parametric K_i images for FDG PET using two 5-min scans. Med Phys. 2021;48(9):5219-31.

[3] Hong YT, Fryer TD. Kinetic modelling using basis functions derived from two-tissue compartmental models with a plasma input function: general principle and application to [^{18}F]fluorodeoxyglucose positron emission tomography. Neuroimage. 2010;51(1):164-72.

[4] Dimitrakopoulou-Strauss A, Pan L, Sachpekidis C. Kinetic modeling and parametric imaging with dynamic PET for oncological applications: general considerations, current clinical applications, and future perspectives. Eur J Nucl Med Mol Imaging. 2021;48:21-39.

[5] Sokoloff L, Reivich M, Kennedy C, Rosiers MHD, Patlak CS, Pettigrew KD, et al. The [^{14}C]deoxyglucose method for the measurement of local cerebral glucose utilization: theory, procedure, and normal values in the conscious and anesthetized albino rat. J Neurochem. 1977;28(5):897-916.

[6] Chen R, Ng YL, Zhao H, Ge Q, Shi F, Cao K, et al. Quantitative parametric imaging added diagnostic values in lesion detection of ^{68}Ga-PSMA-11 in prostate cancer patients identified by dynamic total-body PET/CT. J Nucl Med. 2022;63(suppl 2):2584.

Contacts of the corresponding author:
Author: Paphawarin Burasothikul
Institute: Department of Radiology, Faculty of Medicine, Chulalongkorn University
Street: Rama IV Road
City: Bangkok
Country: Thailand
Email: paphawarin.bur@gmail.com

Accuracy of ^{177}Lu quantification for dosimetry calculation using 12-swiveling CZT detectors SPECT/CT camera

Damthongsen Panattha[1*], Pasawang Panya[2], Sontaraponpol Tanawat[2], Phromphao Benchamat[2], Noipinit Nut[2], Sawatnatee Thunyaluk[2] and Khamwan Kitiwat[1,2]

1 Medical Physics Program, Department of Radiology, Faculty of Medicine, Chulalongkorn University, Pathumwan, Bangkok 10330, Thailand

2 Division of Nuclear Medicine, Department of Radiology, Faculty of Medicine, Chulalongkorn University and King Chulalongkorn Memorial Hospital, Pathumwan, Bangkok 10330, Thailand

**Corresponding author: 6570049330@student.chula.ac.th*

Abstract — **This study aimed to determine the accuracy of ^{177}Lu quantification through an IEC/NEMA phantom study and to evaluate total-body dosimetry in patients undergoing ^{177}Lu therapy using 12-swiveling digital CZT detectors SPECT/CT camera. The NEMA/IEC body phantom inserted with six fillable spheres filled with ^{177}Lu solution of 9.6:1 for target-to-background ratio was acquired by the VERITON-CT at 0.5, 24, 144, and 168 hr post-injection, with a photopeak energy of 113 keV, and ±10% scatter window. The activity concentration was measured in each sphere and compared with known activity. The total-body SPECT/CT images were acquired at 4, 24, and 48 h post-injection, with scan duration of 28 min in four patients who received either ^{177}Lu-DOTATATE or ^{177}Lu-PSMA treatment. SPECT images were reconstructed using quantitative algorithm, and scatter correction was applied. The time-integrated activity (TIA) and absorbed dose in kidneys, liver, spleen, bone marrow, salivary glands, and tumors were calculated according to the Medical Internal Radiation Dose (MIRD) scheme using the voxel S-value convolution (VSV) method. The phantom study demonstrated a good agreement between measured and calculated activity concentrations in the largest sphere over 0.5 to 168 hr post-injection. For clinical study, the absorbed dose coefficients in whole-body, liver, kidneys, spleen, salivary glands, bone marrow and tumors for ^{177}Lu-DOTATATE patients were 0.08, 1.00, 0.78, 0.36, 0.03, 0.02, and 1.77 Gy/GBq, respectively and ^{177}Lu-PSMA patients were 0.05, 0.25, 0.71, 0.13, 0.45, 0.04 and 0.34 Gy/GBq, respectively. The 12-swiveling digital CZT detectors SPECT/CT can provide accurate quantification for determining the dosimetry in clinical study.**

Keywords — **12-swiveling CZT detectors, Quantitative ^{177}Lu SPECT, Theranostics, MIRD, VSV-based dosimetry**

I. INTRODUCTION

A commercially introduced 12-cadmium zinc telluride (CZT) based digital detectors SPECT/CT represents advanced technology that outperforms conventional cameras. This system offers higher sensitivity, count rate performance, reduced acquisition time, and total activity. It improves photon detection and image quality through advanced reconstruction techniques which facilitates fully digital tomographic examinations, capturing photons more effectively and leading to improved image contrast and lesion detection [1]. Prior using the state-of-the-art gamma camera for internal dosimetry calculations for clinical studies, it is crucial to evaluate its feasibility and potential benefits. This study aimed to determine the accuracy of ^{177}Lu SPECT quantification through in vitro studies and subsequently evaluating dosimetry in patients for clinical studies.

II. MATERIALS AND METHODS

A. IEC/NEMA phantom study

The uniform cylindrical phantom filled with ^{177}Lu solution of 1.22 GBq was firstly acquired to calibrate the ^{177}Lu standardized uptake value (SUV) for determining the SUV correction factor. Then, the IEC/NEMA

phantom with inserted six fillable spheres with inner diameters of 10, 13, 17, 22, 28, and 37 mm was acquired using the VERITON-CT 12-swiveling CZT detectors SPECT/CT (Spectrum Dynamics Medical), and the conventional camera, GE Discovery NM 670, at the Division of Nuclear Medicine, King Chulalongkorn Memorial Hospital (KCMH).

Fig. 1 *The IEC/NEMA phantom acquired by12-swiveling CZT detectors SPECT/CT and conventional camera.*

The phantom was filled with ^{177}Lu solution of 9.6:1 for target-to-background ratio (99.16 kBq/mL in background). The phantom was acquired in each time point for 10 minutes during 0.5-168 hr post injection (p.i.), with photopeak energy of 113 keV and a ±10% scatter window for the VERITON-CT, and photopeak energy of 113 keV and 208 keV for Discovery NM 670. The SPECT images were then reconstructed using two sets of reconstruction parameters: quantitative reconstruction (OSEM, 12i8s, with scatter correction) and visualization reconstruction (OSEM, 4i8s with no scatter correction).

B. Evaluation of ^{177}Lu quantification

To measure the activity concentration in the unit of Bq/mL, the 3D regions of interest (ROIs) were manually drawn in each sphere and 12 background ROIs on the phantom images. Subsequently, the measured activity concentration (AC) and the percentage difference (%diff) [2] were calculated for both the spheres and the background at each time point using the following equations:

$$AC = AC_0 e^{-\frac{\ln 2}{T_{1/2}} \times t} \quad (1)$$

where AC is the measured activity concentration in spheres and background at each time point (Bq/mL). AC_0 is the initial activity concentration in spheres and background (Bq/mL), $T_{1/2}$ is the ^{177}Lu physical half-life, and t is time interval from initial time to each time point. The difference between the measure and known activity can be calculated using equation as the followings:

$$\%diff = \frac{A_{measured} - A_{known}}{A_{known}} \times 100 \quad (2)$$

where $A_{measured}$ is the measured activity concentration in spheres and background, A_{known} is the known activity concentration in spheres and background. The percentage difference of activity concentration values should be within 10% according to the recommendation in MIRD Pamphlet No.23 [3].

C. Clinical study

This retrospective study was approved by the Institutional Review Board of the Faculty of Medicine, Chulalongkorn University. The total-body SPECT/CT images of 4 patients treated with either ^{177}Lu-DOTATATE for neuroendocrine tumors or ^{177}Lu-PSMA for prostate cancer were acquired using 12-swiveling CZT detectors SPECT/CT with a photopeak energy of 113 keV with ±10% scatter window. The acquisition scanning protocol consisted of 6 bed positions with scan duration of 28 min from vertex to feet at 2-4, 24-, and 48-hr p.i. according to routine dosimetry protocol at KCMH (Figure 2).

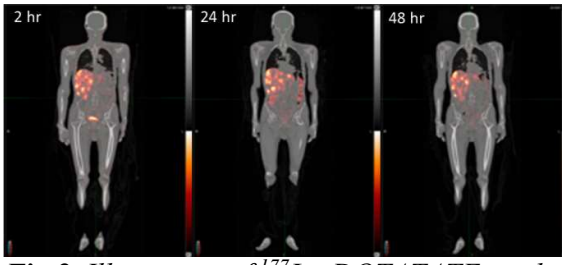

Fig 2. *Illustration of ^{177}Lu-DOTATATE total-body SPECT/CT images at 2, 24, and 48 h post injection acquired by 12-swiveling CZT detectors SPECT/CT camera.*

D. Dosimetry calculation

The 3D ROIs were manually drawn in 7 source organs using MIM SurePlan™ MRT software as the followings: whole body, kidneys, liver, spleen, salivary glands, bone marrow, and tumors. The time-integrated activity (Ã) in each source tissue was determined based on voxel-based dosimetry, obtained by measuring the area under the curve of the time-activity curve (TAC) within the

voxel-source region. The absorbed doses in the target organ and tumors using voxel S-value convolution (VSV) method, described by the MIRD scheme Pamphlet No. 17 [4] were calculated based on the Monte Carlo simulation as follows:

$$\bar{D}(voxel_k) = \sum_{h=0}^{N} \tilde{A}(voxel_h) \cdot S(voxel_k \leftarrow voxel_h) \quad (3)$$

where $\bar{D}(voxel_k)$ is absorbed dose (Gy), $\tilde{A}(voxel_h)$ is time-integrated activity in a source voxel h region, and $S(voxel_k \leftarrow voxel_h)$ is the radionuclide-specific quantity defined as the mean absorbed dose to a target voxel per radioactive decay in a source voxel (mGy/MBq·s). The voxel S value can be calculated using equation as the followings:

$$S(voxel_k \leftarrow voxel_h) = \sum_i \Delta_i \frac{\emptyset_i(voxel_k \leftarrow voxel_h)}{m_{voxel_k}} \quad (4)$$

where Δ_i is the mean energy of radiation particle i per nuclear transition, $\emptyset_i (voxel_k \leftarrow voxel_h)$ is the absorbed fraction to target voxel k per emission of radiation particle i from within source voxel h, m_{voxelk} is the mass of tissue within target $voxel_k$.

III. RESULTS

Fig. 3 shows the results of the percentage difference of 37-mm diameter sphere in different reconstruction algorithms and machines. The difference obtained from the quantitative reconstruction ranged between -8% to 9% during the 0.5-168 hr after injection when acquired using the 12-CZT detectors SPECT/CT. The limit was within 10% according to the MIRD Pamphlet No.23. In contrast, other reconstructions showed larger percentage differences in the largest sphere.

The absorbed dose coefficient in various target organs and tumors are presented in Table 1. The absorbed dose coefficients for ^{177}Lu-DOTATATE patients were 0.08, 1.00, 0.78, 0.36, 0.03, 0.02, and 1.77 Gy/GBq for WB, liver, kidneys, spleen, salivary glands, bone marrow, and tumors respectively and the absorbed dose coefficients for ^{177}Lu-PSMA patients were 0.05, 0.25, 0.71, 0.13, 0.45, 0.04 and 0.34 Gy/GBq, for the WB, liver, kidneys, spleen, salivary gland, bone marrow, and tumors respectively. These absorbed doses did not reach the dose constraint for the liver (32 Gy), salivary gland (20 Gy), kidney (23 Gy), and bone marrow (2 Gy).

IV. DISCUSSION

The difference between -8% and 9% was obtained for the largest sphere of 37-mm diameter when reconstructing using the quantitative reconstruction method with 12i8s OSEM algorithm and scatter correction was applied. This difference was within the acceptable range of 10% according to the MIRD Pamphlet No.23, while other reconstruction methods showed larger percentage differences. The accuracy of quantification for ^{177}Lu SPECT related to the sphere size. The increased percentage differences are associated with smaller sphere sizes. This phenomenon was attributed to the partial volume effect, since smaller structures are more susceptible to inaccuracies in measurements due to limited spatial resolution.

In clinical study, the acquisition time for total-body scan was reduced by almost 3-fold compared with the conventional camera. It is essential for patients who cannot remain still for long periods. The absorbed doses in organs of this study were comparable with previous study [5]. The highest absorbed dose was found in the liver for ^{177}Lu-DOTATATE and the kidneys for ^{177}Lu-PSMA. The reasons behind that were ^{177}Lu-DOTATATE patients had ileal neuroendocrine tumor with liver and node metastasis. It was possible that there were residual tumors, but the absorbed dose in this study was lower than the planar method reported by Handayani et al. (1.17 Gy/GBq). For ^{177}Lu-PSMA patients, the absorbed dose for kidneys was affected from prostate cancer with multiple metastasis and could be associated with physiological uptake in kidneys, but it was still comparable to the study by Chatachot K et al. Therefore, this study indicated that the absorbed doses obtained from ^{177}Lu treatment did not reach the dose constraint and provided valuable personalized dosimetry.

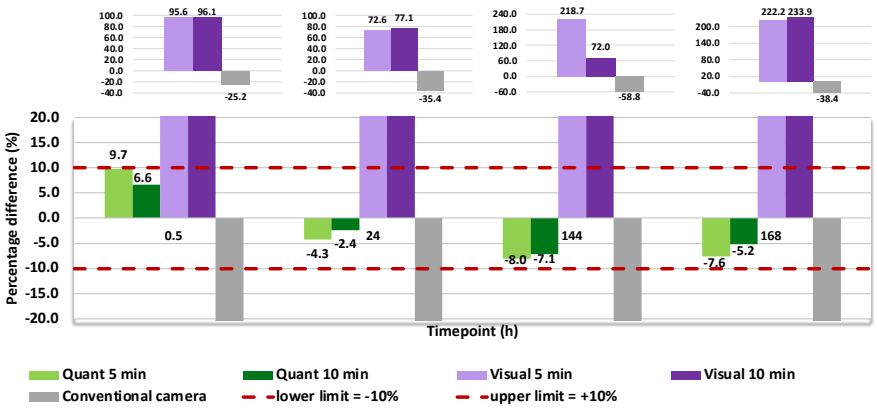

Fig 3. *Comparison of percentage differences of activity concentration obtained from different reconstruction algorithm and SPECT/CT machine.*

Table 1 *absorbed dose coefficient (Gy/GBq) of ^{177}Lu-DOTATATE and ^{177}Lu-PSMA.*

Treatment	Methods	WB	Liver	Kidneys	Spleen	Salivary glands	Bone marrow	Tumors
DOTATATE	MTP: VERITON (pt.1)	0.08	1.00	0.78	0.36	0.03	0.02	1.77
	MTP: GE (pt.1)	0.23	1.12	0.92	0.46	N/A	0.02	2.19
	STP: VERITON (pt.2)	0.07	0.73	0.46	0.56	0.03	0.02	1.17
PSMA	MTP: VERITON (pt.3)	0.05	0.25	0.71	0.13	0.45	0.04	0.34
	MTP: GE (pt.3)	0.06	N/A	0.99	N/A	N/A	0.05	0.05
	STP: VERITON (pt.4)	0.08	0.22	0.98	0.13	0.12	0.02	0.99

MTP – multiple time-point, STP – single time-point

V. CONCLUSION

This study demonstrates that the 12-swiveling digital CZT detectors SPECT/CT can provide an accurate quantification for ^{177}Lu SPECT images based on the IEC/NEMA phantom. This suggests its potential suitability for dosimetry calculations in radiopharmaceutical therapy for clinical studies. The use of 12-swiveling CZT detectors SPECT/CT in clinical studies also reduces acquisition time dramatically for whole-body SPECT/CT images compared to the conventional cameras.

REFERENCES

[1] Desmonts C, Bouthiba MA, Enilorac B, Nganoa C, Agostini D, Aide N. Evaluation of a new multipurpose whole-body CzT-based camera: comparison with a dual-head Anger camera and first clinical images. EJNMMI Physics 2020 Mar; 7:18.

[2] Sjögreen Gleisner K, Chouin N, Gabina PM, Cicone F, Gnesin S, Stokke C, et al. EANM dosimetry committee recommendations for dosimetry of ^{177}Lu-labelled somatostatin-receptor and PSMA-targeting ligands. Eur J Nucl Med Mol Imaging. 2022 May;49(6):1778-1809.

[3] Dewaraja YK, Frey EC, Sgouros G, Brill AB, Roberson P, Zanzonico PB, et al. MIRD Pamphlet No.23: Quantitative SPECT for Patient-Specific 3-Dimensional Dosimetry in Internal Radionuclide Therapy. J Nucl Med. 2012 Jun;53(8):1310-1325.

[4] Bolch W, Bouchet L, Robertson J, Wessels B, Siegel J, Howell R, et al. MIRD Pamphlet No. 17: The Dosimetry of Nonuniform Activity Distributions—Radionuclide S Values at the Voxel Level. J Nucl Med 1999; 40:118-368.

[5] Chatachot K, Shiratori S, Chaiwatanarat T, Khamwan K. Patient dosimetry of ^{177}Lu-PSMA I&T in metastatic prostate cancer treatment: the experience in Thailand. Annals of Nuclear Medicine. 2021 Nov;35(11):1193–202.

Contacts of the corresponding author:
Author: Panattha Damthongsen
Institute: Medical Physics Program, Department of Radiology, Faculty of Medicine, Chulalongkorn University
Street: 1873 Rama IV Road
City: Bangkok 10330
Country: Thailand
Email: 6570049330@student.chula.ac.th

Establishment of typical adult CT diagnostic reference levels (DRLs) in Ramathibodi hospital: A comparison of different dose collection methods

Srisumetawupakit Nichaphat[1], Asavaphatiboon Sawwanee[1,2], Charoenphun Putthiporn[1,3], Chuamsaamarkkee Krisanat[1,3*]

1 Master of Science Program in Medical physics, Department of Diagnostic and Therapeutic Radiology, Faculty of Medicine Ramathibodi Hospital, Mahidol University, Bangkok, Thailand
2 Division of Diagnostic, Department of Diagnostic and Therapeutic Radiology, Faculty of Medicine Ramathibodi Hospital, Mahidol University, Bangkok, Thailand
3 Division of Nuclear Medicine, Department of Diagnostic and Therapeutic Radiology, Faculty of Medicine Ramathibodi Hospital, Mahidol University, Bangkok, Thailand

**Corresponding author: krisanat.ch@gmail.com*

Abstract — **Diagnostic Reference Levels (DRLs) is effective tools for optimization. Generally, typical DRLs can be established through various dose collection methods. Therefore, this study aims to establish typical DRLs for adult CT procedures at Ramathibodi Hospital by comparing the different dose collection methods. The CT dose data (the computed tomography dose index volume ($CTDI_{vol}$) and dose length product (DLP)) were retrospective collected from June 2022 to June 2023 in two CT scanners from the ten most frequent CT examinations. Six dose collection methods have been used in this work: (a) all patient data , (b) weight-specific 45 to 75 kg. from all patient data, (c) a random selection of 30 patients, (d) a random selection of 30 patients with weight-specific, (e) one month with all patient data, and (f) a random selection of 30 patients in one month with weight-specific. Typical DRLs from different methods are established using the median of the dose distribution. The comparison of typical DRLs were performed using non-parametric (Mann-Whitney U test) to ascertain significant differences of typical DRLs from different dose collection methods. The DRLs from different dose collection methods including $CTDI_{vol}$ (median ± SD), DLP (median ± SD) and percentage difference (with all patient data) were reported. Some of the typical DRLs showed significant differences ($P < 0.05$) when compared to dose collection with all patient data. In Conclusion typical DRLs were established in two CT scanners for the ten most frequent at Ramathibodi Hospital. These values can improve dose optimization locally. Our finding reported the variation of typical DRLs results from different dose collection method. The limitations of each method were explained and discussed. This illustrated the importance of the dose collection method on the establishment of typical DRLs at a single hospital site.**

Keywords — **Diagnostic reference levels, DRLs, Typical DRLs, Dose collection, Optimization.**

I. INTRODUCTION

Computed tomography (CT) has become an essential diagnostic tool and its usage increasing over time [1]. However, CT could provide a high radiation exposure dose to patients, consequently the potential risks from radiation exposures should be optimized and monitored.

Diagnostic Reference Levels (DRLs) is served as an effective tools for achieving this optimization of radiation dose and image quality. However, establishing of typical DRLs can be performed by various dose collection methods and this can be lead to different Typical DRLs values [2]. A comparison of these results has not been reported or described. Therefore, this study aims to establish typical DRLs for adult CT procedures at Ramathibodi Hospital by comparing different dose collection methods.

II. MATERIALS AND METHODS

The computed tomography dose index volume ($CTDI_{vol}$) and the dose length product (DLP) were retrospective collected from June 2022 to June 2023 in two CT scanners (the Philips IQon spectral CT 64 slices (Philips Healthcare, Netherland) and the GE Revolution CT 256 slices (General Electric, USA)) from the ten most frequent CT examinations.

Six dose collection methods have been used in this work: (a) all patient data , (b) weight-specific 45 to 75 kg. from all patient data, (c) a random selection of 30 patients, (d) a random

selection of 30 patients with weight-specific, (e) one month with all patient data, and (f) a random selection of 30 patients in one month with weight-specific. Typical DRLs from different methods are established using the median of the dose distribution. The comparison of typical DRLs were performed using non-parametric (Mann-Whitney U test) to ascertain significant differences of typical DRLs from different dose collection methods.

The Radimetrics dose management software (Bayer AG, Leverkusen, Germany) version 3.1, was used in this work. IBM SPSS Statistics software was used for statistical tests to compare typical DRLs obtained from different dose collection methods.

III. RESULTS AND DISCUSSION

The typical values for the ten most frequent examinations in two CT scanners, obtained from all data dose collection methods, including $CTDI_{vol}$ (median ± SD) in unit of mGy and DLP (median ± SD) in unit of mGy.cm, were reported (Table 1).

Table 1. *Typical values obtained from all data dose collection methods in two CT scanners.*

Examination	**CT 1**		**CT 2**	
Chest with Whole abdomen	**$CTDI_{vol}$ mGy (SD)**	**DLP mGy.cm (SD)**	**$CTDI_{vol}$ mGy (SD)**	**DLP mGy.cm (SD)**
Plain	7.7 (2.3)	519.7 (171.3)	10.1 (2.5)	600.4 (203.0)
Late arterial	9.1 (2.7)	266.1 (94.3)	9.5 (2.8)	275 (94.2)
Venous	8.6 (2.5)	546.4 (199.7)	10.4 (3.1)	725.3 (256.3)
Delay liver	8.8 (2.7)	281.8 (161.2)	8.4 (2.9)	258.4 (128.3)
KUB	9.5 (2.9)	309.4 (103.0)	9.0 (2.8)	360.4 (128.8)
Brain without contrast	**$CTDI_{vol}$ mGy (SD)**	**DLP mGy.cm (SD)**	**$CTDI_{vol}$ mGy (SD)**	**DLP mGy.cm (SD)**
Non-contrast	50.9 (5.0)	989.2 (116.7)	46.4 (7.1)	977.5 (147.1)
Whole abdomen	**$CTDI_{vol}$ mGy (SD)**	**DLP mGy.cm (SD)**	**$CTDI_{vol}$ mGy (SD)**	**DLP mGy.cm (SD)**
Plain	8.9 (2.4)	451.4 (148.7)	7.7 (2.5)	402.8 (147.9)
Late arterial	9.0 (2.9)	267.4 (106.0)	n/a	n/a
Venous	8.5 (2.7)	392.5 (151.8)	12.3 (3.8)	631.8 (241.0)
Delay liver	8.6 (2.5)	289.1 (145.1)	7.6 (2.5)	243.5 (128)
KUB	9.5 (2.9)	379.9 (102.1)	9.0 (2.7)	390.1 (126.4)
Chest	**$CTDI_{vol}$ mGy (SD)**	**DLP mGy.cm (SD)**	**$CTDI_{vol}$ mGy (SD)**	**DLP mGy.cm (SD)**
Plain	5.1 (1.4)	189.1 (54.3)	5.8 (1.9)	204.3 (75)
Venous	6.6 (1.8)	249.9 (73.7)	6.5 (2.7)	232.9 (113)
Chest with Upper abdomen	**$CTDI_{vol}$ mGy (SD)**	**DLP mGy.cm (SD)**	**$CTDI_{vol}$ mGy (SD)**	**DLP mGy.cm (SD)**
Plain	7.6 (2.2)	346.2 (102.2)	6.3 (2.5)	294 (116.3)
Late arterial	8.4 (2.6)	240.3 (90.8)	8.0 (2.7)	215.1 (90.6)
Venous	8.2 (2.3)	372.6 (111.4)	8.8 (2.9)	394.9 (150.2)
Delay liver	8.5 (2.5)	243.8 (83.4)	6.8 (2.6)	186.0 (83.5)
Neck	**$CTDI_{vol}$ mGy (SD)**	**DLP mGy.cm (SD)**	**$CTDI_{vol}$ mGy (SD)**	**DLP mGy.cm (SD)**
Plain	6.1 (2.3)	145.5 (87.8)	11.8 (3.2)	240.0 (107.8)
Contrast	8.5 (2.7)	284.4 (103.2)	13.9 (4.0)	446.5 (165.9)
Upper abdomen	**$CTDI_{vol}$ mGy (SD)**	**DLP mGy.cm (SD)**	**$CTDI_{vol}$ mGy (SD)**	**DLP mGy.cm (SD)**
Plain	8.7 (2.6)	253.9 (89.5)	8.3 (3.2)	246.0 (106.7)
Late arterial	9.8 (2.5)	287.9 (91.8)	10.1 (2.6)	305.7 (97.3)
Venous	9.6 (2.4)	267.4 (88.7)	8.0 (3.6)	217.4 (128.2)
Delay liver	10.0 (2.5)	291.6 (90.0)	9.0 (3.2)	266.1 (111.4)
KUB	**$CTDI_{vol}$ mGy (SD)**	**DLP mGy.cm (SD)**	**$CTDI_{vol}$ mGy (SD)**	**DLP mGy.cm (SD)**
Plain	10.4 (3.7)	451.8 (181.7)	9 (2.9)	409.3 (144.9)
Late arterial	11.7 (4.2)	271.6 (118.0)	8.0 (2.5)	196.4 (83.6)
Venous	8.8 (2.8)	406.6 (168.8)	10.1 (3.1)	455.7 (177.6)
Delay KUB	9.6 (3.0)	398.0 (119.4)	9.3 (2.9)	430.1 (149.6)
Chest without contrast	**$CTDI_{vol}$ mGy (SD)**	**DLP mGy.cm (SD)**	**$CTDI_{vol}$ mGy (SD)**	**DLP mGy.cm (SD)**
Plain	6.5 (1.7)	245 (79.6)	5.8 (2.3)	219.7 (96.5)
HRCT	**$CTDI_{vol}$ mGy (SD)**	**DLP mGy.cm (SD)**		
Inspiration	6.1 (1.4)	214.9 (54.6)		
Brain with contrast			**$CTDI_{vol}$ mGy (SD)**	**DLP mGy.cm (SD)**
Plain			46.4 (6.5)	965.6 (123.2)
Contrast			46.6 (7.7)	986.3 (150.2)

The percentage difference between all data dose collection methods and other methods were calculated. The statistical analysis of typical DRLs was performed using the non-parametric Mann-Whitney U-test with a confidence interval of 95% (α=0.05) to determine significant differences among different dose collection methods in the two CT scanners (illustrated in Table 2).

Table 2. *The percentage difference (%) and statistical analysis of typical values from each dose data collection method compared to all data in two CT scanner.*

% difference Statistical*		$CTDI_{vol}$ (DLP)	$CTDI_{vol}$ (DLP)	$CTDI_{vol}$ (DLP)	$CTDI_{vol}$ (DLP)	$CTDI_{vol}$ (DLP)
Chest Whole		**Group (b)**	**Group (c)**	**Group (d)**	**Group (e)**	**Group (f)**
Plain	CT1	0.0 (-0.1)	4.5* (2.4)*	3.9* (2.6)*	1.3* (2.1)*	-7.8* (-5.4)*
	CT2	-3.0 (-0.2)	3.0 (-3.7)	-4.0 (-10.3)	n/a	n/a
LA	CT1	-1.1 (-1.5)	9.9* (12.0)*	-4.9* (-0.2)*	5.5* (6.7)*	0.0* (-4.2)*
	CT2	-5.3 (-9.8)	-3.2 (-2.7)	-5.3 (-2.4)	-27.4* (-30.0)*	-38.9* (-39.6)*
V	CT1	-2.3* (-1.4)	-11.6* (-8.8)*	0.0* (-3.3)*	4.7* (3.4)*	-5.8* (-4.0)*
	CT2	0.0 (-5.8)	12.5 (1.3)	-2.9 (-8.9)	-33.7* (-34.8)*	-33.7* (-34.6)*
Liver	CT1	-1.1 (-4.6)	5.7* (11.1)*	4.5* (1.0)*	6.8* (10.8)*	-4.5* (-8.9)*
	CT2	7.1 (3.7)	-4.8 (-11.9)	8.3 (18.2)	-28.6* (-16.8)	0.0* (-6.2)
KUB	CT1	-3.2 (-2.6)	2.1* (2.0)*	-4.2* (-4.7)*	n/a	n/a
	CT2	-2.2 (-7.1)*	-22.2 (-8.4)	0.0 (-0.9)	n/a	n/a
Brain (NC)		**Group (b)**	**Group (c)**	**Group (d)**	**Group (e)**	**Group (f)**
Plain	CT1	-1.0* (-1.1)*	0.7* (-3.0)*	-2.9 (-2.5)	-3.4* (-2.2)*	-3.7* (-2.2)*
	CT2	15.7* (7.1)*	0.0 (0.0)	(0) (3.5)	0.0 (0.0)	n/a
Whole abdomen		**Group (b)**	**Group (c)**	**Group (d)**	**Group (e)**	**Group (f)**
Plain	CT1	0.0 (-0.5)	-2.8 (-2.8)	-2.2 (1.6)	-4.5 (-2.5)*	-1.7 (5.3)
	CT2	16.9* (11.5)*	0.0 (1.0)	19.5* (12.5)	n/a	n/a
LA	CT1	0.0 (0.7)	0.6 (3.4)	-3.9 (-3.3)	3.3 (9.0)	3.3 (10.6)
	CT2	n/a	n/a	n/a	n/a	n/a
V	CT1	1.2 (0.1)	-6.5 (-5.9)	5.9 (9.9)	0.0 (-3.3)	4.7 (6.2)
	CT2	0.0* (3.5)	-4.9 (-1.7)	0.0 (4.3)	-26.8* (-14.1)*	n/a
Liver	CT1	0.0 (0.2)	-3.5 (-6.1)	4.1 (5.1)	-4.7 (-3.8)	-2.3 (-5.9)
	CT2	5.3 (-1.9)	-2.6 (-3.4)	7.9 (10.9)	-6.6 (-8.9)	n/a
KUB	CT1	-0.5 (-0.7)	6.3 (8.0)	-4.7 (-1.0)	5.3 (6.9)	2.6* (19.8)
	CT2	2.2 (0.1)	0 (-6.7)	7.8 (4.5)	n/a	n/a
Chest		**Group (b)**	**Group (c)**	**Group (d)**	**Group (e)**	**Group (f)**
Plain	CT1	0.0 (0.0)	-2.0 (-2.6)	3.9 (6.7)	0.0 (2.4)	-3.9 (2.1)
	CT2	-1.7 (-1.0)	0.0 (0.0)	-6.9 (-10.5)	-39.7* (-38.8)*	-37.9* (39.8)*
V	CT1	0.0 (-0.2)	4.5 (0.0)	4.5 (1.3)	4.5 (5.5)	-3.8 (-5.5)
	CT2	-1.5 (-2.3)	10.8 (18.1)	-4.6 (-8.0)	-27.7* (-21.6)*	-27.7* (-17.9)*
Chest Upper ab		**Group (b)**	**Group (c)**	**Group (d)**	**Group (e)**	**Group (f)**
Plain	CT1	1.3 (2.5)	2.0 (2.7)	2.6 (6.5)	-6.6 (-6.5)	2.0 (3.9)
	CT2	9.5 (3.6)	13 (5.5)	19.0 (10.8)	-7.9 (-17.3)	n/a
LA	CT1	1.2 (1.8)	-0.6 (1.1)	4.2 (4.3)	-10.1* (-8.5)*	-12.5* (-11.6)*
	CT2	-7.5* (-6.1)*	11.3 (4.9)	10.0 (11.6)	-25.0* (-18.0)*	-27.5* (-21.8)*
V	CT1	0.0 (0.1)	-14.0 (-13.1)	0.6 (1.8)	3.0 (3.7)	-1.8 (1.1)
	CT2	-9.1 (-8.8)	-9.1 (-3.1)	-10.2 (-16.5)	-28.4* (-24.1)*	-34.1* (-24.9)*
Liver	CT1	1.2 (1.4)	5.9 (-1.6)	5.9 (-1.4)	-2.4 (-5.1)	1.8 (-4.8)
	CT2	-5.9 (-9.2)	-4.4 (-12.5)	-5.9 (-7.6)	-27.9* (-22.2)*	-33.8* (-33.1)*
Neck		**Group (b)**	**Group (c)**	**Group (d)**	**Group (e)**	**Group (f)**
Plain	CT1	-4.9 (-6.0)	-8.2 (-6.9)	0.0 (-3.8)	n/a	n/a
	CT2	6.8* (23.4)	-0.9 (23.4)	0.0 (-3.8)	6.8 (22.5)	n/a
V	CT1	0.0* (-0.5)*	5.3* (8.7)*	-1.2* (-0.9)*	-10.6* (-7.8)*	-11.8* (-9.0)*
	CT2	7.9* (9.4)*	0.0 (-3.2)	-1.2 (-0.9)	7.9 (10.3)	n/a
Upper abdomen		**Group (b)**	**Group (c)**	**Group (d)**	**Group (e)**	**Group (f)**
Plain	CT1	-2.3 (-3.5)	5.7 (9.0)	3.4 (-1.3)	n/a	n/a
	CT2	8.4* (-0.2)*	10.8 (11.4)	-2.4 (-0.1)	n/a	n/a
LA	CT1	-5.1 (-3.5)	9.2 (12.3)	-3.1 (-1.7)	n/a	n/a
	CT2	0.0 (-1.7)	0.0 (-0.8)	-20.8* (-29.4)*	n/a	n/a
V	CT1	-1.6 (-0.8)	-0.5 (9.6)	1.6 (0.5)	n/a	n/a
	CT2	n/a	0.0 (12.8)	n/a	n/a	n/a
Liver	CT1	-3.5 (-1.9)	-1.0 (-4.3)	1.5 (-0.6)	n/a	n/a
	CT2	0.0 (-6.2)	-8.9 (-10.0)	3.3 (4.5)	n/a	n/a
KUB		**Group (b)**	**Group (c)**	**Group (d)**	**Group (e)**	**Group (f)**
Plain	CT1	-2.9* (-4.3)*	5.3 (7.9)	2.9 (2.0)	0.5 (-2.8)	-2.4 (-5.8)
	CT2	-4.4 (-4.9)	-5.6 (-2.9)	-8.9 (-11.2)	n/a	n/a
LA	CT1	-2.6 (-4.7)	-2.6 (3.1)	9.0 (2.1)	-2.6 (-7.3)	-12.0* (-11.7)*
	CT2	0.0 (19.6)	0.0 (0.3)	0.0 (19.6)	n/a	n/a
V	CT1	0.0 (-0.3)	-5.7 (-3.3)	-2.3 (-3.0)	-3.4 (-6.5)	-2.8 (-2.2)
	CT2	2.0 (0.9)	3.0 (8.0)	12.9 (11.8)*	n/a	n/a
KUB	CT1	-0.5 (-1.5)	-2.1 (1.4)	-1.0 (-3.1)	5.2 (8.7)	6.8 (11.2)
	CT2	-6.5* (-8.5)	3.2 (5.3)	-11.8* (-11.7)	n/a	n/a
Chest Non contrast		**Group (b)**	**Group (c)**	**Group (d)**	**Group (e)**	**Group (f)**
Plain	CT1	0.0 (0.2)	-5.4 (-6.0)	-3.8 (-9.4)	-5.4 (-1.1)	n/a
	CT2	19.0* (10.2)*	-5.2 (-4.9)	-24.1 (-17.1)	n/a	n/a
HRCT		**Group (b)**	**Group (c)**	**Group (d)**	**Group (e)**	**Group (f)**
Ins.	CT1	-0.8 (-0.6)	-5.8 (-1.2)	-0.8 (-0.1)	n/a	n/a
Brain with Contrast		**Group (b)**	**Group (c)**	**Group (d)**	**Group (e)**	**Group (f)**
Plain	CT2	15.7* (8.8)*	0.4 (-0.9)	0.0 (3.1)	n/a	n/a
V	CT2	23.0* (8.7)*	7.8 (0.4)	15.7* (8.7)*	n/a	n/a

* significant different

The typical DRL values of two CT scanners at Ramathibodi are reported in this work. For chest examinations, the dose range in terms of $CTDI_{vol}$ and DLP is 5-7 mGy and 180-250 mGy.cm, respectively. The dose range for the whole abdomen examination is 7-13 mGy for $CTDI_{vol}$ and 400-700 mGy.cm for DLP. In the upper abdomen examination, the dose range is 8-10 mGy and 200-310 mGy.cm. Chest with whole abdomen examinations have a dose range of 7-11 mGy and 500-750 mGy.cm, and KUB has $CTDI_{vol}$ range is 8-12 mGy, with DLP ranging from 290-460 mGy.cm. For brain examinations, the dose range is 46-51 mGy for $CTDI_{vol}$ and 900-990 mGy.cm for DLP, and neck examinations have a dose range of 6-14 mGy for $CTDI_{vol}$ and 250-450 mGy.cm for DLP.

When compared with the National Diagnostic Reference Levels in Thailand reported in 2023 it is observed that the $CTDI_{vol}$ of chest examinations was 2 times lower than the national value. Radiation doses for other examinations are also lower than the national DRLs. However, for brain examinations with contrast, the typical DLP is slightly higher than the national value [3]. This overall lower results of our typical DRL values were resulted from the implementation of the radiation dose reduction by using iterative model reconstruction in both CT scanners.

To determine the dose collection methods, the percentage difference between all data dose collection methods and other methods were calculated (as illustrated in Table 2). The overall percentage differences in CT1 was lower than in CT2. This higher percentage difference in CT2 was particularly noticeable in dose collection method (e) and (f). We observed in detail and found that the reconstruction software of CT2 was updated in the month that we collected data. This indicated the importance of choosing the period with no updating imaging techniques or software if collected DRL from only one month data.

The statistical analysis indicated significant differences in CT1 for chest, whole abdomen, brain, and neck; however, these differences had a low standard deviation and a percentage difference. For CT2, the most significant differences were observed in groups (e) and (f), which were related to variations in dose data as described earlier. Additionally, CT2 showed significance in groups (b) and (d) when compared with CT1. This was due to the incomplete data on patient weight inputted in CT2. Hence, it was crucial to input patient weight for accurate dose data collection. Taylor et al also found that the variability in dose data was influenced by the sample of dose distribution, patient size, and region [4].

Based on this work, it was also observed that the methods for dose collecting (c) and (d) were suitable for establishing typical DRLs as recommended in the ICRP 135 to collect the DRL with standardized size patients data [2]. In conclusion, a sample size of at least 30 random patients with standard weight was appropriated for establishing typical DRLs

IV. CONCLUSION

Typical DRLs were established in two CT scanners for the ten most frequent examinations at Ramathibodi Hospital, with the typical values lower than the national DRLs. Different dose collection methods resulted in variable of typical DRLs. For the establishment of typical DRLs, it was crucial to collect radiation dose data that accurately represents patient exposures. For data with low SD, a sample size of at least 30 random patients with standard weight was appropriated and yield acceptable result for the establishment of typical DRLs.

REFERENCES

[1] Bolus NE. NCRP report 160 and what it means for medical imaging and nuclear medicine. Journal of nuclear medicine technology. 2013;41(4):255-60.

[2] Vañó E, Miller D, Martin C, Rehani M, Kang K, Rosenstein M, et al. ICRP publication 135: diagnostic reference levels in medical imaging. Annals of the ICRP. 2017;46(1):1-144.

[3] กระทรวงสาธารณสุข กทก. ค่าปริมาณรังสีอ้างอิงในการถ่ายภาพรังสีวินิจฉัยทางการแพทย์ของประเทศไทย 2566 (National Diagnostic Reference Levels in Thailand 2023). 2023.

[4] Taylor S, Van Muylem A, Howarth N, Gevenois PA, Tack D. CT dose survey in adults: what sample size for what precision? European radiology. 2017;27(1):365-73.

Contacts of the corresponding author:
Author: Krisanat Chuamsaamarkkee Ph.D.
Institute: Department of Diagnostic and Therapeutic Radiology, Faculty of Medicine
Ramathibodi Hospital, Mahidol University
Street: Rama 6 Road
City: Bangkok
Country: Thailand
Email: Krisanat.ch@gmail.com

Development of tungsten-doped borosilicate glass as a lead-free transparent radiation shield in nuclear medicine

Suwanprateep S[1*], Charoenphun P[1,2], Chuamsaamarkkee K[1,2], Meechoowas E[3], Sawangboon N[3], Suriyoporn S[3]

1 Master of Science Program in Medical Physics, Department of Diagnostic and Therapeutic Radiology, Faculty of Medicine Ramathibodi Hospital, Mahidol University, Bangkok, Thailand
2 Division of Nuclear medicine, Department of Diagnostic and Therapeutic Radiology, Faculty of Medicine Ramathibodi Hospital, Mahidol University, Bangkok, Thailand
3 Division of Engineering Materials, Department of science service, Bangkok, 10400, Thailand

**Corresponding author: satawatchara.su27@gmail.com*

Abstract — Introduction: **Transparent radiation shield is significantly important for preparation of radiopharmaceuticals and administration to patients in nuclear medicine. Although lead glass is commonly used for radiation protection, lead is a highly toxic metal. The alternative lead-free materials with no toxicity should be beneficial. Therefore, this study aimed to develop a novel lead-free transparent material for using in nuclear medicine and to determine radiation shielding property.**
Materials and methods: **Borosilicate glasses doping with WO_3 filler were produced by melt-quenching technique based on the glass formulation of $25Na_2O$-$15B_2O_3$-(60-x)-SiO_2-(x) WO_3, where x = 0, 0.5, 1.0 and 1.5 %mol. Density of the samples were determined. The radiation shielding properties were investigated using ^{137}Cs, ^{133}Ba and ^{57}Co sources to represent the common energies used in nuclear medicine. Then linear attenuation coefficients of samples were estimated from measurement using NaI(Tl) scintillation detector coupled with multi-channel-analyzer (MCA) in a narrow beam geometry set up. Eventually, mass attenuation coefficients of the samples were calculated.**
Results: **Transparent glasses with various concentrations of WO_3, 0, 0.5, 1.0, 1.5 % were produced and their density were 2.54, 2.57, 2.60 and 2.62 g/cm^3, respectively. The linear attenuation coefficients of the produced samples with varying concentrations of WO_3 were 0.11, 0.22, 0.31 and 0.39 cm^{-1} for ^{137}Cs, 0.26, 0.38, 0.43 and 0.50 cm^{-1} for ^{133}Ba and 0.30, 0.42, 0.50 and 0.58 cm^{-1} for ^{57}Co. Then calculation of mass attenuation coefficients for ^{137}Cs, ^{133}Ba and ^{57}Co sources were 0.04, 0.09, 0.12, 0.15 cm^2/g, 0.10, 0.15, 0.16, 0.19 cm^2/g and 0.12, 0.16, 0.19, 0.22 cm^2/g, respectively, when the concentration of WO_3 varied from 0 to 1.5 %mol.**
Conclusion: **Lead-free transparent material of borosilicate glass doping with WO_3 showed the promising results to attenuate the gamma radiations commonly used in nuclear medicine. Moreover, radiation shielding property was increased with the concentration of the WO_3 filler.**
Keywords: **Lead-free transparent shield, borosilicate glasses doping with WO_3**

I. INTRODUCTION

Transparent radiation shield is one of the most important devices, particularly in nuclear medicine practices, which are required to use transparent radiation shield for preparation of radiopharmaceuticals and used during administration of radiopharmaceuticals to patients. Basically, transparent radiation shield consists of two main components which are transparent based and filler (1-4). In general, the transparent based is made of glass or polymer, while the filler is a material that provides the ability to increase the potential of radiation protection. The different types of glass or polymer as well as the types of filler could affect the radiation shielding efficiency. Lead is widely used material to fabricate in the transparent radiation shield such as lead glass. However, it is highly toxic (5). Therefore, the alternative lead-free materials for producing transparent shield that could effectively reduce radiation exposure to the staff with no toxicity is significantly required. Borosilicate glass is

one of the appropriate transparent based materials (6-10). Tungsten trioxide, WO_3, that has high density and high atomic number should be a high potential material used as a filler (11). The objectives of this study were to develop the novel lead-free transparent material for nuclear medicine application and to determine its radiation protection property.

II. MATERIALS AND METHODS

A. Preparation of borosilicate glass doped with WO_3

The borosilicate glass doping with WO_3 (US Research Nanomaterials, Inc., USA) based on the glass formulation system of $0.25Na_2O – 0.15B_2O_3$ - (0.6-x) SiO_2 - x WO_3, where x = 0, 0.5, 1.0 and 1.5 %mol, was used to prepared the glass samples. All of compositions were mixed in almunia crucible, and then be melted in an electric furnace at 1200 ˚C for 2 hours. After the melting process, the glass molten was became solidify in the pre-heated graphite molds of 4x7 cm^2 in size. Lastly, the solid sample was annealed in the oven at 590 ˚C to 620 ˚C for 30 minutes prior to cooling down to room temperature. The produced glass samples were polished to obtain the optimal flatness and the thickness of 0.3 cm.

B. Density measurement

The densities of all samples were measured using an automatic Buoyancy density analyzer (Sartorius, model RC-250S, Germany), based on the Archimedes water replacement technique with water as the immersion liquid. The density of the glass sample was calculated according to equation 1, where ρ is sample's density (g/cm^3), W_A is the sample's weight in air, W_W is sample's weight in water, and ρ_W is the density of water (ρ_W = 1 g/cm^3).

$$\rho = \frac{W_A}{(W_A - W_W)}\, x\, \rho_W \qquad \text{Equation 1}$$

C. Radiation shielding property

The mass attenuation coefficient (μ_m) was used to determine the radiation shielding ability of the samples. The radiation standard sources of ^{137}Cs (662 keV), ^{133}Ba (356 keV) and ^{57}Co (122 keV) (Epsilon Radioactive Sources (ERS), Istanbul, Turkey) were used for radiation measurement to represent the common gamma energies used in nuclear medicine. The radiation measurement were performed by 3 x 3 inch NaI(Tl) scintillation detector (ORTEC, USA) coupled with multi-channel-analyzer (MCA) MAESTRO-32 software (ORTEC, USA) in a narrow beam geometry set up, with a collimated width of 4 mm and the distances of radiation source to detector and source to sample were 30 cm and 4.5 cm, respectively. Then the incident radiation (I_0) and transmitted radiation (I) were measured without and with glass samples, respectively. Then linear attenuation coefficient (μ, cm^{-1}) of the samples were calculated using the equation 2. Eventually, mass attenuation coefficients (μ_m) of the samples were calculated according to equation 3, where μ is linear attenuation coefficient (cm^{-1}), μ_m is mass attenuation coefficient (cm^2/g), x is sample's thickness (cm) and ρ is sample's density (g/cm^3)

$$\mu = \frac{ln(I/I_0)}{x} \qquad \text{Equation 2}$$

$$\mu_m = \mu/\rho \qquad \text{Equation 3}$$

III. RESULTS

A. Preparation of borosilicate glass doped with WO_3

The 0.3 cm thick borosilicate glass sheets doped with different amount of WO_3 to obtain the final concentration of 0, 0.5, 1.0 and 1.5 %mol were successfully produced as clear transparent glasses as illustrated in Figure 1.

B. Density measurement

The produced glass samples were subjected to determine the density as shown in Figure 2. The densities of glass samples increased with the increment of WO_3 concentration, from 2.54 g/cm^3 to 2.62 g/cm^3 for 0% to 1.5% of WO_3, respectively.

C. Radiation shielding property

Mass attenuation coefficient (μ_m) of the glass samples for the ^{137}Cs, ^{133}Ba and ^{57}Co sources were illustrated in Figure 3 and Table 1. According to the graph, the mass attenuation coefficient values of the glass samples were increased when higher amount of WO_3 was loaded. Besides, at the different energies of the standard sources, the μ_m of each glass sample showed lowest attenuation ability against ^{137}Cs and higher with ^{133}Ba and ^{57}Co.

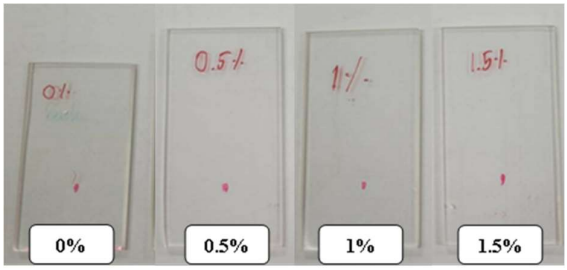

Figure 1. *Borosilicate glass doped with different concentrations of WO_3*

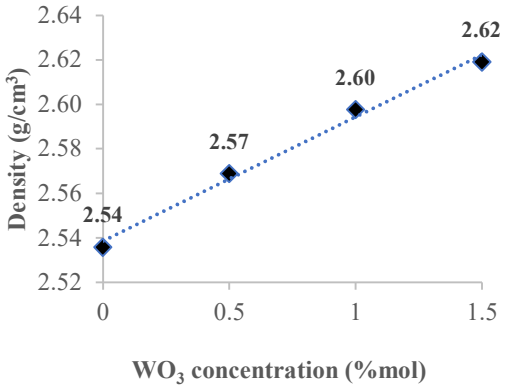

Figure 2. *Densities of the prepared glass sample with different WO_3 concentrations*

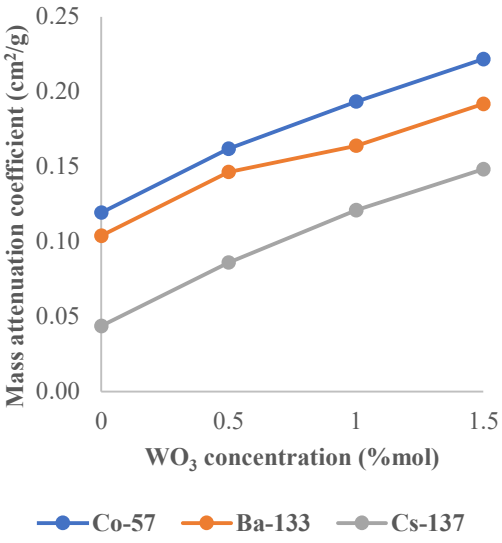

Figure 3. *Mass attenuation coefficient of the prepared glass samples with different WO_3 concentrations*

Table 1. *Mass attenuation coefficient of the prepared glass samples*

Radiation sources	Mass attenuation coefficient (μ_m)			
	WO_3 concentration (%mol)			
	0.0	0.5	1.0	1.5
^{57}Co	0.12	0.16	0.19	0.22
^{133}Ba	0.10	0.05	0.16	0.19
^{137}Cs	0.04	0.09	0.12	0.15

IV. DISCUSSION

From the results of mass attenuation coefficient (μ_m) showed enhancement of radiation shielding ability of glass samples when increasing amount of WO_3 which the amount of WO_3 (1.5 %mol) provided the highest μ_m values for all radiation energy of the sources. Because the density and atomic number of the produced glasses were escalated and then the probability of the photon interaction with the samples should be increased. Similar results were found in several studies that investigated on the effect of WO_3 in glass system (12-14). For instant, Sayyed MI. et al., which studied on the effect of different concentration of WO_3 (10 to 25 %mol) in TeO_2-La_2O_3-WO_3 glass system (13). The radiation shielding property results demonstrated greater radiation attenuation capability of the samples with higher WO_3 content.

Moreover, the results of radiation shielding ability from this study revealed the gamma-ray energy dependence. The lower energy gamma of 122 keV and 356 keV emitted by ^{57}Co and ^{133}Ba standard sources, respectively. The produced glass samples provided greater attenuation due to the dominant interaction of photoelectric effect which can decrease when increasing of gamma-ray energy (15, 16). Meanwhile, ^{137}Cs emitted higher gamma energy then Compton scattering was main interaction leading to less dependent on atomic number of shielding materials (15, 16). Therefore, higher transmission from the produced glass samples was observed, which was agreed well with the other studies (12-14).

V. CONCLUSION

The glass system of $0.25Na_2O – 0.15B_2O_3$ - (0.6-x) SiO_2 - x WO_3 (where x = 0, 0.5, 1.0 and 1.5 %mol) were successfully produced. The densities and linear attenuation coefficient

values of the produced glass samples were increased with the higher concentration of WO_3. Additionally, the promising radiation protection ability of the glass doped with WO_3 against the gamma radiations commonly used in nuclear medicine was revealed based on the mass attenuation coefficient results.

ACKNOWLEDGEMENTS

This research was successfully completed. Thanks to the Division of Engineering Materials, Department of science service that provided equipment for glass production and glass densities tests.

REFERENCES

1. More CV, Alsayed Z, Badawi MS, Thabet AA, Pawar PP. Polymeric composite materials for radiation shielding: a review. Environmental Chemistry Letters. 2021;19(3):2057-90.
2. Hashemi SA, Karimipourfard M, Mousavi SM, Sina S, Bahrani S, Omidifar N, et al. Transparent sodium polytungstate polyoxometalate aquatic shields toward effective X-ray radiation protection: Alternative to lead glasses. Materials Today Communications. 2022;31:103822.
3. Khazaalah T, Shahrim I, Rahman A, Mohd Zaid M, Hisam R, Abdul Malik MFI, et al. Development of Novel Transparent Radiation Shielding Glasses by BaO Doping in Waste Soda Lime Silica (SLS) Glass. Sustainability. 2022;14:937.
4. Al-Hadeethi Y, Tijani SA. The use of lead-free transparent 50BaO-(50-x)borosilicate-xBi2O3 glass system as radiation shields in nuclear medicine. Journal of Alloys and Compounds. 2019;803:625-30.
5. Organization WH. WHO guideline for clinical management of exposure to lead. Toxicity of lead: Geneva: World Health Organization; 2021. p. 92.
6. Wang WH, Dong C, Shek CH. Bulk metallic glasses. Materials Science and Engineering: R: Reports. 2004;44(2):45-89.
7. Wang WH. Dynamic relaxations and relaxation-property relationships in metallic glasses. Progress in Materials Science. 2019;106:100561.
8. Tekin HO, Susoy G, Issa SAM, Ene A, Almisned G, Rammah YS, et al. Heavy metal oxide (HMO) glasses as an effective member of glass shield family: A comprehensive characterization on gamma ray shielding properties of various structures. Journal of Materials Research and Technology. 2022;18:231-44.
9. Ehab M, Salama E, Ashour A, Attallah M, Saleh HM. Optical Properties and Gamma Radiation Shielding Capability of Transparent Barium Borosilicate Glass Composite. Sustainability. 2022;14(20):13298.
10. Kaur P, Singh D, Singh T. Heavy metal oxide glasses as gamma rays shielding material. Nuclear Engineering and Design. 2016;307:364-76.
11. Hayriye Hale A. Epoxy Composites for Radiation Shielding. In: Samson Jerold Samuel C, Ramesh A, M.R.Meera, editors. Epoxy-Based Composites. Rijeka: IntechOpen; 2022. p. Ch. 6.
12. Al-Buriahi M, Hemaida T, Alothman M, Donya H, Olarinoye OI. Influence of WO3 incorporation on synthesis, optical, elastic and radiation shielding properties of borosilicate glass system. The European Physical Journal Plus. 2021;136.
13. Sayyed MI. Effect of WO3 on the attenuation parameters of TeO2–La2O3-WO3 glasses for radiation shielding application. Radiation Physics and Chemistry. 2024;215:111319.
14. Cheewasukhanont W, Limkitjaroenporn P, Sayyed MI, Kothan S, Kim HJ, Kaewkhao J. High density of tungsten gadolinium borate glasses for radiation shielding material: Effect of WO3 concentration. Radiation Physics and Chemistry. 2022;192:109926.
15. Saldaña G, Reyes U, Salazar H, Oscar M, Moreno E, Conde R. High Density Devices Applied to a Gamma-Camera Implementation. 2012.
16. Khan FM, Gibbons JP. Khan's the physics of radiation therapy: Lippincott Williams & Wilkins; 2014.

Contacts of the corresponding author:

Author: Suwanprateep Satawatchara
Institute: Master of Science Program in Medical Physics, Department of Diagnostic and Therapeutic Radiology, Faculty of Medicine Ramathibodi Hospital, Mahidol University
Street: Rama 6
City: Bangkok
Country: Thailand
Email: Satawatchara.su27@gmail.com

Minimizing slice-overlap artifacts in MRI lumbar spine: A phantom study

Kanyakham Kannikar[1]*, Loungwutiwong Jakapat[1], Laothamatas Jiraporn[2], Krisanachinda Anchali[3]

1 Imaging Center, Phyathai 2 Hospital, Bangkok, Thailand
2 Faculty of Health Science Technology, HRH Princess ChulaBhorn College of Medical Science, Chulabhorn Royal Academy. Thailand
3 Department of Radiology, Faculty of Medicine, Chulalongkorn University, Bangkok, Thailand

**Corresponding author: kanni.pp@gmail.com*

Abstract — Introduction: **Cross-talk artifacts or Slice-overlap artifacts are dark signal lines that appear on MR images and are caused by overlapping of multiple slices during an MRI scan, which can occur due to imperfect multi-slice settings. These artifacts can degrade the image quality and make it difficult for radiologists to accurately diagnose patients.**
Objective: **To reduce the effects of slice-overlap artifact on T1W and T2W TSE sequences in MRI lumbosacral Spine imaging and improve the diagnostic value of the images by using an interleave method and optimizing the minimum number of packages based on the basic principles of MRI sequencing on the time concept.**
Methods: The experiment was carried out by scanning a water phantom using a 3.0 T Philips MR System Achieva dStream. Different methods were used, including the slice scan order, interleave method with adjusted minimum number of packages, linear method (slice scan order: FH, HF, default, reverse central). In this study used number of slice 36 slices, the interleave method is set, and the minimum number of packages is estimated by the square root of the number of slices ($\sqrt{36} = 6$).
Results: **The crosstalk artifact did not appear in the interleave method with the square root of the number of slices.**
Conclusions: **The interleave method and optimizing the minimum number of packages appropriately can effectively reduce the effects of overlapping artifacts in MRI imaging. The study found no evidence of overlapping artifacts when using the Interleaved method.**

Keywords- ***interleaved, minimum number of packages, slice-overlap artifact, MRI Lumbar spine***

I. INTRODUCTION

Magnetic resonance imaging (MRI) is a medical imaging technique that uses a magnetic field and radio waves to generate detailed images of the internal structures of the body, including the spine. It is commonly used to assess soft tissues such as muscles, discs, nerves, and ligaments in the spine. MRI provides superior tissue contrast resolution compared to other imaging techniques, specifically radiography (X-rays) and computed tomography (CT). This means that MRI can produce more detailed and clearer images of the body's internal structures, making it particularly suitable for evaluating soft tissues. Computed tomography (CT); imaging modalities that inadequately assess the spinal cord and use ionizing radiation. MRI examination of the lumbar spine has been the standard examination can provide valuable information about the anatomy and potential pathology of the lumbar spine, helping healthcare providers identify the cause of low back pain. The most sensitive examination to evaluate the presence of disc herniation. Disc herniation assessment can be performed in various areas in the axial plane, including the central canal, subarticular foramina, and extra foramina, to examine the protrusion or extrusion of the disc [1]. However, the accuracy of assessment in these areas can be compromised under certain conditions, such as the presence of cross-talk artifacts or overlapping artifacts.

Cross-talk artifacts in MRI occurs when slice groups overlap or slices are positioned too closely together. The slightly curved shape

of the excitation pulse, which can inadvertently excite not only the intended tissue but also the adjacent or overlapping tissue, primarily causes this artifact. As a result, certain areas of tissue may be excited multiple times within a single repetition time (TR), preventing proper relaxation and leading to the loss of signal [3]. The impact of crosstalk artifact on the image can be observed as a loss of signal intensity, particularly in all slices except the first slice of the set. This artifact commonly manifests as black bands that may overlay the region of interest, particularly in axial lumbar spine imaging. There are recommendations to reduce crosstalk artifacts by using slice groups to minimize the intersection angle, avoid small slice gaps, especially in inversion recovery sequences, which are particularly susceptible to crosstalk artifacts. Increase slice gaps distance that is 25 – 30% of the slice thickness between slices [2]. On the other hand, examining a lesion is difficult if the lesion exists in a slice gap. For their reasons, the interleave method was developed. The objective of this study was to reduce the effects of slice-overlap artifact or cross-talk artifact on T1W and T2W TSE sequences in MRI lumbosacral Spine imaging and improve the diagnostic value of the images by using an interleave method and optimizing the minimum number of packages based on the basic principles of MRI sequencing on the time concept.

II. MATERIALS AND METHODS

In this study was an experimental study utilizing water phantom objects with a volume size of 3000 ml. placed on the head coil in longitudinal position and scanned using 3.0T MR system (Achieva dStream ® Phillips). Image acquisition techniques using routinely scanned for lumbar spine examination, Axial T1W, Axial T2TSE and change five different of slice scan order FH, HF, reverse central, defaults, interleaved respectively. The experiment set up the interleave method with used minimum number of packages. The interleave number is estimated by the square root of the number of slices. The minimum number of packages was set equal to six, calculated by square root of the number of 36 slices following the formula.

Minimum number of packages
= √Number of Slices
= √36
= 6

Axial T1WTSE and Axial T2WTSE were performed with 36 slices the set position and angle of slices as shown in Figure 1. Obtain an image in the slice order of 1,7,13,19,25,31, 2,8,14,20,26,32,3,9,15,21,27,33, 4, 10, 16, 22, 28,34,5,11,17,23,29,35,6,12,18,24,30,36. The imaging parameters are shown as in Table 1.

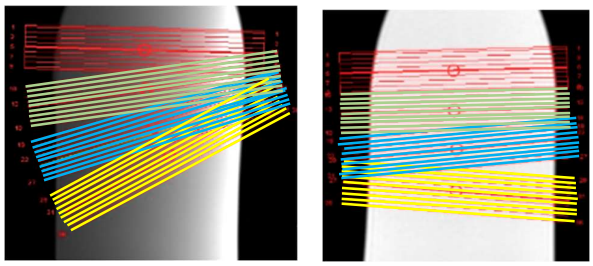

(a) (b)

Figure 1. *The acquisition plane along the long axis of the phantom, place the slice overlap (a) Sagittal view of phantom and (b) Coronal view of phantom. The acquired plane along the long axis of the phantom.*

Table 1. *Imaging parameters.*

Pluse Sequence	Slice scan order	TR (ms)	TE (ms)	Matrix size	NEX	Packages	Number of Slice	Acquisition time (min)
Axial T1W	Default	800	18	228x200	2	2	36	3.25
	FH	800	18	228x140	2	2	36	3.25
	HF	800	18	228x140	2	2	36	3.25
	rev.Central	800	18	228x140	2	2	36	3.25
	Interleaved	600	18	228x160	2	6	36	4.12
Axial T2W	Default	4700	114	228x200	2	2	36	3.20
	FH	4700	114	228x200	2	2	36	3.20
	HF	4700	114	228x200	2	2	36	3.20
	rev.Central	4700	114	228x200	2	2	36	3.20
	Interleaved	3000	114	228x185	2	6	36	4.00

III. RESULTS

The results of the qualitative analysis obtained from 36 slices by changing slice scan order consist of default, FH, HF, reverse central and interleaved. The images data set of a water phantom scan in T1 weighted images TSE are shown as in Figure 2 and T2 weighted images TSE are shown as in Figure 3. Crosstalk artifacts appear as signal lines with dark images in default, FH, HF, and reverse central technique.

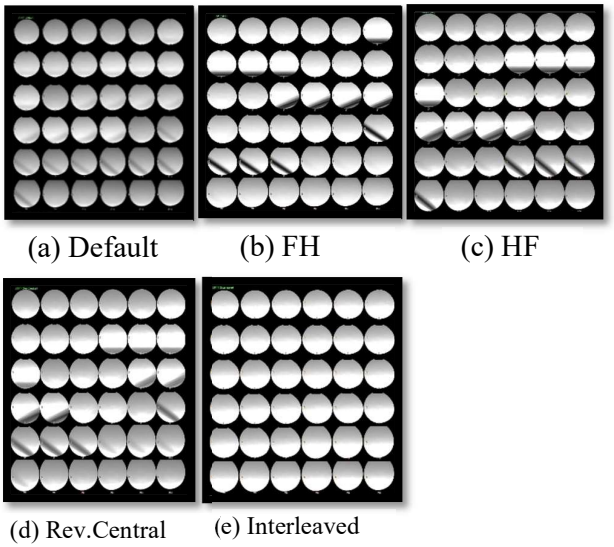

Figure 2. *The images of water phantom T1W TSE, the scan order consists of (a) default, (b) FH, (c) HF, (d) reverse central and (e) interleaved respectively.*

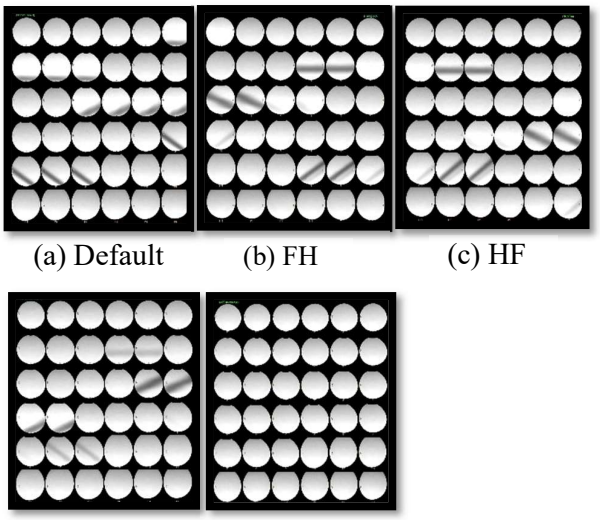

Figure 3. *The images of water phantom T2W TSE, the scan order consists of (a) default, (b) FH, (c) HF, (d) reverse central and (e) interleaved respectively.*

IV. DISCUSSION

Crosstalk artifacts appear as signal lines with dark images in default, FH, HF, and reverse central technique due to slice scan order setup. Slice scan order is parameter controls the order in which the slices are measured and their grouping into packages [4]. The possible values of slice scan order such as

Default is a mechanism applied which tries to maximize the time between the measurements of every pair of adjacent slices. Single package scan A 'first odd, then even' rule is applied within the package. For example, the system chooses the following measurement order in a single package scan: Slice 1,3,5,7... 2,4,6,8... and Multi package scan the slices are first distributed over packages, and the 'first odd, then even' rule is applied within each package. Example for a 2-package scan: For example, the system chooses the following measurement order in a 2-package scan:1,5,9... 3,7,11 in the first package; 2,6,10... 4,8,12... in the second one [4].

FH: Single package scan, Slices are measured in linear order from feet to head. Multi package scan, slices in each package are measured in linear order from feet to head. The measurement order of the packages follows the same rule ('first odd, then even') [4].

HF: Single package scan, Slices are measured in linear order from head to feet. Multi package scan, slices in each package are measured in linear order from head to feet. The measurement order of the packages follows the same rule ('first odd, then even') [4].

Reverse central this setting is available for scan mode M2D only. The slices are measured in a reversed central order, i.e. the outer slices will be measured first, followed by ping pong towards the mid slice. For example, the system chooses the following measurement order: Slice 1,5,2,4,3 or slice 1,6,2,5,3,4.

Interleave method is the aim to reduce the overlapping artifact or crosstalk artifact in this setting is available for scan mode MS and M2D only.

This study sets up the minimum number of packages for the artifact reduction by the square root of the number of slices. The results of the interleave method do not appear as signal lines with dark images.

The limitations in this study are the method of interleave with increase the package, the scan time increased when more packages than

minimally required are selected but spatial resolution and signal to noise ratio (SNR) were maintained.

V. CONCLUSION

By comparing the different slice scan order FH, HF, reverse central and interleaved, the results of the quantitative analysis showed that there was no slice-overlap artifact or cross talk artifact in the interleaved slice acquisition technique.

ACKNOWLEDGEMENTS

The authors forward the sincere thanks to the technologists and staff at the Unit of Magnetic Resonance Imaging, Imaging Center, Phyathai 2 Hospital, Bangkok, Thailand for their kind support in this study.

REFERENCES

[1] Cousins, Joseph P., and Victor M. Haughton. "Magnetic resonance imaging of the spine." JAAOS-Journal of the American Academy of Orthopaedic Surgeons 17.1 (2009): 22-30.

[2] Lavdas, Eleftherios, et al. "Elimination of motion, pulsatile flow and cross-talk artifacts using blade sequences in lumbar spine MR imaging." Magnetic Resonance Imaging 31.6 (2013): 882-890.

[3] Budrys, Tomas, et al. "Artifacts in magnetic resonance imaging: how it can really affect diagnostic image quality and confuse clinical diagnosis?" Journal of Vibroengineering 20.2 (2018): 1202-1213.

[4] Philips Medical Systems Nederland B.V. Veenpluis 4-6 5684 PC Best The Netherlands “MR user: Ingenia/Ingenia S ” 4598 015 42012/781 * 2018-12.

[5] Gandhi, Wingghayarie Patra, et al. "A Phantom Study of Crosstalk Artefact Reduction using Interleaved Method in MR Lumbar." E3S Web of Conferences. Vol. 202. EDP Sciences, 2020.

[6] Lee, Sun-Yeob, et al. "A study on a method to reduce the effect of the cross-talk artifact in a simultaneous, multiple-slice, plane, oblique MRI scan." Journal of the Korean Physical Society 61 (2012): 807-814.

[7] KrupaBDEF, Katarzyna, and Monika Bekiesińska-FigatowskaABDE. "Artifacts in Magnetic Resonance Imaging." (2015).

Contacts of the corresponding author:
Author: Kannikar Kanyakham M.Sc
Institute: Phyathai 2 Hospital
Street: Phaholyothin Road
City: Bangkok
Country: Thailand
Email: *kanni.pp@gmail.com*

Impact of contrast agent administration on water equivalent diameter for size-specific dose estimate (SSDE) calculation in chest CT angiography

Kaewsan Nuttanit[1,2*], Khamwan Kitiwat[1,2]

1 Medical Physics Program, Department of Radiology, Faculty of Medicine, Chulalongkorn University, Pathumwan, Bangkok 10330, Thailand

2 Division of Nuclear Medicine, Department of Radiology, Faculty of Medicine, Chulalongkorn University, Pathumwan, Bangkok 10330, Thailand

**Corresponding author: 6570028130@student.chula.ac.th*

Abstract — **This study aimed to determine the impact of intravenous contrast enhancement on the calculation of water equivalent diameter (D_w) for size-specific dose estimate (SSDE) in chest CT angiography (CTA) using different calculation methods in arterial phase images. A cohort of 230 adult patients who underwent chest CT angiography at King Chulalongkorn Memorial Hospital were included. The 3D Slicer image computing software was used to automatically draw regions of interest in each axial CT image to measure area and mean CT number. The D_w values were calculated in both non-contrast and arterial phase images following the AAPM report 220 utilizing three different methods: the D_w measured at the middle slice ($D_{w,\,mid}$); the average of 3-level slices at the 25th, 50th, and 75th percentiles of CT image series ($D_{w,\,3\text{-}levels}$); and the average of D_w values from the entire scan length ($D_{w,\,whole}$). A paired t-test was used to statistically analyze the differences in D_w values between non-contrast and arterial phase images. Statistically significant differences were observed between D_w values in non-contrast and arterial phases for all calculation methods ($p<0.001$) with the percent difference of 4.24%, 2.67%, and 2.21% for $D_{w,\,mid}$, $D_{w,\,3\text{-}levels}$, and $D_{w,\,whole}$, respectively. Strong correlations were found between $D_{w,\,mid}$ and $D_{w,\,whole}$ as well as $D_{w,\,3\text{-}levels}$ and $D_{w,\,whole}$ with R^2 of 0.90 and 0.97, respectively. The $D_{w,\,3\text{-}levels}$ provided higher accuracy in estimating SSDE for chest CTA compared to $D_{w,\,mid}$, aligning with the values calculated from $D_{w,\,whole}$ approach. This study demonstrated that the enhancement of contrast agent has a notable impact on D_w calculation in chest CTA, particularly concerning D_w calculated at the middle level.**

Keywords — **Water equivalent diameter (D_w), Size-specific dose estimate (SSDE), Chest CT angiography**

I. INTRODUCTION

In 2011, the American Association of Physicists in Medicine (AAPM) published Report No.204, introducing a size-specific dose estimate (SSDE) for estimating radiation dose from CT scanners based on patient size and scanner output [1-2]. The characteristic conversion factor is the patient's physical dimension or the effective diameter (D_{eff}), assuming a uniform patient density and shape. To address this limitation, AAPM Report No.220 [3] recommends the use of a conversion factor based on water equivalent diameter (D_w) to account for variations in both patient dimension and density. However, when the intravenous contrast agent is present in vascular and surrounding tissues during a CT scan, it will increase tissue attenuation and result in an increased CT number. Although contrast agents will increase a patient's D_w, the extent of this increase is unclear. This study aimed to determine the impact of intravenous contrast enhancement on the calculation of D_w for SSDE in chest CTA using the different calculation methods in arterial phase images.

II. MATERIALS AND METHODS

A. Quality control of CT scanner

The quality control of CT scanners was performed following the guidelines of IAEA Human Health Series No.19 [4]. The physics testing consists of mechanical accuracy, radiation output using PMMA phantoms and

pencil IC, and image quality evaluation using Catphan® 600 phantom.

B. Patient enrollment and image acquisition

For this retrospective study, a total of 230 adult patients above the age of 18 years and a weight range of 45 to 75 kg who underwent chest CTA between January 2018 and December 2023, were enrolled. The scans were acquired using three different CT scanners: GE Revolution APEX, GE Revolution EX, and Siemens SOMATOM Force at King Chulalongkorn Memorial Hospital.

Scanning parameters for GE Revolution APEX and GE Revolution EX scanners included a tube voltage of 100 kVp, slice thickness 2.5/1.25 mm, rotation time of 0.5 s, and a pitch of 0.992:1. For the Siemens SOMATOM Force CT scanner, the non-contrast scan was acquired with a tube voltage 120 kVp, slice thickness 2.0/1.0 mm, rotation time of 0.5 s, and a pitch of 1.2, while the arterial phase was acquired with a tube voltage of 100/Sn150 kVp, slice thickness 2.0/1.0 mm, rotation time of 0.28 s, and a pitch of 0.7. All scans were performed with tube current modulation, covering the scan ranges from the lung apex to the adrenal gland. Intravenous injection (IV) of Iopamirol at a concentration of 370 mg/ml was used in the arterial phase of the examination.

C. Calculation of water equivalent diameter

The D_w value was calculated using an axial slice following the AAPM Report No.220 [3] according to the equation as follows:

$$D_w = 2\sqrt{\left(\frac{meanCT}{1000}+1\right)\frac{A_{ROI}}{\pi}}$$

where meanCT is the mean HU value of pixels within the circular ROI of the patient, and A_{ROI} is the total area of the ROI (mm^2). The ROI was contoured following the body of the patient. The 3D Slicer image computing software was used to automatically draw the ROI in each axial CT image to measure area and mean CT number for D_w calculation. The ROI must be large enough to include the entire patient cross-section, but not include irrelevant objects such as the couch.

Each patient image was calculated the D_w value in three methods: the D_w was measured at the middle slice ($D_{w,\,mid}$), the average of 3-level slices at the 25th, 50th, and 75th percentiles of the CT image series ($D_{w,\,3\text{-levels}}$), and the average of D_w values from the entire scan length ($D_{w,\,whole}$). The $D_{w,\,3\text{-levels}}$ calculated by the following equation:

$$D_{w,3-levels} = \frac{D_{w,upper} + D_{w,middle} + D_{w,lower}}{3}$$

where $D_{w,\,upper}$ is the D_w at the 25th percentile, $D_{w,\,middle}$ is the D_w at the 50th percentile, and $D_{w,\,lower}$ is the D_w at the 75th percentile of CT image series. The $D_{w,\,whole}$ can be calculated by the following equation:

$$D_{w,whole} = \frac{\sum_{x=1}^{N} D_w(z)}{N}$$

where z represents the location of each of the N images inside the scan range.

D. Data and statistical analysis

D_w values were reported as mean ± standard deviation, maximum, and minimum. The data were tested for normality using the Kolmogorov-Smirnov test. A paired t-test was used to compare the mean of D_w values between the non-contrast and arterial phases of three calculation methods. The confidence level is set at 95% CI or has a P-value of 0.05 is considered significant. Linear regression analysis was performed to determine the correlation between $D_{w,\,middle}$ and $D_{w,\,whole}$ in arterial phase images, as well as the correlation between $D_{w,\,3\text{-levels}}$ and $D_{w,\,whole}$ of arterial phase images. Statistical analysis was performed using IBM SPSS Statistics software, version 29.0.

The percent difference (%Diff) was used to assess the difference in D_w values between non-contrast and arterial phases. The percentage difference can be calculated by the following equation:

$$\%Diff = \left(\frac{D_w\,(arterial) - D_w(non)}{D_w(non)}\right)$$

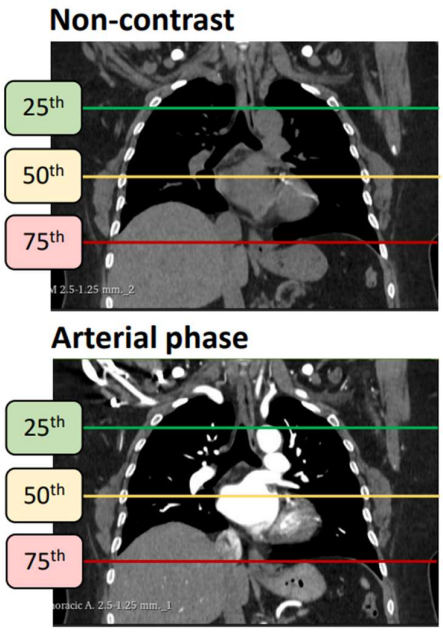

Figure 1. *Illustration of* the location for contouring the ROI to determine the D_w in CT image.

III. RESULTS

A total of 230 patients (144 males and 86 females) with a mean age of 60 ± 17.27 years (ranging from 18 to 93 years) and a mean weight of 61.57 kg (ranging from 45 to 75 kg) were obtained in this study. For non-contrast images, the mean of $D_{w,\,mid}$, $D_{w,\,3\text{-levels}}$, and $D_{w,\,whole}$ was 23.56 ± 2.78 cm (ranged from 16.98 to 32.19 cm), 24.20 ± 2.75 cm (ranged from 17.20 to 32.77 cm), and 24.36 ± 2.63 cm (ranged from 17.39 to 32.95 cm), respectively as shown in Table 1. For arterial phase images, the mean of $D_{w,\,mid}$, $D_{w,\,3\text{-levels}}$, and $D_{w,\,whole}$ was 24.53 ± 2.75 cm (ranged from 18.34 to 33.57 cm), 24.83 ± 2.68 cm (ranged from 18.02 to 33.51 cm), and 24.89 ± 2.59 cm (ranged from 18.17 to 33.39 cm), respectively (Table 1).

The statistical analysis of the data used a paired t-test to determine the difference in D_w values between non-contrast and arterial phase images, showing statistical significance in all calculation methods (P<0.001). Figure 2 shows the box plot of $D_{w,\,mid}$, $D_{w,\,3\text{-levels}}$, and $D_{w,\,whole}$ for non-contrast and arterial phase images. The difference in D_w values between the non-contrast and arterial phases were 4.24, 2.67, and 2.21% for $D_{w,\,mid}$, $D_{w,\,3\text{-levels}}$, and $D_{w,\,whole}$, respectively.

Table 1. *Mean, standard deviation, minimum, and maximum of $D_{w,\,mid}$, $D_{w,\,3\text{-levels}}$, and $D_{w,\,whole}$ for non-contrast and arterial phase images.*

Approach	Non-contrast	Arterial phase
$D_{w,\,mid}$ (cm)	23.56 ± 2.78 (16.98-32.19)	24.53 ± 2.75 (18.34-33.57)
$D_{w,\,3\text{-levels}}$ (cm)	24.20 ± 2.75 (17.20-32.77)	24.83 ± 2.68 (18.02-33.51)
$D_{w,\,whole}$ (cm)	24.36 ± 2.63 (17.39-32.95)	24.89 ± 2.59 (18.17-33.39)

As depicted in Figure 3(a), $D_{w,\,middle}$ (arterial) demonstrated a strong linear correlation with $D_{w,\,whole}$ (arterial), with R^2 values of 0.90. On average, the differences between $D_{w,\,middle}$ (arterial) and $D_{w,\,whole}$ (arterial) were -1.44%, with the largest differences of -13.83%. Figure 3(b) shows a strong linear correlation between $D_{w,\,3\text{-levels}}$ (arterial) and the $D_{w,\,whole}$ (arterial), with R^2 values of 0.97. On average, the differences between $D_{w,\,3\text{-levels}}$ (arterial) and the $D_{w,\,whole}$ (arterial) were -0.27% with the largest differences of -8.11%.

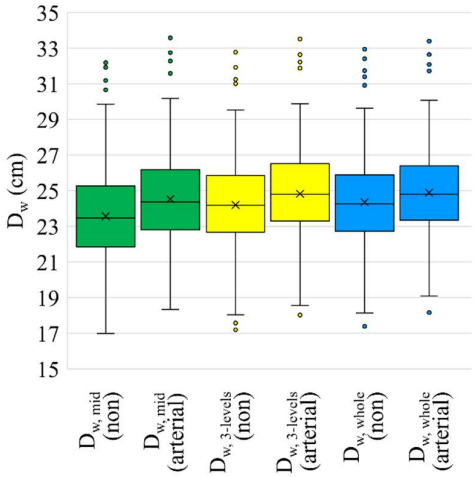

Figure 2. *Box plot of* $D_{w,\,mid}$, $D_{w,\,3\text{-levels}}$, and $D_{w,\,whole}$ for non-contrast and arterial phase images to illustrate the data is distributed.

IV. DISCUSSION

This study used two scanning protocols with different tube voltage settings. According to basic physical principles, the impact of the contrast agent on D_w depends on the tube voltage. However, tube voltages ranging from 70 to 150 kV had a negligible effect on D_w in chest scans [5].

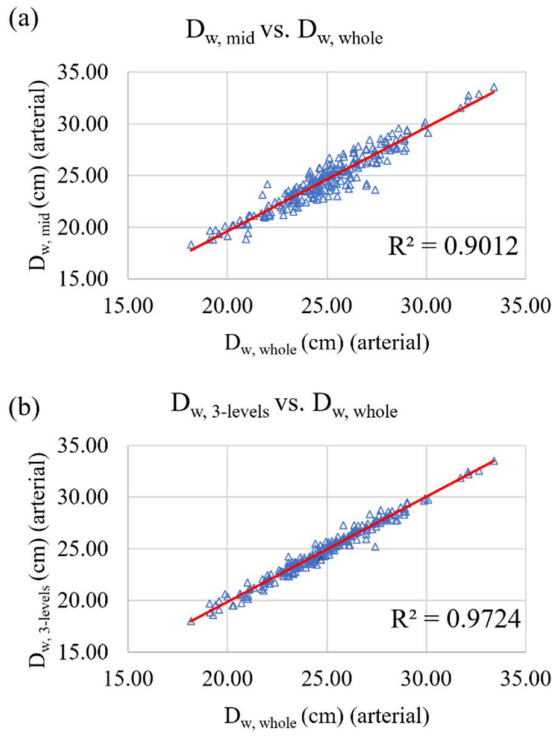

Figure 3. *Scatter plot representing the correlation between two methods. (a)* $D_{w, middle}$ (arterial) and the $D_{w, whole}$ (arterial). (b) $D_{w, 3\text{-levels}}$ (arterial) and the $D_{w, whole}$ (arterial).

To assess the impact of the contrast agent on D_w, the volume of air in the lungs when the patient breathes during the scan should be similar in both non-contrast and arterial phase images. The presence of the contrast agent increases the CT number in vascular and parenchymal tissue, leading to an increase in mean CT number. Consequently, D_w values from arterial phase images increase when compared to non-contrast images. The CT number of air in lung region largely affects mean CT number, especially in the $D_{w, 3\text{-levels}}$ calculation methodology. The slice at 75th percentiles of the CT image series is usually located at the lower part of the lungs. If the patient has poor inspiration in non-contrast and full inspiration in arterial phases, the $D_{w, 3\text{-levels}}$ (arterial) will decrease when compared to the $D_{w, 3\text{-levels}}$ (non).

V. CONCLUSION

This study demonstrated that the contrast agent administration has a notable impact on D_w calculation in chest CTA, particularly concerning D_w calculated at the middle level. D_w based on $D_{w, 3\text{-levels}}$ provides the accuracy for SSDE calculation in chest CTA

REFERENCES

[1] McCollough CH, Leng S, Yu L, Cody DD, Boone JM, McNitt-Gray MF. CT dose index and patient dose: they are not the same thing. Radiology. 2011;259(2):311–6.

[2] American Association of Physicists in Medicine. Size-specific dose estimates (SSDE) in pediatric and adult body CT examinations. AAPM report 204. 2011; 204:1-30.

[3] McCollough C, Bakalyar DM, Bostani M, Brady S, Boedeker K, Boone JM, et al. Use of water equivalent diameter for calculating patient size and size-specific dose estimates (SSDE) in CT: The report of AAPM task group 220. AAPM Rep. 2014;2014:6–23.

[4] Quality assurance programme for computed tomography: diagnostic and therapy applications. Vol. IAEA human health series no. 19. 2012, Vienna, Austria: Inter-national Atomic Energy Agency.

[5] McCollough CH, McCollough SL, Schneider JJ, Moen TR, Weaver JM, Vrieze TJ, et al. Dependence of water-equivalent diameter and size-specific dose estimates on CT tube potential. Radiology [Internet]. 2022;303(2): 404–11. Available from: http://dx.doi.org/10.1148/radiol.210860

Contacts of the corresponding author:
Author: Nuttanit Kaewsan
Institute: Medical Physics Program, Department of Radiology, Faculty of Medicine, Chulalongkorn University
City: Bangkok
Country: Thailand
Email: 6570028130@student.chula.ac.th

Impact of deep learning-based image reconstruction on arm-induced artifacts in abdominal CT

Wongvit-olarn Suppakit[1,2*], Satja Minchanat[2], Bunnag Napisa[2], Khamwan Kitiwat[1,3], Shunhavanich Picha[1,3]

1 Medical Physics Program, Department of Radiology, Faculty of Medicine, Chulalongkorn University, Bangkok, Thailand.

2 Department of Radiology, King Chulalongkorn Memorial Hospital, Thai Red Cross Society, Bangkok, Thailand.

3 Department of Radiology, Faculty of Medicine, Chulalongkorn University, Bangkok, Thailand.

**Corresponding author: suppakit_beem@hotmail.com*

Abstract — **Introduction: Arm-induced streak artifacts are observed in abdominal CT images of patients who cannot elevate their arms during examination. This study aims to compare the arm-induced artifacts in abdominal CT with different arms-down positions between deep learning-based image reconstruction (DLIR), adaptive statistical iterative reconstruction-Veo (ASIR-V) and filtered backprojection (FBP).**

Methods: **A semi-anthropomorphic liver phantom was scanned with three different arm positions: (A) both arms down alongside the body, (B) both arms flexed and forearms on upper abdomen region, and (C) both arms crossed in front of the pelvic area. All scan data were acquired at the same $CTDI_{vol}$ and were reconstructed using DLIR (L-low, M-medium, and H-high), ASIR-V (50% and 100%), and FBP. 40 parallel line segments were placed perpendicular to streak artifacts in a liver parenchyma region and were used to calculate the location parameter of the Gumbel distribution, indicating the strength of the artifacts. Standard deviation in the same region was also examined. In addition, the abdominal contrast-enhanced CT images of 10 patients who underwent CT with arms down in position A were evaluated by two radiologists in terms of artifact and overall image quality on a five- and four-point scale, respectively.**

Results**: For all arm positions of the phantom study, DLIR-H achieved significantly lower image noise and location parameter than DLIR-M, DLIR-L, ASIR-V50%, and FBP ($p < 0.05$). Although DLIR-M and ASIR-V50% were not significantly different in phantom location parameter ($p = 0.0977$), DLIR-M showed better average qualitative scores than ASIR-V50% in patient data both in terms of artifact and overall image quality. ASIR-V100% had lowest SD and location parameter, but performed worst in overall image quality score. Among different arm positions, position C showed the least streaks followed by position B and A, respectively.**

Conclusion**: DLIR reduced arm-induced artifacts in abdominal CT with different arms-down positions more effectively than FBP and ASIR-V, and the image quality was improved with higher strength level of DLIR.**

Keywords**: Abdominal computed tomography, Deep learning-based image reconstruction, Arm-induced artifacts, Gumbel distribution.**

I. INTRODUCTION

Abdominal computed tomography (CT) is normally performed by requiring patients to elevate their arms to prevent streak artifacts which increase image noise and degrade image quality [1].

Iterative reconstruction algorithm (IR) can reduce arm-induced artifacts and improve image quality compared with filtered backprojection (FBP) [1]. However, the limitation of IR is the plastic-looking image when using the high strength level of IR [2].

In recent years, deep learning-based image reconstruction (DLIR) has emerged and become a new method for CT image reconstruction. This method has been developed to achieve better image quality. The performance of DLIR in reducing streak artifacts from different high-attenuation sources has been reported in previous studies [2-4]. To the best of our knowledge, no previous research has studied the effect of DLIR on arm-induced artifacts.

The objective of this study is to compare the arm-induced artifacts in abdominal CT with different arms-down positions between deep learning-based image reconstruction (DLIR; TrueFidelity™), adaptive statistical iterative reconstruction-Veo (ASIR-V) and filtered backprojection (FBP).

II. MATERIALS AND METHODS

A. Phantom study

Phantom and image acquisition

A semi-anthropomorphic liver nodule phantom (QRM, Germany) with both arms of an anthropomorphic CT whole body phantom, PBU-60 (Kyoto Kagaku, Japan), was set in three positions: A) both arms down alongside the body, B) both arms flexed and forearms on upper abdomen region, and C) both arms crossed in front of pelvic area as shown in Figure 1a, 1b, and 1c, respectively. The phantom was scanned on a 256-slice Revolution Apex CT system (GE Healthcare, USA) using a routine protocol for contrast-enhanced upper abdominal CT. The scanning parameters were 120 kVp, smart mA, helical pitch factor of 0.992, and a slice thickness of 2.5 mm, and noise index was adjusted to achieve $CTDI_{vol}$ of 9.90 mGy. Three repeat acquisitions were performed for each arm position.

The images were reconstructed using FBP, two strength levels of ASIR-V (ASIR-V50% and ASIR-V100%), and three strength levels of DLIR (DLIR-L, DLIR-M and DLIR-H).

Quantitative image analysis

Gumbel Evaluation Method

The location parameter of Gumbel plot was calculated using Gumbel evaluation method [5] to represent the strength of streak artifacts. 40 line profiles with 20-pixel length were drawn approximately perpendicular to streak artifact alignment in a liver parenchyma region as shown in Figure 1, and the largest difference between adjacent CT values in each profile was calculated using MATLAB software (MathWorks, Inc.). From the generalized extreme value distribution, the Gumbel distribution shown in Equation 1 can be converted to Equation 2 by applying a double logarithm.

$$F(x) = exp\,[-exp(-\frac{x-\beta}{\gamma})] \qquad \textbf{Equation 1}$$

$$-ln\{-ln[F(x)]\} = \frac{1}{\gamma}x - \frac{\beta}{\gamma} \qquad \textbf{Equation 2}$$

where $F(x)$ is the cumulative probability function when the largest difference in each profile is x, and α, β, and γ are shape, location, and scale parameters, respectively.

The 40 largest differences between adjacent CT values on each image were sorted in ascending orders: $\{x_1 \leq x_2 \leq \ldots \leq x_{40}\}$, and the cumulative probability function was estimated, using the mean rank method, as

$$\hat{F}(x_i) = \frac{i}{n+1}, for\ i = 1,\ldots,n. \qquad \textbf{Equation 3}$$

where n is the number of line profiles. (n=40)

If the plot between x_i and $-ln(-ln[\hat{F}(x_i)])$ is linear, it can be considered to approximate the Gumbel distribution. If we let the fitting line for the plot be $y = mx + c$, the location parameter β can be calculated from

$$\beta = -\frac{c}{m} \qquad \textbf{Equation 4}$$

where c and m are y-interception point and slope of the fitting line.

The location parameter was calculated for three consecutive axial slices of each scan setting.

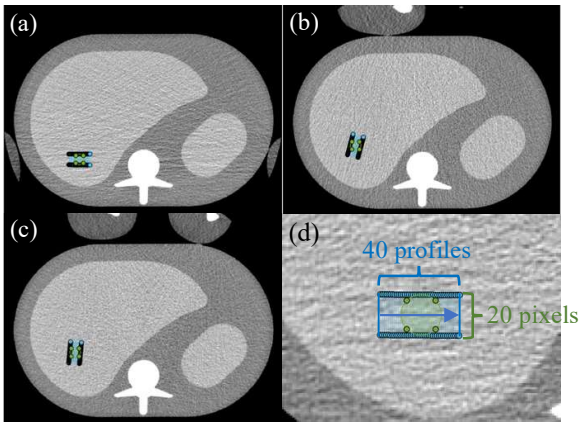

Figure 1. *Example images of phantom in arm position A (a), position B (b), and position C (c), and a zoomed in image of position A (d), showing location of line profiles and ROIs for quantitative image analysis.*

Image noise

The degree of streak artifacts was also evaluated by measuring the standard deviations (SD) of the Hounsfield units (HU). A circular ROI with 20-pixel diameter was placed in the same area as line profiles, as shown in Figure 1.

B. Clinical study

The ethical consideration of this study was approved by Institutional Review Board, Faculty of Medicine, Chulalongkorn University. The abdominal contrast-enhanced CT images of 10 patients who underwent CT scan with arms down alongside the body were retrospectively and prospectively collected from a 256-slice Revolution Apex CT system between February to December 2023 at King Chulalongkorn Memorial Hospital (KCMH). The images were reconstructed using the parameters similar to the phantom images with 1.25 mm slice interval.

Qualitative image analysis

The qualitative image quality evaluation of patient images was performed by 2 radiologists with 3 and 4 years of experiences. The observers were blinded to the reconstruction setting, and the images

were displayed in random order. Artifact and overall image quality were graded using a 5- and 4-point scale, respectively, as shown in Table 1.

Table 1. *Qualitative image analysis criteria.*

Score	Artifacts	Overall image quality
5	No artifacts	-
4	Mild artifacts	Excellent image quality
3	Moderate artifacts	Good image quality without diagnostic limitation
2	Severe artifacts, permits evaluation	Suboptimal, with some diagnostic limitation
1	Very severe artifacts, non-diagnostic image quality	Poor image quality, nondiagnostic

C. Statistical analysis

The comparison of SD and location parameter between different reconstruction methods was performed by Wilcoxon signed rank test using MATLAB software. The p-values < 0.05 was considered to indicate statistically significant difference.

The inter-observer agreement of two observers was evaluated using weighted kappa coefficient (κ). The strength of agreement is classified according to Landis and Koch [6].

III. RESULTS

A. Phantom study

Gumbel plot

Figure 2 shows sample Gumbel plots for FBP. As shown in Table 2, the coefficient of determination (R^2) results ranged from 0.95 to 0.98 over all scan settings. The lowest R^2 was found in ASIR-V100%.

Location parameter of Gumbel plot and standard deviation of the Hounsfield units

The results of location parameter and SD are displayed in Table 2. In order from lowest to highest, ASIR-V100%, DLIR-H, DLIR-M, ASIR-V50%, DLIR-L, and FBP had the average location parameter over three arm positions of 7.64±1.42, 17.81±2.71, 23.69±3.32, 24.28±3.12, 29.18±4.10, and 41.09±4.86, respectively, and had the average SD over three arm positions of 6.10±0.48 HU, 9.11±0.99 HU, 11.87±1.10 HU, 12.92±0.99 HU, 14.41±1.23 HU, and 20.28±1.28 HU, respectively.

Comparing to FBP, the average results over three arm positions of ASIR-V100%, DLIR-H, DLIR-M, ASIR-V50%, and DLIR-L were 81%, 57%, 42%, 41%, and 29% lower for location parameter, respectively, and were 70%, 55%, 41%, 36%, and 29% lower for SD, respectively.

Statistically significant differences were observed between each pairwise comparison of the reconstruction algorithms in both location parameter and SD ($p < 0.05$), except for the location parameter between DLIR-M and ASIR-V50% ($p = 0.0997$).

Among the three arm positions in all reconstructions, position C had lowest location parameter and SD.

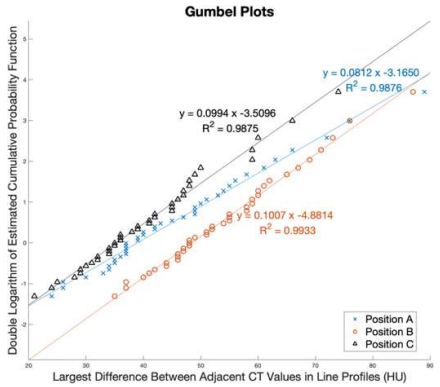

Figure 2. *Gumbel plots of phantom images in three arms-down positions of FBP.*

B. Clinical study

Qualitative image analysis

For the clinical study, the qualitative image quality scores are shown in Table 3. The artifact scores indicated severe to moderate artifacts in FBP, ASIR-V50%, and ASIR-V100%, and moderate to mild artifacts in all DLIRs. The scores of overall image quality were suboptimal with some diagnostic limitations in ASIR-V100% in both observers, suboptimal to good image quality without diagnostic limitation in FBP, ASIR-V50%, and DLIR-L, and good to excellence in some cases of observer 1 in DLIR-M and DLIR-H.

Table 2. *Results of location parameter of Gumbel plot and SD.*

Positions	Reconstruction Algorisms	Location parameter	R^2	SD of the Hounsfield units
A	FBP	41.40±2.16	0.96±0.00	21.06±1.75
	ASIR-V50%	25.32±1.50	0.95±0.01	13.69±1.33
	ASIR-V100%	8.69±0.97	0.95±0.01	6.49±0.86
	DLIR-L	31.01±3.12	0.95±0.01	15.39±2.03
	DLIR-M	25.72±2.62	0.95±0.02	12.90±1.75
	DLIR-H	20.15±2.12	0.95±0.02	10.18±1.40
B	FBP	45.79±1.08	0.98±0.01	20.98±0.43
	ASIR-V50%	26.76±0.54	0.98±0.00	13.26±0.36
	ASIR-V100%	8.20±0.17	0.95±0.01	6.26±0.14
	DLIR-L	32.04±0.90	0.97±0.00	14.80±0.78
	DLIR-M	25.49±0.73	0.97±0.00	12.01±0.66
	DLIR-H	18.43±0.69	0.96±0.01	8.94±0.56
C	FBP	36.09±1.46	0.98±0.00	18.81±0.61
	ASIR-V50%	20.77±0.99	0.98±0.00	11.80±0.46
	ASIR-V100%	6.02±0.53	0.96±0.01	5.56±0.45
	DLIR-L	24.48±1.80	0.98±0.01	13.03±1.00
	DLIR-M	19.85±1.47	0.97±0.01	10.71±0.86
	DLIR-H	14.84±1.27	0.96±0.01	8.21±0.75

DLIR-M showed better average qualitative scores than ASIR-V50% but comparable to DLIR-H in both of artifact and overall image quality scores. ASIR-V100% had the worst overall image quality score.

Table 3. *Qualitative image quality scores.*

Reconstruction Algorisms	Observer 1		Observer 2	
	Artifact	Overall image quality	Artifact	Overall image quality
FBP	2.6±0.5	2.3±0.5	2.5±0.5	2.2±0.4
ASIR-V50%	2.9±0.6	3.0±0.0	2.7±0.5	2.9±0.3
ASIR-V100%	2.5±0.5	2.0±0.0	3.0±0.0	2.0±0.0
DLIR-L	3.4±0.7	3.0±0.5	2.9±0.3	2.8±0.4
DLIR-M	3.5±0.5	3.1±0.3	3.0±0.0	3.0±0.0
DLIR-H	3.5±0.5	3.1±0.3	3.0±0.0	3.0±0.0

κ of artifact was 0.13, indicating slight inter-observer reliability, and κ of overall image quality was 0.66, indicating good inter-observer reliability.

IV. DISCUSSION

This study demonstrated that DLIR can improve arm-induced artifacts and image quality in both quantitative and qualitative image quality scores over FBP and ASIR-V in abdominal CT with different arms-down positions.

Our results were consistent with previous studies [2-4] which reported the ability of DLIR in reducing image noise and improving overall image quality in brain, chest, and abdomen, even though the studies were conducted on images without arm-induce artifacts. We found a slight reduction of artifacts with DLIR, which is consistent with Jensen et al.'s study [4]. Their study was on streak artifacts caused by air in bowel and bone in contrast-enhanced abdominal CT. Our quantitative analysis results indicated that the streak artifacts were reduced when using higher strength level of DLIR. The ASIR-V100% showed least streak artifacts in our quantitative metrics, but it had the worst overall image quality score due to changed image texture [3].

This study had some limitations. First, only DLIR from one vendor was used in this study. Second, this study had limited patient population due to the less common condition of patients studied. Lastly, no abnormal findings were evaluated.

V. CONCLUSION

DLIR algorithm can reduce arm-induced artifacts and image noise in abdominal CT with different arms-down positions more effectively than FBP and ASIR-V. The image quality was improved with higher strength level of DLIR. Changing of arm positions can reduce the arm-induced artifact in abdominal CT examination.

ACKNOWLEDGEMENTS

The authors would like to thank Division of Diagnostic radiology, Department of Radiology, King Chulalongkorn Memorial Hospital for providing instruments in this research.

REFERENCES

[1] Yasaka K, Furuta T, Kubo T, Maeda E, Katsura M, Sato J, Ohtomo K. Full and hybrid iterative reconstruction to reduce artifacts in abdominal CT for patients scanned without arm elevation. Acta Radiol. 2017 Sep;58(9):1085-1093.

[2] Kim I, Kang H, Yoon HJ, Chung BM, Shin NY. Deep learning-based image reconstruction for brain CT: improved image quality compared with adaptive statistical iterative reconstruction-Veo (ASIR-V). Neuroradiology. 2021 Jun;63(6):905-912.

[3] Hata A, Yanagawa M, Yoshida Y, Miyata T, Kikuchi N, Honda O, Tomiyama N. The image quality of deep-learning image reconstruction of chest CT images on a mediastinal window setting. Clin Radiol. 2021 Feb;76(2):155.e15-155.e23.

[4] Jensen, C. T., Liu, X., Tamm, E. P., Chandler, A. G., Sun, J., Morani, A. C., Javadi, S., & Wagner-Bartak, N. A. (2020). Image Quality Assessment of Abdominal CT by Use of New Deep Learning Image Reconstruction: Initial Experience. AJR. American journal of roentgenology, 215(1), 50–57.

[5] Imai K, Ikeda M, Wada S, Enchi Y, Niimi T. Statistical characteristics of streak artifacts on CT images: Relationship between streak artifacts and mA s values. Medical Physics 2009;36:492–9.

[6] Landis JR, Koch GG. The Measurement of Observer Agreement for Categorical Data. Biometrics 1977;33:159.

Contacts of the corresponding author:

Author: Suppakit Wongvit-o-larn
Institute: Medical Physics Program,
Department of Radiology,
Faculty of Medicine,
Chulalongkorn University
Street: Pathumwan
City: Bangkok
Country: Thailand
Email: suppakit_beem@hotmail.com

Localization of epileptogenic zones using radiomic analysis of ictal and interictal SPECT data

Thuwarojsakul Jinjuthathip[1,2*], Sukprakun Chanan[3], Tepmongkol Supatporn[2,3], Sriswasdi Sira[4,5], Rakvongthai Yothin[2,3]

1 Medical Physics Program, Department of Radiology, Faculty of Medicine, Chulalongkorn University, Bangkok, Thailand.
2 Chulalongkorn University Biomedical Imaging Group, Department of Radiology, Faculty of Medicine, Chulalongkorn University, Bangkok, Thailand.
3 Division of Nuclear Medicine, Department of Radiology, Faculty of Medicine, Chulalongkorn University, Bangkok, Thailand.
4 Center of Excellence in Computational Molecular Biology, Chulalongkorn University, Bangkok, Thailand.
5 Center for Artificial Intelligence in Medicine, Research Affairs, Faculty of Medicine, Chulalongkorn University, Bangkok, Thailand.

**Corresponding author: Jinjuthathip29@gmail.com*

Abstract — **Epilepsy is one of the most common and burdensome neurological disorders. Controling postoperative seizures is highly dependent on precise identification of the epileptogenic zone (EZ). In this study, we constructed prediction models to identify the EZ location using radiomic features extracted from SPECT images. Twenty ictal and interictal SPECT datasets were retrospectively collected. All images were preprocessed and registered in the SPECT brain template for statistical parametric mapping (SPM) to calculate the z-score images. Subsequently, the brain was segmented into 85 regions using the AAL2 atlas. For each region, radiomic features were extracted using Pyradiomics. Based on multivariate logistic regression and a five-fold cross-validation strategy, three models were constructed, including the ictal model, the z-score model, and the combined model whose radiomic features were from the ictal image, the z-score image, and their combination, respectively. Their performance was evaluated using the area under the receiver operating characteristic curve (AUC) and compared with readings from nuclear medicine physicians. Validation results showed that, among the three models, the combined model had the highest AUC value (AUC = 0.918 ± 0.044) and sensitivity (0.954 ± 0.044), while the ictal model achieved the highest specificity (0.848 ± 0.052). In comparison, physician readings exhibited a sensitivity of 0.679 ± 0.277 and a specificity of 0.980 ± 0.007. Radiomic analysis showed promising potential for identifying EZ locations from SPECT images in patients with epilepsy. These findings suggested that our radiomic models could serve as an initial screening tool for identifying potential EZ locations, thus potentially aiding physicians in clinical decision making.**

Keywords — **Epilepsy, SPECT imaging, Ictal-Interictal SPECT, Radiomics**

I. INTRODUCTION

Epilepsy is a common burden neurological disorder that affects people of all ages, with its prevalence being more pronounced in both young and old people [1]. For those with refractory focal epilepsy, neurosurgical resection holds the promise of a transformative and life-changing cure [2]. Therefore, achieving control over postoperative seizures is highly dependent on the precise identification of epileptogenic zones (EZs). The occurrence of synchronized neuronal discharge activity during epileptic seizures leads to a substantial increase in regional cerebral blood flow (rCBF), which can be seen using single-photon emission computed tomography (SPECT) with ^{99m}Tc-ethylene-cysteine diethylester (^{99m}Tc-ECD) as an imaging agent [3]. Furthermore, SPECT imaging with ^{99m}Tc-ECD exhibits promising

potential as a noninvasive tool for presurgical evaluation of EZs [4]. However, the interpretation of brain SPECT images remains subjective and poses challenges [5]. Recent advances in quantitative analysis have improved the diagnostic efficacy of SPECT imaging, including radiomics, which involves the extraction of quantitative imaging features through high-throughput methods, allowing the identification of features related to target information [6]. In this study, we constructed radiomic predictive models based on ictal and interictal SPECT images to localize the EZs.

II. MATERIALS AND METHODS

A. Data collection

This study involved imaging data from 18 patients who underwent SPECT scans at King Chulalongkorn Memorial Hospital between 2016 and 2021. The inclusion criteria were as follows: (a) had complete ictal-interictal SPECT data; (b) had epileptogenic zone resection; (c) classified as Engel class I at one-year follow-up. Data collection was approved by the Institutional Review Board of the Faculty of Medicine, Chulalongkorn University, Bangkok, Thailand.

B. Preprocessing

All ictal and interictal SPECT images were preprocessed using statistical parametric mapping (SPM) 12 software, which ran on MATLAB. This process involved normalizing and registering all images to the SPM SPECT brain template for calculating the z-score images using the following equation:

$$z\text{-}score = \frac{I_{subtract} - mean_{subtract}}{SD_{subtract}}$$

where $I_{subtract}$ refers to the subtraction image of coregistered ictal and interictal images, $mean_{subtract}$ is the average pixel value in the subtraction image, and $SD_{subtract}$ is the standard deviation (SD) of the pixel values within the subtraction image.

C. Segmentation and feature extraction

The 120 regions of Automated Anatomical Labeling (AAL) atlas version 2 were combined by two nuclear medicine physicians to achieve 85 regions in total. Radiomic analysis areas were defined by these 85 regions of interest (ROIs) of the combined AAL2 atlas. Each ROI was labeled as EZ or non-EZ based on neurosurgical reports. Within each of these regions, radiomic features were subsequently extracted in three categories—histogram, texture, and wavelet-based—across all ictal and z-score images, using PyRadiomics on Python 3.11.1.

D. Feature selection and model construction

The univariate logistic regression algorithm was used to identify essential features associated with EZ. All patient data were split into training and validation sets using a 4:1 ratio. Subsequently, recursive feature elimination (RFE) with five-fold cross-validation (CV) was applied to achieve crucial features. Following this, prediction models including the ictal model, the z-score model, and the combined model, whose radiomic features were from the ictal image, the z-score image, and their combination, were then constructed using multivariate logistic regression. The performances of the models were evaluated in terms of AUC, sensitivity and specificity.

E. Nuclear medicine physician readings

In this study, the EZs of each patient were localized by two nuclear medicine physicians using ictal images and z-score images without any clinical information or other imaging examinations. The physicians gave their opinion on which regions of 85 ROIs of the AAL2 atlas were the location of the EZ. Their performances were evaluated in terms of sensitivity and specificity.

F. Statistical analysis

The sensitivity and specificity of the three models were calculated at the operating point using the Youden index and subsequently compared to the performance of the nuclear medicine physician readings. All statistical analyses were performed in Python.

III. RESULTS

A. Radiomic features

In this study, ictal and interictal SPECT data from 18 epilepsy patients were used to build three prediction models. From each patient, a total of 1,183 radiomic features were extracted from each of the 85 regions of the combined AAL2 atlas. After RFECV, 14 features were selected for the ictal model and 16 features for the z-score model, resulting in 30 features for the combined model.

B. Radiomic models

The AUC values of the validation set of the three models were calculated and depicted in Table 1.

Table 1. *Mean and standard deviation (SD) of the AUROC of the three models.*

Model	AUC
Ictal model	0.885 ± 0.059
Z-score model	0.813 ± 0.069
Combined model	0.918 ± 0.044

Table 2. *Sensitivity and specificity of the three models and nuclear medicine physician readings.*

Model	Sensitivity	Specificity
Ictal model	0.851 ± 0.149	0.848 ± 0.052
Z-score model	0.758 ± 0.105	0.780 ± 0.068
Combined model	0.954 ± 0.044	0.824 ± 0.078
Physician	0.679 ± 0.277	0.980 ± 0.007

The combined model exhibited the highest AUC value (0.918 ± 0.044) and sensitivity (0.954 ± 0.044). Meanwhile, the ictal model achieved the highest specificity (0.848 ± 0.052) among the three models.

C. Nuclear medicine physician readings

The performances of two nuclear medicine physician readings were evaluated in terms of sensitivity and specificity, as shown and compared to the models' performances in Table 2. The sensitivity of the physicians was 0.679 ± 0.277 and the specificity was remarkably high at 0.980 ± 0.007.

Figure 1 shows the ROC curves of the three models, along with a physician reading comparison.

IV. DISCUSSION

In this study, we constructed three radiomic models based on ictal images, z-score images, and the combination of both image types to localize the EZs using SPECT images. The performances of these models were compared with NM physician readings.

Our preliminary findings showed that the ictal model outperformed the z-score model, potentially attributed to radiomic analysis that captures subtle information beyond human observation. The combined model obtained the highest performance in terms of AUC (0.918 ± 0.044) and sensitivity (0.954 ± 0.044) among the three radiomic models in localizing the

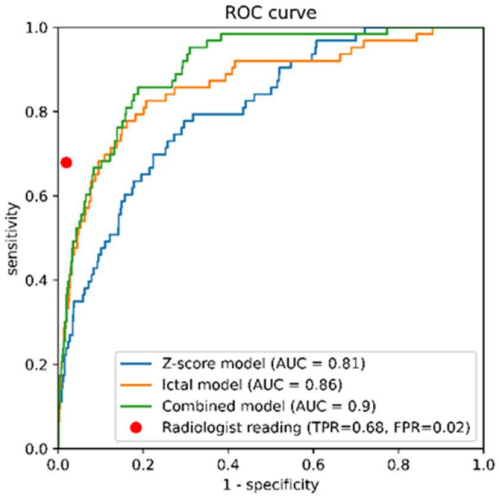

Figure 1. *Receiver operating characteristic (ROC) curve of 3 models compared to physician reading.*

EZs. However, nuclear medicine physicians achieved the highest specificity, confirming that although our models had high performance, they could not replace the role of physician interpretation. The high sensitivity of the combined model and the high specificity of physician readings suggest the possibility of using our model as an initial screening tool to identify potential EZ locations, which could provide crucial guidance to radiologists in verifying and confirming results.

However, it is essential to note that there are some limitations in this study. The small sample size, the retrospective design and the lack of a test dataset may affect the generalizability of our preliminary findings.

V. CONCLUSION

Our preliminary findings show that radiomic analysis has shown promising potential in localizing the EZs from SPECT images. The efficiency of our models suggests an important step in applying radiomic models as preliminary screening tools to identify potential EZ locations, which could offer valuable assistance to radiologists in achieving enhanced accuracy in EZ location.

ACKNOWLEDGEMENTS

The authors thank Sararas Intarak for her help with the model construction.

REFERENCES

[1] Strzelczyk A, Aledo-Serrano A, Coppola A, Didelot A, Bates E, Sainz-Fuertes R, et al. The impact of epilepsy on quality of life: Findings from a European survey. Epilepsy & Behavior. 2023; 142:109179.

[2] Duncan JS, Sander JW, Sisodiya SM, Walker MC. Adult epilepsy. The Lancet. 2006;367(9516):1087–100.

[3] von Oertzen TJ, Gröppel G, Katletz S, Weiß M, Sonnberger M, Pichler R. SPECT and PET in nonlesional epilepsy. Clinical Epileptology. 2023;36(2):104–10.

[4] Fougère Cl, Rominger A, Förster S, Geisler J, Bartenstein P. Pet and SPECT in epilepsy: A critical review. Epilepsy Behav. 2009;15(1):50-5. McNally KA, Paige ALB, Varghese G, Zhang H, Novotny EJ, Spencer SS, et al. Localizing value of ictal-interictal SPECT analyzed by SPM (ISAS). Epilepsia. 2005;46(9):1450–64.

[5] Kumar V, Gu Y, Basu S, Berglund A, Eschrich SA, Schabath MB, et al. Radiomics: The process and the challenges. Magnetic Resonance Imaging. 2012;30(9):1234–48.

Contacts of the corresponding author:
Author: Jinjuthathip Thuwarojsakul
Institute: Division of Nuclear Medicine, Department of Radiology, King Chulalongkorn Memorial Hospital
Street: Pathumwan
City: Bangkok
Country: Thailand
Email: Jinjuthathip29@gmail.com

Prediction of axillary lymph node metastasis in clinically node-negative breast cancer using magnetic resonance imaging-based radiomics

Sukumwattana Wichasa[1,2*], Chirachamnienkal Ruchira[3], Sawaddeemongkhon Varachaya[3], Jirarayapong Jirarat[4], Khongwirotphan Sararas[2,5], Sriswasdi Sira[6,7], Pipatpajong Somchanin[3,8], Rakvongthai Yothin[2,9]

1 Medical Physics Program, Department of Radiology, Faculty of Medicine, Chulalongkorn University, Bangkok, Thailand.
2 Chulalongkorn University Biomedical Imaging Group, Department of Radiology, Faculty of Medicine, Chulalongkorn University, Bangkok, Thailand.
3 Department of Radiology, King Chulalongkorn Memorial Hospital, Bangkok, Thailand.
4 Department of Radiology, King Chulalongkorn Memorial Hospital and The Thai Red Cross Society, Chulalongkorn University, Bangkok, Thailand.
5 Department of Radiological Technology and Medical Physics, Faculty of Allied Health Sciences, Chulalongkorn University, Bangkok, Thailand.
6 Center of Excellence in Computational Molecular Biology, Chulalongkorn University, Bangkok, Thailand.
7 Center for Artificial Intelligence in Medicine, Research Affairs, Faculty of Medicine, Chulalongkorn University, Bangkok, Thailand.
8 Department of Radiology, Faculty of Medicine, Chulalongkorn University, Bangkok, Thailand.
9 Division of Nuclear Medicine, Department of Radiology, Faculty of Medicine, Chulalongkorn University, Bangkok, Thailand.

**Corresponding author: wichasa.suk@gmail.com*

Abstract — **The status of axillary lymph node metastasis (ALNM) is a crucial prognostic factor for breast cancer. It is typically evaluated invasively by sentinel lymph node biopsy (SLNB) or axillary lymph node dissection (ALND). Imaging examination is a noninvasive tool to evaluate ALNM, but it has a high false negative rate. Therefore, this study purposed to construct a radiomic model computed from magnetic resonance imaging (as well as a combined model, which integrated radiomic and clinical models to predict ALNM in breast cancer patients. An entire of 181 patients with clinically node-negative breast cancer were collected and divided into 150 patients for training and validation and 31 patients for test. The model construction involved 4 steps. First, segmentation of the tumor was performed on MRI by 3 delineators. Second, radiomic features were computed via Pyradiomics. Third, the features were selected through the intraclass correlation coefficient (ICC) and recursive feature elimination (RFE). Finally, a multivariate logistic regression model was constructed. The effectiveness of the model was evaluated using the area under the receiver operating characteristic curve (AUC) and was compared using the Benjamini–Hochberg procedure. Of 3,577 radiomic features, six features were chosen to develop the MRI-based radiomic model. It achieved AUC values of 0.805 ± 0.009, 0.807 ± 0.043 in train and validation, and 0.800 in test, outperforming the clinical model in all datasets (p<0.05). The combined model yielded even better performance than the MRI-based radiomic model with an AUC of 0.836 ± 0.012 and 0.793 ± 0.050 in training and validation, and 0.845 in testing, but the difference was only significant at p = 0.07. The MRI-based radiomic model outperformed the clinical model in predicting ALNM in breast cancer patients who were diagnosed as clinically node-negative, enhancing treatment decisions and reducing overtreatment.**

Keywords — **Clinically node-negative breast cancer, Axillary lymph node metastasis, Magnetic resonance imaging, Radiomics**

I. INTRODUCTION

More than 2.26 million cases of breast cancer occurred in 2020 and 685,000 reported deaths. Consequently, it is the most prevalent

cancer among women [1]. The status of axillary lymph node metastasis (ALNM) is the prognostic factor for recurrence and survival of breast cancer. Therefore, the ALNM status is important. The gold standard method for evaluating ALNM status is pathological results of sentinel lymph node biopsy (SLNB) or axillary lymph node dissection (ALND). However, both procedures are invasive and carry a significant risk of complications [2]. The noninvasive method of assessing the ALNM status is physical and imaging examinations, but there are high false negative rates. Therefore, patients initially diagnosed as clinically node-negative must confirm the status of ALNM by pathological examination. This leads to overtreatment for patients with negative ALNM. Consequently, an effective noninvasive tool to evaluate the ALNM status is required. Recently, radiomics has been introduced into medical imaging used for prediction and diagnosis. It is a quantitative information extracted from the images. In this study, we purposed to establish a radiomic model computed from magnetic resonance imaging (MRI) as well as a combined model, which integrated radiomic and clinical models to predict ALNM in breast cancer patients.

II. MATERIALS AND METHODS

A. Patient Selection

This study was granted by the Institutional Review Board of the Faculty of Medicine of Chulalongkorn University in Bangkok, Thailand. A total of 181 invasive breast cancer with diagnosed as clinically node-negative patients at King Chulalongkorn Memorial Hospital between 2010 and 2022 were retrospectively collected. Inclusion criteria were patients who met the following conditions: (i) confirmation of invasive breast cancer, (ii) completion of breast MRI for preoperative evaluation, and (iii) pathologically confirmed ALNM status. The exclusion criteria were patients who (i) had incomplete clinical data; and (ii) received neoadjuvant chemotherapy before MRI examination.

B. Collection of imaging and clinical data

The MRI sequences used in this study consist of (i) dynamic contrast enhancement in the second phase (2^{nd} DCE); (ii) diffusion-weighted imaging (DWI) b-value 800; and (iii) apparent diffusion coefficient (ADC).

For clinical data, we collected the patient's data of age, family history of breast cancer, symptoms, pathological T stage, pathological N stage, histological types, tumor grade, tumor size, and molecular subtypes.

C. Segmentation and feature extraction

The delineators including 2 radiologists and 1 radiology resident who were blinded to the patient's pathology report manually drew the region of interest (ROI) around the tumor on each slice on an axial view using the 3D slicer program version 5.2.1.[3]. In the case of multiple lesions, the largest lesion was selected as the index lesion and the other small lesions were omitted. Radiomic features were calculated from each ROI via Pyradiomics package version 3.0.1.[4]

D. Feature selection and model construction

There were 3 steps in feature selection. First, the independent features of the delineator were assessed using the intraclass correlation coefficient (ICC) at 0.75, 0.90, and 0.95. Second, univariate analysis was used to evaluate the performance of each feature and then rank according to the area under the receiver operating characteristic curve (AUC). Finally, the optimal set of features was obtained using recursive feature elimination (RFE) with split 5-fold cross-validation to remove the unimportant features.

For model construction, an entire 181 patients were partitioned into 120, 30, and 31 patients in training, validation, and test datasets, respectively. The selected features from RFE were used to develop the model using multivariate logistic regression on training and validation datasets with 5-fold cross-validation. The hyperparameters including regularization (L1 and L2) and inverse of regularization strength (0.0001-100) were adjusted to obtain the best model. The most effective model in the validation dataset according to the AUC values was chosen for further performance evaluation in the test dataset.

Table 1. *The performance of axillary lymph node metastasis prediction models.*

Dataset	Model performance (AUC ± SD)			p-value
	Clinical	MRI	Combined	
Train	0.783 ± 0.016	0.805 ± 0.009	0.836 ± 0.012	$< 0.05^{a,b,c}$
Validation	0.754 ± 0.021	0.807 ± 0.043	0.793 ± 0.050	$< 0.05^{a,c}$, 0.07^{b}
Test	0.755	0.800	0.845	-

a: p-value of the comparison between the clinical model and MRI model; b: p-value of the comparison between the MRI and the combined model; c: p-value of the comparison between the clinical model and the combined model.

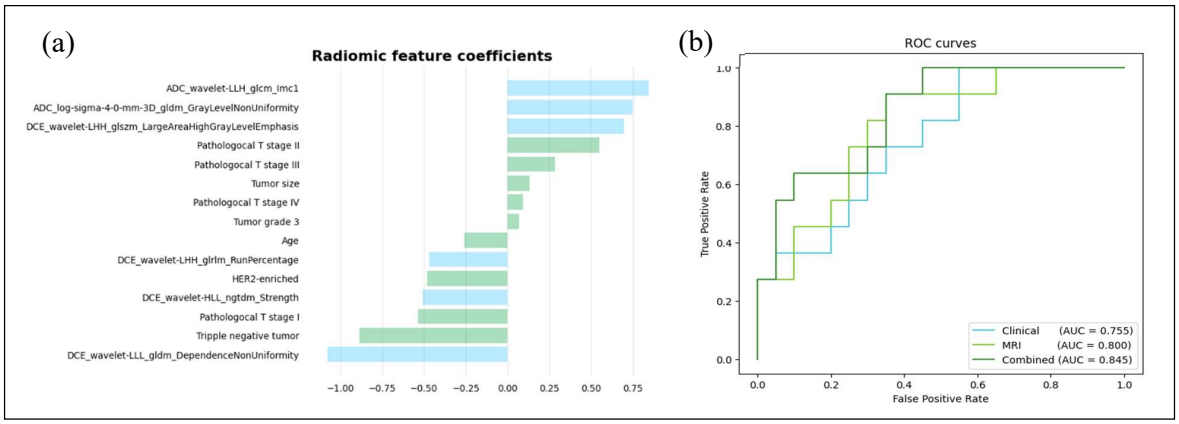

Figure 1. *(a) Features and corresponding coefficients of the combined model. (b) The ROC curves depict the performance of the clinical, MRI, and combined models on the test dataset.*

After constructing clinical and MRI models, the combined model was developed based on the features used in both models with fine-tuning of the new coefficients.

E. Statistical Analysis

The interobserver reliability in delineating the ROI was assessed through ICC. The model performance was evaluated using AUC values and comparisons were made using the Benjamini–Hochberg procedure. All statistical analyses were performed with Python.

III. RESULTS

Table 1 shows the performance of the model in predicting ALNM. The clinical model showed moderate performance in predicting ALNM yielding AUC values of 0.783 ± 0.016, 0.754 ± 0.021, and 0.755 in the training, validation, and test datasets, respectively.

From the ROIs of each patient, 3577 radiomic features were calculated. Features with ICC values exceeding 0.95 were chosen, totaling 3010 features. This suggests excellent consistency among various delineators during the ROI segmentation process [5]. Of these features, the 200 best performing features based on AUC were chosen and utilized as input for RFE. Subsequently, 6 optimal features were chosen from this process to build the MRI model. It achieved effective performance, yielding AUC values of 0.805 ± 0.009 in training, 0.807 ± 0.043 in validation, and 0.800 in testing. The MRI model showed significantly superior performance compared to the clinical model in all datasets ($p < 0.05$).

Additionally, the combined model integrating the clinical and MRI models was established using 15 features with corresponding coefficients as depicted in Figure 1(a). The combined model produced the AUC values of 0.836 ± 0.012, 0.793 ± 0.050, and 0.845 in the training, validation, and test datasets, respectively. The combined model exhibited higher performance than the clinical model across all datasets ($p < 0.05$). Compared to the MRI model, performance was significantly different in training but reached statistical significance only at $p = 0.07$ in validation. However, the combined model exhibited the highest performance in the test dataset. Figure 1(b) illustrates the ROC curve of the models in the test dataset.

IV. DISCUSSION

This study purposed to construct the MRI-based radiomic model as well as the combined model incorporating clinical and MRI models to predict ALNM in patients with breast cancer. Since ALNM status is important for treatment management and prognosis of patients. There is a considerable need for noninvasive tools to assess ALNM status effectively.

Our study used multiple MRI sequences including the 2nd DCE, DWI, and ADC to calculate radiomic features for each patient. Since the 2nd DCE typically reveals peak enhancement and comprehensive tumor boundary, and the DWI-ADC provides information on water restriction within the tumor, which can be detected before morphological changes [6]. Moreover, the study of Chen et al. suggested that utilizing a combination of muti-sequences MRI produced better outcomes compared to an individual sequence. Our MRI model was composed of a combination of features computed from ADC and the 2nd DCE, achieving effective performance. The results demonstrated that the MRI-based radiomic model outperformed the clinical model alone in predicting ALNM, whether using the MRI model alone or in combination with the clinical model.

Nevertheless, this study has limitations. First, being retrospective, it lacks control over scanning parameters that might influence radiomic features. Second, the participants were only from a single institution.

V. CONCLUSION

The MRI-based radiomic model outperformed the clinical model in predicting ALNM in breast cancer patients diagnosed as clinically node-negative, promising in guiding treatment decisions and reducing the risk of overtreatment.

ACKNOWLEDGEMENTS

The authors express gratitude to Napat Ritlumlert for providing valuable suggestions during the construction of the model.

REFERENCES

[1] Ferlay J, Ervik M, Lam F, Colombet M, Mery L, Piñeros M, et al. Global Cancer Observatory: Cancer Today. Lyon: International Agency for Research on Cancer; 2020 Available from: https://gco.iarc.fr/today

[2] Lucci A, McCall LM, Beitsch PD, Whitworth PW, Reintgen DS, Blumencranz PW, et al. Surgical complications associated with sentinel lymph node dissection (SLND) plus axillary lymph node dissection compared with SLND alone in the American College of Surgeons Oncology Group Trial Z0011. J Clin Oncol. 2007;25(24):3657-63.

[3] Fedorov A, Beichel R, Kalpathy-Cramer J, Finet J, Fillion-Robin J-C, Pujol S, et al. 3D Slicer as an Image Computing Platform for the Quantitative Imaging Network. Magn Reson Imaging. 2012;30(9):1323-41.

[4] van Griethuysen JJM., Fedorov A, Parmar C, Hosny A, Aucoin N, Narayan V, et al. Computational Radiomics System to Decode the Radiographic Phenotype. Cancer Res. 2017;77(21):e104–e7.

[5] Koo TK, Li MY. A Guideline of Selecting and Reporting Intraclass Correlation Coefficients for Reliability Research. J Chiropr Med. 2016;15(2):155-63.

[6] Chatterji M, Mercado CL, Moy L. Optimizing 1.5-Tesla and 3-Tesla dynamic contrast-enhanced magnetic resonance imaging of the breasts. Magn Reson Imaging Clin N Am. 2010;18(2):207-8.

[7] Chen Y, Wang L, Dong X, et al. Deep Learning Radiomics of Preoperative Breast MRI for Prediction of Axillary Lymph Node Metastasis in Breast Cancer. J Digit Imaging. 2023;36(4):1323-31.

Contacts of the corresponding author:
Author: Wichasa Sukumwattana
Institute: Medical Physics Program,
Department of Radiology,
Faculty of Medicine,
Chulalongkorn University
Street: Pathumwan
City: Bangkok
Country: Thailand
Email: wichasa.suk@gmail.com

Distant metastasis prediction after radiation treatment in patients with esophageal squamous cell carcinoma using CT-based radiomics

Chanchayanon Thanakrit[1,2*], Kitpanit Sarin[3], Kannarunimit Danita[4], Chakkabat Chakkapong[4], Lertbutsayanukul Chawalit[4], Sriswasdi Sira[5,6], Khongwirotphan Sararas[2,7], Prayongrat Anussara[3], Rakvongthai Yothin[2,8]

1 Medical Physics Program, Department of Radiology, Faculty of Medicine, Chulalongkorn University, Bangkok, Thailand.
2 Chulalongkorn University Biomedical Imaging Group, Department of Radiology, Faculty of Medicine, Chulalongkorn University, Bangkok, Thailand.
3 Division of Radiation Oncology, Department of Radiology, King Chulalongkorn Memorial Hospital, Bangkok, Thailand.
4 Division of Radiation Oncology, Department of Radiology, Faculty of Medicine, Chulalongkorn University, Bangkok, Thailand.
5 Center for Artificial Intelligence in Medicine, Research Affairs, Faculty of Medicine, Chulalongkorn University, Bangkok, Thailand.
6 Center of Excellence in Computational Molecular Biology, Chulalongkorn University, Bangkok, Thailand.
7 Department of Radiological Technology and Medical Physics, Faculty of Allied Health Sciences, Chulalongkorn University, Bangkok, Thailand
8 Division of Nuclear Medicine, Department of Radiology, Faculty of Medicine, Chulalongkorn University, Bangkok, Thailand.

**Corresponding author: 6570036130@student.chula.ac.th*

Abstract — **Esophageal cancer (EC) is the eighth most prevalent malignancy and the sixth leading cause of mortality worldwide. Its unfavorable prognosis and survival rates. We built a radiomic-based model utilizing contrast-enhanced computed tomography (CECT) data, which aims to predict distant metastasis after chemoradiotherapy in patients with esophageal cancer. We retrospectively enrolled 143 patients from King Chulalongkorn Memorial Hospital, analyzing CECT images. Segmentation of the gross tumour volume (GTV) was performed by radiation oncologists. PyRadiomics was employed to extract radiomic features. Feature selection is the use of the intraclass correlation coefficient (ICC) and recursive feature elimination with cross-validation (RFECV). The predictive performance of radiomic features was evaluated through the area under the receiver operating characteristic curve (AUROC), with statistical analysis using the sign test and the Benjamini-Hochberg procedure. Of 1288 radiomic features extracted from the CECT image, a set of 34 radiomic features was selected and incorporated with clinical and dosimetric variables to construct the optimal multivariate model. In validation, this combined radiomic-clinical-dosimetric model yielded an AUROC of 0.725±0.084, which was significantly higher than an AUROC of 0.613±0.048 from the combined clinical-dosimetric model ($p < 0.05$). Our multivariate radiomic model has the potential for an impressive implementation to predict patients with distant metastases of esophageal cancer.**

Keywords — **Esophageal cancer, chemoradiotherapy, Distant metastasis, Radiomic features, CECT imaging**

I. INTRODUCTION

Esophageal cancer (EC) is the eighth most prevalent malignancy, the sixth leading cause of mortality worldwide, and the 10th most common cancer at King Chulalongkorn Memorial Hospital. Esophageal squamous cell carcinoma (ESCC) accounts for more than 70% of cases worldwide, it remains a significant problem in Thailand with a poor prognosis and low survival rates. The

treatment algorithms for ESCC depend on the characteristics of the patient and the tumour, with concurrent chemoradiotherapy (CCRT) showing improved outcomes, especially for locally advanced cases [1]. predicting ESCC patients without relying on radiomics and machine learning is challenging, but radiomics-based approaches have shown significant potential in enhancing ESCC prediction accuracy compared to non-radiomics-based methods [2]. The study aims to develop a predictive radiomic model based on contrast-enhanced CT images to predict distant metastasis after radiation treatment in groups of patients with esophageal cancer, contributing to improved treatment planning and patient management.

II. MATERIALS AND METHODS

A. Patient enrollment

This study was carried out as a single-center retrospective cohort study, including 143 patients diagnosed with ESCC and treated with CCRT at King Chulalongkorn Memorial Hospital between 2006 and 2019. The data collection received approval from the Institutional Review Board of the Faculty of Medicine at Chulalongkorn University in Bangkok, Thailand. The inclusion criteria were as follows: (a) more than 18 years old, (b) patients without distant metastasis, (c) patients with trackable treatment results, and (d) follow-up of more than 2 years.

B. Clinical and dosimetry features

Clinical features were obtained from electronic medical records and the treatment planning system. Data collected included age, sex, EGD location, length of the lesion, T and N stages, body weight, Concurrent chemoradiotherapy, Cumulative radiation dose, Dose per fraction, and number of fractions.

C. Segmentation and feature extraction

Radiomics analysis area is defined by contouring a gross tumor volume (GTV). The GTV was manually drawn by a radiation oncologist in the treatment planning system. Then, three radiation oncologists drew the GTV in 30 patients to measure interobserver variability. The radiomic signatures were extracted using PyRadiomics software version 3.0.1

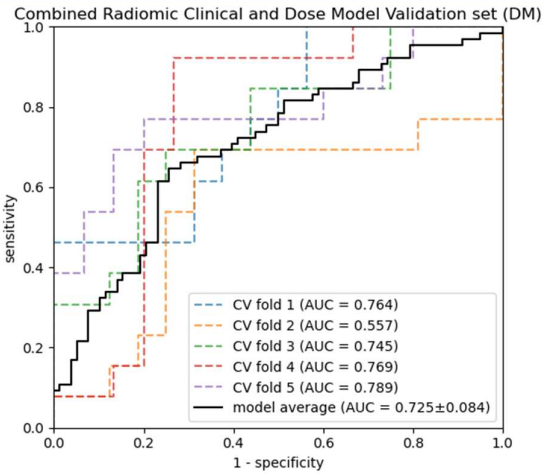

Figure 1. *Receiver operating characteristic (ROC) curve* of the best model for predicting DM.

D. Feature selection

The features dependent on ROI delineators were removed using intraclass correlation (ICC) analysis with a cutoff of 0.50, 0.60, and 0.70 [3]. Subsequently, backward feature elimination was performed to select important features.

F. Statistical analysis

The differential diagnosis model was constructed using multivariate logistic regression analysis. The patients were divided into train and validation groups with a 4:1 ratio and a 5-fold cross-validation (CV) was applied. The best model, with different inverse strengths ranging from 0.001 to 100 and regularization L1 (Lasso) or L2 (Ridge), was chosen based on the area under the receiver operating characteristic curve (AUROC) of 20 5-fold CV (total of 100 repetitions). The mean and standard deviation (SD) of the AUC for each run were calculated by the sign test, and the Benjamini-Hochberg procedure was used to evaluate the p-value of the models. All statistical analyses were conducted with Python.

III. RESULTS

In each patient, 1,288 radiomic signatures were extracted from each region. After RFECV, radiomic, clinical, and dosimetric features were selected to build the models using L2 regularization with an inverse strength of 100 that yielded the highest AUC value in predicting distant metastasis, in

validation, this combined radiomic-clinical-dosimetric model yielded an AUROC of 0.725±0.084, which was significantly higher than an AUROC of 0.613±0.048 from the combined clinical-dosimetric model ($p < 0.05$). as shown in Table 1. The best model ROC curve is shown in Figure 1.

In our model, the selected radiomic features were mainly from CECT images. A wavelet feature; wavelet-HLH_glrlm_LongRunLowGrayLevelEmphasis is for predicting distant metastasis was the feature that had the highest coefficient magnitude.

IV. DISCUSSION

This study focused on the construction of treatment prediction radiomics models, a quantitative approach based on CECT images. Because the simulation of radiotherapy of esophageal squamous cell cancer has significant prognostic and therapeutic consequences.

Our preliminary results showed that radiomic models for treatment prediction could potentially be used as an effective and accurate tool to predict distant metastases. Moreover, the radiomic features called "wavelet-HLH_glrlm_LongRunLowGrayLevelEmphasis" which are wavelet features, have the highest coefficient magnitude in our model.

However, this study had limitations. It was a retrospective study, so the CECT scanning protocol and parameters cannot be controlled, and this work was collected from CT simulation images on different machines. These could affect the radiomic features.

Table 1. *Mean and standard deviation (SD) of the best model to predict distant metastasis (DM) area under the receiver operating characteristic curve (AUROC).*

Models	Mean ± SD	P-value
radiomic-clinical-dosimetric	0.725±0.084	0.05
clinical-dosimetric	0.613±0.048	-

V. CONCLUSION

Our radiomic models could potentially be used as an effective and accurate tool to predict distant metastases. Therefore, it may help radiation oncologists in making treatment decisions and managing distant metastases in patients with ESCC.

REFERENCES

[1] Smyth, E. C., Lagergren, J., Fitzgerald, R. C., Lordick, F., Shah, M. A., Lagergren, P., & Cunningham, D. (2017). Oesophageal Cancer. Nature reviews. Disease primers, 3, 17048.

[2] Wu, L. L., Wang, J. L., Huang, W. et al. (2021). Prognostic Modeling of Patients Undergoing Surgery Alone for Esophageal Squamous Cell Carcinoma: A Histopathological and Computed Tomography Based Quantitative Analysis. Frontiers in oncology, 11, 565755.

[3] Koo, T. K., and Li, M. Y. (2016). A Guideline of Selecting and Reporting Intraclass Correlation Coefficients for Reliability Research. Journal of Chiropractic Medicine, 15(2), 155–163.

Contacts of the corresponding author:
Author: Thanakrit Chanchayanon
Institute: Medical Physics Program,
Department of Radiology,
Faculty of Medicine,
Chulalongkorn University
Street: Pathumwan
City: Bangkok
Country: Thailand
Email: 6570036130@student.chula.ac.th

Development of gold nanoparticle-incorporated gelatin-based hydrogel for radiation dosimetry

Choosin Phavinee[1,3], Thongnuek Peerapat[1], Pungkun Vithit[3], Nguanthean Woraya[4], Tippayamontri Thititip[2*]

1 Department of Biomedical Engineering, Faculty of Engineering, Chulalongkorn University, Bangkok, Thailand.

2 Department of Radiological Technology and Medical Physics, Faculty of Allied Health Sciences, Chulalongkorn University, Bangkok, Thailand.

3 Nuclear and Radiation Metrology Section, Regulatory Technical Support Division, Office of Atoms for Peace, Bangkok, Thailand

4 Division of radiation oncology, Department of radiology, King chulalongkorn Memorial, Thai Red Cross Society

**Corresponding author: Thititip.t@chula.ac.th*

Abstract –

Introduction: **Radiation dosimetry are required for the control of delivered dose and prediction of radiation effects which can be performed with a help of nano-sensors made of radiation sensitive materials - whose physical and/or chemical properties change due to exposure to radiation. Hydrogels, characterized by their hydrophilic- 3D porous polymer networks, offer a versatile platform that can be tailored through the incorporation of noble metal nanoparticles. In this study, we present a novel approach involving the utilization of gold nanoparticles to engineer a colorimetric plasmonic gelatin- based hydrogel nanocomposite.**

Methods: **The investigation involved determining the optimal solution concentration of gelatin- based hydrogel gold nanosensors. Subsequently, the hydrogel was subjected to clinical radiation absorbed doses ranging from 1 to 5 Gy. To analyze the radiation-induced alterations in the hydrogels, a well- established UV- VIS spectrometry method was employed. Consequently, an assessment was conducted to evaluate the radiation response with respect to linearity, accuracy, reproducibility, and stability of the gelatin-based hydrogel gold nanosensors.**

Results: **In the development of this nanosensor, gold ions are confined within a gelatin hydrogel matrix. Upon exposure to radiation, a reduction process ensues, resulting in the formation of gold nanoparticles. This transformation leads to a swift and visually perceptible change in color, converting the initially colorless hydrogel into a distinctly colored state. The introduction of gold nanoparticles serves to augment the generation of hydroxyl radicals through the radiolysis of water, enabling effective clinical radiation-dose verification within the range of 0–5 Gy. This verification is supported by a high linear correlation coefficient, indicative of the nanosensor's strong sensitivity to radiation levels. Notably, the stability of the nanosensor was observed and maintained over a period of 72 hours, highlighting its robustness and reliability for extended use.**

Conclusion: **This innovative approach establishes a reliable and effective method for 3D dose verification, thereby ensuring the safety and efficiency of medical treatments.**

Keywords: **Gold nanoparticle, Gelatin-based hydrogel, Nanosensor, Radiation dosimeter**

I. INTRODUCTION

In modern medical applications, radiation physics and chemistry play a crucial role. Knowledge of ionizing radiation energy

transfer and absorption processes in biological tissue is essential for diagnostics of diseases in radiology and treatment of cancer in radiotherapy. It is necessary to evaluate even the lowest doses of radiation, considering that radiation doses are always associated with radiobiological effects, in order to reduce the potential radiation risk to the patient. Therefore, accurate and sensitive radiation dosimetry are required for the control of delivered dose and prediction of radiation effects [1,2].

Recent advancements in molecular, nanotechnology- enabled sensors provide a novel dosimeter for the detection of ionizing radiation, offering increased selectivity and sensitivity. In clinical radiotherapy, the use of gel dosimeters is beneficial for the high-resolution and precise verification of 3D dose distributions obtained through treatment planning facilities. However, most current dosimeters, e.g. thermoluminescent dosimeters, ionization chambers, and radiographic methods, measure the dose in one or two dimensions only [3]. Owning to enhance sensitivity and efficiency for a lower dose range, nanoparticles like gold, bismuth, platinum, and silver can be incorporated into the gel dosimeter [4].

Gold nanoparticles possess unique optical and physicochemical properties, making them valuable for applications in diagnostics, imaging, and drug delivery [5-7]. Taking advantage of the plasmonic properties of gold nanoparticles, in this study, we present a novel detection system involving the generation of gold nanoparticles within a hydrogel in response to various doses of therapeutic ionizing electrons.

II. MATERIALS AND METHODS

A. Materials

All chemicals were of the highest purity available and were used as received without further purification.

B. Preparation of the Precursor Hydrogel

Stock solutions of C_{16}TAB (50 mM), ascorbic acid (10 mM), and hydrogentetra chloroaurate (10 mM) were prepared in MilliQ water. The C_{16}TAB surfactant was added to hydrogen tetrachloroaurate initially and left undisturbed for 5 min prior to the addition of ascorbic acid. To this mixture, an equal volume of liquid 3% (w/v) gelatin at 25 °C was added and allowed to gel at low temperature prior to irradiation experiments. To prepare 3D gel nanosensors with a final volume of 20 mL, 10.00 mL C_{16}TAB was mixed with 200 μL of hydrogen tetrachloroaurate and 1.0 mL of the ascorbic acid solution (10 mM) was added to this mixture. Finally, 10 mL of 3% (w/v) gelatin at 25 °C was added to this mixture and allowed to gel.

C. Irradiation

The hydrogel nanosensor was exposed to gamma radiation in a Co-60 Gamma Cell 220 Excel (MDS Nordion, Canada). All samples were uniformly irradiated by placing hydrogel cuvettes in a specially designed, in-house polymethylmethacrylate phantom. The samples were exposed to gamma radiation in the central position of the un-rotated chamber of the cell. The dose rate at the central position was equal to 0.6055 ± 0.23 Gy/sec at the time of the experimental procedure.

D. Absorbance spectroscopy

Following irradiation with different doses, the absorbance spectra of the gel samples were measured at wavelengths ranging from 250 to 800 nm using a UV-Visible spectrophotometer (PerkinElmer Lambda 650). All absorbance measurements were carried out 2 hours following irradiation. The absorbance values obtained were offset by subtracting the wavelength at 800 nm. The peak between 500 and 600 nm was used as an indicator for the formation of gold nanoparticles. A maximum absorbance value between 500 and 600 nm versus radiation dose was plotted for all hydrogel samples.

III. RESULTS AND DISCUSSION

Figure 1 shows images of plasmonic gel gold nanocomposites formed following exposure to different radiation doses (0-5 Gy). The underlying principle of this gold nanosensor involves exposing a precursor hydrogel to high-energy radiation. This exposure leads to the hydrolysis

of the hydrogel, generating free radicals that subsequently reduce encapsulated gold ions to form gold nanoparticles within the gel matrix. The intensity of this coloration is determined by the quantity of nanoparticles formed, a factor directly influenced by the absorbed dose of radiation.

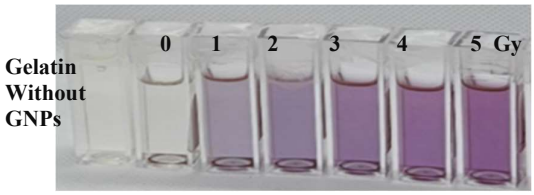

Figure 1*. Images of plasmonic hydrogel gold nanocomposites formed following exposure to different radiation doses (0-5 Gy).*

The calibration curve for hydrogel gold nanosensor using maximum absorbance against radiation dose within the range of 0−5 Gy as shown in Figure 2. Similar result was observed by Lima and coworkers [9].

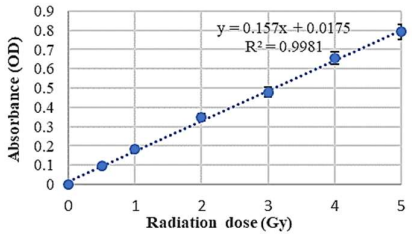

Figure 2*. Calibration curve for hydrogel nanosensor using maximum absorbance against radiation dose within the range of 0−5 Gy, at 2 h post-irradiation.*

Figure 3 shows a schematic illustrates the sequential reaction progression upon the addition of gold nanosensor designed for ionizing radiation detection. Upon the combination of HAuCl4 and C_{16}TAB with heated gelatin, an intense yellow coloration of the hydrogel was observed. This color transformation is attributed to the ligand exchange phenomenon, where Cl− in $AuCl_4$ − is replaced by Br− present in C_{16}TAB. It is postulated that $AuBr_4$ − exists as stable CTA−$AuBr_4$ − metallomicelles within the gelatin matrix. The subsequent addition of ascorbic acid results in the reduction of $AuBr_4$− to $AuBr_2$−, indicating the conversion of gold ions from the trivalent Au(III) state to the monovalent Au(I) state. Due to the weak reducing nature of ascorbic acid, only a partial reduction of gold (from Au(III) to Au(I)) is anticipated in the presence of a high surfactant concentration, attributed to the reduction in the oxidation potential of ascorbic acid within micellar environments [7].

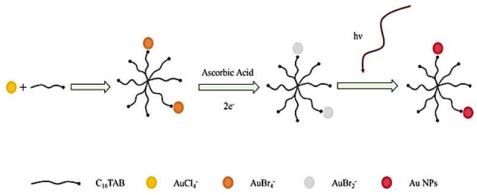

Figure 3*. A schematic illustrates the sequential reaction progression upon the addition of gold components in the plasmonic nanosensor designed for ionizing radiation detection.*

The transition in color, shifting from colorless to violet in C_{16}TAB-loaded hydrogels, was observed within 1-10 minutes post-irradiation (Figure 4), signifying the sensitivity of the plasmonic nanocomposites to radiation.

Figure 4*. Images of the colorimetric response of the plasmonic gel nanocomposites formed in response to a 1 and 4 Gy radiation dose.*

A characteristic spectral peak corresponding to the presence of gold nanoparticles was observed at 540 nm, which exhibited an increase corresponding to the escalating dose of radiation (Figure 5).

Stability of the colorimetric response of the hydrogel nanosensor was investigated for a duration of up to 14 days post-irradiation of gel samples with gamma radiation. Once the change of color in hydrogel gold nanosensor occurred, no further change in color was observed for up to 4 h, indicating stability of the generated nanoparticles over time. (Figure 6)

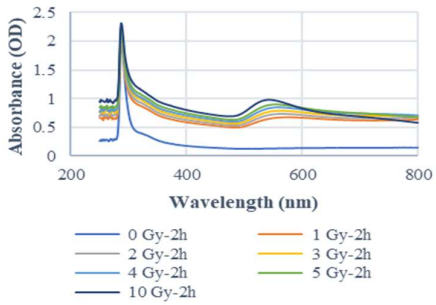

Figure 5*. The UV-vis absorption spectra of both the control (0 Gy) and gamma- irradiated hydrogel samples were acquired at 2-hour post-irradiation.*

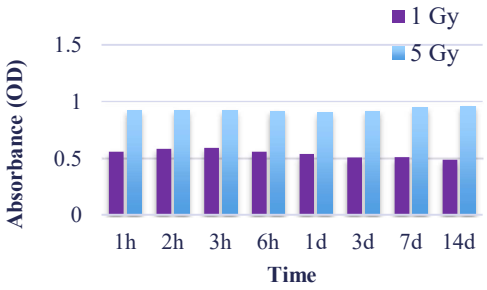

Figure 6*.* Stability of the colorimetric response of the hydrogel gold nanosensor.

IV. CONCLUSION

In this study, we present the successful development of the inaugural gel-based colorimetric nanosensor designed for the detection and prediction of radiation dose in radiotherapy. The outcomes of this study not only contribute to the advancement of 3D dose verification techniques but also serve as inspiration for the development of additional radio-nanosensing hydrogels. This collective progress holds promising implications for enhancing the accuracy and reliability of medical treatments in the field.

ACKNOWLEDGEMENTS

This research was granted by Office of Atoms for Peace and Faculty of Allied Health Sciences, Chulalongkorn university.

REFERENCES

[1] Abu-Gheida, C. A. Reddy, R. Kotecha, M. A. Weller, C. Shah, P. A. Kupelian, O. Mian, J. P. Ciezki, K. L. Stephans and R. D. Tendulkar, Ten-Year Outcomes of Moderately Hypofractionated(70 Gy in 28 fractions) Intensity Modulated Radiation Therapy for Localized Prostate Cancer, Int. J. Radiat. Oncol., Biol., Phys., 2019, 104(2), 325-333.

[2] N. Patel, S. Faria, F. Cury, M. David, M. Duclos, G. Shenouda, R. Ruo and L. Souhami, Hypofractionated Radiation Therapy for Favorable-Risk Prostate Cancer: Long-term Outcomes, Int. J. Radiat. Oncol., Biol., Phys., 2013, 86(3), 534-539.

[3] S. M. Jafari, T. J. Jordan, G. Distefano, D. A. Bradley, N. M. Spyrou, A. Nisbet and C. H. Clark, Feasibility of using glass-bead thermoluminescent dosimeters for radiotherapy treatment plan verification, Br. J. Radiol., 2015, 88(1055), 20140804

[4] K. Pushpavanam, E. Narayanan and K. Rege, Molecular and Nanoscale Sensors for Detecting Ionizing Radiation in Radiotherapy, ChemNanoMat, 2016, 2(5), 385-395.

[5] K. Pushpavanam, E. Narayanan and K. Rege, Molecular and Nanoscale Sensors for Detecting Ionizing Radiation in Radiotherapy, ChemNanoMat, 2016, 2(5), 385-395.

[6] P. R. Chandran and R. T. Thomas, Chapter 14-Gold Nanoparticles in Cancer Drug Delivery, in Nanotechnology Applications for Tissue Engineering, ed. S. Thomas, Y. Grohens and N. Ninan, William Andrew Publishing, Oxford, 2015, pp. 221-237.

[7] K. Pushpavanam, E. Narayanan, J. Chang, S. Sapareto and K. Rege, A Colorimetric Plasmonic Nanosensor for Dosimetry of Therapeutic Levels of Ionizing Radiation, ACS Nano, 2015, 9(12), 11540-11550

[8] C. Daniela, C. Andreea, P. Rebecca and G. Alexandru Mihai, Biomedical Applications of Gold Nanoparticles, Curr. Top. Med. Chem., 2015, 15(16), 1605-1613.

[9] Lima, I. S. ; Guidelli, E. J. ; Baffa, O. Dose Enhancement Factor Caused by Gold Nanoparticles: Influence of the Dosimetric Sensitivity and Radiation Dose Assessed by Electron Spin Resonance Dosimetry. Phys. Med. Biol. 2021, 66, 215013.

Contacts of the corresponding author:
Author: Thititip Tippayamontri
Institute: Department of Radiological Technology and Medical Physics, Faculty of Allied Health Sciences, Chulalongkorn University
City: Bangkok
Country: Thailand
Email: Thititip.T@chula.ac.th

List of Participants

กนกกาญจน์ กึกก้อง
กมลรัตน์ เสืองามเอี่ยม
กรกนก เชวงศักดิ์โสภาคย์
กรกนก ทองบุญมี
กรกมล ประจำเชื้อ
กษมา หอมขาว
กัญจนพร โตชัยกุล
กัณญภัทร ปรางนวล
กาญจนา โชติเลอศักดิ์
กานต์ธิดา จิตตระกูล
กานต์ธิดา จิตตระกูล
กิตติพล เดชะวรกุล
กิตติภัฏ ศรีเมือง
กิติวัฒน์ คำวัน
กุมุทินี ไพรัตน์
เกรียงเดช บุญลือลักษณ์
เกศนภา ชาตินำเพชร
เกศวลัย รักษ์จิรวัฒน์
เกศสุดา จันแก้ว
ขนิดาวุฒิประเสริฐพงศ์
คณนันท์ อุทิตสาร
คมกริช ครองเกียรติเลิศ
จเร วุฒิศาสน์
จงวัฒน์ ชีวกุล
จรูญโรจน์ วงษ์นิล
จองชัย ติลภัทร
จำเนียรพันธ์ เรือนศรี
จิตรลดา จิตรมั่น
จินจุฑาธิบดิ์ ธุวโรจน์สกุล
จินตนา อุ่นจันทร์
จีรวัฒน์ พิมพ์ทอง
จีระภา ตันนานนท์
จีระศักดิ์ คำฟองเครือ
จุฑามาศ ขาวผ่อง
จุมพฏ คัคนาพร
เจษฎาพงษ์ พุ่มร่วมใจ
ฉัตรนภา นันตื้อ
เฉลิมชาติ บุญส่ง
ชลเกียรติ ขอประเสริฐ
ชลธร พิหูสูตร
ชลิญญา บุญสู
ชัยสิทธิ์ สนิทกลาง
ชิษณุพงศ์ บุตรดี
ชุลี วรรณวิจิตร
ไชยา ช่างทุ่งใหญ่
ญานิกา แสวงดี
ญาศุมณฑน์ ถิ่นการ์
ฐิติทิพย์ ทิพยมนตรี
ณฐพร บัวแก้ว
ณปภัช อมรวิเชษฐ์
ณภัทร ฤทธิ์ล้ำเลิศ
ณัฐ น้อยพินิจ
ณัฐกานต์ กิจทิวา
ณัฐชนา วงศ์อินทร์
ณัฐนภา พิณสายทอง
ณัฐนิช แก้วแสน
ณัฐพร ยามรัมย์
ณัฐิดา ระวิวรรณ
ณิชาภัทร ศรีสุเมธาวุปกฤต
ดารณี ภิริยะแสง
ดารัตน์ คำชมภู
ดำรงค์ศักดิ์ ทิพย์ปัญญา
ต้องรัก ยิ้มพักตร์
ทรงธรรม ทุมดี
ทวีป แสงแห่งธรรม
ทิพวรรณ ปอปรีดา
เทพพิทักษ์ วัฒนสาร
ธนกฤต ชาญชญานนท์
ธนภรณ์ กอกำเนิดทอง
ธนภัทร เตียเจริญ
ธนวัฒน์ ถาวรวงษ์
ธนวัฒน์ สนทราพรพล
ธนวิทย์ พิมพ์หงษ์
ธนัชญา หล่อวงค์
ธนัญญา จันปัญญา
ธมลวรรณ เชิดชิด
ธรรม์พิสิษฐ์ หมั่นดี
ธราทิพย์ นาราวงศ์
ธัญรัตน์ ชูศิลป์
ธิดา นิยมไทย
ธีรภัทร ศิริสืบ
เธียรสิน เลี่ยมสุวรรณ
นฤภร พิศโฉม
นลินพันธุ์ บูรณวณิชวงศ์
นวลจันทร์ สท้านสุข
นัฐพงษ์ มูลคำ
นันทวัฒน์ อู่ดี

นันทวุฒิ ธิรานันทกุล
นิพนธ์ สายโย
บริพัฒน์ กัดมั่น
บุญรัตน์ วุฒิประเสริฐพงศ์
เบญจมาศ พรหมเผ่า
ปญา ทรรทรานนท์
ปณัฏฐา ดำทองเสน
ปภัชญา เขียวย้อย
ปภาวรินท์ บูรโสถิกุล
ปรเมษฐ์ วงษา
ประภา สดโคกกรวด
ประสิทธิ์ ตันสังวรณ์
ปริตต์ วงศ์ตระกูล
ปวริศ พจนปรีชา
ปัญญา ภาสว่าง
ปิยทัศน์ แสงดาว
ปิยะพร รัตนะชโยโต
ผกาทิพย์ บุณยะตุลานนท์
พยอม ขันเงิน
พรไพลิน ไพโรจน์สันติกุล
พรชนิตว์ ปุจฉากาญจน์
พรชัย แช่มตา
พรพรรณ นวรุ่งเรือง
พรพรรณ ยงวิทิตสถิต
พฤทธิพร เธียรสิทธิพร
พวงเพ็ญ ตั้งบุญดวงจิตร
พัชรีพร เดชสุภา
พัฒนพงษ์ แสนชนม์
พิชชา ชุณหวาณิชย์
พิชญุตม์ นาคกระแสร์
พุฒิพงษ์ ชาญวิชชุ
ภัคจิรา สาเรือง
ภัทรกันย์ สุวรรณบุตร
ภัทรพล ภัทรกิจบวรกุล
ภัทรวรินทร์ รัตนะมงคลกุล
ภัทรา จันทวรรณโณ
ภัทราพร ฐาศศิร์
ภารณี สหัชเจษฎากุล
ภาริดา ปีติรักษ์สกุล
ภาวิณี ชูสินธ์
ภูมิพัฒน์ ชัยกำธร
เภาวรินทร์ ขยายวงศ์
มงคล คงศักดิ์
มินตรา แก้วเสมอ
โยธิน รักวงษ์ไทย
รวิพิมพ์ สงวนทรัพย์
รัดใจ ใจสุทธิ
รัตนา วัฒน์จิรานนท์
รัสลิน ฐานะ
รุจยา อินต๊ะพรม
ลดาวัลย์ วรพฤกษ์จารุ
ลัคนา อภิปัญญาโสภณ
วรญา เงินเถื่อน
วรรณภา นบนอบ
วรรณวนัช ใจห้าว
วรรณวนัช สุมนาพันธุ์
วรรณวิษา บำรุงภักดี
วรรณิดา พูลนาปล
วราภรณ์ หาญตระกูลสุข
วรินทร รัตนอารียกรณ์
วลัยภรณ์ สุขสันต์เจริญ
วันเฉลิม ทรัพย์รังสี
วาทิณี บุระ
วิชศา สุขุมวัฒนะ
วิภาพร เนืองวงค์
วิมลมาศ ทองงาม
วิยะดา เสนาะสันต์
วิราศิณี เฉลิมชวลิต
วิรุฬห์ มั่นคงทรัพย์สิน
วิศวะ พงษ์ประพันธ์
วิศวะ พงษ์ประพันธ์
วีรชัย อินใจ
ศรายุทธ ครโสภา
ศศิ บุญสวน
ศศิธร อำนวยวัตถากร
ศศิประภา เนียมสวรรค์
ศศิประภา โป๋ชัน
ศักดิ์ชัย บุพอังกูร
ศิริญญา เรืองชาญ
ศิริลักษณ์ ปลัดรักษา
ศิริวรรณ บุญขรัตน์
ศิริวรรณ ศรีใส
ศิวพล หมันสิงห์
ศิวลี สุริยาปี
ศุภกิตติ์ ว่องวิทย์โอฬาร
ศุภลักษณ์ ขจรคำ
สกุลตลา รื่นจิตร์
สมศักดิ์ เขื่อนชนะ
สราณัฐ จันทร์เพ็ญมงคล
สละ อุบลฉาย

สวนีย์ สันติวงศ์
สอางค์ทิพย์ เนตรประเสริฐ
สัจจพร พอใจ
สัตตวัชรา สุวรรณประทีป
สัมฤทธิ์ กิตติพยัคฆ์
สายวรุณ เทียนเครือ
สาวิณี ศรีคล้าย
สิตานัน เมฆนิติกุล
สิทธิพงษ์ สุภาพงษ์
สิรดา เขียนเมืองน้อย
สิรินทรา คล้ายใจตรง
สิริพร ต้นโนนเชียง
สิริพร ว่อง
สิรีธร ชูเชิด
สุเกสรณ์ ปัญญาวงค์
สุชาติ ช้างมณี
สุชีรา ธัญญรักษ์
สุธามาศ วัฒนาชัยสิทธิ์
สุปราณี สุภานันท์
สุพจน์ ศรีมหาโชตะ
สุภลักษณ์ คำเรือง มาร์แชลล์
สุภาดา คำมุกชิก
สุมนา ปะดุกา
สุมลมาลย์ วรพิพัฒน์
สุมาลี ยับสันเทียะ
สุรภี อ่ำโต
สุรินทร์ อวดร่าง
สุริยาพร ธุระทอง
สุวดี โพยมทิพย์
สุวพิมพ์ จันทร์ละออ
สุวิทย์ นวนสาย
เสาวภาคย์ ภูศิริ
แสงเดือน ทรงศรี
แสงสิรินทร์ วงศ์สิรินานนท์
อธิศพันธุ์ จุลกทัพพะ
อนิรุทธ์ วัชรวิภา
อนุพงษ์ คงสา
อภิสรา ดีหะริง
อภิสรา สมบูรณ์ถานะ
อรทัย สิงห์อุสาหะ
อักษราภัค ถาวรนิตยกุล
อัจฉรี ศรีนุเคราะห์
อัญชลี กฤษณจินดา
อัมพร ฝันเซียน
อานนท์ ศรีสุข
อาภาวดี จักราพงษ์
อิสสระ เล็กคง
ไอลดา กุ้ยบำรุง
Choirul Anam
Franco Milano
Huang Shih Hsun
Ke Ching Hsiu
Kosuke Matsubara
Kotaro Fukushima
May Thu Htet
Noriyuki Tawara
Shu Watanabe
Shuichi Shiratori
Sonam Choki
Supriyanto Pawiro
Takayuki Ishida
Yasuo Takatsu
Yin Moe Aye

Sponsors

ABEX
Biz Line
Brainlab
Business Alignment
Dispomed
Elekta
GE Healthcare
GMS
Med I
Nagase
PBI
PT Healthcare
Sukosol
Transmedic
United Imaging
Varian
เพ็ชรคีรี
สถาบันเทคโนโลยีนิวเคลียร์แห่งชาติ

Sponsors


B|A
Business Alignment


varian
A Siemens Healthineers Company


MEDI (Thailand) Co. Ltd.


UNITED
IMAGING


ABEX


Biz Line


BRAINLAB


DISPO-MED
THAILAND


Elekta


GE Healthcare


GMS
global medical solutions


NAGASE


PBI
PREMIER BUSINESS INTER


PolchKiri


PT
HEALTHCARE


SUKOSOL
HEALTHCARE


anu
TINT


Transmedic
Advancing Medical Technologies